Integrated silicon photonics for quantum optics

Dorian Oser

université PARIS-SACLAY

UNIVERSITÉ PARIS SUD
Comprendre le monde, construire l'avenir

NNT : 2019SACLS455

Thèse de doctorat

Integrated silicon photonics for quantum optics

Thèse de doctorat de l'Université Paris-Saclay
préparée à l'Université Paris-Sud

Ecole doctorale n°575 Physique et ingénierie : électrons, photons, sciences du vivant (EOBE)
Spécialité de doctorat : Physique

Thèse présentée et soutenue à Palaiseau, le 28/11/2019, par

DORIAN OSER

Composition du Jury :

Philippe Grangier Directeur de recherche CNRS, Institut d'Optique Graduate School (LCF)	Président
Christophe Galland Professeur des universités, École polytechnique fédérale de Lausanne (LQNO)	Rapporteur
Wim Bogaerts Professeur des universités, Ghent University (IMEC)	Rapporteur
Ségolène Olivier Ingénieure de recherche, Commissariat à l'énergie atomique et aux énergies alternatives (LETI)	Examinatrice
Éric Cassan Professeur des universités, Université Paris-Sud (C2N)	Directeur de thèse
Laurent Labonté Maître de conférences, Université Côte d'Azur (InPhyNi)	Co-encadrant de thèse
Carlos Alonso-Ramos Chargé de recherche CNRS, Université Paris-Sud (C2N)	Invité

Contents

Acknowledgments

Before going into the scientific content of this thesis, I would like to thank all the wonderful people I met and worked with during these three years.

First, I would like to thank the president of the jury, Philippe Grangier, and the jury members, Christophe Galland, Wim Bogaerts, and Ségolène Olivier. Thank you for taking the time to read my manuscript and for having accepted to come to my defense.

I want to particularly thank Laurent, Éric and Carlos. You took me on this incredible journey. I couldn't be happier to have chosen this PhD and, of course, that you chose me.

Éric, merci pour votre soutien et votre aide. Être directeur de l'école doctorale, enseignant à Orsay et suivre les nombreux autres doctorants, ne laisse pas beaucoup de temps libre. Malgré tout, vous avez toujours été disponible quand j'en avais besoin. Merci aussi de ne m'avoir jamais mis de pression et de m'avoir laissé une grande autonomie.

Laurent, *Mr Goodness*, merci énormément, pour ta bonne humeur en toute circonstance, pour ton aide constante, et ton écoute indéfectible de mes problèmes dans la "cafet". Venir à Nice a toujours été un plaisir grâce à toi!

Carlos! ¡Muchas gracias! My work at the C2N would not have been the same without you. On top of teaching me all the little joys of guided optics, you helped me every step of the way.

Laurent et Seb, vous êtes un peu les papas de deux belles familles dont j'ai été heureux de faire partie. Merci à tous les deux me m'y avoir accueilli. Merci pour vos expertises et vos conseils immenses.

Florent, merci pour ton aide dans le froid et l'obscurité de la salle de manip. Faire des expériences quantiques n'aurait pas été aussi amusant seul !

Xavier, sans toi je n'aurai rien pu faire. C'est grâce à ton acharnement à faire marcher la NanoBeam que j'ai pu avoir des échantillons. Je te remercie infiniment.

Greg, merci de faire tourner Nice. Merci pour le soutien technique. Merci pour tout les programmes LabView qui m'ont faire gagner un temps fou.

Olivier and Xin, thank you for the kind help during the experiments, for sharing the equipments and your knowledge with me.

Diego, Elena, and Dinh, it was a lot of fun sharing the office with you. You were the people that I saw almost every day and I am thankful for it. We had a lot of good times and it was a pleasure to come to the lab also thanks to you.

Samueeeeeel! Too bad you had to leave during my PhD. It was too early, but anyway it would have always been too early. Thanks for all the interesting and the amazing times my friend!

I also want to thank all the others members of the teams, Delphine, Qiankun, Daisy, Weiwei, Daniel, Jianhoa, Jerry, Mattias, Guillaume, Vladyslav, Lucas, Christan, Joan, Alicia, Miguel, Sylvain, Francois, Nino, Tommaso, Floriane, Mattis, Florent, Djelan, Florian, and specially Martina. Thank you for your advices, your help, your good mood, and for sharing so many good moments with me during these three years. Finally, to everyone else I had the pleasure to share the lab with, Thank You!

Acronyms

ADR Add-Drop Ring. 70, 76

ASE Amplified Spontaneous Emission. 116, 120, 129, 133, 138, 139, 140, 141, 142, 156

BOX Buried Oxide layer. 53, 55

BS Beam Splitter. 73, 75, 116, 123, 130, 139, 140, 141, 150

BWF Biphoton Wave Function. 128, 129, 131

CAR Coincidence-to-Accidental Ratio. 117, 120, 121, 122, 134, 135

CBG Closure of the Band Gap. 88, 89, 90, 91, 92, 93, 94, 95, 96, 104, 107, 109, 110

CMOS Complementary Metal-Oxide-Semiconductor. 46

CMT Coupled Mode Theory. 104, 106

CSBF Corrugation-Shifted Bragg Filter. 85, 86, 88

CW Continuous Wave. 32, 45, 59, 116, 120, 128, 129, 131, 133, 135, 143, 150

DCWBF Double Corrugation Width Bragg Filter. 85, 86

DWDM Dense Wavelength-Division Multiplexers. 120, 138, 139, 140, 141, 142

EBL Electronic Beam Lithography. 53, 54, 55, 56, 58, 59, 96

F-MI Franson-type Michelson Interferometer. 133, 135, 138, 140, 141

FDTD Finite-Difference Time-Domain method. 86, 89, 93, 98, 99, 100

FSR Free Spectral Range. 65, 67, 69, 70, 74, 75, 76, 78, 105, 110, 119, 120, 128, 130, 134, 135, 136

FWHM Full Width at Half Maximum. 64, 66, 67, 117, 130

GC Grating Coupler. 59, 60

GDS Graphic Database System. 54, 56, 58, 59, 95

ITU International Telecommunication Union. 48, 51, 53, 64, 67, 68, 76, 110, 120, 144

JSA Joint Spectral Amplitude. 39, 128, 129, 130

MAD Modal Add-Drop. 71, 72, 73, 76, 107, 109, 110, 115

MMI Multi-Mode Interferometers. 73, 74

MZI Mach-Zehnder Interferometer. 32, 52, 65, 73, 74, 75, 76, 78, 79, 111, 132, 144, 145

OCSBF One-sided Corrugation-Shifted Bragg Filter. 85, 88

ODCWBF One-sided Double Corrugation Width Bragg Filter. 85

OSA Optical Spectrum Analyzer. 87, 103, 130

PC Polarization Controler. 116, 120, 129

PDC Parametric Down Conversion. 31, 32, 44, 45, 46

PMMA polymethylmethacrylate. 55, 61, 63, 64, 68, 73, 76, 81, 93, 94, 105

PPLN Periodically Poled Lithium Niobate. 44, 45

QD Quantum Dot. 41, 44, 46

QIP Quantum Integrated Photonics. 40

QIS Quantum Information Science. 20, 114, 135, 137

QKD Quantum Key Distribution. 20, 21, 45, 138, 157

SEM Scanning Election Microscope. 43, 55, 58, 60, 65, 67, 69, 82, 83, 85, 97, 105

SET Stimulated Emission Tomography. 129, 130

SFWM Spontaneous Four-Wave Mixing. 36, 37, 38, 46, 47, 50, 51, 52, 63, 64, 65, 75, 78, 114, 115, 132

SNSPD Superconducting Nanowire Single-Photon Detector. 43, 115, 124, 125, 134, 135

SOI Silicon-On-Insulator. 21, 47, 48, 53, 78, 81, 128

SPAD Single Photon Avalance Detector. 43, 130

SPDC Spontaneous Parametric Down Conversion. 36, 37

SWG Sub-Wwavelength Grating. 107, 109

TBS Tunable Beam Splitter. 73, 76

TDC Time-to-Digital Converter. 116, 117, 120, 124, 134, 135

TE Transverse-Electric. 61, 62, 82, 90, 92, 100, 111, 116, 134, 156

TF Tunable passband Filter. 116, 117

TM Transverse-Magnetic. 60, 61, 62, 75, 105, 106, 111, 134, 138, 156

TPA Two-Photon Absorption. 38, 47, 78, 121

UNF Ultra-Narrow Filter. 130, 131

UV Ultraviolet. 44, 55, 56, 100, 101

Résumé en français

La recherche et le développement dans le domaine de la photonique ont connu une croissance considérable durant les dernières décennies [1]. Ses applications ont rapidement été industrialisées puis commercialisées en ouvrant de nouveaux marchés, comme en attestent par exemple les télécommunications par fibres optiques, les CD/DVD, les lecteurs de codes-barres ou encore les écrans plats. Dans tous ces systèmes, de nombreuses fonctionnalités sont présentes : émission, amplification, détection, modulation et transmission de la lumière. Dans le même temps, la photonique souffre dans son ensemble d'un degré d'intégration plus modeste que d'autres domaines tels que l'électronique intégrée, limitant aujourd'hui la complexité et le nombre de fonctions ainsi que leur potentiel de rupture technologique. Depuis quelques années, ce trait caractéristique s'est atténué avec le développement rapide de la photonique silicium, exploitant à des fins optiques et optoélectroniques, les processus de fabrication planaires de la microélectronique. Cette évolution a profité non seulement au développement de nouvelles applications, mais a aussi ouvert un vaste champ d'investigations dans plusieurs domaines de la physique (optique quantique, métrologie sur puce, etc), pour lesquels l'intégration photonique silicium sert de support et se voit simultanément induire par ces défis plus exploratoires de nouveaux enjeux en termes de développement de composants et de circuits optiques.

La physique quantique a été, quant à elle, au cœur de grandes avancées du dernier siècle [2]. Les propriétés comme la superposition d'états, la dualité onde-corpuscule et l'intrication sont complètements contre-intuitives. Pourtant, elles ont été la base d'une meilleure compréhension physique de la matière. La manipulation directe des états quantiques permet déjà des avancées technologiques fantastiques, une d'elles étant le développement de nouvelles fonctionnalités dans le domaine des télécommunications quantiques. La cryptographie quantique est la technologie quantique la plus proche des applications [3]. Elle permet de vérifier qu'une clé de cryptage a été échangée de manière sécurisée. L'étape suivante concerne les communications par canaux quantiques, requérant des sources d'intrication. Néanmoins, la plupart des démonstrations de systèmes d'optique quantique sont actuellement déployées en espace libre sur des tables optiques. Ces expériences sont coûteuses et encombrantes, difficiles à envisager pour des applications à grande échelle. En revanche, ces inconvénients peuvent être précisément contournés par l'utilisation de la photonique car elle permet assez naturellement de fabriquer des circuits optiques stables et compacts combinant les fonctions essentielles nécessaires à la mise en œuvre d'expériences quantiques.

Toute implémentation expérimentale d'optique quantique requiert trois étapes principales : la production d'états quantiques de la lumière, la manipulation de ces états et leurs détection. Il est difficile d'intégrer simultanément deux ou trois de ces étapes. Il existe de nombreuses plateformes technologiques pour l'intégration d'expériences d'optique

quantique, comme les plateformes III-V [4], niobate de lithium [5], silicium [6], etc. La plateforme silicium possède en revanche une avance en terme de fabrication car elle s'appuie sur tous les développements précédents effectués pour la microélectronique qui offre des possibilités de fabrication et d'intégration à grande échelle. Le choix de cette thèse a donc été de s'appuyer sur cette voie technologique privilégiant la conception et l'assemblage, la fabrication, et la caractérisation de composants et de circuits en photonique silicium. Les étapes de réalisation et de fabrication en salle blanche ont toutes été réalisées à partir de substrats silicium sur isolant (SOI) au sein de la centrale de technologie du C2N, essentiellement par lithographie électronique et gravure. Les mesures d'optiques quantiques ont quant à elles été realisées à l'INPHINI.

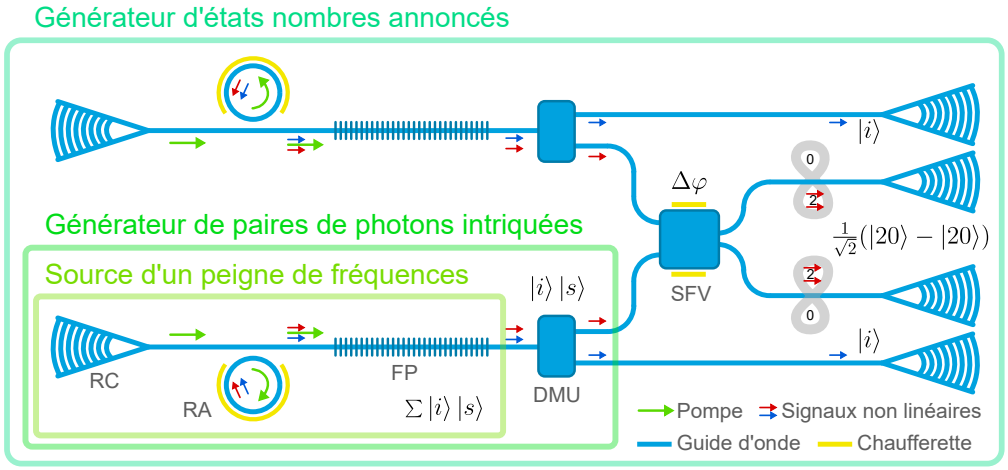

Figure 0.1.: Schéma de circuit photonique quantique possible avec différents composants indiqués, réseau de couplage (RC), résonateur en anneau (RA), filtre de pompe (FP), démultiplexeur (DMU) et diviseur de faisceau ajustable (DFA). Le RA produit des paires de photons une fois pompé. Les paires sont alors séparées puis combinées pour produire des états NOON annoncés.

Cette thèse s'inscrit ainsi dans le domaine de l'optique quantique sur puce, et aborde parmi ses objectifs essentiels la réalisation d'un générateur de paires de photons intriqués en énergie-temps sur puce, ressource essentielle pour l'établissement d'un réseau de télécommunications quantiques ou pour effectuer des calculs quantiques intégrant des générateurs d'états quantiques. Un schéma représentant une source d'un peigne de fréquences et son extension en un générateur de paires de photons intriqués est montré en figure 0.1. La source est constituée d'une cavité en anneau qui produit un peigne de fréquences centré sur la raie d'un laser de pompe utilisé pour exciter les effets non linéaires du silicium. Dans notre cas, les paires sont générées par mélange à quatre ondes spontané (SFWM), processus dans lequel deux photons de pompe sont convertis en deux photons appelés signal et idler dont les fréquences sont respectivement plus élevée et inférieure à celle de la pompe. Cependant, une fois générées, les paires de photons doivent être séparées du laser de pompe. La différence de puissance entre la pompe et la lumière non linéaire doit être de l'ordre de 100 dB. Une opération de filtrage extrêmement

efficace doit donc être implémentée après la cavité. Or, la distance spectrale entre la pompe et les paires n'est que de quelques nanomètres, ce qui limite la bande passante disponible pour la réjection optique de la pompe.

La problématique du filtrage d'un signal optique de pompe a été largement explorée dans la littérature [7, 8, 9, 10, 11, 12, 13]. L'utilisation d'interféromètres ou de résonateurs en anneaux cascadés permet de réaliser un filtrage optique actif, chaque composant étant contrôlé séparément pour aligner leur longueur d'onde sur celle de la pompe. Cette solution fonctionne en effet, mais requiert une grande complexité d'utilisation et de calibration. Une autre solution consiste à implémenter un long filtre de Bragg (conventionnel) ne requérant cette fois-ci pas de contrôle actif. Toutes ces approches conduisent cela dit à de fortes pertes en transmission des paires de photons, rendant inaccessible la réalisation effective d'une source intégrée incluant un filtrage efficace de la pompe optique. En dehors même de ces aspects, les paires de photons produites doivent présenter certaines propriétés particulières afin de pouvoir les dédier à des applications quantiques. Les photons de chaque paire doivent être bien sûr intriquées, indiscernables, posséder le bon type d'état spectral anti-corrélé, mais aussi ne doivent pas se superposer les unes aux autres. L'indiscernabilité et l'intrication quantiques peuvent être testées par une mesure de visibilité d'interférences à deux photons dans une expérience de type Franson [14]. Pour caractériser le type d'état à deux photons générés, une mesure de densité spectrale jointe doit être simultanément effectuée. Finalement, afin de s'assurer qu'une seule paire est générée, une expérience de corrélation d'ordre deux doit compléter le tout. Toutes ces expériences, relativement complexes dans leur implémentation du fait des très faibles niveaux de signaux, ont été réalisées dans le cadre de la thèse.

Le premier enjeu auquel nous nous sommes attachés a été la réjection de la pompe optique servant à produire les paires de photons, car elle constitue la principale limitation de l'intégration d'une source paramétrique sur la plateforme silicium. Un autre aspect a concerné la production des paires de photons par des cavités optiques diélectriques. Ces dernières doivent à la fois présenter les caractéristiques à même de produire de manière efficace des paires de photons sur une large bande spectrale (> 40 nm), mais nous nous sommes également attachés à ce que leurs spectres de résonances optiques soient compatibles avec les canaux de télécommunication standard internationaux (ITU) afin d'apporter une démonstration de principe. Finalement, nous avons caractérisé les propriétés quantiques et statistiques des paires de photons produites.

La thèse s'est articulée autour du schéma de principe représenté en figure 0.1. Les composants et circuits photoniques (silicium) ont été conçus et fabriqués, puis caractérisés pour réaliser la fonction décrite sur cette figure, nécessitant le développement de réseaux de couplage, de guides d'ondes, de résonateurs en anneaux, de filtres de Bragg en guide d'ondes, leur assemblage et l'ajustement de leurs propriétés pour la réalisation d'un générateur de photons intriqués.

Notre stratégie a été, pour commencer, d'améliorer les structures de filtres de Bragg proposées dans la littérature et buttant toutes sur deux limitations importantes : un compromis réjection / bande passante optique très défavorable à l'obtention d'une forte réjection ($\gg 40$ dB) couplée à une faible bande passante ($\ll 10$ nm), et par ailleurs un

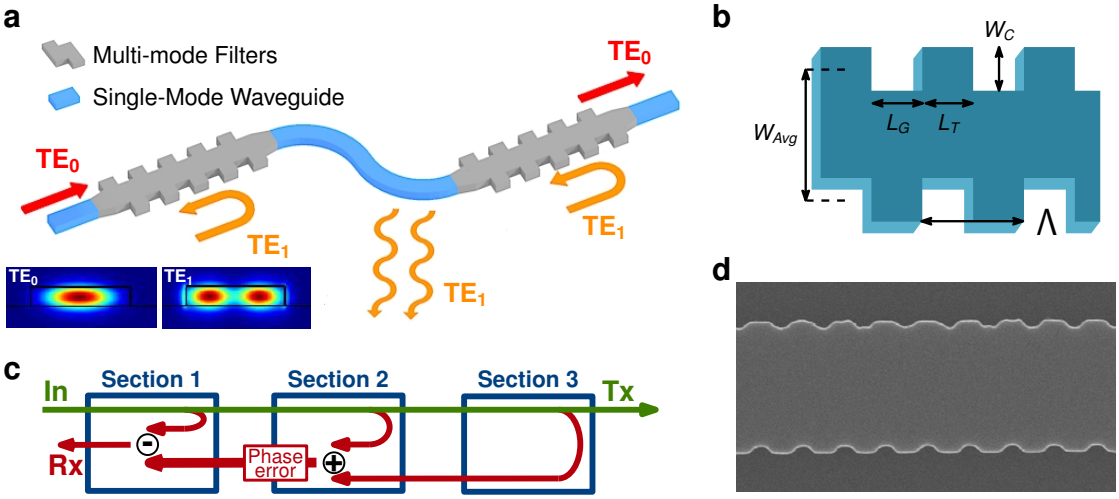

Figure 0.2.: (a) Vu schématique du filtre de Bragg multimode cascadé. Le mode fondamental TE_0 est réfléchi dans le mode supérieur TE_1. Des guides d'onde monomode connectent les filtres, ce qui force TE_1 à être radier, brisant ainsi la cohérence de phase entre les filtres. (b) Schéma de la géométrie du guide d'onde de Bragg. (c) Diagramme illustrant la propagation de la lumière dans le système. (d) Image par microscope électronique à balayage du filtre fabriqué. [15]

effet de saturation du maximum de réjection optique des filtres, ce, indépendamment de leur longueur. Pour palier ce problème, nous avons proposé une approche originale consistant en une mise en cascade non conventionnelle de sections de filtrage garantissant l'indépendance de phase des sections successives entre elles par une ingénierie modale de la réflexion de Bragg dans un mode d'ordre supérieur du guide faiblement multimode véhiculant les signaux. Un réseau de Bragg multimode a ainsi été conçu et implémenté. Par cette stratégie, le mode incident est porté par le mode fondamental transverse électrique TE_0 du guide tandis que le mode réfléchi est le mode d'ordre supérieur TE_1. En plaçant entre les filtres un guide d'onde monomode, qui ne propage à faibles pertes que le mode TE_0, il est possible de laisser radier les signaux correspondant à la réflexion par une section donnée et ainsi de briser la cohérence de phase globale de la structure, voir figure 0.2 [15]. Cette stratégie nous a permis de démontrer un filtre passif rejetant 85 dB (figure 0.4) avec des pertes de transmission équivalentes à un guide d'onde de même longueur (2 mm).

Grâce à ce filtre, nous avons pu intégrer un résonateur en anneau et le système de réjection de la pompe optique conçu. Afin de permettre une production efficace de paires de photons, la largeur des guides d'ondes a été ajustée afin d'opérer dans la zone classique de dispersion anormale, garantissant la condition d'accord de phase entre la longueur d'onde de pompe et les résonances de la cavité nécessaire au renforcement des effets nonlinéaires d'ordre 3. Les cavités réalisées ont été légèrement surcouplées afin de permettre une meilleure extraction des paires de photons depuis le guide adjacent à chaque résonateur en anneau. Un intervalle spectral libre (ISL) de 200 GHz a été

choisi afin d'assurer la compatibilité avec les 100 GHz des canaux ITU, comme indiqué précédemment, visible dans la figure 0.4.

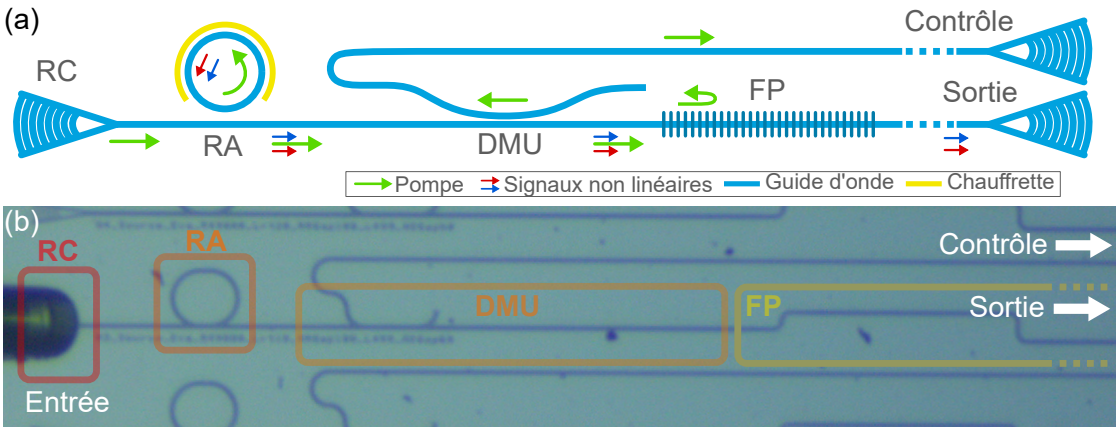

Figure 0.3.: (a) Schéma de la source de peigne de fréquence avec (b) une image microscopique du circuit fabriqué, sont indiqués : les réseaux de couplages (RC), résonateur en anneau (RA), le démultiplexeur (DMU) et le filtre de pompe (FP). La lumière est injectée à gauche puis récoltée à la sortie. Le contrôle permet de vérifier la transmission et l'alignement de la cavité dans le filtre.

En associant ces deux composants, nous avons pu produire un peigne de fréquences de paires de photons, voir figure 0.3. Ces paires ont été analysées afin de vérifier leur possible utilisation dans un système quantique sur puce plus complexe. La première étape a été de vérifier la statistique des paires de photons afin de s'assurer que deux paires n'étaient pas produites simultanément. Nous avons donc mesuré la fonction de corrélation temporelle d'ordre deux des photons ($g_h^{(2)}(0)$), un photon 'signal' étant annoncé par un photon 'idler'. Cette mesure a donné un $g_h^{(2)}(0) \simeq 3.07 \cdot 10^{-3}$, correspondant à une probabilité négligeable que deux photons 'signal' soient annoncés par un seul photon 'idler'.

Dans un second temps, nous avons vérifié la qualité et les propriétés des états à deux photons produits. Une fonction d'onde présentant une anti-corrélation spectrale est le signe d'une intrication en longueur d'onde prédite par le modèle [16]. Cette anti-corrélation est dûe au type de pompe utilisé, dans notre cas un laser continu. Pour mesurer la fonction de corrélation spectrale des photons produits, nous avons utilisé une technique par stimulation du mélange à quatre ondes, forçant ainsi la longueur d'onde du photon signal. Nous avons alors pu relever un spectre des photons 'idler' produits afin de remonter aux corrélations à la longueur d'onde du photon signal. En répétant cette opération pour différentes longueurs d'onde du photon signal, nous avons reconstruit la fonction corrélation spectrale désirée des états à deux photons. Nous avons alors observé une grande concordance avec le modèle avec une forte anti-corrélation et un nombre de Schmidt $K_{exp} = 5.5$ ($K_{sim} = 107$), voir figure 0.5. La disparité entre les deux valeurs a été attribuée à la résolution de la mesure, limitée, lors des expériences menées, par l'utilisation d'un filtre optique ajustable de 6 pm. Le modèle développé a aussi permis de prédire qu'en modifiant le signal de pompe d'un laser continu à un laser pulsé, il serait

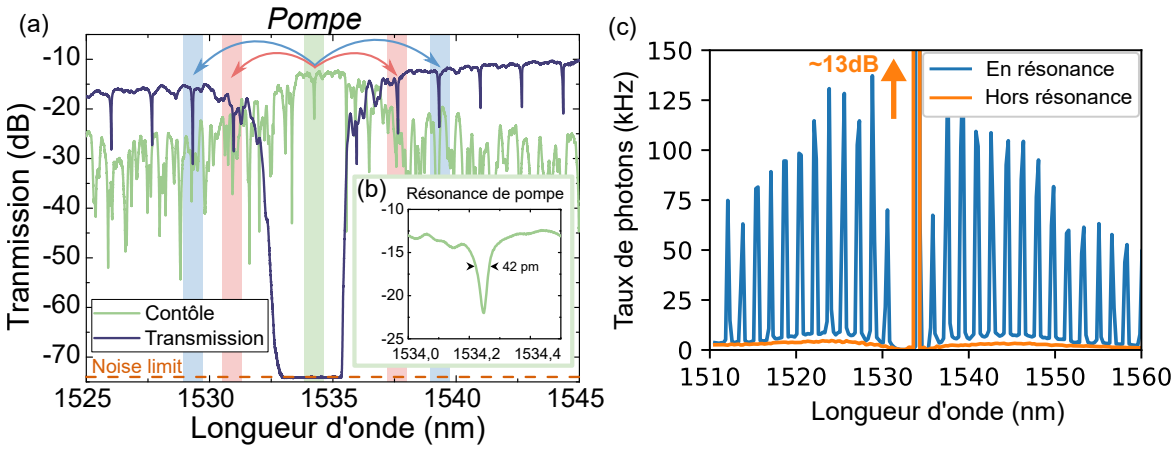

Figure 0.4.: (a) Spectre de transmission de la source de peigne par la sortie (transmission) et par le contrôle, avec (b) la résonance pompée. (c) Spectre d'émission du peigne de fréquence quand la cavité est pompée et le bruit si le laser est hors de la cavité.

probablement possible de produire des paires de photons séparables. Ces investigations par simulation ont ainsi mis en avant la versatilité des circuits photoniques réalisés au cours de la thèse, qui pourraient être utilisés pour la réalisation de sources de photons uniques annoncés.

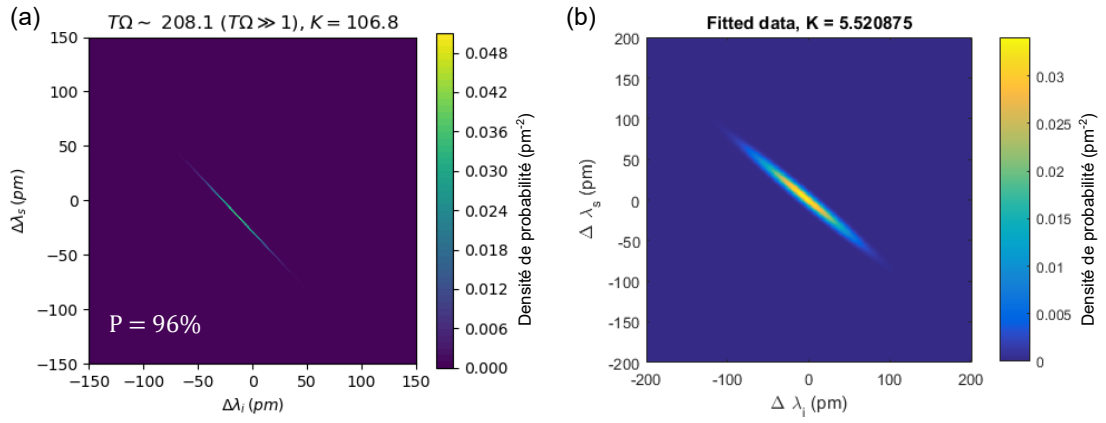

Figure 0.5.: (a) Modèle théorique de la corrélation spectrale des photons de chaque paire et (b) donnée ajustée de la mesure de corrélations spectrale. Les axes correspondant aux longueurs d'onde des photons de la paire et leur forte anti-corrélation en longueur d'onde indiquent un état intriqué.

Finalement, nous avons vérifié l'intrication des paires de photons en énergie-temps produites. Ce type d'intrication est un des modes d'encodage fondamentaux en optique quantique. Pour cela, nous avons mesuré la visibilité des franges d'interférences à deux photons dans un interféromètre de Michelson en configuration Franson [14]. Cette

expérience nous a donné à la fois des informations sur la qualité de l'intrication des paires de photons, mais également sur la qualité du filtrage réalisé de la pompe optique. Une visibilité proche 100% indique une bonne intrication mais aussi que la pompe a bien été rejetée par le filtrage sur la puce. Les paires de photons de la source de peigne de fréquences ont donc été testées, ce qui a conduit à des visibilités de 98% et 97% pour les résonances distantes de 2 et 3 ISL de la pompe, voir figure 0.6. Ces visibilités élevées indiquent une forte intrication des photons de chaque paire mais aussi une réjection très efficace de la pompe. Nous avons également exploré les résultats de cette même mesure pour les résonances plus éloignées, et nous en avons déduit une visibilité au-delà de 92% pour tous les ISL mesurés.

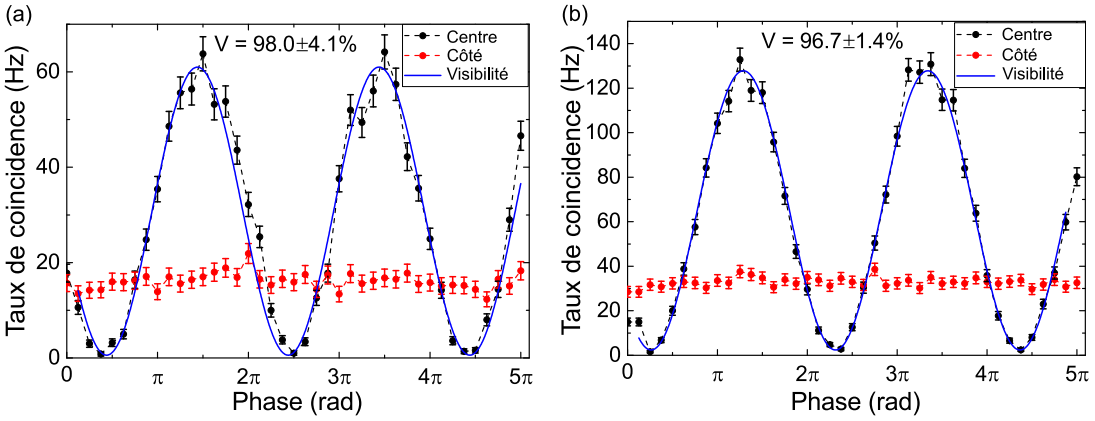

Figure 0.6.: (a) et (b) correspondent au nombre de coïncidences par seconde pour 2 et 3 ISL respectivement. Les côtés indiquent la stabilité de la mesure. On peut alors évaluer la visibilité des interférences à deux photons pour les deux cas qui indiquées en haut.

En associant les points d'étapes précédents, nous avons pu montrer l'intégration d'une source de peignes de fréquences utilisable pour des applications quantiques, à base de circuits photoniques planaires en photonique silicium. Ceci a conduit à poursuivre dans la perspective d'une intégration de l'ensemble des éléments, en ajoutant une étape de démultiplexage en longueur d'onde sur la puce, située après la source, l'ensemble formant alors un générateur de paires de photons intriqués. Un tel circuit sépare les photons 'signal' et 'idler' des paires produites ; ils peuvent alors être envoyés directement aux utilisateurs du réseau de communications quantiques, par exemple. Au final, notre étude a montré qu'il était possible d'intégrer un système de réjection très efficace du signal pompe optique permettant de générer les paires de photons par mélange à quatre ondes spontané (SFWM) sans affecter les propriétés des paires de photons. Les travaux de la thèse apportent une contribution vers l'intégration de sources de paires de photons intriqués reposant sur des technologies très proches des circuits intégrés silicium de la microélectronique, pouvant donc être intégrées et produites à échelle industrielle et induire un développement important des applications de l'information quantique. Il resterait à combiner plusieurs de ces générateurs de photons dans un système plus complexe tel

qu'un générateur d'états quantiques annoncés. L'ensemble dessine une perspective très prometteuse pour le développement de la photonique quantique.

Introduction

Research and development in photonic technologies have witnessed quite fast and durable growing advances in various fundamental and applied areas [1]. It goes from the most mundane item of our daily life to industrial or military applications. A few notable examples are in the telecommunications, optical fibers are now connecting all of us. They allow to transfer terabits per second of information over lengths larger than 15 000 km [17] while the miniaturization of lasers and photo-diodes has now brought the optical fiber into our home.

In each of these systems, a lot of components are working together to provide their functionality. Light emission, amplification, detection, modulation, and transmission are integrated on chips of a few millimeters length. They are cheap and can be produced in industrial quantities. Fabrication improvements in microelectronicd has been transferred to photonic platforms, pushing the miniaturization limit and making structures only hundreds of atoms long, with still improving reproducibility.

Quantum physics has been at the heart of major technological advances in the last century [2]. Properties like the superposition of the states, particle-wave duality, or entanglement are completely alien to common sense. Yet they are the basis of a better understanding of physics. Quantum mechanics is the best tested theory with extraordinary precision [18]. The application of quantum mechanics in optics has shown marvelous promises. As photons interact less than charged particles, they are perfect to exploit long range quantum effects. Quantum Information Science (QIS) such as Quantum Key Distribution (QKD) [3] or boson sampling are powerful tools coming from quantum optics [19]. QKD provides a substantial improvement in secure communications. As the encryption key is protected by the laws of physics: it is possible to know if the communication has been eavesdropped, so a new key can be chosen [20, 21]. The next step is quantum communications, where not only the keys are sent via a quantum channel but the messages as well [22, 23]. This breaks the paradigm of encryption, as so far non-reversible mathematical operation is the norm for securing information. Thanks to the quantum communication properties, the transmitted information is destroyed by the reader, making it almost perfectly secure [22]. Boson sampling, on the other hand, opens the way for quantum computing. It is used to simulate complex systems much faster than with a classical computer [24]. For the moment, the main application is for protein folding [24]. All these systems can be realized with bulk optical elements, but this leads to large and heavy systems that are cumbersome and awkward to use which restrict potential applications and markets. In brief, such an approach is not scalable.

Photonics provides platforms to integrate quantum optics into stable, easy-to-use, and reproducible components. Thanks to their small size, quantum photonic circuits are tolerant to large thermal fluctuations, scalable and easy to combine into more complex

systems. Monolithic components are naturally aligned, and insensitive to vibrations. However, the challenge is to make the jump from the optical table to the chip. Integration requires to completely rethink these complex systems.

As such, we will describe the development of quantum photonic circuits on the Silicon-On-Insulator (SOI) platform. This platform is compatible with industrial processes and the goal is to keep this compatibility not only for the fabrication but also when used. Plug-and-play approaches will be prioritized, *i.e.* only standard fibered "off-the-shelf" telecom components are preferred. All of this while keeping everything compatible with photonic industrial fabrication processes.

In this context my PhD project is devoted to the emerging field of quantum information on scalable and flexible silicon photonic chips. Its aim is to exploit the particular capabilities of dense functionality integration achievable using the silicon photonic platform to push quantum-enabled technologies one step further, by merging quantum light sources and single photon manipulation stages in both the wavelength and spatial domains and to develop advanced quantum circuits.

Two circuits will be presented: (i) A micro-ring based entangled photon-pair source creating a comb when pumped and outputting a wavelength comb of photon pairs. The pairs can be entangled (distant correlation) so they can be used in QKD systems. (ii) In the integrated entangled photon-pair generator, pairs will be separated into different channels. Signal and idler photon pairs can directly be sent to users, or depending on the pump, the idler can be detected, to make it a heralding source of single photons. They are the basis to build a heralded photon-number state generators, capable of generating complex quantum states.

This thesis was done at both the Centre de Nanosciences et de Nanotechnologies (C2N) in Palaiseau and the Institute de Physique in Nice (InPhyNi). The design, fabrication and classical experiments were performed at the C2N. The quantum experiments and interpretations were performed at the InPhyNi.

- **Chapter 1:** It will introduce some fundamentals of quantum mechanics. We will go over the different properties of quantum states and how to test them, as well as through the main types of entanglement. We will also introduce non-linear processes allowing to create non-classical states of light.

- **Chapter 2:** We will introduce integrated telecom components, like ring resonators, filters and others, and redesign them to suit our platform and quantum requirements. A first source of correlated pairs will be designed, then active tuning, grating couplers, routing will be implemented.

- **Chapter 3:** We will then tackle the problem of on-chip pump rejection, which is a main limitation of integration of quantum circuits based on the spontaneous four-wave mixing process. This will be done with Bragg filters. We will see different possible design strategies for waveguide corrugations to tailor the performances of the components. Finally, we will see how to limit the effect of their optical saturation for large rejections.

– **Chapter 4:** Fabricated of quantum circuits will be presented using the developed library of components. First, classical performances will be assessed. Then the quantum performances of the samples will be evaluated with a statistical study, a state tomography, and indistinguishability measurements.

Chapter 1.

Fundamentals for Integrated Quantum Photonics

1.1. Quantum information

1.1.1. Classical information

The bit is the fundamental unit of information used in computers systems and communication. It is a two-state unit, with a 0 and a 1 or True and False. A bit of information can be encoded into any binary physical systems, such as: holes (punch cards), magnetization (hard drive or floppy disk), height (CD or DVD), voltage (RAM or processors), etc. This two-level system allows for a simple and robust way to store and move information. It keeps the computer architecture simple when processing, without introducing large amounts of errors. Arithmetic in base two can be achieved using Boolean operations. Encoding text can be done by assigning a sequence of bits to a letter/symbol. Usually, for simplicity, bits are combined into fixed length groups, usually but not exclusively, powers of 2 (*e.g.* 8-bit 2^3, 16-bit 2^4, 32-bit 2^5, 64-bit 2^6), for better efficiency. For instance, ASCII (American Standard Code for Information Interchange) started as a 7-bit code, only needing 128 characters.

Whatever the compression or amount of information, it is mostly the media that is changing and getting denser over the years. Information is now written on smaller objects reaching the limit of the classical world. But they still are at the same type, nothing has fundamentally changed. Until we reach the quantum world.

1.1.2. Quantum states and information

Quantum information is fundamentally different form the classical one. Due to the few principles that rule all of quantum physics. A quantum bit (qubit) is also made of a two level system. We will describe it by $|0\rangle$ and $|1\rangle$, corresponding to a state 0 (False), 1 (True), respectively. They represent any two-level system: spin (spin up $|\uparrow\rangle$ and spin down $|\downarrow\rangle$), energy level (fundamental $|f\rangle$ and exited $|e\rangle$), polarization (vertical $|V\rangle$ and horizontal $|H\rangle$), etc. Of course, they can have more than two levels, such as the photon number in a pulse, or can have even continuous, with position/momentum quantities. These "new" two-level systems do not behave as the classical ones. They cannot be thought of as simply 0 or 1 but complex vector. Each qubit gives us a bit when measured. Only the values 0 or 1 are accessible when measuring a qubit.

It is also important to acknowledge that a quantum object is not a wave or a particle. It does not behave like a particle sometimes and like a wave in others. It is a new type of object that is both a particle and a wave. It is a quantum object. This is well illustrated in the delay choice or quantum eraser experiments [25, 26], where in a single experiment it is possible to see both wave-like and particle-like behaviors.

Quantum Bit

Quantum bit is the fundamental unit of quantum information called also qubit. It is different from a classical bit. Its state is defined as a unitary vector which can take an infinite amount of values. However, only a single classical bit of information can be accessed with it. As, when a qubit is measured, the state collapses into 0 or 1. Its value is only defined after it is measured. When using qubits to transport information or perform computation, the goal is to make qubits interact in a way that only the wanted state (*i.e.* the solution) constructively interfere.

All the following properties introduced in this section are making qubits more powerful than their classical counterpart. However, errors can accumulate much faster, making error correction a fundamental step to create useful quantum technologies. To make a single effective qubit, one requires about 1000 physical qubits due to error corrections [27]. Moreover, decoherence of the qubit is also a limitation. In some technological platforms, interaction with the environment can over time destroy the information contained in the qubits.

The information can be encoded on any physical properties. For light, there are four discrete variables: polarization, path, time-bin, energy, orbital angular momentum, see figure 1.1 [28]. Polarization encoding is straight forward, any orthogonal pair of polarization of a single photon (Fock state) can be a basis of a Bloch sphere, see figure 1.2. Path encoding is when the photon is separated into at least two spatial modes. A controllable beam splitter and a phase shifter allow to reach the whole sphere. Time-bin on the other hand is a bit more abstract as it spreads the photon into two or more pulses with different delays, referenced as early and late states. They can interact in the same way on the Bloch sphere. Similarly, energy-time adds another layer to this scheme where the arrival time, or delay, depends on the energy of the photon. Lastly, there is the orbital angular momentum which is encodes using field spatial distributions of light, *i.e.* its wavefront.

Representation

All of these states can be represented in the so-called bra-ket notation. They can be understood as complex vectors (Eq. 1.1 and 1.2)

$$|0\rangle = \begin{pmatrix} 1 \\ 0 \end{pmatrix}, |1\rangle = \begin{pmatrix} 0 \\ 1 \end{pmatrix} \tag{1.1}$$

$$|\psi\rangle = \begin{pmatrix} a \\ b \end{pmatrix} = a\,|0\rangle + b\,|1\rangle\,, \quad a, b \in \mathbb{C} \tag{1.2}$$

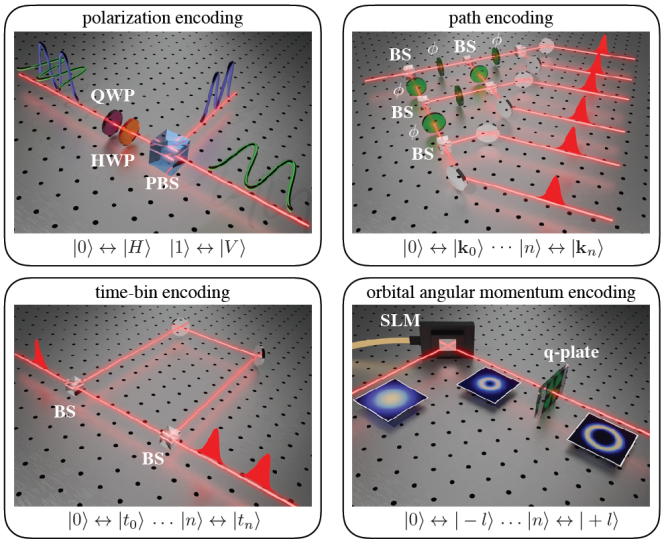

Figure 1.1.: Discrete variable Encoding quantum information in a single photon exploiting different degrees of freedom. Possible choices include polarization (only a qubit of information can be carried in this case), path, time-bin and orbital angular momentum (larger dimensionalities can be riched). Legend - QWP: quarter-wave plate, HWP: half-wave plate, PBS: polarizing beam splitter, BS: beam splitter, phi : phase shift, SLM: spatial light modulator. Reproduced from Ref. [28]

So that any state can be written as a sum of the base vectors. Any physical state must be normalized[1] such as written in equation 1.3. Another important change is that the components a and b of the state (vector) $|\psi\rangle$ can be complex numbers.

$$\langle\psi|\psi\rangle = |\psi|^2 = |a|^2 + |b|^2 = 1 \tag{1.3}$$

Such a state can be represented on a sphere of unitary radius (Bloch-Poincaré sphere). It represents all the possible combinations of $|0\rangle$ and $|1\rangle$ that $|\psi\rangle$ can take. We can rewrite the state as a function of the angles on the sphere with $\theta, \phi \in \mathbb{R}$ from equation 1.4, shown in Figure 1.2

$$|\psi\rangle = \cos(\theta/2)\,|0\rangle + \sin(\theta/2)e^{i\phi}\,|1\rangle \tag{1.4}$$

The poles are the vectors of the basis. The states along the equator of the sphere are the combination of the base, shown in equations 1.5, 1.6, 1.7, and 1.8. Any basis[2] of measurements used can represent the poles. (The other points must be changed accordingly). For example, choosing as base $|0\rangle = |H\rangle$ and $|1\rangle = |V\rangle$, means that in the x-y plane the polarization diagonal, anti-diagonal, circular right, circular left are on $+x$, $-x$, $+y$, and $-y$ points (Eq. 1.5, 1.6, 1.7, and 1.8), respectively.

[1]The notation $\langle\psi|$ correspond to the vector conjugated and transposed
[2]Set of unitary orthogonal vectors

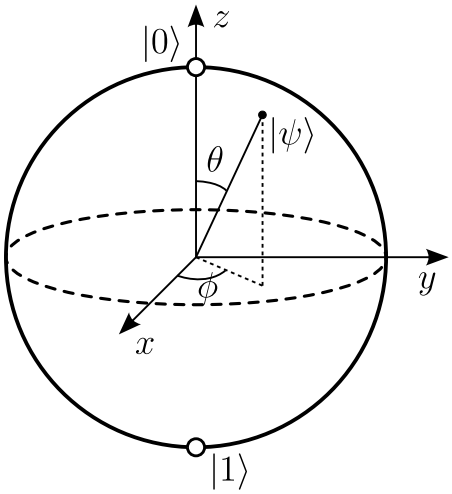

Figure 1.2.: Bloch-Poincaré sphere representation of the qubit state.

$$+x : 1/\sqrt{2}\,|0\rangle + 1/\sqrt{2}\,|1\rangle = |D\rangle \tag{1.5}$$

$$-x : 1/\sqrt{2}\,|0\rangle - 1/\sqrt{2}\,|1\rangle = |A\rangle \tag{1.6}$$

$$+y : 1/\sqrt{2}\,|0\rangle + i/\sqrt{2}\,|1\rangle = |R\rangle \tag{1.7}$$

$$-y : 1/\sqrt{2}\,|0\rangle - i/\sqrt{2}\,|1\rangle = |L\rangle \tag{1.8}$$

The measurement of the single photon is done on the basis (*i.e.* polarization $|V\rangle$ and $|H\rangle$). The state vector is projected on it. This results in a probability $|a|^2$ of getting $|V\rangle$ and $|b|^2$ of getting $|H\rangle$.

One can also define operators, written as a capital letter (*e.g.* unitary operator U). They represent physical processes or measurements applied on the qubit. They can be thought as matrices that are applied to the vector state. The conjugated of an operator is $U^\dagger$ with $U^\dagger U = I$, the identity matrix.

Measurement

When a state is measured, it is projected onto one of the (orthonormal) eigen-states, *i.e.* on the basis. There is no way to know onto which eigen-state it will be projected. This is a random process with the probability being the squared norm. Quantum physics does not explain where these properties come from, but to date no experiment has contradicted this statement. If we look at the Bloch sphere, and we want to measure θ for a fixed state that we prepared, we have to measure multiple times. In the case of polarization, it would be a horizontal polarizer. We get $|H\rangle$ (*e.g.* transmission of the photon) with probability p_0, else it means we measured $|V\rangle$ or that the measurement failed (loss of the photon).

$$p_0 = |\langle 0|\psi\rangle|^2 = \cos^2\frac{\theta}{2} \tag{1.9}$$

$$p_1 = |\langle 1|\psi\rangle|^2 = \sin^2\frac{\theta}{2} \tag{1.10}$$

After the state projection, any repetition of the same measurement results deterministically in the same outcome. The fact that the quantum state is projected means, in general, that information about the initial quantum state is irreversibly lost. So we can only "measure" θ once per qubit. To reconstruct its value we have to repeatedly prepare and measure the same state.

Superposition of states

A particle has the ability to be in multiple states at the same time. As we saw before, it is in a superposition of the basis[3]. This is well demonstrated with a single photon in a Mach-Zehnder interferometer (figure 1.3) or with the two-slit experiments [29].

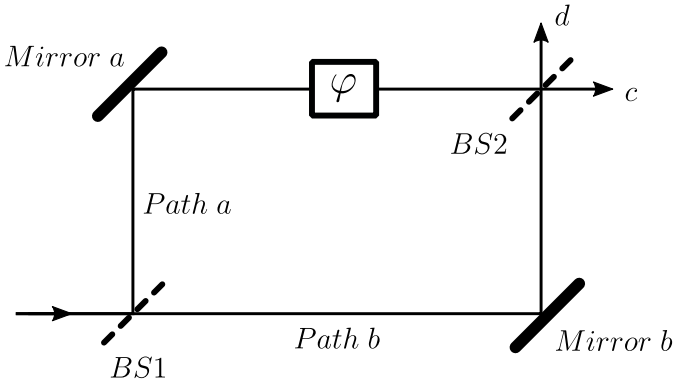

Figure 1.3.: Schematic of a Mach-Zehnder interferometer, the photons can take path a and path b.

If we send a single photon in the interferometer, "classically", one could think it can only go in one arm. At BS1, it goes either to path a or b. When the photon gets to BS2 it just goes through since there is nothing on the other path. Thus there should be a 50% chance to detect something in the output c whatever the phase φ of the interferometer. But this is not at all what happens, the detection rate in fact sinusoidally oscillates with the phase. The single photon takes both path a and b at the same time as probability amplitudes. On each path, it picks up a different phase resulting in a phase shift φ. The states in each path a and b are $|a\rangle$ and $|b\rangle$, respectively, with values:

$$|a\rangle = \frac{e^{i\varphi}}{\sqrt{2}}(|0\rangle + |1\rangle) \tag{1.11}$$

[3]The Copenhagen interpretation of quantum mechanics is used throughout the thesis.

$$|b\rangle = \frac{1}{\sqrt{2}}(|0\rangle + |1\rangle) \tag{1.12}$$

These probability waves then interfere on the BS2, creating oscillations in detection at the output. These are single photon interferences. The states at the output c and d are then $|c\rangle$ and $|d\rangle$, respectively:

$$|c\rangle = \left(\frac{1}{2} - \frac{1}{2}e^{i\varphi}\right)|0\rangle + \left(\frac{1}{2} + \frac{1}{2}e^{i\varphi}\right)|1\rangle \tag{1.13}$$

$$|d\rangle = \left(\frac{1}{2} + \frac{1}{2}e^{i\varphi}\right)|0\rangle + \left(-\frac{1}{2} + \frac{1}{2}e^{i\varphi}\right)|1\rangle \tag{1.14}$$

If we look at the probability to have a photon at the output c, we get a sinusoidal variation as a function of the phase shift φ.

$$|\langle 1|c\rangle|^2 = \left(\frac{1}{2} + \frac{1}{2}e^{-i\varphi}\right)\left(\frac{1}{2} + \frac{1}{2}e^{i\varphi}\right) = \frac{1}{2}\left(1 + \cos\varphi\right) \tag{1.15}$$

This is not restricted to photons and similar experiments can be done with electrons or atoms [30, 31]. Superposition happens anytime a particle/quantum object has an interaction ("a choice"). It becomes a superposition which depends on probability amplitudes. For instance the superposition of states after a 50:50 or a 10:90 beam splitter will not be the same.

No-cloning theorem

The no-cloning theorem is fundamental in quantum mechanics and easy to show. It is impossible to make a perfect copy of a state without changing the original. Let define the cloning operator C with the property : $C|\phi\rangle|\psi\rangle = C|\phi\rangle|\phi\rangle$, assuming $\langle\psi|\psi\rangle = 1$. Then we can write:

$$\begin{aligned} C|a\rangle|\psi\rangle &= C|a\rangle|a\rangle \\ C|b\rangle|\psi\rangle &= C|b\rangle|b\rangle \end{aligned}$$

Starting from the definition with arbitrary states, we can write the following equations 1.16, 1.17, and 1.18. In that case, $|\langle b|a\rangle|$ is equal to 0 or 1. Thus by the Cauchy-Schwarz inequality either $a = e^{i\beta}b$ or a is orthogonal to b. This cannot be the case for two arbitrary states. This makes a universal cloning operation impossible.

$$\langle\psi|\langle b|C^\dagger C|a\rangle|\psi\rangle = \langle b|\langle b|C^\dagger C|a\rangle|a\rangle \tag{1.16}$$

$$\Leftrightarrow \langle\psi|\langle b|a\rangle|\psi\rangle = \langle b|\langle b|a\rangle|a\rangle \tag{1.17}$$

$$\Leftrightarrow |\langle b|a\rangle| = |\langle b|a\rangle|^2 \tag{1.18}$$

It is however possible to clone states in very specific conditions. It is also possible to make imperfect copies of states without affecting them too much. This is the basis of quantum telecommunication hacking, which is possible when the states used for telecommunications are not well prepared [32].

1.1.3. Entanglement and its applications

In classical encoding, combining two bits increases the number of possibilities to 2^2 with the possible combinations 00, 01, 10, and 11. When combining two qubits, we get a superposition of all the possible combinations. The most general two qubit state is

$$|\psi\rangle_{\text{II}} = \alpha\,|0\rangle_a\,|0\rangle_b + \beta\,|0\rangle_a\,|1\rangle_b + \gamma\,|1\rangle_a\,|0\rangle_b + \delta\,|1\rangle_a\,|1\rangle_b \tag{1.19}$$

with the normalization $|\alpha|^2 + |\beta|^2 + |\gamma|^2 + |\delta|^2 = 1$. However, there are special cases where this state cannot be written as a product of two individual qubits[4]. In these cases, the state is called entangled. If it can be factorized, it is a separable state.

In a two level system, there are 4 states maximally[5] entangled. They are called Bell's states and are as follows:

$$\begin{cases} |\Psi^+\rangle = \frac{1}{\sqrt{2}}(|01\rangle + |10\rangle) & \text{if } \alpha = \delta = 0,\ \beta = \gamma = \frac{1}{\sqrt{2}} \\ |\Psi^-\rangle = \frac{1}{\sqrt{2}}(|01\rangle - |10\rangle) & \text{if } \alpha = \delta = 0,\ \beta = -\gamma = \frac{1}{\sqrt{2}} \\ |\Phi^+\rangle = \frac{1}{\sqrt{2}}(|00\rangle + |11\rangle) & \text{if } \alpha = \delta = \frac{1}{\sqrt{2}},\ \beta = \gamma = 0 \\ |\Phi^-\rangle = \frac{1}{\sqrt{2}}(|00\rangle - |11\rangle) & \text{if } \alpha = -\delta = \frac{1}{\sqrt{2}},\ \beta = \gamma = 0 \end{cases} \tag{1.20}$$

Here, we simplify the notation with $|X\rangle\,|Y\rangle = |XY\rangle$. These 4 states form a basis, so they are orthogonal to each others.

Entanglement is in every natural state of matter. There is no good analogies in the classical world. It is when two or more states become correlated, for instance the state $|\Phi^+\rangle$ gives a 0 (resp. 1), the other must be in 0 (resp. 1) without needing to measure it. Most quantum states in nature are partially entangled. The most interesting ones are the separable states (no entanglement) and the maximally entangled states (completely entangled). This can happen naturally thanks to conservation laws/symmetries. For instance energy-time entanglement created from the energy-conservation.

Once two particles are entangled they become a single entity. They will stay as such regardless of the distance that may separate them. This "spooky" distant interaction allows to collapse a state instantly at an arbitrary distance. However, this does not break the speed of light, as no information can be transmitted by entanglement alone. Without knowing the original measurement from the first particle, the second state looks just random. Meaning another channel is necessary to transfer information, which is constrained by the speed of light.

[4] This is the tensorial product of the two Hilbert space. We will leave the tensorial product out as it simplifies the notation. It can be understood as a product between vector states.

[5] Perfect correlations between the measurements of the two photons

There are multiple types of entanglements. Next we will see the entanglement available with light. All the properties previously cited can generate entanglement. More than one property can be entangled, like polarization and energy-time or path and time-bin, this is refereed to as hyper-entanglement.

Polarization

Polarization is the most used type of entanglement (figure 1.1) as it is easy to generate using bulk nonlinear crystals with the Parametric Down Conversion (PDC) process [33]. It can be of two types Type I is when the polarizations are opposed $1/\sqrt{2}\left(|H\rangle|V\rangle + |V\rangle|H\rangle\right)$, and type II is when they are aligned $1/\sqrt{2}\left(|H\rangle|H\rangle + |V\rangle|V\rangle\right)$. For instance, in type I, if photon 1 is measured as H (V), then photon 2 is in state V (H resp.) without the need of a second measurement. Polarization entanglement is also easy to manipulate and detect with half-wave plates and polarization beam splitters. However, its integration is difficult as most platforms are polarization sensitive and thus require special designs or specific technologies. Polarization entanglement is very easy to transmit over long distances. Light polarization is indeed weakly affected by the large distance as long as the propagation channel is relatively stable and invariant in time. Many of the first quantum telecommunication and cryptography experiences were demonstrated with polarization entanglement for these reasons [34]. Finally, thanks to 2D grating couplers, it is simple and natural to go from polarization to path encoding when passing from the fiber network to the chip [35].

Path encoding

Path encoding is the simplest way to consider entanglement on chip, as the number of waveguides that can then be implemented is large, over hundreds or even thousands (figure 1.1). The photons are delocalized over multiple waveguides. On a single chip, they are perfectly stable thanks to monolithic fabrication and the small size of the whole ensemble limits overall fluctuations. Path encoding happens any time a photon has a path choice, *e.g.* in beam splitters [36, 37]. An interesting state is the NOON state written as $|\psi\rangle_{\mathrm{N00N}} = 1/\sqrt{2}\left(|N\rangle|0\rangle + |0\rangle|N\rangle\right)$, where each ket is a path/channel taken by either N or 0 photons. However, it is a poor choice for long-distance telecommunications as all paths must be perfectly stable in time (no index, temperature, length variations), fibers are not suitable for it. But as previously mentioned, it is natural to go from path to polarization encoding by accepting some losses from the network to the chip. This type of entanglement is mostly used for quantum walks of entangled photons [38], Boson sampling [39, 40], and quantum teleportation [41].

Time-bin

Time-bin encoding uses time instead of space. Multiple time-bins (time-delays) are defined so that a photon is in a superposition of multiple delays (figure 1.1). This happens when light can take multiple paths with different delays. As long as the photons

cannot interfere, when the path are recombined, they are in a superposition. In the case of 2 time-bins, they can be called early $|e\rangle$ (short path) and late $|l\rangle$ (long path) states. They are generated by a Mach-Zehnder Interferometer (MZI) with a delay on one arm larger than the coherence time of the single photon, to avoid single photon interferences.

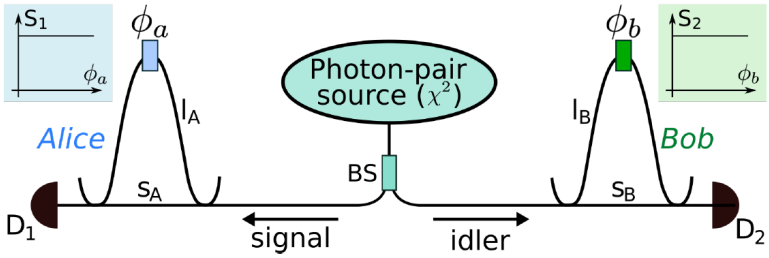

Figure 1.4.: Schematic of the principle for generating and analyzing energy-time entangled photons. The pairs are photons are generated by Parametric Down Conversion in a χ^2 nonlinear crystal by strong Continuous Wave laser. Entangled pairs of photons are sent to two unbalanced interferometers. This is a Franson configuration [42] as the number of photons at the output is constant as a function of the phase. These interferometers can be placed arbitrarily far from each other. Reproduced from Ref. [43].

Photons created during the same process, they are entangled in time. So using two MZI, one can create a state $|\psi\rangle = 1/\sqrt{2}\,(|e\rangle\,|e\rangle + |l\rangle\,|l\rangle)$ if they are indistinguishable from one another, see figure 1.4. This type of encoding is very robust, to dispersion, polarization change, path difference, it works on chip and in long distance fibers. However, it is more difficult to measure it, compared to polarization encoding, as a MZI and a time-to-digital conversion scheme must be used. Nevertheless, a lot of time-bin experiments have been demonstrated in fibers and on chip [44, 45, 46].

1.1.4. Bell type violation

Quantum mechanics has many concepts and philosophical implications were considered as unsettling for many people. But the most problematic is called entanglement. This property, as we have seen it, exhibits a distant and instantaneous "interaction" between distant objects, in which correlation appears without any apparent physical interaction. Many funders of quantum mechanics (*e.g.* Einstein, Podolsky, Rosen [47], Schrödinger) argued against it by developing the local[6]-realism[7] theory of hidden variables. It states that correlations are generated by hidden variables that are inaccessible to the observer. But also, that the results of observations exist regardless of the observations[8].

This was also tied to the completeness of quantum mechanics. If a hidden variable exist, then the model would not be complete since it would not take it into direct account. Bell replaced these postulates by a physically reasonable condition of locality. Bell's

[6] There is no communication between systems, no-signal that could be faster than light
[7] That the system are not fundamentally random but deterministic
[8] *e.g.* the property (position, spin, etc.) has a defined value even if we do not measure it.

theorem tells that no local hidden-variable theory can reproduce all of the statistical predictions of quantum mechanics [48]. Also that either locality or realism must be dropped to explain entanglement. This is thanks to Bell's inequality.

Bell's inequality

There are in facts an infinite numbers of Bell's inequalities. They are constructed from the properties of the system being probed [49, 50]. However, the first inequality was proposed by Clauser, Horne, Shimony, and Holt (CHSH) [51] to test the hidden-variable model. The following demonstration shows the Bell's inequality for two level systems [52].

Let us define two sets of particles A and B. Their properties depend on the parameters a and b, respectively. Each set, once measured, can give a results $\{A_1, A_2, ..., A_n\}$ and $\{B_1, B_2, ..., B_n\}$, respectively, depending on the value of a and b. Measurements of the particles give only two possible outcomes ± 1, *i.e.* $|A_k| = 1$ and $|B_k| = 1$. $P(a, b)$ is the correlation function between of the results A and B. It is defined as the average product of the results obtained by the joint measurements. In the most general case, $-1 \leq P(a, b) \leq +1$ as $A_k B_k = \pm 1$.

$$P(a, b) = \frac{1}{n} \sum_{k=0}^{n} A_k B_k \tag{1.21}$$

Now, by considering the hidden variable model, we can define λ which is a parameter that fixes all measurements if it is constant. It can take any value in the set Λ. So the probability density over this set is $\rho(\lambda)$.

$$\int_{\Lambda} \rho(\lambda) d\lambda = 1 \tag{1.22}$$

As the measurements depend on λ, we can write the new functions $A(a, \lambda)$ and $B(b, \lambda)$, which are discontinuous, and can only have the values ± 1. The correlation function (Eq. 1.21) then becomes

$$P(a, b) = \int \rho(\lambda) A(a, \lambda) B(b, \lambda) d\lambda. \tag{1.23}$$

This is a local expression as A does not depend on b, nor B depends on a. If we repeat the experiment with new variables of a' and b', we could define the quantity Δ and try to explore the boundary of its values.

$$\Delta = |P(a, b) - P(a, b')| + |P(a', b) + P(a', b')| \tag{1.24}$$

Using the properties $|A(a, \lambda)| = 1$, we can find an expression for the two terms of equation 1.24.

$$|P(a,b) - P(a,b')| = \left| \int \rho(\lambda) A(a,\lambda)(B(b,\lambda) - B(b',\lambda)) d\lambda \right| \tag{1.25}$$

$$\leq \int \rho(\lambda)|A(a,\lambda)||B(b,\lambda) - B(b',\lambda)|d\lambda \tag{1.26}$$

$$\leq \int \rho(\lambda)|B(b,\lambda) - B(b',\lambda)|d\lambda \tag{1.27}$$

Similarly to equation 1.27, we get equation 1.28.

$$|P(a',b) + P(a',b')| \leq \int \rho(\lambda)|B(b,\lambda) + B(b',\lambda)|d\lambda \tag{1.28}$$

Since $|B(b,\lambda)| = |B(b',\lambda)| = 1$, the sum of the right-hand side of equations 1.27 and 1.28 is constant.

$$|B(b,\lambda) - B(b',\lambda)| + |B(b,\lambda) + B(b',\lambda)| = 2 \tag{1.29}$$

This gives us the Bell's inequality, equation 1.30. It is a criteria using correlation between measurements only based on the fact that a common unknown parameter controls the outcome of the measurements.

$$\Delta = |P(a,b) - P(a,b')| + |P(a',b) + P(a',b')| \leq 2 \tag{1.30}$$

We now consider the quantum mechanical correlation function between the two states $|a\rangle$ and $|b\rangle$. We now get the following equation 1.31 for P. If we consider all the possible states, one may find states $|a\rangle$ and $|b\rangle$ with rotation of $\pi/4$ between them. This would give to their correlation function the value $\sqrt{2}/2$.

$$P(|a\rangle, |b\rangle) = -\langle a|b\rangle = -(a_1^* b_1 + a_2^* b_2 + ... + a_p^* b_p) = -\vec{a} \cdot \vec{b} \tag{1.31}$$

The criterion Δ thus becomes equation 1.33. By carefully choosing $|a\rangle$, $|a'\rangle$, $|b\rangle$, and $|b'\rangle$ (or by starting with orthogonal states and inducing a rotation of $\pi/4$), it is possible to have $\Delta > 2$.

$$\Delta = |P(|a\rangle, |b\rangle) - P(|a\rangle, |b'\rangle)| + |P(|a'\rangle, |b\rangle) + P(|a'\rangle, |b'\rangle)| \tag{1.32}$$

$$= |\langle a|b\rangle - \langle a|b'\rangle| + |\langle a'|b\rangle + \langle a'|b'\rangle| = 2\sqrt{2} \tag{1.33}$$

Any system or experiment that exhibits this property, cannot be explained by a hidden variable model. This shows that the true nature of the entanglement correlation is not classical but something never seen before, purely coming from quantum mechanics.

Bell test experiments

The most famous test of the Bell's theorem is the demonstration of Alain Aspect in 1982 [53]. Many other experiments have been conducted to show violation of the Bell's inequality, increasing distance [54, 55, 56], using electrons [57], photons [54], and other particles [58, 59, 60]. In all these experiments, Bell's inequality was violated.

In some experiments, require random setting to be performed. Random numbers can be used to choose the base of polarization or the orientation of the magnetic field in the experiment without introducing a bias. Which type of random numbers are then used can be important. Usual random numbers are pseudo random: they are generated by complex functions with a changing seed (typically time). They are not, mathematically, true random numbers and may contain statistical artifacts [61, 62]. It is also possible to use physical random numbers coming from the natural properties, like atom decays or beam splitters. They have been considered as a loophole in the model, since they could be "selecting" the data as they are dependent themselves on physical laws. Since both pseudo and physical random numbers exhibit Bell violations, it has been tried to only use human choices to set the experiments. People were asked numbers that were then used to make simultaneous experiments around the world for 12 hours continuously. The results were Bell violations in all cases [63].

Moreover, recently loophole-free[9] experiments have been conducted [57, 64, 65], making criticism against the Bell's theorem even more difficult. All experiments pointing in the same direction, there is no hidden variable. Locality[10] cannot be kept if one wants to save the realism interpretation[11], and vice versa.

1.1.5. Non-linear processes

In the last few years, entanglement went from demonstrations to resources. Generating entangle states has become a necessity for applications of quantum mechanics, from telecommunications to computation, metrology, and more. Atom-like structures are one way to produce quantum states. Another is using nonlinear processes that rely on conservation laws.

Nonlinear optical properties are present in all materials. Optical nonlinearities arise from the crystalline structure of the materials and their atomic and electronic responses to an electro-magnetic field. This response can affect electro-magnetic waves and change their properties. As it starts as an unknown function, we can describe the response by a Taylor series expansion. If we call the dielectric polarization density (the response to the electric field) $\vec{P}(t)$ at time t and the electrical field $\vec{E}(t)$, one can write,

$$\vec{P}(t) = \varepsilon_0(\chi^{(1)}\vec{E}(t) + \chi^{(2)}\vec{E}^2(t) + \chi^{(3)}\vec{E}^3(t) + \ldots) \tag{1.34}$$

[9] Critics of Bell's theorem used loopholes in the experimental demonstrations which were the inefficiency of the detection and random number generation. This made it possible for the detector to "select" the results which could have created the statistical anomaly, *e.g.* Bell violation.

[10] No instantaneous information exchange between system.

[11] The system is predetermined regardless of the observation.

with ϵ_0 the vacuum permittivity and the coefficients $\chi^{(n)}$ are the n-th-order susceptibilities of the isotropic medium. The first term $\chi^{(1)}$ is the linear optical susceptibility. It is linked to the index of the material, dispersion, etc. All others are the nonlinear coefficients. They have much smaller effect than $\chi^{(1)}$, and large fields must be applied to take them into account. The higher order coefficients make the field response change such that new frequencies can emerge. $\chi^{(2)}$ is the second-order nonlinear term : it describes processes such as second harmonic generation or parametric down-conversion. It exhibits a 3-photon interaction, the decay of a photon into two others or the merge of two photons into a higher energy one. $\chi^{(3)}$ is the third-order nonlinear therm, it describes processes such as third-harmonic generation, four wave mixing and the intensity-dependent refractive index. Some are 4-photon interaction, with inelastic scattering of light changing two photons into two new ones with different frequencies or three photons merging into one.

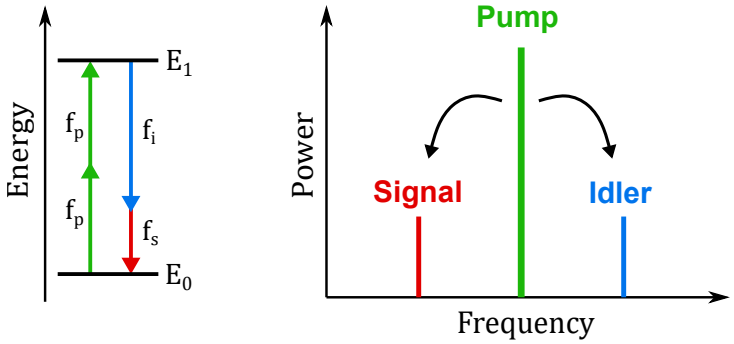

Figure 1.5.: One example of $\chi^{(3)}$ effect Spontaneous Four Wave Mixing (SFWM) process

A single photon is often thought as a particle with a set energies, which is the ideal case or at least a classical approximation. It has in fact a spectrum. Its state is represented by

$$|\psi\rangle = \int_0^\infty \phi(\omega) a_\omega^\dagger |vac\rangle \, d\omega \tag{1.35}$$

where $a_\omega^\dagger$ is the photon creation operator at frequency ω, satisfying $[a_\omega, a_{\omega'}^\dagger] = \delta(\omega - \omega')$. It is applied on the vacuum represented by $|vac\rangle$. Finally, $\phi(\omega)$ is the spectral distribution function normalized such that $\int_0^\infty |\phi(\omega)|^2 d\omega = 1$. An ideal photon with a single frequency would be

$$|\psi\rangle_{ideal} = a_{\omega_0}^\dagger |vac\rangle \, . \tag{1.36}$$

Here a photon is created from the vacuum with the frequency ω_0. Two-photon states can also be produced. The most common way is to use Spontaneous Parametric Down Conversion (SPDC) or Spontaneous Four-Wave Mixing (SFWM). The generated pairs are generally non-separable states (*i.e.* entangled) [66].

Yet just because an energy exchanging process is possible, it does not mean that it is efficient. The conversion efficiency of a process can be limited by fluctuations in

the incident field(s). (For instance, the polarization induced by the incident field(s) is composed of many local polarizations, which may or may not be radiating in phase.) Nonlinearly-generated fields at different points within the material accumulate phase as they travel. They may add constructively or destructively at the exit surface of the material. The technique of phase matching ensures that: for at least one energy exchanging process, the sum of these fields at the exit only increases with increasing path length, through the nonlinear optical material. Thus, phase matching can determine which energy exchanging processes are most efficient. All others will have sums of locally-generated fields that at some point decrease with increasing path length [66].

The phase matching condition means that the sum of the wave-vectors in the process must be null, $\Delta k = 0$, such as described by equation 1.37, where k_p are the annihilated (pumps) photons and k_n are the created (signals) photons.

$$\Delta k = \sum_p k_p - \sum_n k_n = 0 \tag{1.37}$$

For SPDC and SFWM processes, the conditions are simply equations 1.38 and 1.39, respectively, with k_p the pump, k_i the idler, and k_s the signal photons.

$$k_p - k_i - k_s = 0 \tag{1.38}$$

$$2k_p - k_i - k_s = 0 \tag{1.39}$$

The nonlinear process generates a two-photon wave-function,

$$|\psi\rangle_{\mathrm{II}} = \frac{1}{\sqrt{2}} \int_0^\infty \int_0^\infty \phi(\omega_i, \omega_s) a^\dagger_{\omega_i} a^\dagger_{\omega_s} |vac\rangle \, d\omega_i d\omega_s, \tag{1.40}$$

containing frequency correlations between the two photons. The biphoton wave function (BWF) $\phi(\omega_i, \omega_s)$ is normalized $\int_0^\infty \int_0^\infty |\phi(\omega_i, \omega_s)|^2 d\omega_i d\omega_s = 1$. In the general case, it cannot be factorized into a product of a function of ω_i and a function of ω_s, *i.e.* $\phi(\omega_i, \omega_s) \neq f_i(\omega_i) f_s(\omega_s)$ [66]. This is, at least, partial entanglement of the two photons. The BWF gives its properties to the two-photon state. It can go from a separable state ($\phi(\omega_i, \omega_s) = f_i(\omega_i) f_s(\omega_s)$) to a maximally entangled state.

Nonlinear processes occur both in free space and guided-wave configurations. In the latter case, not only the energy conservation must be satisfied, but the momentum condition is now tied to the properties of the available modes. We still want $\Delta k = 0$. It is now decomposed, in the following way :

$$\Delta k_B + \Delta k_{WG} + \Delta k_{Mat} + \Delta k_P = 0. \tag{1.41}$$

Here, Δk_B is the wavevector mismatch being induced by the waveguide birefringence, Δk_{WG} by the waveguide dispersion, Δk_{Mat} by the material dispersion, and Δk_P by the self-phase modulation of the pump wave and the cross-phase modulation of the sidebands due to the pump wave. In the normal dispersion regime of the material, $0 < \Delta k_{Mat}$. So we must design our waveguide to operate in the anomalous regime $\Delta k_{WG} < 0$ to

compensate for it and the pump contribution. When the nonlinear susceptibility has positive sign, which is the case in silicon, $0 < \Delta k_P$. The birefringence contribution can be positive or negative depending on the relative polarization of the sidebands with respect to the pump [67]. The amount of light being converted in a waveguide by SFWM over the spectrum is approximately

$$P_{wg} = \frac{h\omega_p^2}{6\pi^2}(\gamma P_p L)^2 \tag{1.42}$$

with L the length of the waveguide, h Planck's constant, ω_p and P_p the pump's frequency and power, respectively [66]. γ is the usual nonlinear parameter [68] which can be approximated to

$$\gamma = \frac{n_2\omega_p}{c\mathcal{A}} \tag{1.43}$$

where n_2 in the nonlinear refractive index, c is the speed of light in a vacuum and $\mathcal{A}$ is the effective area of the waveguide.

The nonlinear generation is broadband over all the phase matching conditions. But the power conversion can be improved by using a cavity. In a ring resonator, the power converted is enhanced by the photon cavity increased field and recycling effects, giving equation 1.44,

$$P_{ring} = h(\gamma P_p)^2 \frac{4\nu_p^4}{\pi^3\omega_p^3}\left(\frac{Q_p^3}{R^2}\right) \tag{1.44}$$

with R as the ring's radius, Q_p the pump quality factor of the loaded cavity, and ν_p the group velocity. Both expressions 1.42 and 1.42 neglect the free carrier effects in the materials. This approximation does not hold at high input powers when Two-Photon Absorption (TPA) occurs. The equations 1.42 and 1.44 does not indicate which frequency is converted. This is deduced from the phase matching condition 1.37, as long as it is true there is frequency conversion. It is difficult to compare directly the two expressions as they do not have the same behavior. All other parameters being fixed, enhancement from a cavity can be further increased by tuning its quality factor [66]. In a ring, photon generation preferentially happens in the resonances, meaning a wavelength comb of light is emitted over the full phase matching condition range.

1.2. State of the art: Quantum characterizations

Quantum characterization or state tomography is fundamental to make use of generated states. Not only do we need to know the state we are creating to use it, but we also need to know its performances, as they limit the application we can target. There are multiple properties that can be investigated: spectrum, statistics, indistinguishability, entanglement.

Photon statistics

The statistics of the photon states determines the nature of the generated light. Since we work here in a discreet variable scheme, we will not consider the coherent state statistics.

Single photons are characterized by their non-classical statistics. Indeed, to be single photon, they should be anti-bunched, *i.e.* they must be separated in space/time and not bunch. This is not a trivial behavior to obtain and usually requires single photon sources [69]. Statistical characterization of single photon sources is done with a second-order correlation ($g^{(2)}$) measurement (see section 4.2). To do so a Hanbury-Brown-Twiss (HBT) type experiment must be realized [70]. A beam splitter sends the light beam to two photo-detectors. The correlations between the two detector's measurements inform on the statistics of the light [70]. The criterion is the level of correlations at zero delay, which for a beam of single photon should go down to zero (anti-correlation).

Such measurement is the first proof that a quantum emission has been achieved. [71, 72, 73, 74, 4, 75, 76, 77]. Below a value of 0.5 at zero delay, it is considered as a quantum light source. However, for a source of single photon, its $g^{(2)}$ must be close to zero, see table 1.1.

Spectrum & Joint spectral amplitude

The spectrum of the emitted photons determines the platform on which it can be manipulated but also what type of interactions are available. At telecom wavelength, the photons can be guided in optical fibers and transmitted over a few km with minimal loss. In the near infrared (700-900 nm), they can be used with high efficiency single photon detector made of silicon working at room temperature [78].

The spectrum of the photon states also determines the type of interaction that a photon can have. Two photons with identical spectra (as well as all other properties) can interact and interfere.

Finally, there can be correlations within the spectra mode of different photons. In this case the photons are entangled. The Joint Spectral Amplitude (JSA) measures the spectrum correlation level between two photons. It is the probability to have a frequency of the first photon as function of the frequency of the other. The JSA can be performed with correlation measurements using dispersive fibers [79], narrow filters [80], interferometry [81]. Seeding of the photon pair is possible, a single spectrometer is needed and allows to retrieve the JSA [82]. There are then two extreme cases depending on the JSA shape: Separable photons or Entangled photons [83].

Indistinguishability

Indistinguishability tests the possibility of labeling different object. If there is no way to label them as photon A or B, they are indistinguishable. The indistinguishability depends on the type of measurement performed on the photon; they are indistinguishable with respect to a measurement. Any two photons interference can provide information on the indistinguishability of the interfering photons [42, 84]. Indistinguishability has

been characterized in polarization [85], time-bin [86, 46], path with an Hong-Ou-Mandel (HOM) experiment [87].

In this last case, each photon is sent at the input of a perfect beam splitter. Depending on the time delay between the two incoming photons, a dip in the coincidence can be measured. These coincidences arise between the two outputs of the beam splitter. At zero delay, the coincidences should go to zero if the photons are perfectly indistinguishable as the photons bunch. This type of experiments has been performed between pairs of photons [88], which were generated with quantum dotes [89, 90], or point defects [91]. In all these cases the photons had a highly indistinguishability (>80%).

1.3. State of the art: Integrated quantum photonics

The combination of photonics and quantum optics is promising. It allows stable optical circuits, compact, scalable, and amenable to large scale production. Numerous functionalities have been integrated from photon sources [4, 92], to quantum calculators [39, 93], and quantum memories [94, 95], to name a few. The main limitation is the difficulty to combine them all into a single device. However, multiple strategies and technological platforms exist. We will see here the current state of the art of Quantum Integrated Photonics (QIP).

QIP exploit the fundamental properties of quantum physics to code and manipulate quantum states. QIP are regarded as the one of most promising pathway towards disruptive technologies, envisioning major improvements in processing capabilities and communication security [96, 97]. However, practical implementations, such as quantum key distribution systems or quantum processors, require a large amount of compatible building-blocks [98, 99, 100, 101]. Integrated photonics provides efficient and reliable solutions for realizing advanced quantum communication systems based on both linear and nonlinear elements [102, 103, 104, 105, 106, 107, 108]. One of the crucial limitation of all these realizations is the on-chip filtering. Pump lasers are used to excite/generate nonlinear light. This pump light has much higher intensity then the generated photon state. So it must be removed. Most of the time, this operation is externalized, using fiber or bulk optical components, and hinders the benefit of both the compactness and stability of the whole system [109].

The three stages of quantum photonics are the generation, manipulation, and detection of quantum light states. We will go through the state of the art of the three.

Single photon sources A fundamental component is the single photon source. It needs to send photons with a large rate, predictable in time, and generate pure single photons. They need to be indistinguishable, in the same spatial, temporal, polarization, and spectral mode [77], see table 1.1. Multiple platforms have developed these sources, we will see a few of them below. There are multiple types of sources, some generating a unique photon, some a pair of photons each time, see figure 1.6. There is also *on-demand sources* where a state is generated after a trigger pulse and *heralded sources* where a quantum state is generated at a random time.

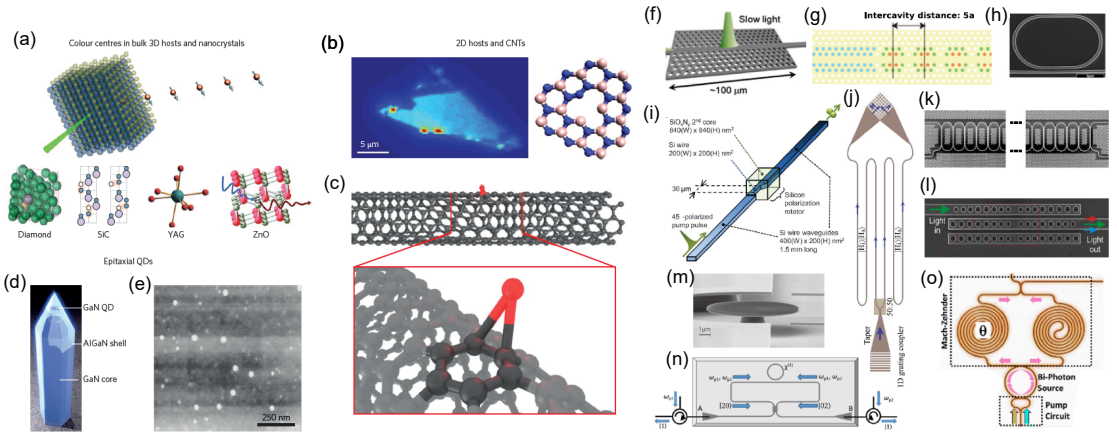

Figure 1.6.: Examples of structures used for the generation of single photons: (a) Defects in bulk 3D crystals and nanocrystals that emit single photons when excited with sub-bandgap light (illustrated with a green incoming laser beam). The insets show the most studied crystals — diamond, silicon carbide (SiC), yttrium aluminium garnet (YAG) and zinc oxide (ZnO). (b) Emitters in 2D hosts. Single-photon emission at cryogenic temperatures was realized from localized excitons in several transition metal dichalcogenide monolayers including WSe2 and MoSe2, as shown in the confocal map (left). Room-temperature operation was realized from defects in monolayer hBN and few-layer flakes of hBN (right). (c) Single-photon emission was recorded from excitons localized at oxygen-related defects in single-walled carbon nanotubes. (d) Nitride Quantum Dot (QD) embedded in a nanowire waveguide in order to enhance emission. (e) Self-assembled InAs QDs. Both QD systems are representative of epitaxial (non-colloidal) QD-based single photon emission platforms. The InAs QDs were the first system used to demonstrate triggered single photon emissions. Examples of structures used for the generation of photon pairs: (f) photonic crystal waveguide, (g) coupled photonic crystal cavities, (h) ring resonator, (i) waveguide with polarisation rotator, (j) two-path source with a 2D-grating combiner, (k) coupled ring resonator optical waveguide, (l) coupled one-dimensional photonic crystal resonators, (m) microdisc resonator, (n) bidirectionally, non-degenerately pumped all-pass ring, and (o) bidirectionally, non-degenerately pumped add-drop ring. Reproduced from Ref. [77, 110].

Manipulation Once we can generate well defined states, we need to be able to change them, *i.e.* to make them interact in a controlled way. Wavelength (de)multiplexing is an important tool separate or combine photon pairs at different frequencies. Actively tuned components are fundamental to direct dynamically photons together. For instance, a photon can be sent to a quantum memory for storage or re-routed to be processed. The processing is done differently depending on the encoding. It is done by gates in the circuit. They can be static or reconfigurable. Since we are using light, these gates consist of optical elements like phase shifters and beam splitters. The idea is to apply a linear matrix operation of the photon states. For instance, in the case of path encoding, the most useful gate is the Controlled NOT gate. It requires two input photons, a *control*

	Photon purity $g^{(2)}(0)$	Indistinguishability	Efficiency η	Repetition rate
Quantum key distribution	< 0.1	Not critical, photons must be uncorrelated	> 0.5	$> GHz$
Cluster-state quantum computing	< 0.001	> 0.99	> 0.99	Ideally $> GHz$ to avoid long buffers
All-optical quantum repeater	< 0.001	> 0.99	> 0.99	$> GHz$
Bell-state sources for memory-based repeaters	< 0.01	> 0.9	> 0.9	Ideally $> GHz$

Table 1.1.: Summary of source requirements for different applications. Photon purity describes how close the produced states are from the modeled ones (here how close we are from a single photon). Indistinguishability reflects how subsequent photons can be recognized, *i.e.* how identical they are. Efficiency is simply the probability to have a photon when we expect one. Repetition rate is the number of times we get a photon per second. Table reproduced from Ref. [77]

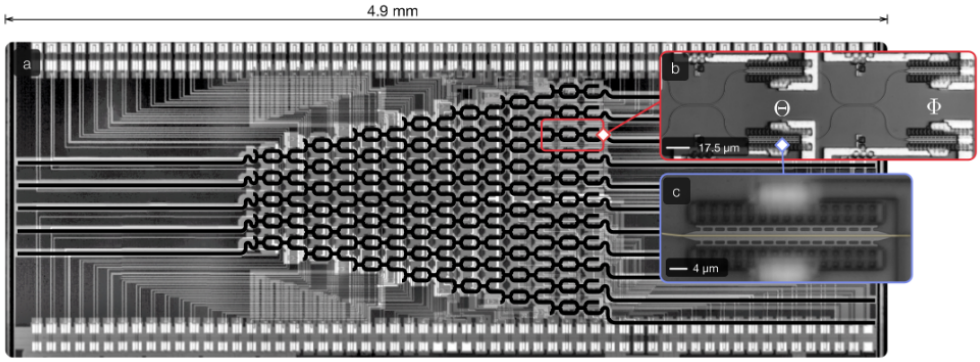

Figure 1.7.: (a) Optical micrographs of programmable nanophotonic processor, the system is 4.9 mm by 1.7 mm and is composed of 56 Mach-Zehnder interferometers, 213 phase shifters, and 112 directional couplers. Waveguides are outlined in black. (b) RBS unit cell with two directional couplers and two internal ($\theta_{1,2}$) and two external ($\phi_{1,2}$) low-loss, thermo-optic phase shifters. (c) Thermo-optic phase shifter. Heat is localized to the waveguide using narrow thermal bridges. Reproduced from Ref. [111].

photon and a *target photon*. The target state will be flip (reverse the values of $|0\rangle$ and $|1\rangle$) if and only if the control qubit is $|1\rangle$. The gate is composed of a Mach-Zehnder interferometer, to act as a controllable beam splitter, and a phase shifter, see figure 1.7 [112, 111]. However, depending on the level of precision, more complex circuit must be used to achieve a Controlled NOT gate [113, 114, 115]. Nonlinear gates can also be considered, like two-level or multi-level systems. These types of interactions between photons can be expended to created more complex architectures [112].

Detection Finally, after the states have been manipulated in the desired way, one needs to measure the results by detecting photons. They are absorbed into a detecting structure (PN junction, superconducting nanowires, ...) that transforms the photon's

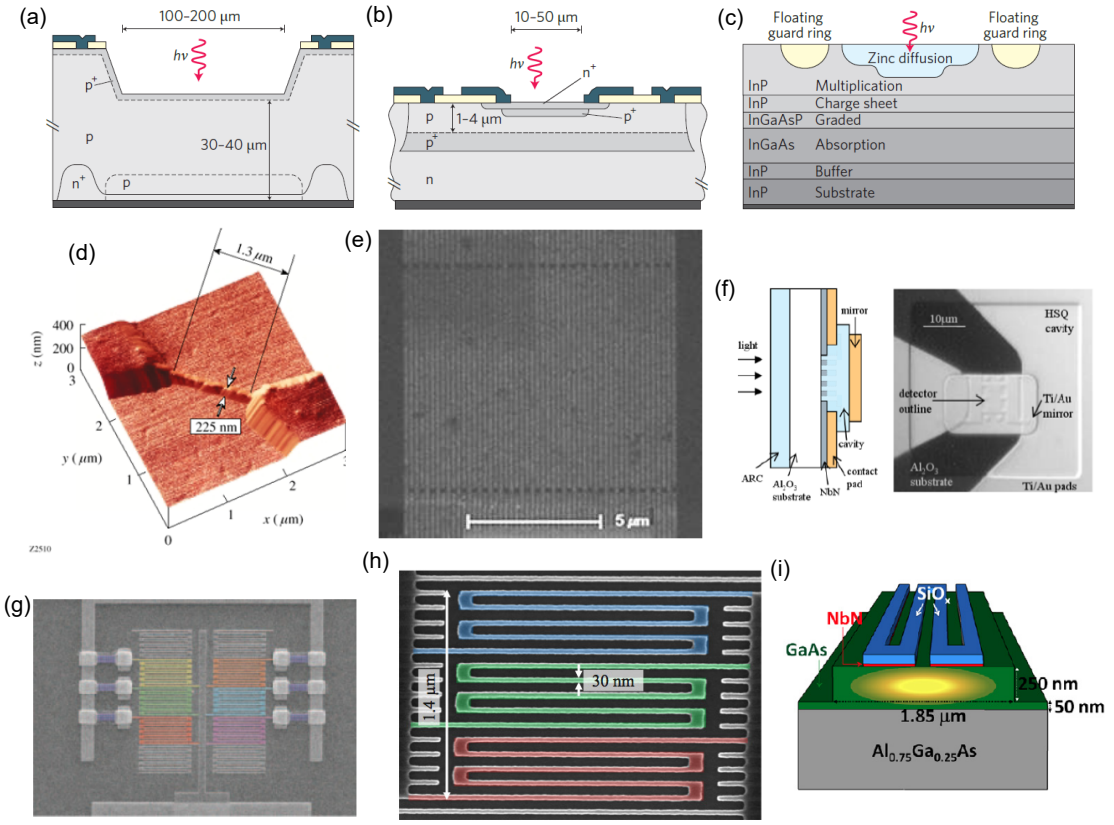

Figure 1.8.: Established photon-counting technologies based on reverse-biased avalanche photodiodes. (a) Thick-junction Si Single Photon Avalance Detector (SPAD), a device structure optimized for high detection efficiency and low dark counts. (b) Shallow-junction planar Si SPAD, a device structure optimized for low timing jitter requiring low bias voltages. (c) InGaAs/InP SPAD structure, where the use of a smaller-bandgap semiconductor extends single-photon sensitivity to telecommunications wavelengths. The evolution of Superconducting Nanowire Single-Photon Detector (SNSPD) design. (d) An atomic force microscopy (AFM) image of an early 1.3 μm x 225 nm NbN nanowire. (b) A Scanning Election Microscope (SEM) of NbN meander SNSPD covering a 10 μm x 10 μm area. (c) A 3 μm x 3 μm NbN meander SNSPD embedded in an optical cavity, designed for optical illumination via the substrate. (d) Multiple nanowire elements are biased in parallel via independent resistors resulting in a photon-number-resolving SNSPD. (e) Ultrathin nanowires (30 nm wide) are connected in parallel to improve the sensitivity (registering efficiency) of the SNSPD. This device is known as a superconducting nanowire avalanche photodetector (SNAP). (f) A SNSPD fabricated on an optical waveguide structure to improve the optical coupling efficiency. Reproduced from Ref. [116, 117].

energy into an electrical current. This current is then can be amplified and used, see figure 1.8 [116, 117]. Except for the time-bin and time-energy states, we do not di-

rectly probe the properties of photons. We filter them and see if they pass the test. Recent developments in detectors have enabled photon-number-resolving detectors to reach high efficiency $> 80\%$. Such detectors allow to access the photon number with greater certainty than ever before, opening new experimental possibilities [118, 119].

1.3.1. III-V platforms

Using Quantum Dot (QD) in InGaAs, InAs/GaAs, InAsP, and more, many groups have been able to generate on-demand single photon sources, see figures 1.6 and 1.8 [71, 72, 73, 74, 4]. These artificial atoms contain at least two energy levels. An electron-hole pair can be exited and relaxed inside the QD to create a photon [120].

The main difficulty is the integration of the QD into integrated structures. QD are generally randomly distributed in positions and energy levels. This issue can be resolved by customizing the lithographic process, sometimes called in-situ lithography. It requires locating, measuring and patterning the QD in a single fabrication process. The same optical path is used for all the steps but at different wavelengths. The localization and characterization of QD is usually made by photoluminescence in the near infrared ($\sim$900-1000 nm), whereas lithography is realized in the Ultraviolet range [121, 122]. Such sources yield very efficient single photon generation per pump laser pulse [71, 72, 73, 74, 4]. They require very low amount of pump power (down to the nW) to emit a single photon. Their firing probability per pulse is also close to one. But both indistinguishably and multi-photon emission are still problems. They reduce the quantum performance of the source as the generated states cannot be trusted. They also require very low temperature to operate (about 4K), thus a cryostat and other adapted equipment are required. However, this might not be a problem for a fully integrated system as ultra-low noise detectors also generally require low temperature to operate.

Another way is to manually move the QD to a position suited for integration. This was shown in the InP platform [123]. The quantum emitter, an InAsP QD, was embedded in a pure InP nanowire. It was then moved into a site to be integrated into a waveguide. This allowed for in plane QD excitation and extraction of the generated photons.

1.3.2. Periodically Poled Lithium Niobate

Lithium Niobate has now been used in photonics for almost 50 years. Waveguides and various active devices on this platform (modulators [124], phase shifters [125], etc [126]). But the most interesting structures are Periodically Poled Lithium Niobate (PPLN) waveguides. A high second order nonlinear effective coefficient can be achieved in them. They are great candidates for frequency conversion, for instance using PDC. Since Lithium Niobate is a ferroelectric crystal, it has a dipole moment. PPLN are periodic structures with successive moment inversions.

PPLN are almost working at room temperature (RT). Instead of being cooled, they must be heated at around 100°C to 200°C to achieve the phase matching condition. They cannot be too compact due to the low index contrast (< 0.1), making turns millimeter

long, limiting their use [127]. Nonetheless, many applications have been demonstrated in the approach.

PDC has been used for a long time to generate entangled photons mainly in polarization. The pump laser is converted in the PPLN waveguide into a pair of photons satisfying the matching phase and energy conditions. This is a broadband process that creates entangled pairs [5] which can be used for application like QKD [92, 128] or quantum relays [129]. It is also possible to add a filter after the PPLN waveguide that narrows enough the emission bandwidth to generate separable states, at the price of heavy losses. In this case, it becomes a heralded single photon source that delivers single photons at random intervals. The pumping laser can be in Continuous Wave or pulse regimes, resulting in high heralding efficiencies ($\sim 60\%$ probability). However, a main limitation is the pair statistics being generated. The probability of accidentally heralding two photons instead of a single one increasing with the rate. The higher the pump power, the higher photon rate, but also the lower the single photon quality [130]. This is true for all nonlinear processes.

More elaborated systems can also be implemented: hyper-entangled pairs in time-bin and polarization have been demonstrated [131, 132]. In this case, each photon of the pair has both a time-bin and polarization entanglement simultaneously. Path entanglement demonstrations have been used to produce NOON states, mostly used in metrology [133]. This was achieved by having evanescent coupling between two PPLN waveguides, which delocalizes the pairs. When properly engineering the coupling constant and the phase matching condition, path entangled two-photon states are naturally created, *i.e.* NOON states or entangled two-photon states [134, 135].

Squeezing is also possible in PPLN waveguides. This is when the fluctuations of one of the two quadratures of the light electrical field is compressed below the Planck's constant. Different realizations of squeezing at telecom wavelengths have been demonstrated [136, 137]. One notable example that makes use of squeezing is in Laser Interferometer Gravitational-Wave Observatory (LIGO). Its Michelson interferometers use squeezing to reduce noise in the detection of gravitational waves. Finally, quantum memories can also be made in PPLN waveguides [138]. The encoding and reading is done by sending bright pulses along the stored state. Quantum memories are key elements for long distance quantum communications, to build true quantum networks. The main advantage here is that the natural acceptance bandwidth of the quantum memory is in telecom wavelengths.

1.3.3. Diamond Defects, Nanotubes, and Organic Molecules

Other platforms are emerging as quantum photonic platform candidates. They do not have technological ascendant over the III-V, Lithium Niobate, or Silicon platforms, but show interesting properties for quantum optics. Among them are a few notable ones, color centers in diamond, nanomaterials like carbon nanotubes, single-atom layers, or organic molecules. All of them are alternative routes to a on demand single photon source but still suffer often from poor light coupling, low indistinguishability, as well as reproducibility issues.

The nitrogen-vacancy (NV) and the silicon-vacancy (SiV) defects in diamond have been the most studied. Their crystallographic and electronic structures are well established. At low temperature (<5 K), the emitter's bandwidth are narrow enough to allow two-photon interference between different emitters, although poor visibility is then reached ($72 \pm 5\%$ and $66 \pm 10\%$ for the SiV and the NV centres, respectively [139, 91]). But they have a high-count rates, at the same level as QD. [75, 76, 77]

Nanomaterials such as semi-conductive carbon nanotubes or defects in single-atom layers also allow to generate single photons thanks to their electronic band structure. As the others, they work at cryogenic temperatures. Reproducibility and brightness still remain challenges. Development in the fabrication process may be able to reduce differences between samples. [140]

Organic Molecules have naturally the needed level structure for quantum emission. Fluorescent light from molecules provides high photon rate with simple integration approaches [141, 142], but they also often require to operate at low temperature to reduce the phonon perturbations. They also present low indistinguishability [143]. However, thanks to their complex structure, they provide interesting solutions for more complex interactions such as polarization-controlled emission.

1.3.4. Silica and Silicon

Silicon based platforms (silica on silicon, Silicon on Insulator, Silicon Nitride) are very promising for large scale applications as they rely on the technological advancements of the Complementary Metal-Oxide-Semiconductor (CMOS) processes. Fabrication processes use for the fabrication of microprocessor and computer systems [144]. CMOS components have been improved and refined form more than 50 years and has led to large-scale microelectronic industrial production. CMOS processes has been the basis of the industrial photonic development. Such commercial platforms allow the large scale reproducible production of photonic system. Manipulation of quantum states was demonstrated in previous works with commercially fabricated devices [110, 111]. However, the generation and detection of photons are still limited by losses and heralding process. Most of these works make use of the SFWM process as the mean to generate quantum states. This is the only solution as there is no Parametric Down Conversion (PDC), nor artificial atoms available on these platforms. This is restrictive as it is a random process. So it reduces the scalability of multi photon states generation. SFWM comes also from a third order nonlinearity, decreasing the efficiency of the pump conversion compared to PDC. Finally, the pump and generated pairs are in the same wavelength range, which makes it difficult to clean up the quantum signal.

Silica on silicon is the most difficult to scale both in complexity and fabrication. The waveguides are made by doping the silica creating an index change. The index contrast (<0.1) is low, making compact turns impossible, thus limiting the density of integration. Silica has also a lower nonlinearity than both silicon and silicon nitride. It has however extremely low losses (<0.1 dB/cm [145]) and very good coupling to standard single mode fibers; two very important properties for quantum photonics [146]. Silica waveguides can also be realized with laser writing. A high power laser is used to heat locally the silica

and create the waveguide. This restrains the type of possible waveguide/components geometries compared to other lithographic techniques. But it allows for 3D waveguide positioning, as the waveguides are basically fibers. This is a industrially compatible each waveguide been written one by one. However, if the fabrication process does not require a cleanroom, it makes a more affordable on-site fabrication method.

Material	n	n_2 (m^2/W)	Transparency (μm)	TPA
SiO_2	1.44	3×10^{-20}	0.2 - 4	No
Si	3.47	5×10^{-18}	1.2 - 8	Yes
Si_3N_4	2	2.5×10^{-19}	0.4 - 4.6	No
Platform	**Lin. losses (dB/cm)**	**Coupling (dB)**	**Typical Q**	**Themo-optical coeff. (RIU/°K)**
SiO_2	< 0.1	< 0.1	-	0.95×10^{-5}
Si/SiO_2	> 1	~ 3	10^4	1.9×10^{-4}
Si_3N_4/SiO_2	< 1	~ 3	10^6	1.45×10^{-5}

Table 1.2.: Summary of the silicon materials and platforms at 1550 nm. [147, 148, 149]

Silicon-On-Insulator (SOI) allows for ultra-dense circuits, as a result of the large index contrast between silicon and silica. It also allows for large scale fabrication capability, thanks to its well-known technology. It has the highest nonlinearity of the three platforms, but suffers from TPA at telecommunication wavelength (in the near-infrared), which limits the pump power in waveguides. TPA will not be a problem in this work as the photon rate at low power is enough for our applications. SOI has higher losses (>1 dB/cm), poor fiber coupling (>3 dB), and still uses random process to generate states. But SOI is also the main platform of classical photonics. Thanks to this, various classical photonics functionalities have been already integrated (*e.g.* lasers, photodiodes, ...) that are not native to silicon. The integration of III-Vs or superconducting materials on silicon has been demonstrated [110, 150, 151, 152, 153, 154]. They could make SOI a unifying platform where all other functionalities (generation, manipulation and detection) are possible.

Silicon nitride has the advantage of silicon (for the production and an acceptable level of integration of circuits), while having low losses (<1 dB/cm). It has a lower nonlinearity than silicon. This can be compensated by the higher enhancement of its cavities (*e.g.* higher quality factor up to 10^6), while not being limited by TPA. It has also been integrated on silicon and is becoming a standard photonic platform in industrial foundries.

Many quantum demonstrations have been realized on these platforms. Spirals [155, 156], rings [46, 157], and photonic crystals [158] based SFWM emission have been demonstrated allowing the generation of photon pairs. They can be demultiplexed without altering their properties [11, 159]. These pairs can then be used in programmable photonic processors [111] or combined to create multi-photon states [37], all on a single chip. These developments allowed for the implementation of two photon quantum logic gates [160].

In all of these platforms, the pump rejection is one of the main limitation. A few experiments based on this technology have been carried out to address the pump rejection challenge using on-chip solutions [7, 8, 9, 10, 11, 12, 13]. This is due to the close spectral

proximity between the pump and the generated light.

For instance, let us compare a silicon ring with a quality factor of 10^4. If 1 mW of pump power is injected, 8.1×10^6 pairs are generated per second (using equation 1.44). However, 1 mW of optical power at 1550 nm is roughly 10^{16} photons per second. We can see that for the pump to reach the same power level as the light generated, a $\sim 10^{10}$ reduction is required. So one way or another a 100 dB filtering must be applied to the pump light.

The current filtering strategies suffer from two main limitations: i) the continuous monitoring of the filter response to maintain proper performance [7, 8, 9], and ii) prohibitive additional interconnection losses between components [10, 11] (up to 9 dB [12]). We will see our strategy to reject the pump in chapter 3.

For all these advantages, we chose to use the SOI platform to develop quantum optical circuits. The well-known fabrication processes will allow us to increment quickly our designs, while the versatility in the platform allows various functionalities to be implemented on a single sample. We will be able to design in the next chapters all the building blocks for the nonlinear generation of light. We will also propose and demonstrate a solution for on-chip pump rejection. All of this while staying compatible with the industrial fabrication standards and the telecom channels from the International Telecommunication Union (ITU grid).

Chapter 2.

Silicon Photonic Platform

The development of a quantum photonic platform requires a high level of fabrication control as well as a library of components. The goal is to fabricate reliable devices with a high degree of reproducibility [110, 161]. We will re-design our platform to be compliant with quantum needs. The more components are available, the more various functionalities and versatility are given to the platform. One can implement then different circuits on the same chip with the same fabrication process. Here, we aim at generating and manipulating non-classical states of light on a single device.

We will first go over the lithographic and fabrication processes. Then, we will see what are the components and functionalities needed to achieve a complex quantum circuit. Finally, we will build all the needed components of the platform, including waveguides, active-tuning, generation of non-classical light, and demultiplexing components to extract or separate photon pairs, see figure 2.1.

2.1. On-chip quantum circuits

Our goal is first to generate quantum states on chip. Then we will make them usable by cleaning noise and pump in the signal. This quantum light will then be manipulated using demultiplexing stages and/or beam splitters for various tasks. The integration of all the functionalities requires: the development of components, a way to connect them all, and to control them. Let see all the functionalities we need to achieve a quantum circuit. More explicitly, this thesis has been largely based on the architecture presented in figure 2.1. Inside, pairs of photons are generated then manipulated into different quantum states. The rather crucial aspect of this small circuit on a chip is a good control of optical losses, an extreme rejection of the optical pump signal (see chapter 3) and a spectral alignment of the ring resonances with the rejection band of the pump filter (see chapter 4). In other words, the different sub-blocks that make up the whole must not only have correct individual performances, but must also be able to work effectively with the other elements. Without going into a deep level of detail further at this stage, here are the various optical functions that must be combined to generate pairs of entangled photons.

Non-linear light generation is done with a ring cavity. This will allow to amplify the efficiency of the Spontaneous Four-Wave Mixing (SFWM) effect in Silicon waveguides

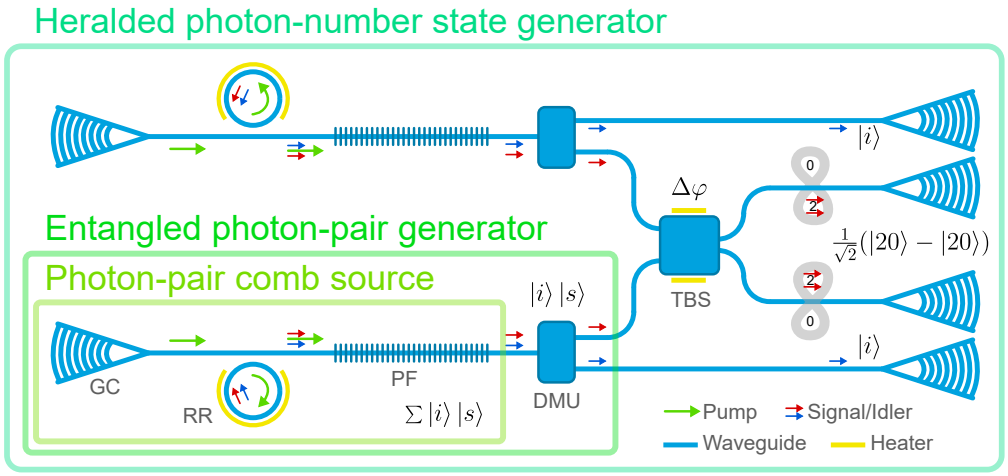

Figure 2.1.: Schematic of the target quantum circuit comprising different components: grating couplers (GC), ring resonators (RR), pump filters (PF), demultiplexers (DMU), and a tunable beam splitter (TBS). Here a *photon-pair comb source* outputs multiplexed frequency combs of photon pairs; the *entangled photon-pairs generator* outputs in separated waveguides the signals and idlers of the pairs (it can have more than two outputs); the *heralded photon-number state generator* outputs NOON states or pairs of indistinguishable photons when two heralded photons (here idlers) are detected simultaneously.

(section 1.1.5). It localizes the pump conversion to the cavity's resonance wavelengths. This aims at creating a frequency comb of photons pairs. To be compatible with standard telecom network components, we will stay at telecom wavelengths and try to match our wavelength comb with the International Telecommunication Union (ITU) standards. The cavities will thus have to generate light directly in the standard ITU grid channels. This should allow to use off-the-shelf components when using the nonlinear light being generated through the SFWM process.

The pump rejection filter cleans the nonlinear light from the pump. The needed large level rejection ($\sim$ 100 dB [6]) makes it challenging to design and fabricate. In silicon photonics, we will use an optimized Bragg grating based on an original approach to remove the pump from the comb (see sections 3.5 & 3.6). At the end, only photon-pairs are left, ready to be manipulated. This will be addressed and discussed in more details in a separated chapter, see chapter 3.

De-multiplexing allows to separate the different wavelengths generated in the comb. Each pair is separated into two channels, they can then be used as resources for different users. De-multiplexing can be achieved with an active (*e.g.* add-drop ring), or a passive solution (*e.g.* modal add-drop device). The add-drop ring is a cavity with a secondary coupled output channel. It allows the resonating light to be extracted while the rest is transmitted. It is very selective with a low crosstalk level but requires active tuning

of the cavity to work properly (see section 2.7.1). The modal add-drop on the other hand uses a grating to selectively back reflect the light, which is then coupled into another waveguide. This strategy can be used without active tuning thanks to its large bandwidth (see section 2.7.2).

A tunable beam splitter is simply a Mach-Zehnder Interferometer (MZI). It can tune the power injected into its two outputs. If two entangled photons are sent simultaneously in the inputs of the MZI, they can form a number state (*e.g.* NOON state [112, 162]) depending on the interferometer's phase.

Let us call an *entangled photon-pair comb source* the combination of a ring cavity and a pump rejection filter (see figure 2.1). Its output is a cleaned comb of nonlinear light. If we now integrate a demultiplexing stage, we get an *integrated entangled photon-pair generator* (see figure 2.1). Its outputs are directly (groups of) photons pairs that can be sent to users. Depending on the type of pump used for the SFWM process, it can output entangled-mixed or separable-pure photons. When entangled, they can be used for quantum telecommunications. Or, if separable, they can be used as a heralded photon source. In that case, we get a *Heralded photon-number states generator* by combining two pair generators with a MZI (see figure 2.1).

When we change the phase imbalance of the MZI ($\Delta\varphi$), the splitting ratio at the output changes. At a fixed wavelength (here the signal wavelength), the output for an arbitrary phase is

$$|\Phi_{out}\rangle \simeq 2i\left(1+e^{2i\Delta\varphi}\right)|\Phi_{sep}\rangle + \left(1-e^{2i\Delta\varphi}\right)|\Phi_{N00N}\rangle\,. \tag{2.1}$$

Here, $|\Phi_{sep}\rangle$ describes the path product state $|11\rangle$ (a single photon is in each output of the chip), while $|\Phi_{N00N}\rangle$ describes a two-photon N00N state of the form $1/\sqrt{2}(|20\rangle - |20\rangle)$ (a coherent superposition of 2 photons being delocalized over the two output modes). So the state generated can be dynamically configured from $|\Phi_{sep}\rangle$ to $|\Phi_{N00N}\rangle$ by setting the phase $\Delta\varphi$ to the right value, summarized in equation 2.2 [108].

$$|\Phi_{out}\rangle = \begin{cases} |11\rangle\,, & \Delta\varphi = 0 \\ 1/\sqrt{2}(|20\rangle - |02\rangle), & \Delta\varphi = \frac{\pi}{2} \end{cases}. \tag{2.2}$$

However, this is only the case if we have a trigger (detection of a photon) for both idlers at the same times. Otherwise, if a single idler is detected, the system outputs:

$$|\Phi_{out}\rangle \simeq -\sin\left(\frac{\Delta\varphi}{2}\right)|10\rangle + \cos\left(\frac{\Delta\varphi}{2}\right)|01\rangle\,. \tag{2.3}$$

2.2. Mask conception & Fabrication

To create a circuit we must first design its components. All the dimensions are set then drawn so that is can be implemented onto a wafer. This process requires various tasks and iterations that we will see in this section.

The fabrication of silicon waveguides is a structuration of the materials with nanometric precision. High accuracy is necessary to obtain reproducible devices. The material to build the circuit is a planar disk of silicon. It is made of a crystalline layer of a few hundreds of microns in thickness. This substrate can be uniformly coated with other materials, like silica, polymers, metals, *etc.* Then parts of the layers are removed to create a pattern. There are multiples types of fabrication processes each with different strategies. Some change the material properties by doping. Others etch it with a beam of ions to create a pattern. They all have their advantages and weaknesses. We use lithography which is typically used in planar technologies to fabricate microprocessors. It is now used to make photonic circuits in the compatible silicon family materials [163].

Since we use silicon, we will work in its low loss transmission window in the near infrared ($\sim$ 1550 nm). This is also the wavelength for optical telecommunications in typical fiber network (ITU wavelength range).

Lithography consists of multiple fabrication steps: deposition of a photoresist, exposure of the mask, development of the photoresist. It is similar to a photographic chemical process but in silicon wafers, see figure 2.4. Photoresist is exposed to light that changes its chemical properties. If a mask or shape blocks the light, its shadow will form a pattern in the photoresist. Then the pattern is transferred on the materials by etching. Finally, a cleaning step removes any unwanted residue. It can then be transferred on the silicon by a chemical treatment, see figure 2.4. [164, 165]

2.2.1. Fabrication process

The Silicon-On-Insulator (SOI) photonic platform uses silicon wafers for device production. They are made of a silicon base (750 μm), with above a Buried Oxide layer (BOX) made of silica, and on top a thin silicon layer. The silicon base is monocrystalline which is fundamental when growing materials or making depositions. It avoids mismatches but also allows clean cleaving of the wafer. Wafers can have various diameters depending on the fabrication process, from 25 to 450 mm (1 to 12 inches). We use typically 200 mm (8 inches) wafers. The BOX is either 2 or 3 μm thick. We use a top silicon layer of 220 nm also monocrystalline. This is important for the quality of the photonic structures. Thanks to the absence of crystalline boundaries or defects, less light scattering or absorption can occur. Except the wafers, that are commercially bought, all fabrication processes reported in the presented manuscript have been achieved at C2N. The wafers were cleaved into rectangles of 1 cm $\times$ 1 cm or 1 cm $\times$ 2 cm so they could fit in the Electronic Beam Lithography (EBL) system, be spin-coated, or have chemical bath with ease. Moreover, such a size was better suited for the experimental measurement and our setup. Our processes are not industry standard, and our goal is to prototype circuits that have the same fabrication requirements as in the industry.

After a cleaning in a hydro-fluoric solution, a thin layer of primer was deposited to help the next layer stick to the wafer. This allowed to spin-coat a 90 nm thick layer of ZEP520A positive photoresist [166]. The spin-coating created a uniform layer at the center of the wafer. But close to its edges, the thickness was not homogeneous and increased (edge effect). In its center, pieces of 1 cm by 1 cm squares or 1 cm by 2 cm

rectangles were cleaved from the wafer to fit the EBL chamber holder size. The rest of the wafer is discarded and not used for photonic fabrication. This allows to have a more homogeneous resit between samples as dozens of them could be extracted from a single wafer. Moreover, the ZEP520A photoresist being stable over long periods of time when well stored. We could keep the samples for weeks before doing the lithography. Finally, the resist was annealed at 180°C for 3 minutes to make it ready for the lithographic process step (see figure 2.2a and 2.2b).

As mentioned previously, we are equipped with an EBL Nanobeam NB-4 system [167]. It can go up to an electron acceleration voltage of 80 kV. This insures a penetration of the beam of a few microns in the planar layer. Loading of the samples is done on a sample-holder or chuck. Once loaded into the EBL, the writing step starts. Depending on the step size (2 or 5 nm) and the Graphic Database System (GDS) file size (see section 2.2.2), it last from a few minutes to more than 24 hours (see figure 2.2c).

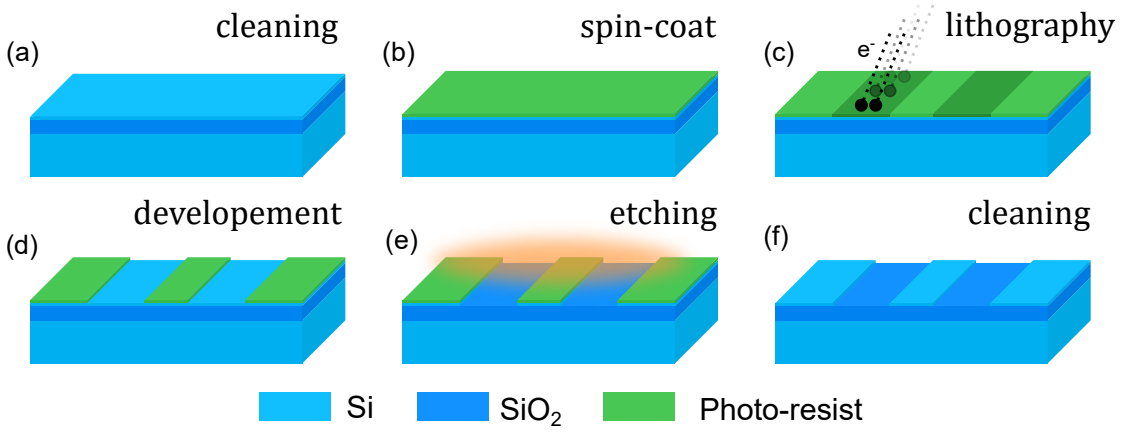

Figure 2.2.: Schematic view of the silicon photonic fabrication process.

Once the patterns were written, a solution of ZEDN50 was applied for 30 seconds. It removed the resist that had been exposed to the beam, leaving a protective mask of the desired structures (see figure 2.2d). To transfer this patterns to the silicon, we used a dry etching, *i.e.* reactive ion etching with inductively coupled plasma (ICP-RIE). A mix of octafluorocyclobutane (C_4F_8) and sulfur hexafluoride (SF_6) gas was used to remove silicon. An oscillating magnetic field create a ionized gas in the chamber. This process reproduced well the shapes of the resist on the silicon. Well defined vertical edges in the resist will result in well defined vertical waveguide edges (see figure 2.2e). A Teflon (C_2F_n) residue was left by the chemical reaction with the resist. It was removed by a cleaning step using a solution of hydrogen peroxide (H_2O_2) and sulfuric acid (H_2SO_4) (see figure 2.2f).

To actively tune some of the photonic components, we deposited metal layers next to the waveguides. A thin (∼100 nm) and a thick (∼500 nm) layers of gold were added as heating elements and electrical contacts, respectively. We repeated the previous lithographic process with a resist layer of 300 nm. We then deposited 10 nm of Titanium

on top 100 nm of Gold. The thin layer was then lift-off to remove the excess gold leaving the heaters on the BOX (see figure 2.3). For the contacts, the resist must be changed to SML1000, as the resist layers must be thicker than the metal had to deposited. The lithographic process was repeated for about 2 μm of resist, Ti layer and 500 nm of Gold were deposited. Finally, the lift-off was performed. The lift-off is a dangerous step as an insufficient resist thickness, or a metal deposition not directional enough, can prevent the removal of the excess metal. This effectively destroys the sample as the transparency is lost.

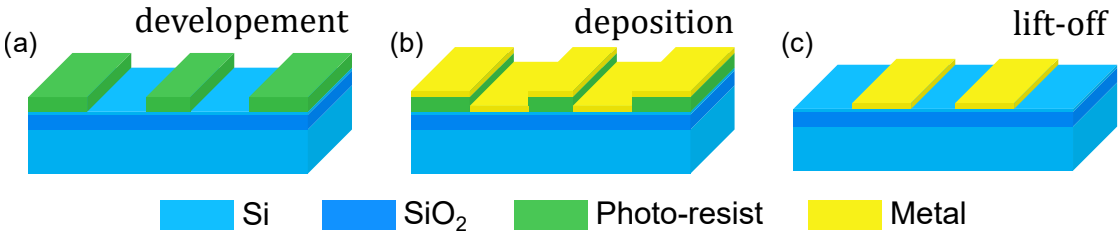

Figure 2.3.: Schematic view of the metal fabrication process by lift-off.

Checks of the dimensions were done using a Scanning Election Microscope (SEM) Raith150. As the silicon's dimensions were smaller than the wavelength of light, classical optical microscopy could not be used to check the fabrication process. But an SEM allowed to see beyond the rayleigh scattering and diffraction limit of UV light. An example of image is shown in figure 2.8b. On top of the photonic circuit, a cladding could be deposited if necessary. In some cases, we spin-coated polymethylmethacrylate (PMMA) on top as a protective layer. This thickness varied but typically was of a few microns. PMMA prevents any SEM imaging once deposited. But it can be easily removed with a bath of acetone and oxygen plasma.

2.2.2. Mask conception

To print the patterns, energy needs to be given to the resist. This extra energy changes the photoresist chemical composition to allow for the chemical treatments. There are two main types of lithographic processes: Ultraviolet (UV) or electronic. The first one makes use of using UV light to give this energy while the second uses an electron beam. The UV approach allows for a fast exposure that is easily reproduced on large scales. It uses a hard mask that must be fabricated for each design. This last step is costly and slow, making it not practical when prototyping. The EBL on the other hand has much higher resolution (a few nanometers instead 100 nanometers for UV) and does not require a hard mask, making it very practical for prototyping. It is however not scalable, as the beam is writing every pixel on the photoresist. The dimensions that can be written with EBL can be down to 50 nm, *i.e.* the shortest straight line, while in UV it is typically 100. In situ fabrication, in our case, was only done with electronic lithography so I will only describe it. That said, it should be noted that all the components designs used in this thesis are compatible with UV lithography, which means that the proofs of concept

that will be presented in the rest of the manuscript are all transferable to industrial fabrication.

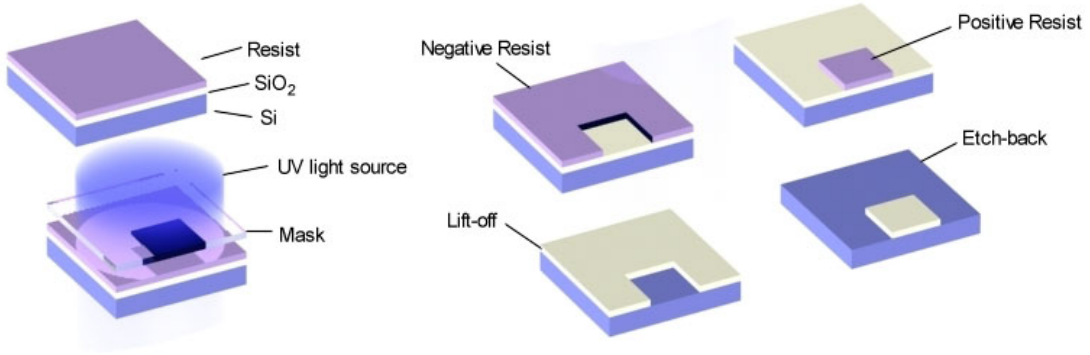

Figure 2.4.: Schematic view of the lithography and differences between a positive and a negative photoresist. (http://www.blackholelab-soft-lithography.com)

There are in fact large similarities between UV and EBL masks. Once the dimensions of the designed structure have been chosen, via simulations or taken from a reliable source. They must be implemented into a GDS file. Such a file format contains a series of points defining polygons, *i.e.* the geometry of the mask. Each polygon is attached to a *layer* and *datatype*. They are additional informations on the polygons that can be used for grouping them or realizing operations on them, *e.g.* boolean ones. The polygons form the structure geometry in the wafer plane. Whereas the layer and datatype are used to establish the moment in the fabrication process when a polygon is exposed. This usually sets the vertical position and thickness of the structure.

There are numerous tools to generate a GDS file, some are free like LayoutEditor or klayout, others are not, CleWin or AppProcessComposer to name a few. On our side, we have used klayout for manual changes and the python library gdspy [168] to generate automatically the GDS files via scripts.

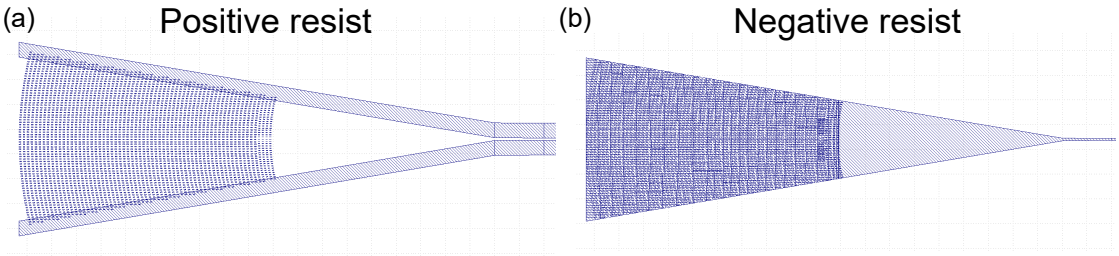

Figure 2.5.: Difference between a positive (a) and a negative (b) GDS file of the same grating coupler.

The GDS files must be fundamentally modified depending on which type of photoresist is used. It is either a positive or a negative photoresist (figure 2.4). Positive resist leaves a hole where it is exposed to radiation. Negative resist, when exposed, creates a

protective layer that prevent etching. To get the same result on the wafer, the geometry or its outline must be implemented, see figure 2.5.

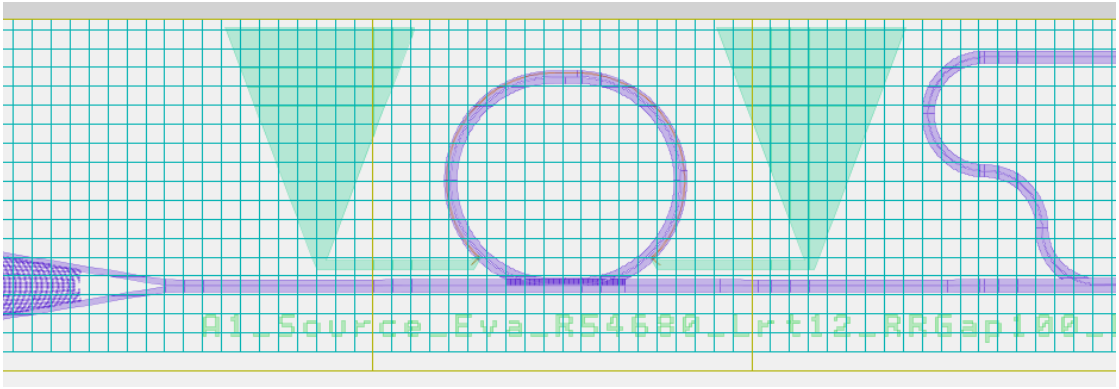

Figure 2.6.: Screen-shot of the GSD once fractured into mainfields (yellow lines) and subfields (blue mesh).

Since our lithographic process is electronic, we had faster incrementations with quick changes between samples (compared to a hard mask). Electron beam lithography is done with a Nanobeam NB-4 system 80kV, with a step size of 5 nm, or 2 nm in some cases. We use the ZEP resist which is negative. The Nanobeam writer has limited writing fields, it can only deflect the electron beam over a limited distance before it gets distorted. They are rectangles of sides ranging between 100 μm and 500 μm. It is these areas that the electron beam scans. The points exposed to the beam form the lithographic pattern. In the *mainfields*, no mechanical movement of the stage (*i.e.* sample) is necessary. When changing between mainfield the sample is moved, so the beam does not have to be deviated too much from the center. The mainfields are divided into *subfields* which have sides ranging between 10 μm and 30 μm, here only the beam moves using magnetic lens. Due to the stage movement, the precision between the mainfields is lower than between the subfields. Misalignments of the beam between fields can create discontinuities in the pattern. Some have only small effects but others can prevent the circuit from working (*e.g.* interrupted waveguides, missing structures, deformed corrugations, *etc.*). When stitching errors are too large, they can create misalignment between fields, see figure 2.7a. It is then important to have the least number of fields as possible. This is also to have the smallest fields to limit distortions. Large structures (grating couplers, ring resonators, *etc.*) should be kept in a single mainfield to avoid large misalignments. Waveguides or long structures (Bragg filter, directional couplers, *etc.*) must be aligned to the subfield grid to limit stitching effects. The choice of these grids and the positions of waveguides must then be integers of one another.

Another effect to take into account is the backscattering of electrons during the lithography, represented in figure 2.7b. As the electrons are backscattered by the substrate, they slowly expose the resist. This dose accumulates for every pixel written. It creates proximity effects where the shapes drawn by the beam are deformed. For instance, sharp corners can be smoothed and the exposed dimensions tend to increase, see figure 2.8. In

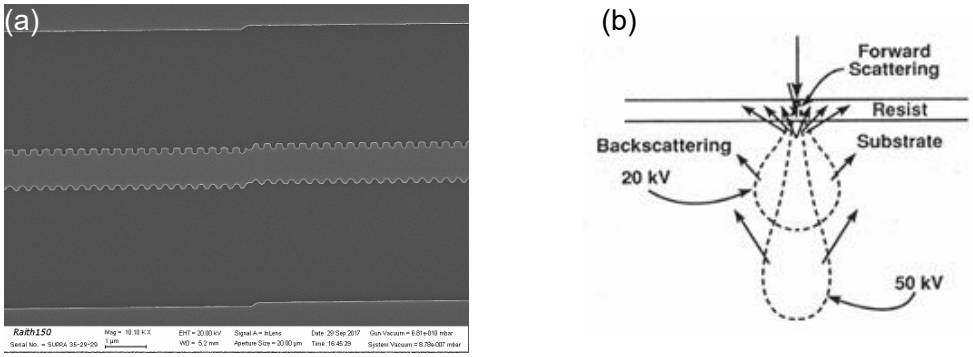

Figure 2.7.: (a) Stitching error during the lithographic process, (b) Schematic view of electron beam scattering during the lithography (henderson.chbe.gatech.edu).

this configuration, the exposed shapes increase in size depending on the dose. For large areas, it can increase, for example by 25 nm in every direction. Since waveguides are defined by the negative of GDS file. An exposed rail defines their paths. This makes the waveguides 50 nm smaller compare to the GDS file. Similarly, for all other structures, bias values must be used in the GDS files so that fabricated dimensions are the desired ones.

Depending on the level of precision needed and the smartness of the EBL, one may need to break a the GDS file apart into individual circuits (waveguides and connected components). Each one should be prepared into a separate file so the EBL only writes one at a time, and no writing jump is possible between them. When giving multiple unrelated structures to the EBL machine, it may (due to proximity between them or other internal parameters) jump between polygons that are not adjacent. Then when the beam comes back, misalignment can occur.

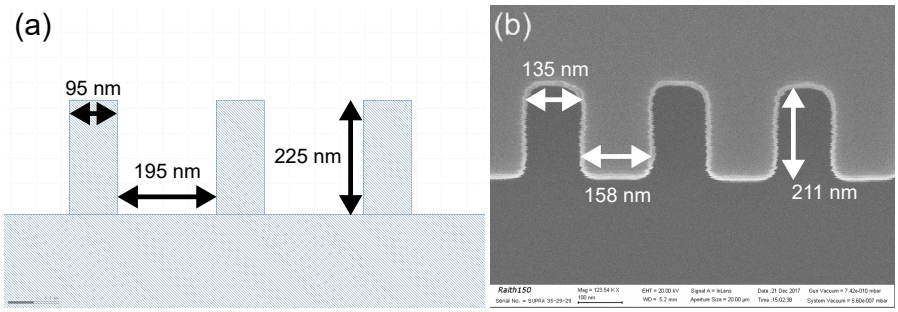

Figure 2.8.: Comparison between the GDS mask and a fabricated structure, (a) GDS mask with the input dimensions, (b) SEM image of the fabricated structure.

When multiple layers are used, it is important to have alignment marks for all of them. Each layer must indeed be accurately positioned with respect to a previous one. After each layer is exposed, the sample must go through a full processing cycle. In some cases, reaching the desired structures requires these alignment marks. If the writing time is

long (more than a few hours), the position of the beam drifts from the origin (0, 0). The last polygon drawn can have drifted by a few microns from the origin, which also depends on thermal effects, the writing time, and the stage precision. So, aligning the next layer to the nanometer clearly requires local alignment marks.

Finally, something that can seem trivial but is often overlooked are labels. Labeling with some dimensions or an id for each device can ease testing and search in the sample. Similarly, adding some unique markings on each sample avoids any confusion. It can also save time when one needs to identify a sample. After all of this is done, the GDS files must be converted into an EBL-compatible file. This depends on the machine itself. In our case, this is Nanobeam Pattern file (NPF). In it, the grids are set and the GDS is fractured (spitted) into mainfields and subfields, see figure 2.6. The NPF files were made automatically with python scripts. The NPF files contain the data but the instructions (which layer to use, with what grid and dose, *etc.*) are in separate files, the Nanobeam job files (NJF). Together they are given to the EBL system, and after an alignment of the sample, it can proceed to write the GDS file.

2.3. Grating couplers

The first functionality we need is a way to inject and extract the light from the silicon layer. To do so, we use Grating Coupler (GC), which are periodic structures scatting the light in specific directions (angles) depending on its wavelength [169].

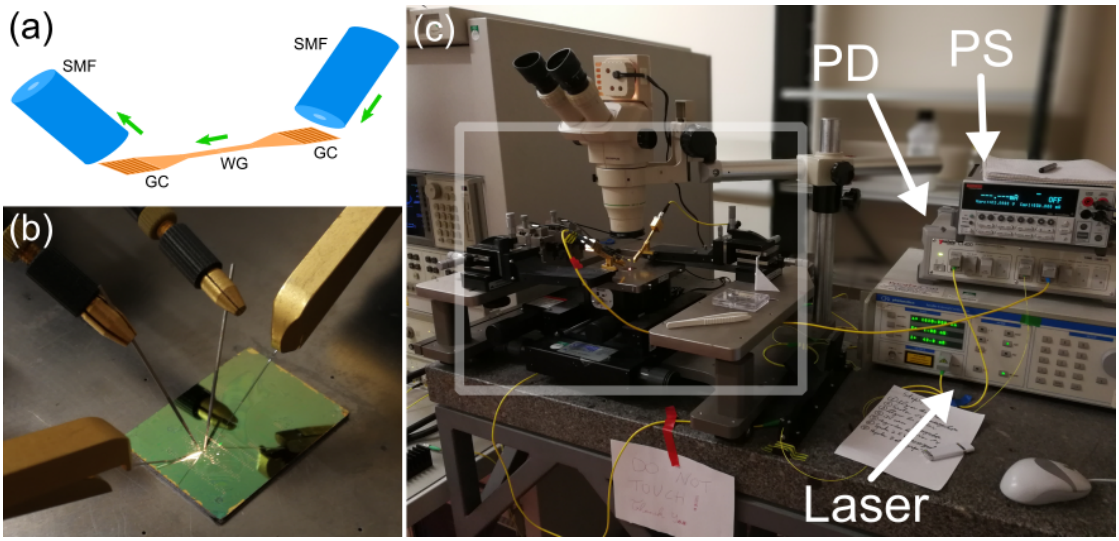

Figure 2.9.: (a) Schematic of the transmission through a sample using single mode fibers (SMF), two grating couplers (GC), connected by a waveguide (WG). (b) Picture of the sample connected by two fibers and two electrical contacts, it is under the microscope on the stage of (c) the picture of the setup used to measure the sample with a Continuous Wave tunable laser, a photo-detector (PD), and a power supply (PS).

Two fibers are cut to leave their core exposed. They are mounted at an angle on a

micro-metric stage, see figure 2.9a. Once the light is injected in the fiber it goes into the grating where it is diffracted into the silicon layer, see figure 2.9b. This is a practical way to get the light in and out, as the reverse process is also possible.

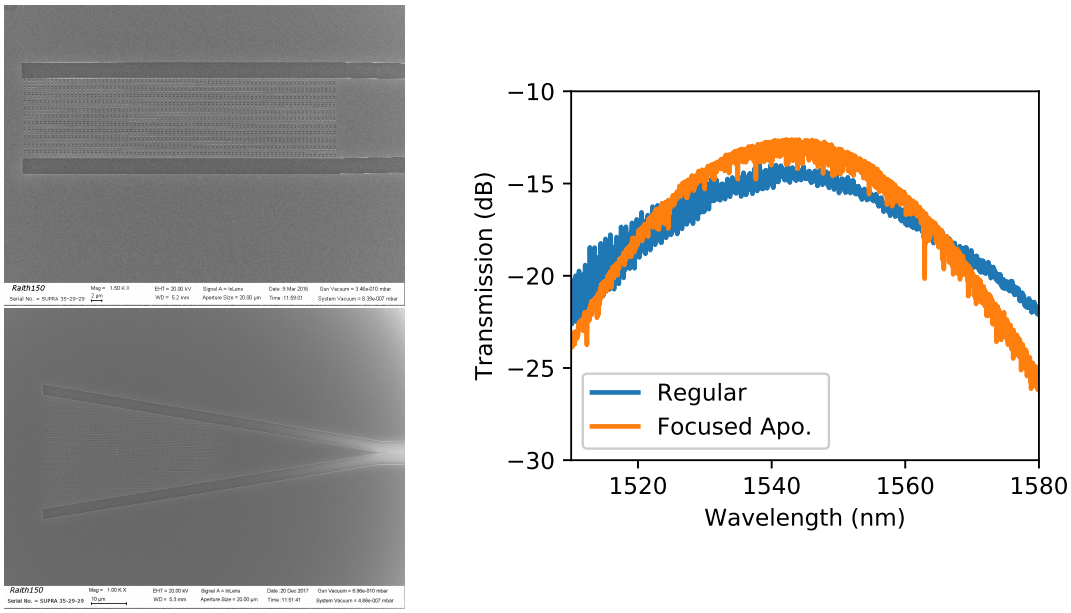

Figure 2.10.: (a) SEM image of the regular grating coupler, (b) focused grating coupler, and (c) transmission spectrum of two GC connected by a straight waveguide.

The advantages of using GC are numerous. They can be placed anywhere on the sample, no cleaving is needed. They have a strong polarization dependency, filtering Transverse-Magnetic (TM) waves. They can be low loss and have do not excite multiple modes. They can have negligible back reflection into waveguide [170]. But they also suffer from a limited 3dB-bandwidth ($\sim$ 30 nm), are sensitive to fabrication, and are intrinsically large, about 500 μm (even if they can be made more compact $< 100\ \mu m$).

We use sub-wavelength GC to reduce the back reflection and thus their Fabry-Perot effect [170]. Gratings are achieved by etching holes in the 220 nm thick silicon layer. As a consequence, the duty cycle and pitch of the rows create an effective material. We could engineer its effective index to have a good grating directionality and good profile mode matching with the single mode fiber. Iterations of simulation and fabrication were done over samples to reduce the coupler losses down to 4.6 dB/coupler, see figure 2.11. A two-stage apodization of the grating was also added improving the coupling to 3.8 dB/coupler. Moreover, to decrease the large size of the taper (500 μm), we used a focused grating [171] which allowed to decrease by 10-fold the taper length down to 50 μm. This saved a lot of space in our samples without affecting their performances. This level of coupling performances was sufficient for the physics experiments that were conducted on the samples.

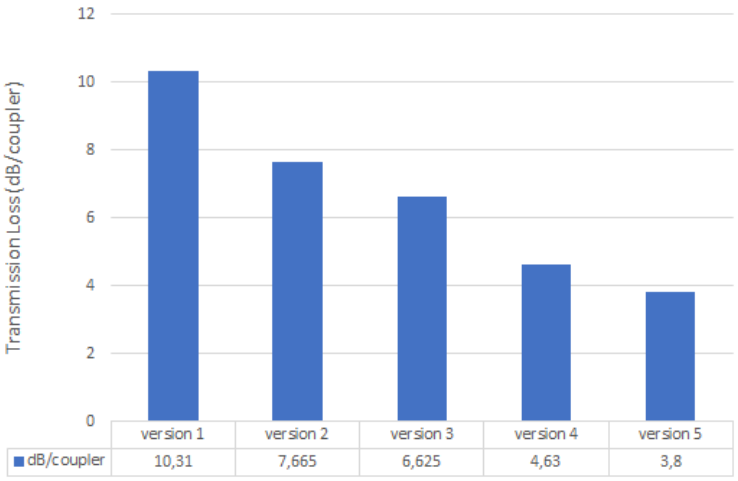

Figure 2.11.: Summary of the grating coupler transmission for different design iterations all along the PhD project.

2.4. Waveguides

Since the height of silicon layer is set by our wafers to 220 nm, we adjust the width of the waveguide to tailor its properties. To simulate the waveguides, we use Lumerical MODE Solutions, a 2D eigenmode solver software [172]. The most important is the bus waveguide, which is the default way for guiding the light between components. It must be single mode at the operational wavelength of 1.55 μm (only the fundamental mode can propagate) and low loss. Moreover, we want these properties for Transverse-Electric (TE) polarization, as its field is along the wafer plane, see figure 2.12. This gives TE a stronger evanescent coupling with other in-plane waveguides, although, it has stronger interaction with the side corrugation of the single fabrication step waveguide.

We use both PMMA and air cladding. PMMA is practical to deposit and is removable, giving flexibility. It provides a symmetric index cladding as its index $n_{\mathrm{PMMA}} = 1.48$ [173] is close to the index of silica $n_{\mathrm{SiO_2}} = 1.44$. It also protects the photonic structures from the environment, dust, and rapid thermal changes. Air is used to create an asymmetric index cladding. This helps to filter TM modes that are coupled to the substrate (see figure 2.12b). Other materials can be used instead for adding protection but air the simplest to implement.

At 1550 nm, the waveguide starts becoming single mode around 550 nm width in PMMA and 650 nm width in air. Increasing the width allows higher order modes to propagate. It also reduces the optical losses as the mode field gets more confined in silicon and does not see as much defects (localized at the edges). We thus need the largest width with single mode property. We choose a 400 nm width which is a good trade-off for the bus, between a reliable single-mode and a large field confinement. The bending losses in silicon waveguide are small thanks to the index contrast, even for bends down to 10 μm radius [163]. The minimum bend radius we have used in all samples is

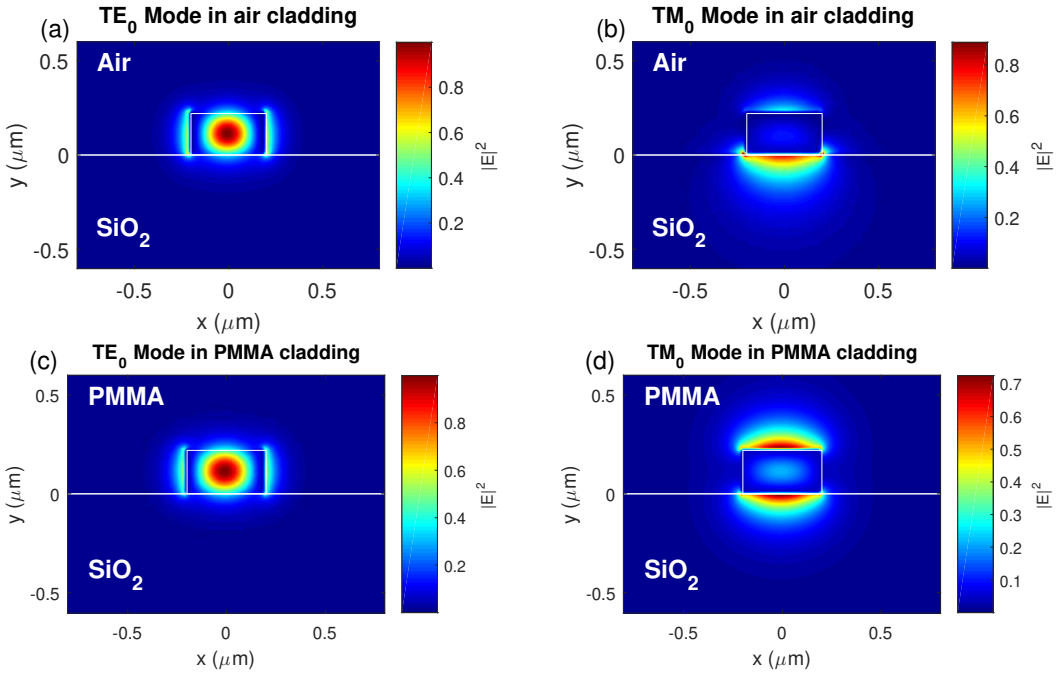

Figure 2.12.: Mode profiles of the electric field intensity $|E|^2$ for the fundamental modes (a) TE and (b) TM with air cladding and (c) TE and (d) TM with a PMMA cladding at 1550 nm. Waveguide width is 400 nm with a height of 220 nm.

25 μm, which let to negligible bending losses (see figure 2.13a).

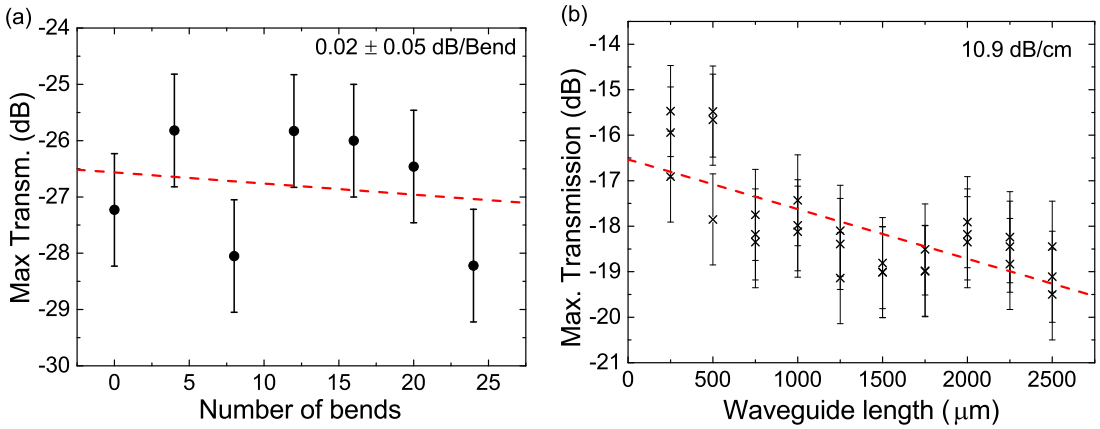

Figure 2.13.: (a) Plot of bending losses for 25 microns radius turns and (b) plot of the linear losses as a function of the waveguide length.

Meanwhile, the propagation losses are high compared to other platforms like Silicon Nitride or Silica (<1dB/cm) [174]. These losses are mainly due to the roughness of the sidewall created by the lithography. In our case, they average to around 11 dB/cm, see

figure 2.13b, but vary between chips due to variations in the fabrication process.

To measure the bending losses, we keep the length of the waveguide fixed and increase the number of bends. For the propagation losses, we simply increase the length of the waveguide. In both cases the effect of grating coupler can be removed by linear fitting of the data, see figure 2.13. The slops indicates the losses per bend and the propagation losses, respectively.

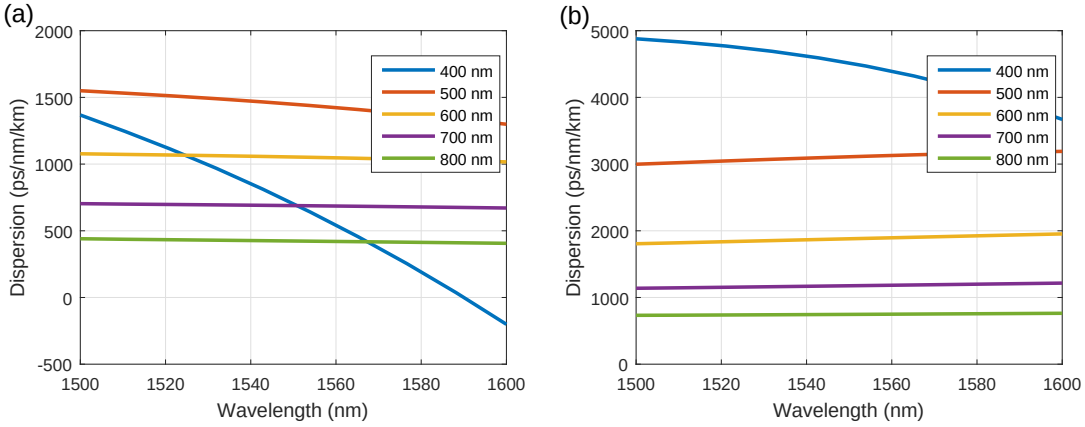

Figure 2.14.: Plots of the waveguide mode chromatic dispersion of the fundamental mode (TE0) as a function of wavelength for different waveguide widths, (a) with PMMA cladding, (b) with air cladding.

The SFWM process needs valid phase matching condition to happen. We must engineer the effective chormatic dispersion experienced by the guided mode. As mentioned in section 1.1.5, we need to tailor the mode dispersion to be anomalous. The single-mode bus waveguide is not efficient for the nonlinear generation of the photons. It has a partial normal dispersion[1] with PMMA cladding (see figure 2.14a) and is too anomalous regime[2] with air cladding (see figure 2.14b). We need another waveguide that can be used specifically for efficient SFWM. Changing waveguide width reveals smaller anomalous dispersions for larger waveguides over the S and C band, see figure 2.14. But a too large waveguide can support more modes and 90°-bends can then excite them, generating undesired effects.

As a first approximation, we can only consider the wavevector mismatch from the waveguide and the self modulation of the pump. In this case, we have to satisfy,

$$\frac{\partial^2 \beta}{\partial \omega^2} \Delta\omega^2 + 2\gamma P = 0 \tag{2.4}$$

where $\Delta\omega^2$ is the bandwidth of the SFWM process, γ the effective waveguide nonlinear susceptibility, and P the peak pump power. Reformulating this equation, we can write that the dispersion D_λ is equal to

[1] normal dispersion regime in our modeling is for negative values if D
[2] anormal dispersion regime is at positive values if D

$$D_\lambda = \frac{\gamma P}{\pi c}\frac{\lambda^2}{\Delta\lambda^2} \tag{2.5}$$

The value of $\gamma \simeq k_0 n_2/A_{eff} \simeq 400\ \mathrm{W^{-1}m^{-1}}$ is typical in a silicon waveguide, where k_0 is the wavevector, n_2 the nonlinear index, and A_{eff} the effective nonlinear interaction area [175]. We take a laser power of 1 mW, since we are using a cavity the power inside can be approximated by the power injected times the finesse of the cavity $\mathcal{F}$ = FSR/FWHM. If we consider a finesse $\mathcal{F} = 30$ (FSR = 1.5 nm and Full Width at Half Maximum (FWHM) = 50 pm) with a bandwidth of 10 nm corresponding to 14 ITU channels, we get a $D_\lambda \simeq 3.05 \times 10^{-4}\ \mathrm{s\,m^{-2}} = 305\ \mathrm{ps/nm/km}$ at 1550 nm. This value would require a very multimode waveguide which not suitable for ring resonator cavities. A compromise must be made between possible multimode excitation in the cavity (due to defects and the waveguide bending) and the dispersion condition.

A width of 600 nm is chosen for the nonlinear waveguides. This allows to have a small anomalous dispersion for both air and PMMA cladding while limiting the multimode behavior. This type of waveguide will thus be used in the cavity for the generation of photon pairs. As we will see in chapter 4, it is enough to have a good SFWM process generation over most of the S and C telecom band.

2.5. Heaters

Heaters are necessary to control the ring resonator cavity, phase shifter, and some demultiplexing stages, seen in section 2.1 (figure 2.1). To do so, one needs to change the effective index of the modes. We exploit the high thermal thermo-optic coefficient of silicon ($dn/dT = 1.8 \times 10^{-4} K^{-1}$). Heaters are therefore deposited as mentioned in section 2.2.1. They are composed of 100 μm $\times$ 100 μm contact pads made of a thick metal layer (500 nm) that extends to the heating element. A thin line with 500 nm width is used as a heater. It can follow the waveguide and is precisely placed with $\pm$ 200 nm position accuracy. The resistance difference between the two layers, confines the heat in the heating element.

By changing the length of the heating line, we can extract its resistances, see figure 2.15. The contacts resistance is about 39.5 Ω and the linear resistance of the line is 0.458 $\Omega/\mu m$. However, the maximum supported power density or breaking power varies largely between devices $\mathrm{W_{max}} = 1.21 \pm 0.88\ \mathrm{mW}/\mu\mathrm{m}$. This can be explained by defects in the metal lines. They can heat up much faster, lowering the maximum power supported by the heater.

The maximum temperature supported by the heater is close to 150°C. However, it is very difficult to know how much the waveguide is heated. The closer the heater is to the waveguide, the more efficient it is. To know the closest possible distance, simulations were made with Lumerical MODE solution [172], see figure 2.16. Losses start to appear below 800 nm of distance. This is due to the evanescent coupling of the guided optical mode with the metal. A safe distance of 1 micron is thus chosen for the most efficient heater distance.

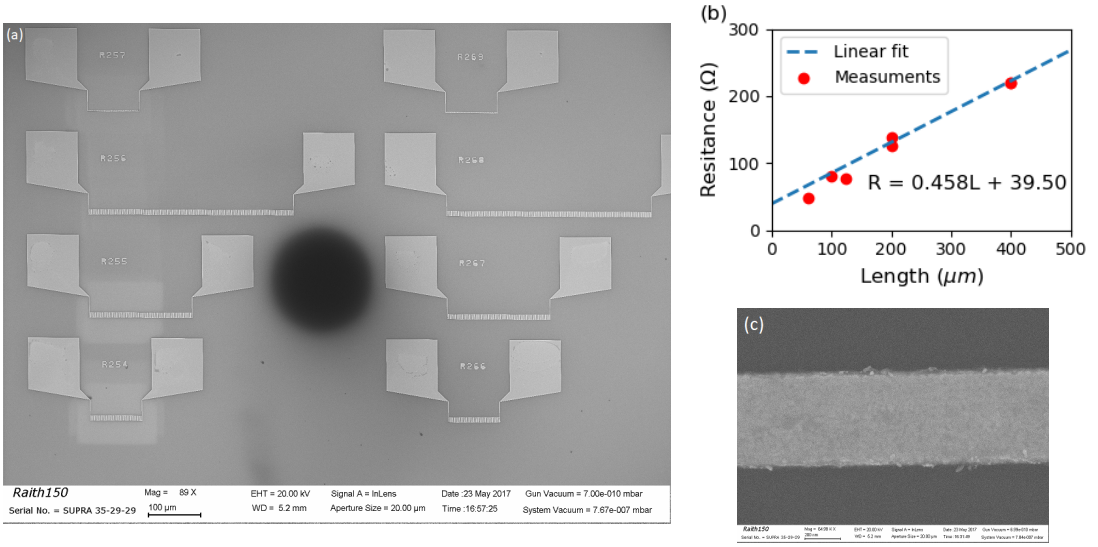

Figure 2.15.: (a) SEM image of various heater lengths. (b) Plot of the heater resistance as a function of length giving pad resistance of 39.5 Ohm and the line linear resistance of 0.458 Ohm per micron. (c) SEM of the Gold heating line.

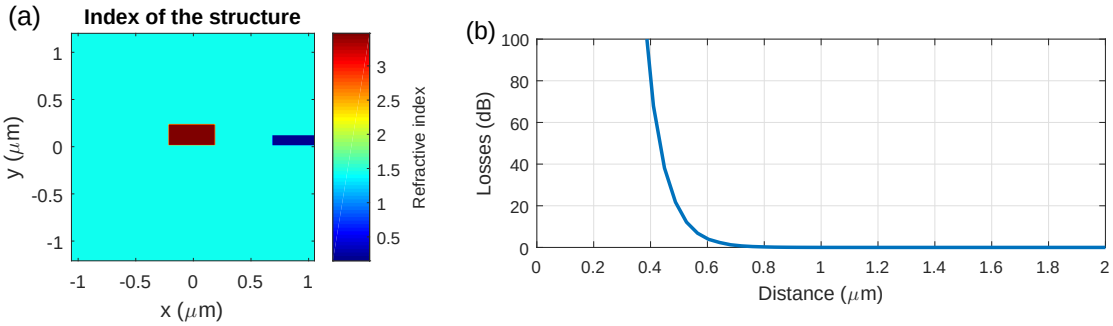

Figure 2.16.: (a) Index of the simulated waveguide with Au heater on its side with PMMA cladding (b) Plot of the simulated mode losses as a function of the heater distance with the waveguide.

The maximum usable frequency is about 1kHz. This moderate frequency is due to the thermal relaxation time of a few milliseconds. The ultimate test is to see if the heater provides a full tunable range. On a ring cavity (or add-drop), it must shift the wavelength by a full micro-ring resonator Free Spectral Range (FSR). Used in a MZI, we need a phase-shifter capable of a phase π-shift.

2.6. All-pass ring resonator

A ring resonator is a type of cavity. It is where the SFWM occurs, creating the photon-pairs mentioned in section 2.1. It is a waveguide folded on itself evanescently coupled

to an input bus waveguide, figure 2.18 [176, 8, 9]. It works as an interferometer where the light after each round trip accumulates a fixed phase $\Delta\phi$. If $\Delta\phi = \beta L = 2\pi m$, with β the propagation constant, and m an integer, light interferes constructively with the incoming signal from the input bus waveguide. The light that did one round trip is in phase with the bus, and similarly for two, three, *etc.* round trips.

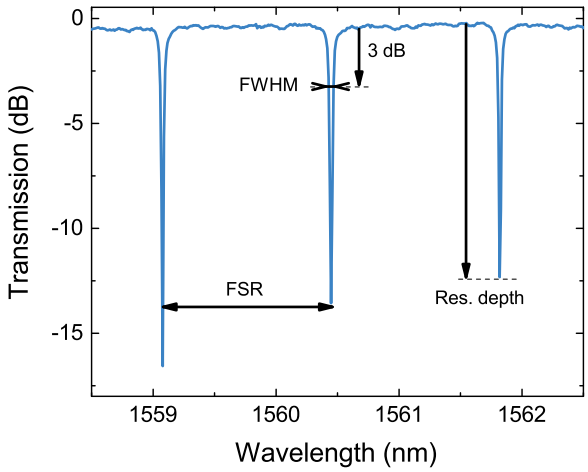

Figure 2.17.: Transmission spectrum of a typical all-pass micro ring resonator. The free spectral range (FSR) is the spectral distance between the resonances, the resonance depth is the minimum level at which the resonance gets, the FWHM is the bandwidth of the resonance at 3 dB of transmission.

The resonance wavelengths are given by:

$$\lambda_{res} = \frac{n_{eff} L}{m} \tag{2.6}$$

with n_{eff} and L are the effective index of the mode, and the cavity length, respectively [163]. For these wavelengths, light is confined in the ring with an increased field, see figure 2.17. The enhanced intensity of the field in the cavity makes it suitable for nonlinear applications, as they depend on a power of the electric field.

Evanescent coupling is used to inject light in the ring. When the field of the mode extends outside the bus waveguide up to the ring, they are coupled. This changes the boundary condition of the field. The waveguides now support super-modes, combinations of the field in the two locally nearly parallel waveguides (for weak coupling). Light from the bus waveguide then excites the two supermodes of this coupling region, they propagate with different phase velocities. This difference creates a beating to the field going from one waveguide to the other with a spatial period of

$$L_\pi = \frac{\lambda}{2\Delta n} = \frac{\pi}{2\kappa} \tag{2.7}$$

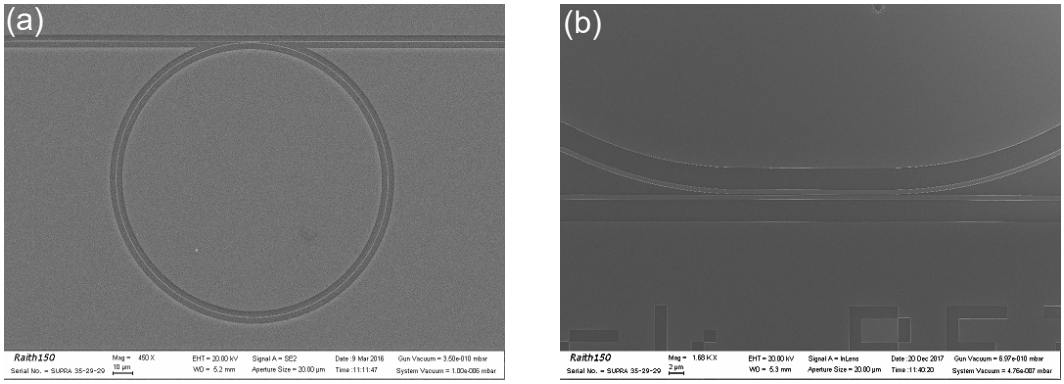

Figure 2.18.: Scanning Election Microscope, (a) circular ring resonator, (b) coupler of a race-track ring resonator.

with Δn the index difference between the two super-modes, and κ the coupling coefficient. So, to couple more or less power in the cavity, one can increase the length of interaction or change the coupling coefficient between the waveguides modes.

The power injected in the cavity can be lower (under-coupled), equal (critical coupling), or higher (over-coupled) than its losses. It is fundamental to over couple the cavity for non linear generation [177, 178]. Over-coupling will reduce the Q-factor of the cavity as well as the generation rate. But the higher the Q-factor, the longueur the photon lifetime in the cavity is. This increases the chance that one photon escape before its twin. This is the jitter of the pairs which, when large, reduces the time-correlation of the photon pairs. In the worst case the pairs can be lost if one of the photon is scattered. A small over-coupling gives a good trade-off between these parameters. The quality factor (Q-factor) of a cavity is defined as

$$Q = \frac{\lambda_{res}}{\delta\lambda} \tag{2.8}$$

with λ_{res} the considered resonance wavelength and $\delta\lambda$ its FWHM, see figure 2.17. The Q-factor represents the number of oscillations of the field before the circulating energy is depleted to 1/e of the initial energy [176]. The Q-factor decreases with the coupling strength but also with the cavity losses. Our losses are set by our waveguides and the coupler losses. We can only play with the coupling coefficient of the cavity to get in over-coupling regime. A slight over-coupling is achieved when the transmission depth of the resonance is maximum. Similarly, we can define the finesse of the resonances as $\mathcal{F} = \mathrm{FSR}/\delta\lambda$, which is between 16 and 32 for rings with Q-factors of 40k to 80k, respectively.

Finally, the Free Spectral Range (FSR) is the spectral distance between two successive resonances, see figure 2.17. To be compatible with the wavelength of the telecom channels from the International Telecommunication Union (ITU grid), we choose a FSR to be a multiple of 100 GHz. The FSR can be written as

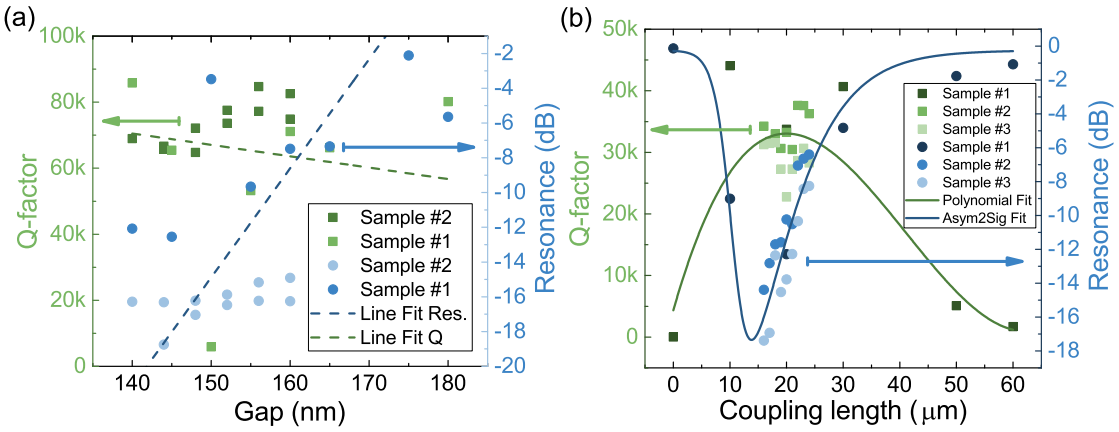

Figure 2.19.: (a) Plot of the Q-factor and resonance depth of circular rings as a function of the gap for two samples, on top are linear fit to show the trend. (b) Plot of the Q-factor and resonance depth of racetrack rings as a function of the gap for three samples, on top are polynomial fits of the Q-factor and an asymmetric two sigma fit of the depth to show the trend.

$$FSR = \frac{\lambda^2}{n_g L} \tag{2.9}$$

with n_g the propagation mode group index. We will choose a cavity length to be compliant with the ITU grid.

Circular rings were mostly used with PMMA cladding (see figure 2.18a). In this case, a few microns of interaction are enough to induce light coupling. The gap between the ring and the bus waveguide is changed accordingly to find the proper coupling strength.

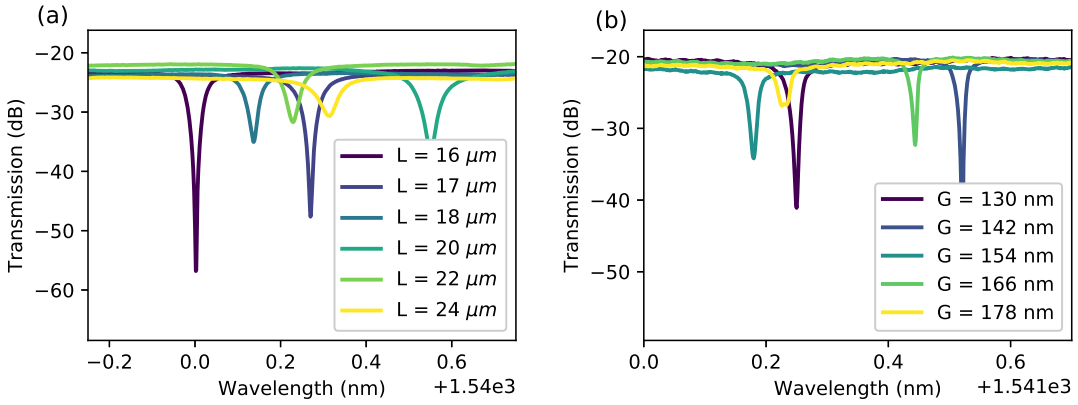

Figure 2.20.: (a) Spectra at a racetrack ring resonance for multiple coupling length (b) Spectra of a ring with a radius of 58.5 microns with multiple gaps.

A few geometries have been tested to evaluate the balance between the ring radius

($P_{ring} \propto R^{-2}$), the Q-factor ($P_{ring} \propto Q^3$), and the FSR ($P_{ring} \propto R^{-2}$), see equation 1.44. We need a small radius as it increases the pair generation but as losses increase with curvature, Q-factor decreases. A compromise was found with a radius around 60 μm and a FSR close to 200 GHz. Accordingly, the source rings have been chosen throughout this work with radius values of 58.5 or 59.5 μm, which correspond to FSR of 1.6 and 1.58 nm, respectively. This variation induces a half FSR shift in wavelength, which is practical to roughly align the ring with other components. To find a good bus waveguide/micro-ring coupling, a large and then a small variations of the gap are performed. The critical coupling was found around 140 nm (see figure 2.19a).

Since waveguide loss depends on the sample, it is necessary to have multiple gaps, ±10 nm, to find an over-coupling regime every time. The major problem with rings is the fine tuning of the resonance must be done actively. Any change in the fabrication process or changing the gap can shift them by hundreds of pm (see figure 2.20a).

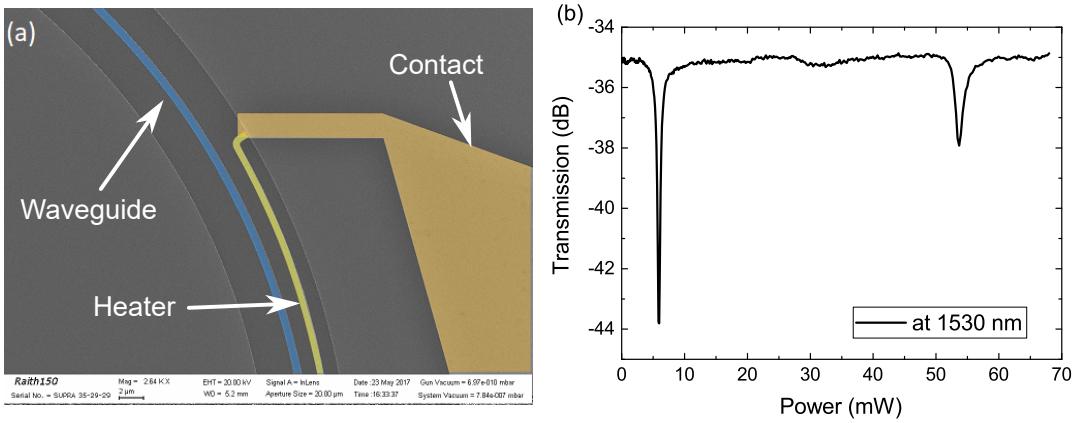

Figure 2.21.: (a) SEM image of the ring heater and the contact pad junction (b) Plot transmission at 1530 nm as a function of the electrical power.

Since evanescent coupling depends on the field leakage into the cladding, it is very dependent on its index. Evanescent coupling is much weaker in air due to the greater index contrast between the waveguide core and cladding material. Different designs of cavities have thus been used for each cladding condition.

A racetrack ring was used for air cladding. Even with the minimum reproducible gap of 50 nm (minimum feature size enable by our fabrication process flow), no resonances were visible. So we needed to move from a classical ring resonator geometry to an elongated coupling region, *i.e.* a so-called racetrack ring resonator (see figure 2.18b). The maximum transmission was achieved for a length of 103.2 μm (First super-mode effective index $n_1 \simeq 2.528$, second super-mode effective index $n_2 \simeq 2.520$, $L_\pi \simeq 103.2$ μm at 1550 nm). After fabrication of a range of coupling lengths, over-coupling condition was found around 16 μm for a gap of 150 nm, see figure 2.19b. As for circular ring, the coupling coefficient must be adjusted. So a variation of ±4 μm, was made in every cavity to find appropriate coupling regime in every condition (see figure 2.20b).

A heater was added next to the ring, as explained in section 2.2.1, at a distance of 1 micron (see figure 2.21a). It followed the ring on two thirds of this circumference. The large resistance and the large interacting length of the heater allowed to move resonances over more than a FSR. In figure 2.21, we can see the transmission of the cavity at 1530 nm as function of the electrical power. We can see two dips in the transmission corresponding to a resonance passing over the pumped wavelength. We can thus move the ring over more than a FSR, allowing the ring to be aligned with any pump wavelength.

2.7. Wavelength demultiplexing

On chip demultiplexing enables splitting of wavelengths into different waveguides. Multiple wavelengths can be multiplexed together or each one must be demultiplexed. It can be done via a cavity like a ring resonator with a second coupled waveguide or a Mach-Zehnder interferometer. These are active solutions as they require a heater and a controller. Other strategies do not need heaters, so less fabrication steps, such as Bragg gratings.

These components are used to separate produced photons pairs in the circuit. Groups or each resonances of the ring resonator are selected by the demultiplexing component. In section 2.1, it is the demultiplexing stage which is fundamental for heralding or sending the resources to different users.

2.7.1. Add drop ring resonator

By adding a second coupled waveguide to the ring cavity, it becomes an Add-Drop Ring (ADR). At the resonant wavelengths, light can be coupled back into the second (drop) waveguide, see figure 2.22. It can also be used to combine wavelengths using the add port. Since we want to demultiplex pairs from the resonance of the source ring, we need the FSR to be different from it, to avoid crosstalk. A radius of 28 microns is chosen to have an $\mathrm{FSR}_{\mathrm{add-drop}} \sim 2.1 \times \mathrm{FSR}_{\mathrm{ring}}$. Moreover, to avoid crosstalk between the idler and signal, their ADR have a radius difference of 2.5 μm (*i.e.* R = 30 μm, $\mathrm{FSR}_{\mathrm{add-drop}} \sim 1.9 \times \mathrm{FSR}_{\mathrm{Ring}}$).

To get the maximum extinction ratio, we must change the gap of the ring. A minimum of crosstalk was found to around -20 dB for gaps of 200 nm on both waveguides. However, as for the source ring, the exact position of the resonances is random. Heaters must be implemented to control and spectrally align them with the generating cavity. A high Q-factor is not important here. If it is too high, it may even make it impossible to align the spectra. The typical Q-factor for the add-drop was thus set between 1000 and 2000.

A line heater was deposited next to the ring, as explained in section 2.2.1, at 1 μm from the waveguide. Unfortunately, the heated length of waveguide was too short and did not provide an index change sufficient to have a full FSR shift (see figure 2.23b). It was possible to shift by 800 pm before the heater burnt, which was less than the 3 nm needed. Another demultiplexing strategy was thus used.

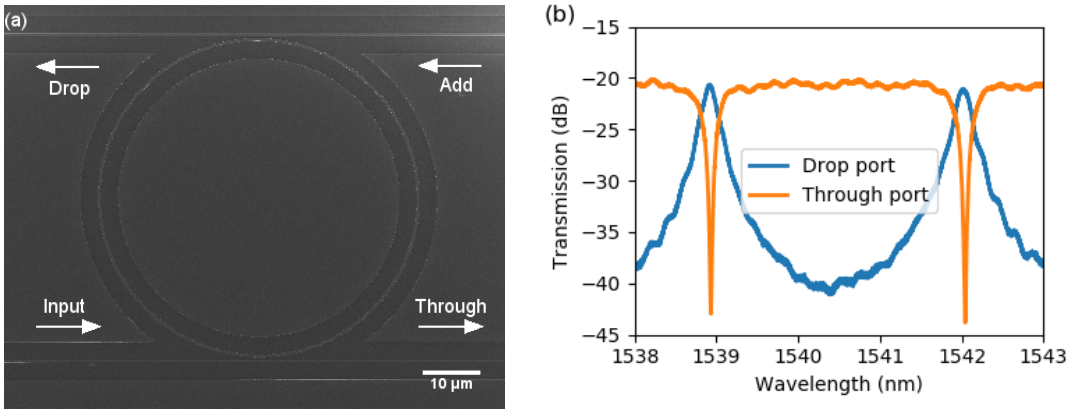

Figure 2.22.: (a) Scanning electron microscope image showing an add-drop ring with the port labeled. (b) Spectrum of the through and drop ports of the structure with a 150 nm gap.

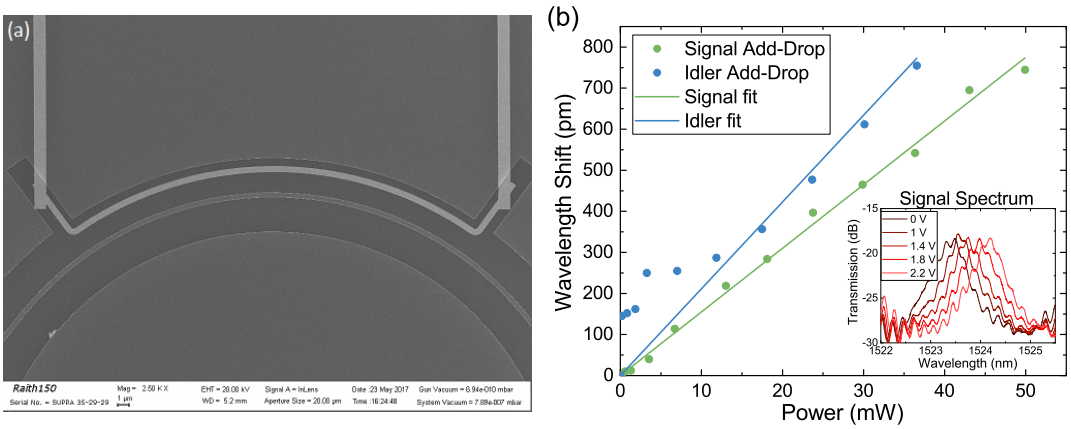

Figure 2.23.: (a) Scanning electron microscope image of the add-drop heater, (b) plot of the wavelength shift as a function of the electrical power.

2.7.2. Modal add drop coupler

A Modal Add-Drop (MAD) device is composed a modal directional coupler [179] and multi-mode Bragg grating. The coupler creates a phase matching between different modes (*e.g.* TE0 and TE1). It is tolerant to fabrication thanks to adiabatic tapering [180]. When combined with a multi-mode Bragg grating, since the back reflected light is in a different mode (see chapter 3), it creates a MAD over the bandwidth of the filter [181]. We have only used the drop configuration of a MAD, *i.e.* only one modal coupler.

The coupler is made of two waveguides, a multi-mode and a single-mode one, see figure 2.24. The phase matching condition is achieved between TE1 in wg1 and TE0 in wg2 during the tapering of the waveguides (see figure 2.25). The two waveguides are separated by a fixed distance of 160 nm. Wg1 starts with a width of 610 nm and ends

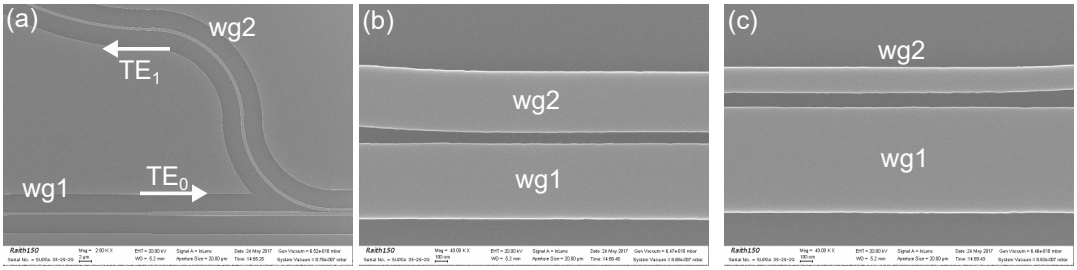

Figure 2.24.: (a) Scanning electron microscope image of a modal add drop, (b) the beginning and (c) the end of the coupler.

with 860 nm, whereas wg2 starts with 490 nm and ends with 240 nm.

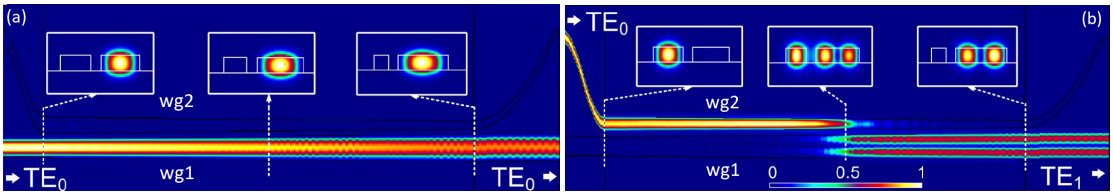

Figure 2.25.: Mode simulation of the transmission of the coupler, (a) in transmission and (b) in the drop port after mode conversion. Reproduced from Ref. [180].

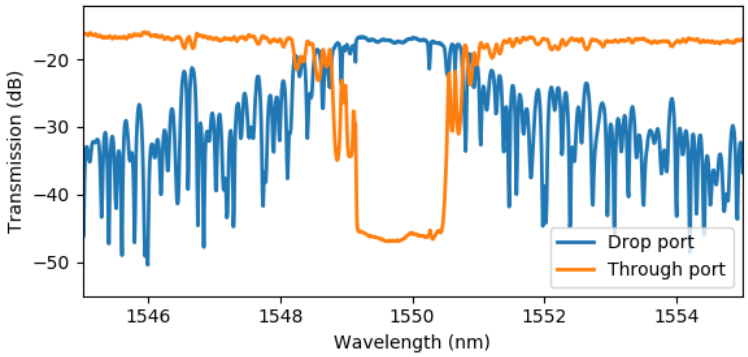

Figure 2.26.: Spectra of the through port and the drop port of a modal add-drop.

There are a few advantages to use MAD: tolerant to fabrication, no active tuning necessary, works for both cladding types, and has a large bandwidth. The lack of active tuning is thanks to the filter self-aligning in wavelength on the same sample, if the geometries are similar enough[3]. Moreover, as they can have large bandwidths, it relaxes

[3]If the fabrication process affect them in a similar way, they have the same wavelength shift. This can happen when the geometries are close, with the same density of edges, the same proximity effects, *etc.*

the requirements on the wavelength alignment (as long as we are in inside the bandwidth). They are simple to cascade for the same reasons. But they suffer from a poor crosstalk of -10 dB/-15 dB, at least in our case (see figure 2.26). MAD have been used for photon demultiplexing, but also to information on the alignment of the ring cavity with the pump rejection filter. This is necessary when working with deep filters as there is no way of knowing the exact position inside of it, see chapter 3.

2.8. Mach-Zehnder Interferometers

A Mach-Zehnder Interferometer (MZI) is composed of two Beam Splitter (BS) connected together. It is a very simple structure, of which the most important components are the BS. We use Multi-Mode Interferometers (MMI) to split the power between two waveguides (see figure 2.27). It works by allowing the input modes to propagate into a multi-mode waveguide. The multiple exited modes interfere creating a field interference pattern that changes with distance. Stopping the propagation when a two-lobe-field profile appears allows to split the power into two single-mode waveguides. These structures are large band and tolerant to fabrication [182, 183].

To change the phase of the interferometer, a phase shifter is added. This is a waveguide with a heater on its side. It can tune in which output the light goes out of the MZI. When it is balanced, a MZI acts as a variable BS.

We use the MZI as a Tunable Beam Splitter (TBS). Depending on the phase shift applied, the powers at the two outputs can be changed. This is to create number states on-chip when single photons are injected, as explained in section 2.1.

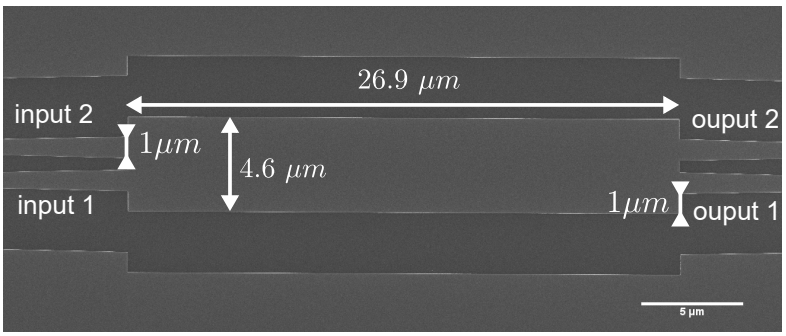

Figure 2.27.: Scanning electron microscope images of the multi-mode interferometer (MMI) with dimensions.

To test its properties, we use an unbalanced MZI, making easier to see changes in the phase. Two types of heaters are used: a regular one with just a metal line next to the waveguide and a heater with a sub-wavelength heat-guiding structure. In both cases, only one arm of the interferometer was equipped with the heater. The sub-wavelength pillars are made of silicon which has a better heat conduction than PMMA or silica. This makes the heat flux increase towards the waveguide. The pillars have a width of 100 nm and are spaced by 100 nm. This pitch is much smaller than the wavelength

allowing to operate in the sub-wavelength regime. This is when the light is sensitive to an effective material and is not scattered.

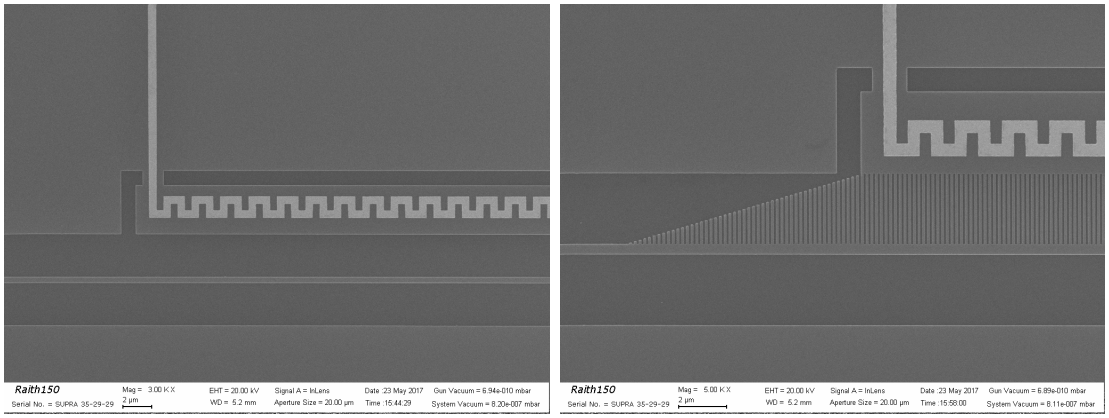

Figure 2.28.: Scanning electron microscope image of a heaters of MZI, (left) regular heater, (right) heater with sub-wavelength heat-guiding structure.

The splitting ratio of the MMI is shown by the good measurement spectral extinction ratio >25 dB, see (figure 2.30a). This means that the power imbalance of the MMI is <1 %. Oscillations visible in the spectrum are due to the 40 μm imbalance in the MZI arms. All the heaters follow the waveguide for 400 μm at various distances. They are made of the same heating line described previously in section 2.2.1. They make a wiggle as shown in figure 2.28 of 1.5 μm width. This is to increase the local resistance and thus the joule effect produced. As previously, the contacts are made of pads 100 μm × 100 μm reaching the ends of the heater.

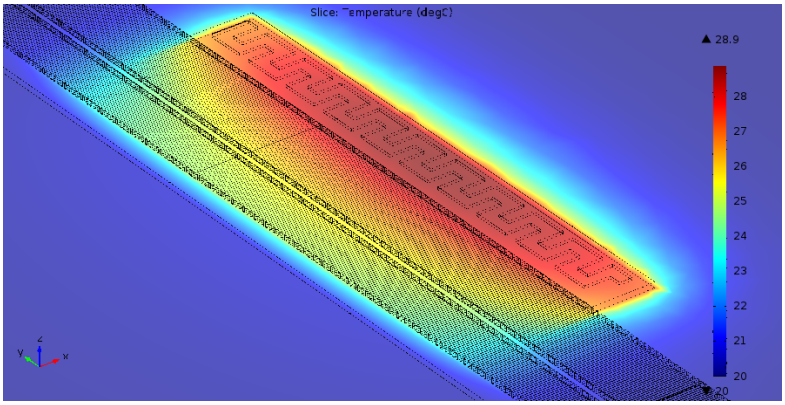

Figure 2.29.: Simulation of the heat flow in the sub-wavelength pillar structure with the COMSOL software [184].

In figure 2.30b, we can see how much the MZI shifts as a function of considered electrical power. The shift fraction is simply the wavelength shift normalized by the FSR of the MZI. As one can see, the closer the heater the more efficient it is, but

the pillars are the most effective by far. Heaters at 3.5 and 4 μm from the waveguide and comprising pillars perform better than the closest regular one. They also have the advantage of being more tolerant to misalignments during the fabrication processes. The clear winner is the 1.5 μm with pillars as it has both the close distance and the pillar enhancement effect. It has twice the shift fraction of the others.

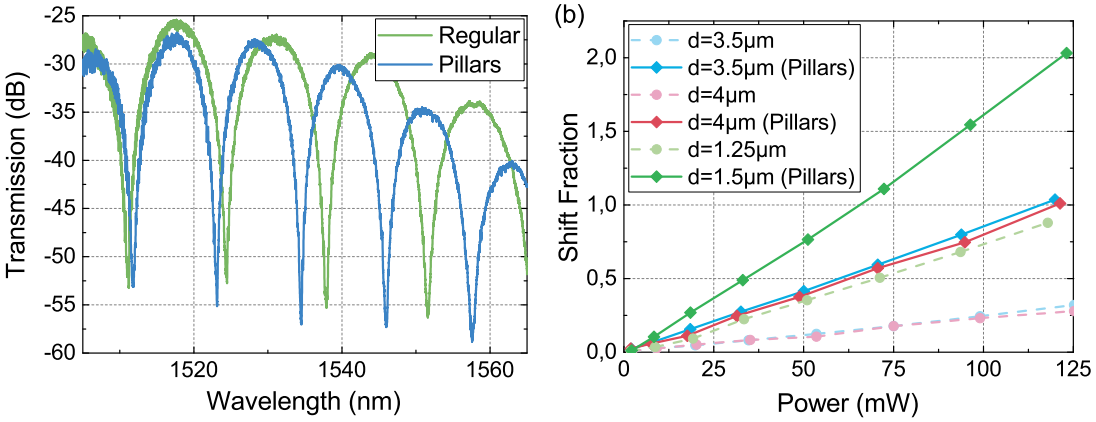

Figure 2.30.: (a) Spectrum of the MZI with and without sub-wavelength pillars, (b) Heater performances shown with the wavelength shift normalized by the FSR as a function of the input electrical power.

In figure 2.29, we can see why it is more efficient. Simulating the structure with the COMSOL Multiphysics software [184], we can see a clear asymmetry in the heat flow. This increases the temperature in the waveguide as the heat transfer is now greater in its direction.

Since most of the design can reach a shift of at least one FSR, any could be used on a future MZI. The maximum frequency of use is, like other heaters, close to 1 kHz, due to the slow thermal relaxation of the structure. MZI will be implemented into a final design of the chip as a variable BS, which should allow to generate special quantum states called NOON states (figure 2.1).

2.9. Summary of the performances

We can summarize the performances of all the components we have developed so far, see table 2.1. We can interconnect all components with the bus waveguides, control them with heaters, and injection/extraction of the light. The design generates the SFWM in ring resonators to create photons. They can be manipulated or de-multiplexed with the MZI or the add-drops resonators.

We are able to inject and extract light from the samples thanks to the grating couplers. They allow to place the circuits anywhere on the chip while suppressing the TM mode injection.

We now have a cavity to generate the photon-pairs via SFWM. It has anomalous

Structure	Properties	Values
Waveguide	Linear losses (dB/cm)	∼10.9
	Bend losses (dB/25μm-bend)	∼0.02
Heater	Linear resistance (Ohm/μm)	0.458
Contact	Resistance (Ohm)	39.5
Ring resonator	Q-factor	10 000 − 80 000
	Resonance depth (dB)	6 − 19
	FSR (nm)	1.58 − 1.6
Add-drop ring	Crosstalk (dB)	20
	FSR (nm)	3 − 4.41
Modal add-drop	Crosstalk (dB)	15
Grating coupler	Transmission (dB/coupler)	3.8
	5dB-bandwidth (nm)	50
MZI	Crosstalk (dB)	25
	Splitting ratio (%)	49/51

Table 2.1.: Summary of the typical performances obtained for the components introduced in this chapter. All components have negligible insertion losses which are smaller than our alignment precision (< 0.5 dB).

dispersion providing acceptable phase matching condition of the nonlinear process. With the FSR close to the ITU grid, it is easy to demultiplex the different parts of the photon-pair comb. We can have critical coupling for both the ring and racetrack configurations, working with PMMA and air claddings, respectively. This is the basis of the photon-pair comb source of the section 2.1.

This cavity can be controlled with heaters that are placed next to the waveguide. They allow for a full wavelength alignment control of the cavity, making it easy to spectrally align with the other components. A heater can also be used in the demultiplexing stage on the add drop ring. The demultiplexing, with the ADR and MAD, separates part of the comb photon-pairs to sent them into different outputs. This is important for heralding or network applications. With this, we can make an entangled photon-pairs generator (section 2.1 and chapter 4).

Finally, we have a TBS in the form of a MZI. It can be controlled again thanks to a heating element creating a phase shift in the arm of the MZI. The TBS could be useful in a heralded photon-number state generator (section 2.1).

So we have almost everything we need to create a full quantum circuit on chip. But we still need the pump rejection function. This function is quite challenging due to the quantum requirement imposted on it: very large rejection in a narrow band of a few nanometers (around 100 dB and 2 nm, respectively). We will use Bragg filters to achieve the pump rejection. We will see it in the next chapter.

Chapter 3.

Pump Rejection Bragg Filter

Generating nonlinear light in silicon requires large enough pump power. Even if we are limited by Two-Photon Absorption (TPA) (in the case of silicon around 1.55 μm wavelength), we still need mW of pump laser. On-chip pump rejection is challenging as the typically needed pump rejection levels are larger than 100 dB, as seen in section 1.3 of chapter 1. On top of this, in the Spontaneous Four-Wave Mixing precess, if the rejection bandwidth is large, the photon source brightness of the nonlinear conversion is spoiled [6, 185]. With a ring resonator cavity, we want to avoid it as well. So the rejection bandwidth should be close to the Free Spectral Range (FSR) of the cavity. We want a 100 dB rejection in a few nanometers bandwidth.

A myriad of optical filters has been reported for the silicon photonics technology, including Bragg grating filters [186, 187, 188], cascaded micro-resonators [189, 190] and Mach-Zehnder Interferometer (MZI) [191, 192]. Although theoretical designs can achieve remarkably large rejection levels, most practical implementations are limited to the 30-60 dB range [189, 190, 191, 186, 192, 193, 194, 187, 188].

The main limiting factor to the achievable on-chip optical rejection currently lies in fabrication imperfections. More specifically, the high index contrast of the Silicon-On-Insulator (SOI) platform makes these circuits very sensitive to fabrication errors. As small deviations in waveguide width and height strongly affect the propagation constant of light, resulting in large phase errors [195]. This detrimental effect distorts filter response, thus compromising rejection capability. In the case of cascaded multi-stage filters, relative phase errors may result in destructive interferences or relative wavelength shifts that offset the benefits of cascading. These interference effects have been minimized in optical fibers [196, 197, 198] and Si chips [199] by cascading grating sections with different Bragg resonance wavelengths. Although effective for dispersion compensation or tuning of the filter bandwidth, this strategy does not overcome rejection depth limitations as each grating section reflects in a different wavelength range. On the other hand, multistage filters combining nominally identical ring resonators or MZI sections are strongly affected by fabrication imperfections, as phase errors actually shift the wavelength response of each filter section offsetting the benefits of the cascading. The wavelength of the notch in ring resonators and MZIs is determined by the total phase accumulated along the full optical path. Then, any punctual waveguide error can alter the accumulated phase, shifting the wavelength of the notch.

These drawbacks have been partially alleviated by implementing active phase-tuning in multistage filters [6, 185, 200, 201]. For instance, 60 dB rejection has been shown on

a single chip with cascaded MZI [185], and 100 dB has been demonstrated for a tenth order micro-ring-based filter [200]. Still, this approach complicates device fabrication and operation, as it requires implementation of tuning circuitry and continuous monitoring of the filter response to maintain proper performance.

In this chapter, we use Bragg gratings to reject the optical pump on-chip. We will first recall the principles of Bragg gratings, then the various ways to tailor their properties. Finally, we introduce an original approach based on multimode gratings to cascade them and break the guided waves coherency between successive filter sections [15]. As it will be shown in section 3.5 of this chapter, they have the advantages to be all-passive, are easy to spectrally align with one another, and can provide the necessary performance for on chip pump rejection.

3.1. Introduction to Bragg filters

A Bragg filter is a periodic refractive index change in a multi-layer stack of an optical waveguide. It can be made of stacks of materials or by periodically changing the waveguide geometry (*e.g.* modulating its width).

Let us define a 1D periodic structure of pitch Λ, with N periods. In the most general case, each period has an index profile function $n(x, y, z) = n(x, y, z + \Lambda)$, see figure 3.1, where the x and y coordinates define the waveguide cross section and z is along the Bragg grating perturbation. This function can be simplified into a series of Q constant sections with $n_q(x, y)$. We can then easily study the interaction between these sections.

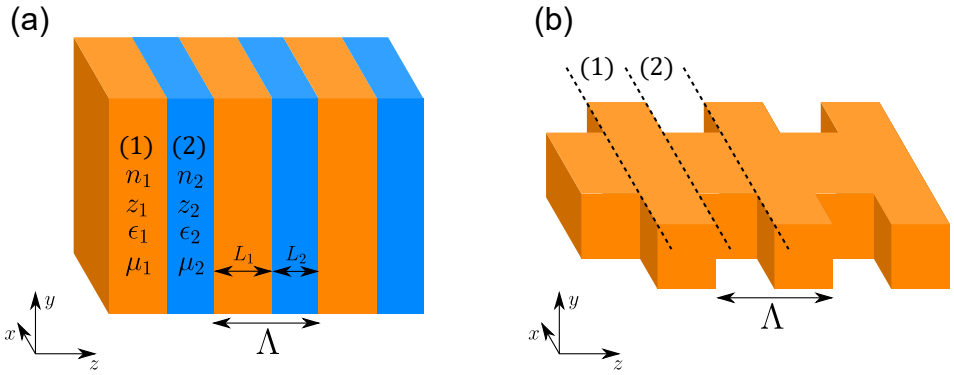

Figure 3.1.: (a) Periodic 1D Bragg stack of materials (1) and (2). (b) Waveguide with width corrugation which acts as a Bragg grating. The z axis is the light propagation axis.

Using the coupled mode theory [202, 203], we can consider the multiple normal modes that are traveling in the waveguide, in both directions. When a perturbation occurs, the transition from the unperturbed waveguide to the perturbed one forces the field to transfer on a new base of normal modes. The field overlap between the two bases allows for the coupling between the two mode bases. If we consider the field as a projection on the basis of modes, we can write it as a vector. Then, coupling between mode can then be written as a matrix M made of the modes coupling coefficients between each period.

The coupling matrix M contains the effect of the thickness of each layer P and the effect of each interface transition D. The propagation matrix P mostly adds a phase shift depending on the layer thickness. The interface matrix D can be found using the overlap of the modes on each side and applying the boundary conditions from Maxwell's equations. For Q sections in the period, we can then write M as,

$$M = D_0^{-1} \left(\prod_{q=1}^{Q-1} D_q P_q D_q^{-} 1 \right) D_Q \tag{3.1}$$

Then the N periods are considered by taking the N-th power of the coupling matrix M. For a set of input modes a_0, the output modes after N periods is then $a_N = M^{-N} a_0$. Due to the periodicity, the Block theorem imposes a periodic field, leading to phase factor $e^{-iK\Lambda}$ being the eigenvalue of the matrix M.

$$a_n = e^{-iK\Lambda} a_{n-1} \Leftrightarrow M a_n = e^{-iK\Lambda} a_n \Leftrightarrow det(M - e^{-iK\Lambda} I) = 0 \tag{3.2}$$

If we consider only two propagating modes, one in each direction, we can simplify it to

$$M = \begin{pmatrix} m_1 & m_2 \\ m_3 & m_4 \end{pmatrix} \Rightarrow e^{-iK\Lambda} = \frac{1}{2}(m_1 + m_4) \pm \sqrt{\left(\frac{1}{2}(m_1 + m_4)\right)^2 - 1} \tag{3.3}$$

Which gives the following dispersion relation,

$$K(\beta, \omega) = \frac{1}{\Lambda} \arccos\left(\frac{1}{2}(m_1 + m_4)\right) \tag{3.4}$$

$|(m_1 + m_4)/2| < 1$ corresponds to a real K, so there is propagation of the Bloch wave. When $|(m_1 + m_4)/2| > 1$, an imaginary part appears in K making the Bloch wave evanescent. This forces a contra-direction coupling due to the periodicity of the perturbation. As it adds a wave-vector mismatch, $K = 2\pi/\Lambda$, in the phase-matching condition, $k_i - k_f + K = 0$, only contra-directional modes can be coupled. Finally, if $|(m_1 + m_4)/2| = 1$, we get the Bragg structure band edge.

To simplify the modeling, we can get the properties of the Bragg filter for weak perturbations $\delta n \ll 1$ model [204]. This gives the following equations that determines the main optical properties, where n_1 and n_2 are the effective index of the first and second propagating modes, respectively.

- The resonant wavelength:

$$\lambda_0 = \Lambda(n_1 + n_2) \tag{3.5}$$

- The coupling strength:

$$\kappa = \frac{2\Delta n}{\lambda_0} \sin(\pi f) \tag{3.6}$$

- The 3 dB-bandwidth of the filter:

$$\Delta\lambda = \frac{\lambda_0^2}{\pi n_g}\sqrt{\kappa^2 + \left(\frac{\pi}{L}\right)^2} \tag{3.7}$$

- Its power reflectivity:

$$R = \tanh^2(\kappa L) \tag{3.8}$$

Here, n_g is the group velocity of the mode unperturbed waveguide, f the periodic corrugation duty cycle, $L = N\Lambda$ the length of the filter, and $\Delta n = |n_1 - n_2|$ the effective index contrast. This works for any two modes traveling in the same waveguide with a large mode overlap. Note that here the coupling coefficient (κ) is mainly governed by the grating geometry.

Interestingly, we get from equation 3.8 the striking result that arbitrarily large rejections can be achieved just by implementing a strong coupling coefficient or a sufficiently long filter, *i.e.* provided that $\kappa, L \gg 1$. Unfortunately, the achievable rejection saturates beyond a certain filter length in practice [186, 187, 188].

As a matter of illustration, we plot in figure 3.2 a typical filter reflectivity and bandwidth in the simple case of a Bragg mirror. We can see various conditions depending on the two-period index contrast, the Bragg mirror length, and its duty cycle, respectively. The bandwidth of the filter decreases with the filter length. It saturates after a certain value that depends on the coupling coefficient. Changing the duty cycle leads to a reduction of the filter bandwidth but also the rejection level. To have the strongest filter, a 50% duty cycle must be used, see figure 3.2c and 3.2d.

Note that for a fixed length (fixed N), the relation between the bandwidth and the rejection of the filter is set. We can only play on the length and the group index to change the bandwidth independently of the rejection. Any Bragg grating with these same parameters has a bandwidth / rejection relation, whatever the way we change the coupling strength.

$$\Delta\lambda = \frac{\lambda_0^2}{\pi n_g N\Lambda}\sqrt{\operatorname{atanh}^2(\sqrt{R}) + \pi^2} \tag{3.9}$$

3.2. 1D photonic crystal / Bragg filter

As quickly illustrated in section 3.1, to create a Bragg filter using SOI waveguides, a first obvious approach is to perturb the width symmetrically. The corrugation can be rectangular, sinusoidal, or of an arbitrary shape [205]. Taking our bus waveguide with a width of $W_{wg} = 400$ nm, we can get an approximate value of the pitch for the resonance to be around 1550 nm. After simulating the effective index of the fundamental mode, we get $\Lambda = 1550/(2\times 2.237) \simeq 346.5$ nm with a polymethylmethacrylate (PMMA) cladding. To compensate for the corrugation, we can repeat the process with a perturbed waveguide with a width of 450 nm. We take our smallest repeatable corrugation (*i.e.* the minimum

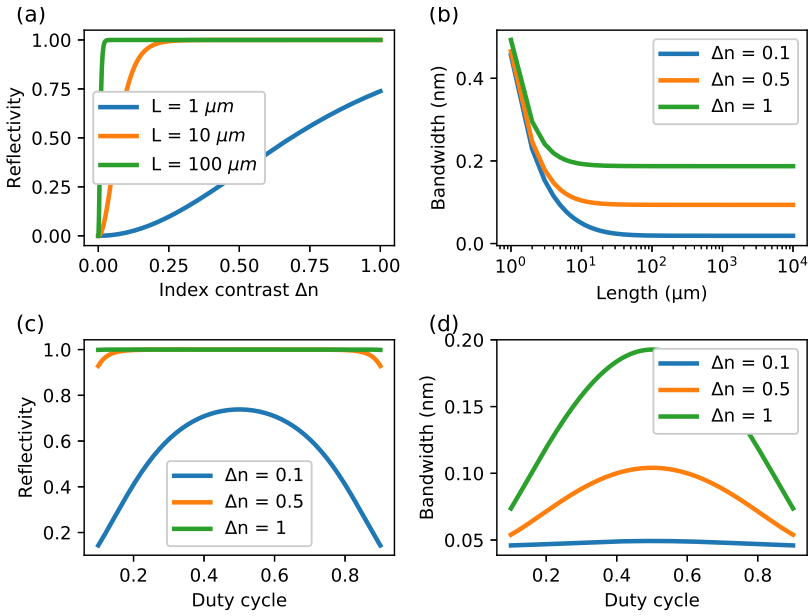

Figure 3.2.: Plots of the Bragg filter behaviors for 1550 nm central wavelength, a group index of 1, 50% duty cycle and a length of 10 microns, (a) bandwidth as a function of the index contrast, (b) bandwidth as a function of the filter length, (c) rejection as a function of the index contrast, (d) rejection as a function of duty cycle.

feature size) of 50 nm as a starting corrugation. We also increase it to 60 and 70 nm. The duty cycle is fixed to 50%.

We computed the effective index difference Δn_{eff} between the modes of the wide and narrow regions to estimated the coupling coefficient (Eq. 3.6). We considered a mode group index n_g of 4.2. The calculated bandwidth is 23 nm for the previous geometrical parameters, and a corrugation width of 50 nm.

We fabricated the devices with lengths ranging between 500 μm to 2 mm, see figure 3.3. A cladding of PMMA was added at the end of the process to protect the devices. As mentioned previously (Section 2.3), we use sub-wavelength grating couplers. They have been optimized to reduce Fabry-Perot ripples in the collected signal for an easier analysis of the transmission spectrum. The couplers were used to inject and extract Transverse-Electric (TE) polarized light with standard single mode (SMF-28) optical fibers [170]. We measured the transmission spectra of the filters using a tunable laser and an associated data acquisition system (Yenista tunics and CT400). We used a polarization rotator to inject TE-polarized light into the gratings. All filter spectra were normalized to the maximum transmission to remove insertion loss from the fiber-chip gratings.

The Scanning Election Microscope (SEM) image of figure 3.3, shows the typical rounding in fabricated devices due to the proximity effects (Section 2.2.1). This mainly results in a blue shift of the resonant wavelength and a slight reduction of the coupling coeffi-

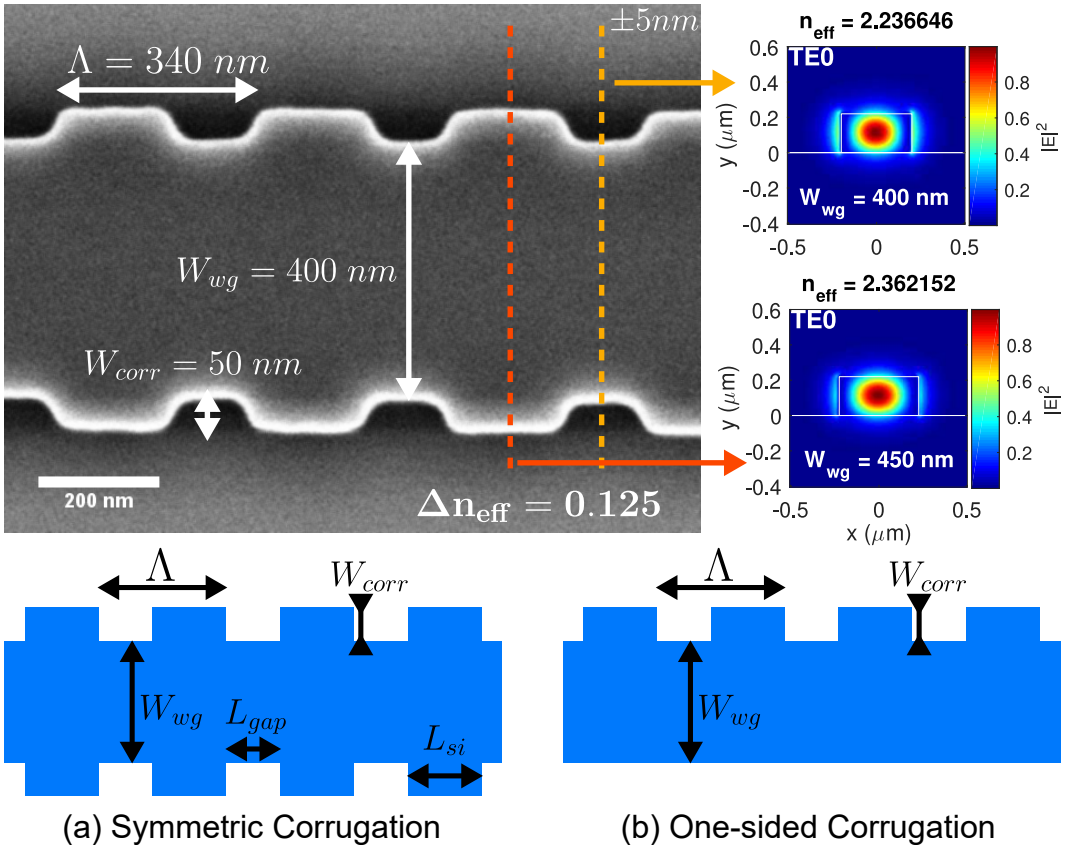

Figure 3.3.: SEM image of a regular Bragg grating implemented with its dimensions. On the right are the simulated modes in each region of the teeth and waveguide. (a) and (b) are the schematic of the geometry for the symmetric and one-sided corrugations, respectively.

cient. But does not alter the operating principle of the Bragg mirrors, nor the desired function of rejection a pump signal.

As visible a large rejection >40 dB with bandwidth larger than 20 nm can be obtained for the three corrugations, see figure 3.4a. This is close to the expected value. Since we do not compensate the average index, the resonance shifts as the corrugation increases. This is good for broadband application but not in our case. The variation of the rejection in the spectrum is caused by the normalization. Since the transmission has a Gaussian shape, we see it imprinted on the fixed noise floor of the detector (around -68 dBm).

To reduce the bandwidth, one can reduce the strength of the grating (see relation 3.7). One way to reduce the filter coupling coefficient, while keeping the same minimum feature size, is to implement a one-sided corrugation. This geometry approximately halves the Δn_{eff}, providing a two-fold reduction in filter bandwidth. This has the added effect of increasing the overlap between the modes.

We fabricated the same filters as before only removing the corrugation on one side of

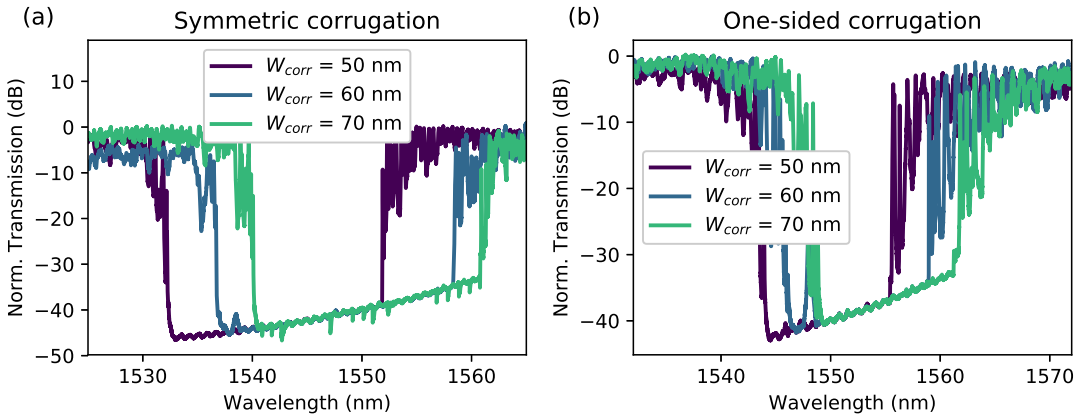

Figure 3.4.: Transmission spectra of the (a) symmetric and (b) one-sided corrugation filters for different corrugation widths, with length of 500 microns and a width of 400 nm.

the waveguide. We indeed got a reduction of the bandwidth and rejection level, as shown in figure 3.4b. The bandwidth was divided by half to 12 nm as expected since the index contrast was too. But the rejection stayed the same, due to the rejection saturation. Because of defects induced in the fabrication process, waves reflected over a given period are then not all in phase with others reflected over the filter. This effectively reduces the length of the grating. The overall behavior then does not follow the bandwidth / rejection relation stated by 3.9 where L is the geometrical Bragg mirror length, meaning that $L_{\text{eff}} < L$ (Fig. 3.7).

3.3. Improved Bragg mirrors based on subwavelength engineering

To partially resolve the previous limitations, an interesting additional degree of freedom consists in the use of sub-wavelength guiding structures. This is when a subwavelength engineering approach is used on the Bragg unit cell [206, 207, 193, 208]. This keeps relaxed the constraints on the minimum feature size while providing corrugation restrained only by the precision of the lithography. Subwavelength waveguides exploit periodic patterns with a periodicity smaller than half of the wavelength to tune index values or dispersion properties. Light then only sees an effective material that can be tailored [209]. In subwavelength engineered Bragg filters, the total period is divided in two subwavelength sub-periods. This mimic the narrow and wide parts of the conventional Bragg geometry. The pattern variation needed to induce this spatially averaged index modulation (*e.g.* the difference between two teeth widths) is limited by the lithography precision. It is usually 10 times smaller than its minimum feature size. This configuration allows weaker index modulations with comparatively large corrugations, relaxing minimum feature size constraints.

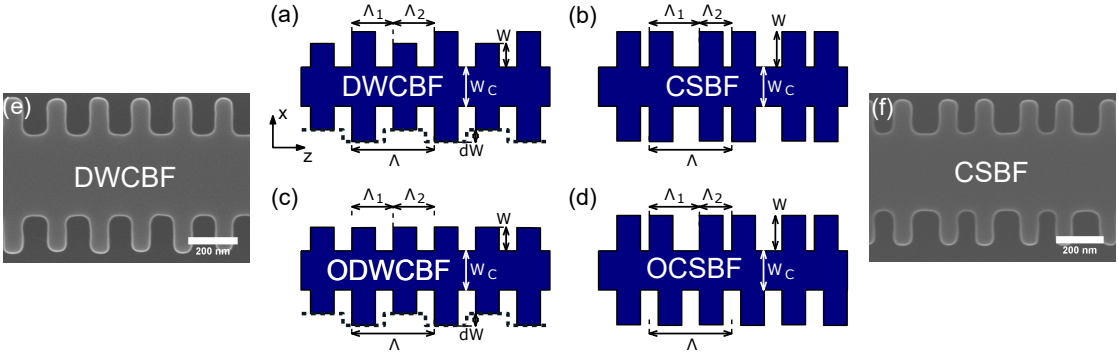

Figure 3.5.: Top-view schematics of the subwavelength Bragg geometries, (a) Double Corrugation Width Bragg Filter (DCWBF), (b) Corrugation-Shifted Bragg Filter (CSBF), (c) One-sided Double Corrugation Width Bragg Filter (ODCWBF), and (d) One-sided Corrugation-Shifted Bragg Filter (OCSBF), finally (e) and (f) are SEM images of DCWBF and CSBF with $dW = dL = 5$ nm, respectively.

We have mainly tested two types of subwavelength geometries, the Double-Width Corrugation Bragg Filters (DWCBF) [187] and the Corrugation-Shifted Bragg Filter (CSBF) [206]. In the DWCBF configuration, the index modulation is realized by the relative width difference between the two subwavelength teeth $dW \neq 0$ (Fig. 3.5(a)). Conversely, in the CSBF approach, both subwavelength teeth have the same width, with the position of one of them longitudinally shifted. This can be seen as a compression of the sub-period $dL = \Lambda_1 - \Lambda_2 \neq 0$ (with $\Lambda = \Lambda_1 + \Lambda_2$) (Fig. 3.5(b)). This way, the index modulation maintains the same amount of Si in both sub-periods. As both teeth may be affected by proximity effects in the same fashion, this geometry that could provide relaxed fabrication tolerances of one-side Bragg filters configurations. The two kinds of Bragg filters has also been included to our study.

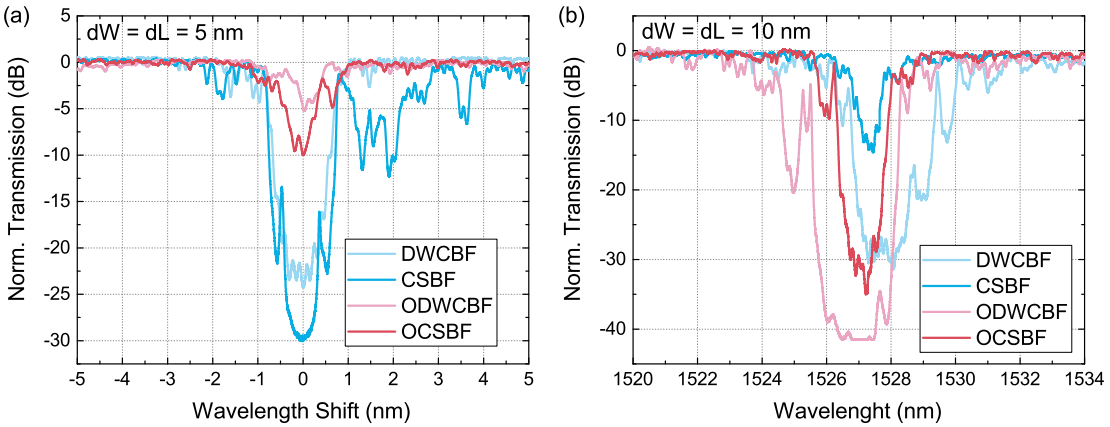

Figure 3.6.: Measured transmission spectra of the different geometries with a pitch of 320 nm, $W_c = 300$ nm, $W = 150$ nm, length of 0.5 mm, (a) $dL = dW = 5$ nm, and (b) $dL = dW = 10$ nm.

To compensate for the larger corrugation, the core waveguide width was changed to $W_c = 300$ nm. This made the pitch $\Lambda = 320$ nm for the subwavelength filters. For the DWCBF, we fixed a duty cycle of 50% in the sub-periods and a corrugation of $W = 150$ nm. We implemented differential waveguide widths of $dW = 5$ nm, 10 nm, and 15 nm. For the CSBF, we set the corrugation to $W = 150$ nm, then scanned the longitudinal shift dL between 5 nm and 15 nm.

As a first approximation to the problem, we the used coupled mode theory to estimate the filter bandwidth from the coupling coefficient and group index. For the DCWBF, we estimated Δn_{eff} by zero-order approximation of the subwavelength index [209]. For the CSBF, we used 2.5D Finite-Difference Time-Domain method (FDTD) simulation (Lumerical Mode Solution) to estimate the bandwidth. In both cases, we calculated a bandwidth of ~ 6 nm. This was for differential waveguide width and longitudinal shift (dW and dL) of 5 nm with a group index of $n_g = 3.5$. This represents a 4-fold bandwidth reduction compared to the conventional approach.

Figure 3.6 compares the measured bandwidths of subwavelength engineered filters in symmetric and one-sided configurations, with differential corrugations (dW and dL) of (a) 5 nm and (b) 10 nm. Both symmetric designs provide a bandwidth reduction more than 5 times greater compared to the conventional design. As previously, the one-sided design yields a substantial bandwidth reduction.

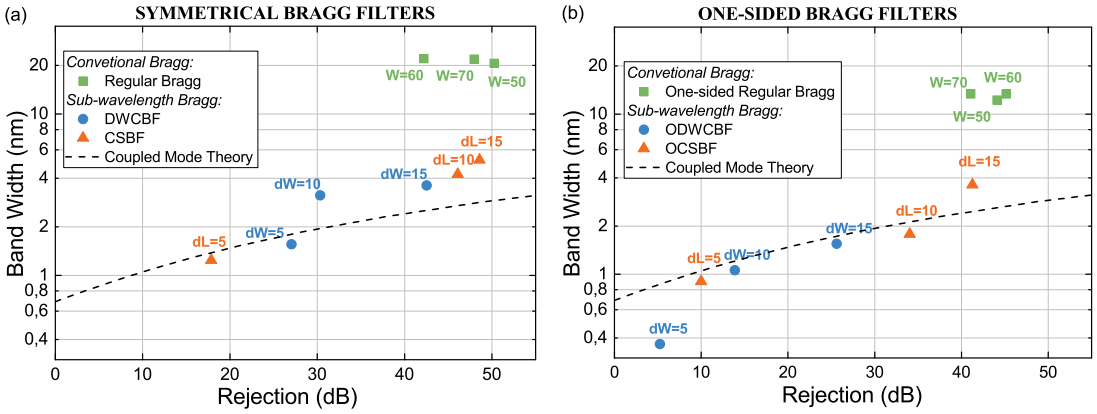

Figure 3.7.: Experimental bandwidth and rejection of different Bragg filters based on (a) symmetric, and (b) one-sided geometries. All the studied Bragg filters have a length of 500 microns. Labels indicate the different geometries, following notations in Fig. 3.5.

A summary of the Bragg grating properties is shown in figure 3.7. It shows all the filter geometries studied in terms of bandwidth and rejection levels. The length of all filters is $L = 500$ μm, ensuring reasonably compact devices and measurable optical resonances. As a guide for analysis, we also plot the theoretical bandwidth-rejection curve from equation 3.9 (dashed line in Fig. 3.7), with a group index of $n_g = 3.5$, which models subwavelength filters.

In all cases, the one-sided filter configuration provides a great bandwidth reduction,

widening the design space for a given minimum feature size. For instance, both the symmetric DWCBF with $dW = 5$ nm and the one-sided ODWCBF with $dW = 15$ nm, experimentally provide an order of magnitude bandwidth reduction, compared with the regular filter geometries. However, the one-sided configuration relies in a three-times wider differential corrugation, relaxing lithography resolution requirements.

This way, the combination of subwavelength engineering and single side corrugation provides a useful design flexibility. It allows for ultra-narrowband response with 400 pm width, or large rejection levels, close to 50 dB. Yet it provides a five-times bandwidth reduction, compared to conventional Bragg filter counterparts. The behavior of subwavelength filters follows the trends predicted by coupled mode theory, with experimental points following the theoretical curves (dashed lines in Fig. 3.7). However, conventional designs presented here are considerably deviated. The reason for this is while theory predicts a rejection exceeding 100 dB or even 200 dB. None of the measurement showed a rejection larger than 50 dB.

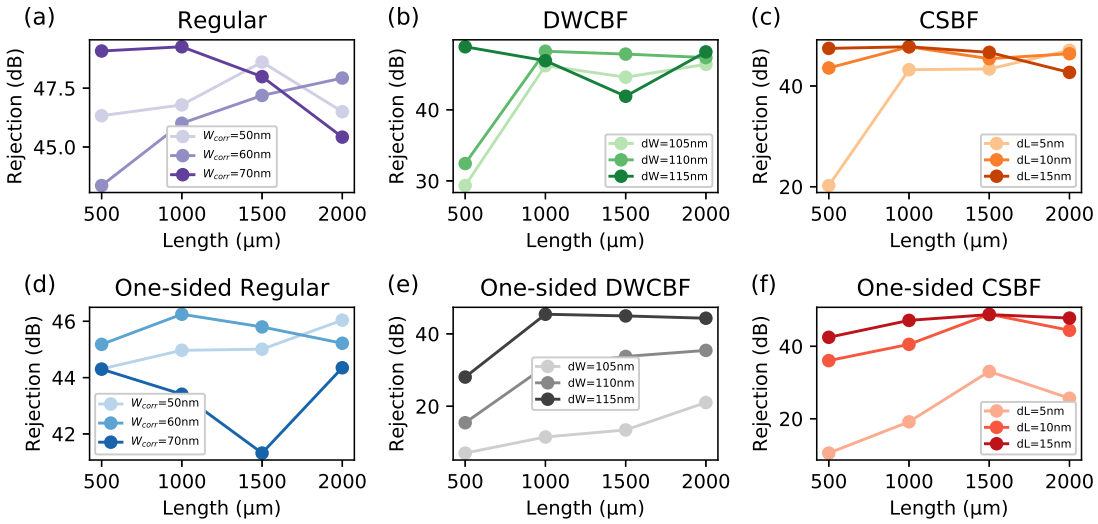

Figure 3.8.: Plot of the rejection as a function of the filter length for all regular and subwavelength geometries. A rejection saturation around 50 dB is visible for all of them. Measurement performed with an OSA (-90 dBm noise floor).

To make sure the photon-detector (Yenista CT400) is not a limitation, manual measurements of the rejection using an Optical Spectrum Analyzer (OSA), Anritsu MS9710B, were performed. The noise floor at -90 dBm was much lower than the CT400 level of -68 dBm. In figure 3.8, we see the rejection as a function of the filter length. All the filters saturate around 50 to 55 dB whatever the geometry is. This is due to the fabrication defects accumulated along the structure as previously mentioned already for the regular Bragg filters. In spite of their intrinsic merits, subwavelength designs are not immune to defects. Their optical power rejection tends to saturate as for the Bragg filter regular designs. There is no solution to the saturation keeping the same strategy. Improving the

fabrication process of samples is an option which can constantly be pursued but which is a long and slow way. Moreover, it is subject to the hazards of clean room maintenance or machine breakdowns. It cannot, ultimately, lead in itself to a substantial improvement in the filter rejection rates.

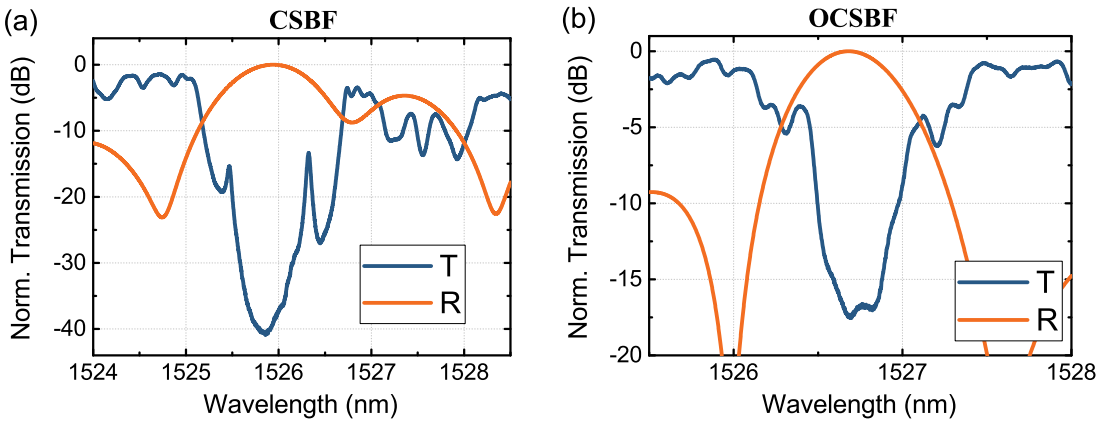

Figure 3.9.: Transmission (T) and reflection (R) CSBF and the OCSBF, both with a shift dL of 5 nm and a length of 1 mm.

We can still see the potential of the shifted subwavelength filters in the symmetric (CSBF) and one-sided configurations (OCSBF) with $dL = 5$ nm and 1 mm length. Figure 3.9 shows the transmission and reflection spectra for the two filters. Back-reflections are collected using a circulator connected to the input fiber. The measured reflection spectra are processed with the minimum phase technique [210] to remove the direct reflection from the input grating couplers. Both filters yield sub-nanometer bandwidth. The symmetric geometry exhibits a null-to-null bandwidth of 0.8 nm with a rejection exceeding 40 dB, while the one-sided design provides a bandwidth of 0.6 nm and a rejection of 15 dB.

Although the bandwidth performances are largely reduced getting closer quantum-usable filter, the rejection is still too small. The maximum rejection of 50 dB is still not enough for quantum applications

3.4. Closure of the gap

In the course of our investigation to try overcoming the rejection / bandwidth trade-off of conventional Bragg filter, we observed a narrowing effect of the filter bandwidth under non-standard conditions. This effect called hereafter Closure of the Band Gap (CBG), or simply closure of the gap [211], is a photonic crystal effect occurring for large corrugations of Bragg filters, *i.e.* meaning large coupling coefficients. Yet the photonic stop band vanishes. This effect happens for specific sets of the filter geometrical parameters, corrugation and duty cycles, see figure 3.10. The CBG allows to create narrow band filters with large corrugations, *i.e.* larger than the minimum feature size.

The only trade-off is that the target filter dimensions must be controlled with high accuracy to meet the CBG conditions. This effect is known for the non-fundamental band gap (see appendix A), but is not well modeled for the first band gap.

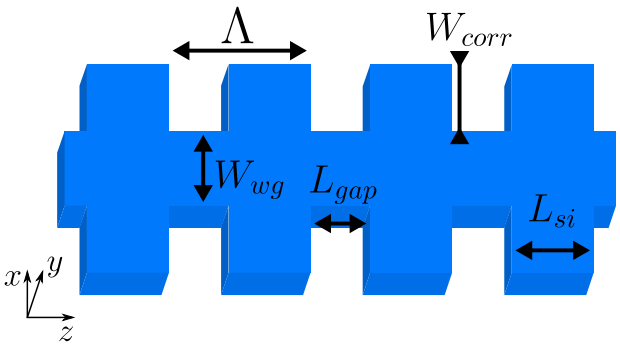

Figure 3.10.: Schematic of the Bragg geometry used for the closure of the bandgap, the light propagates along the z axis.

A Bragg grating is a 1D photonic crystal. As mentioned earlier in section 3.1 of this chapter, it thus supports Bloch modes, periodic with the grating period. The Bloch modes field, as in waveguides, are normal to each others. The first Bloch mode occupies the lowest allowed energy (frequency). Then each subsequent mode increases in energy. They satisfy the propagation equation in the grating, which for each wave-vector β gives a set of frequency solutions, known as the band-structure. However, some frequencies may not have any associated k-vector, so they cannot propagate in the grating, it is the stopband.

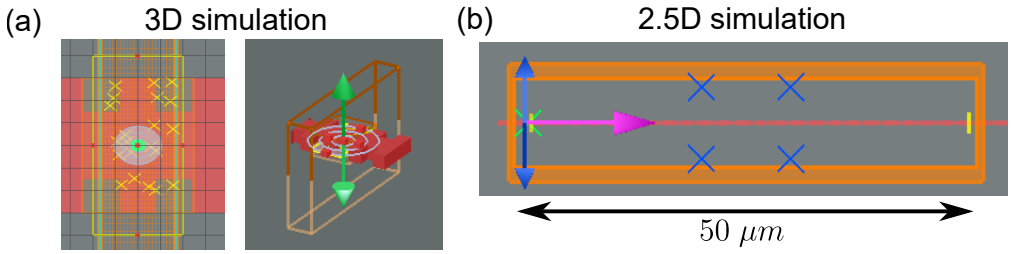

Figure 3.11.: (a) Screen shot of the 3D simulation realized in lumerical FDTD solution over a single period. (b) Screen shot of the 2.5D simulation realized in lumerical MODE solution over 50 microns of filter.

Let us investigate this effect, starting from the previously used Bragg grating geometry. The Bragg filter pitch is $\Lambda = 340$ nm and a waveguide width of $W_{wg} = 400$ nm is considered. We will use at first a duty cycle of 50%. We will then change W_{corr} and see how it affects the transmission

Using Lumerical FDTD solution [172], one can simulate the 3D structure of Bragg gratings and their band structures, see figure 3.11a. A single period is used with periodic constrains along the propagation axis and with perfectly matched layer conditions on

all others. We excite only the TE modes with a vertical magnetic dipole. We sweep the k-space and get the resonant frequencies of the crystal. The band diagram is given by the changes of each resonance frequency as a function of wave-vector k.

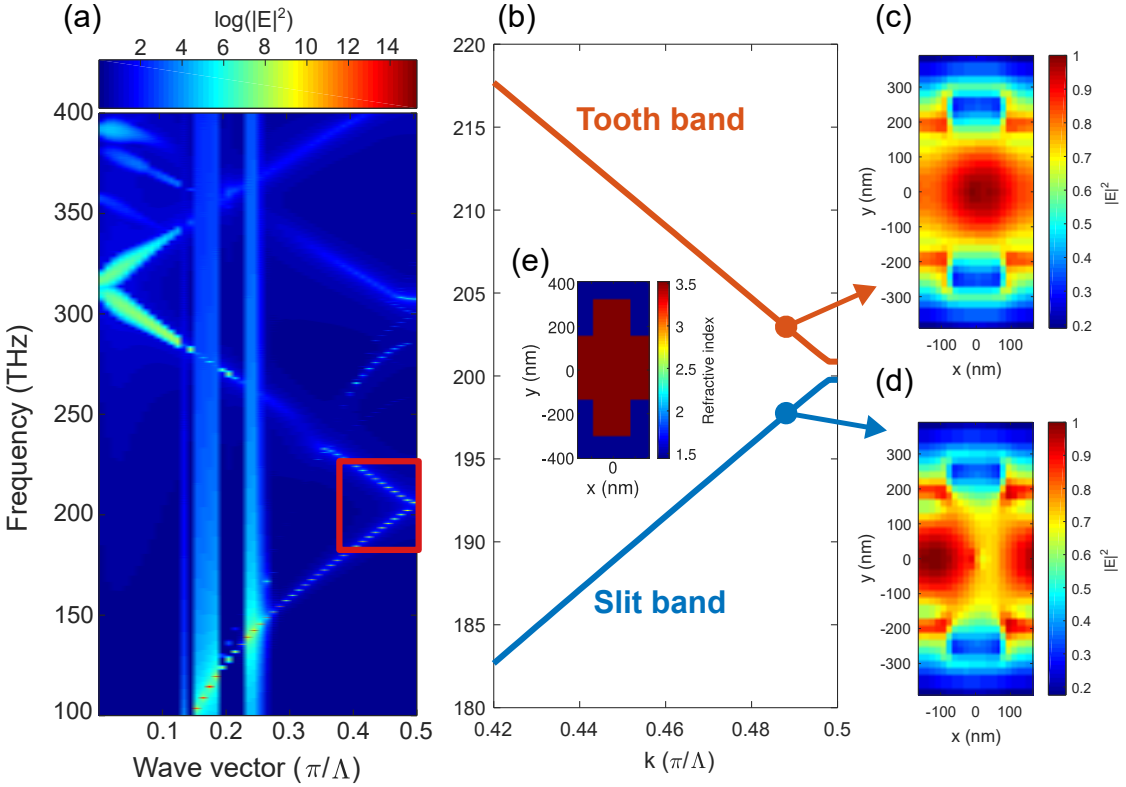

Figure 3.12.: Band structure (TE) of the 1D waveguide grating, with a pitch of 320 nm, a waveguide width of 400 nm and a corrugation of 100 nm. (a) is a spectrum of the resonate frequencies as a function of the wave-vector k. (b) Zoom of the first band gap of (a) with the slit band and the tooth band. (c) and (d) are the Bloch mode field profiles for the tooth and slit bands, respectively. (e) Map of the refractive index simulated in (c) and (d), red corresponding to silicon and the blue to the silica.

As the geometry changes, the frequency of each Bloch mode varies. With the proper conditions, the eigen-frequency can cross, making the two first Bloch modes swap. Precisely, at the crossing point, the forbidden photonic gap disappears, no reflection then occurs. There, two normal modes become degenerate and get the same propagation constant, rendering their effective index contrast null. This effect can be investigated by scanning the geometrical dimension, corrugation, duty cycle, pitch, and average waveguide width.

We can write a simple condition for the CBG with a geometrical parameter X for the edge frequency $f_n(\beta = \pi/2a, X) = f_n(X)$ of band n, with a bandwidth equal to $\Delta f_n(X) = f_{n+1}(X) - f_n(X)$. We can define the variation D_n of the band gap between

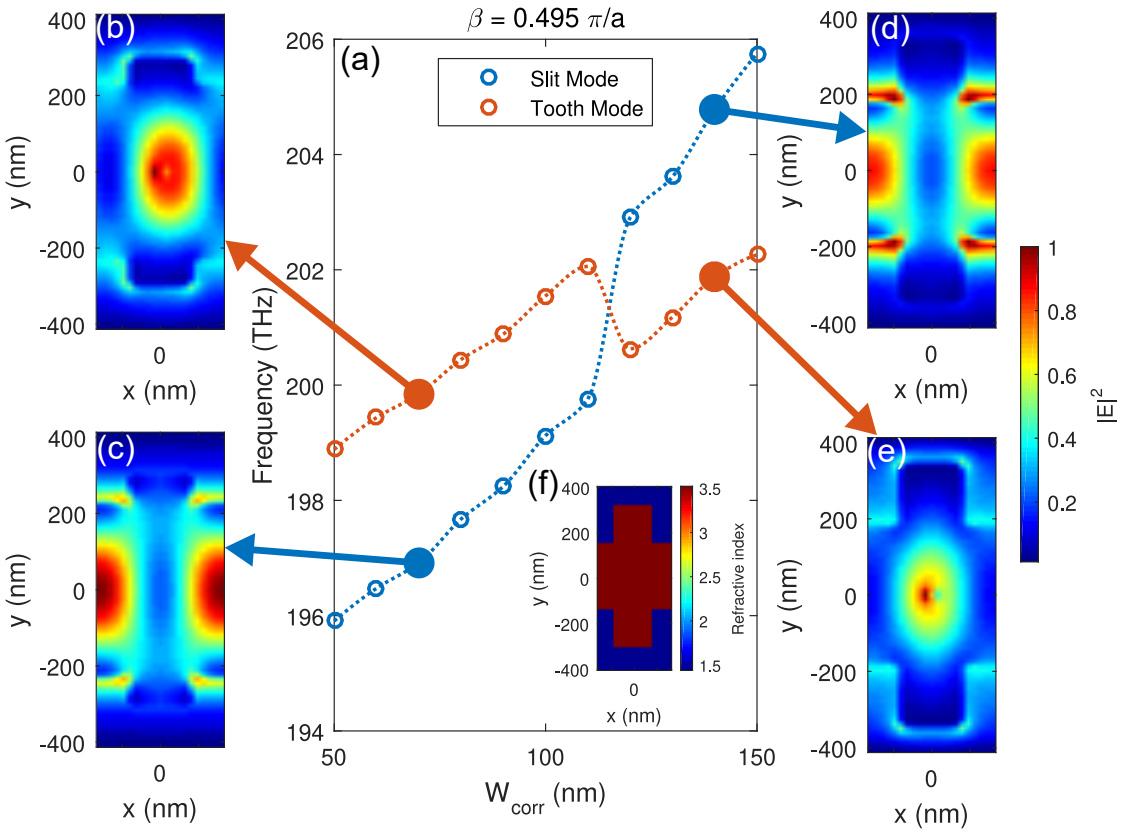

Figure 3.13.: (a) Frequency of the slit and tooth band at $\beta = 0.495\pi/a$ for different corrugation widths. A swap of the two band happens around 120 nm of corrugation. (b), (c), (d), and (e) are the corresponding Bloch modes before and after the CBG. (e) Example map of the refractive index been simulated, red corresponding to silicon and the blue to the silica.

the band n and $n+1$ as a function of dX. Locally for X small, if Df_n is negative a CBG can occur.

$$Df_n(X) = \frac{d(f_{n+1}(X) - f_n(X))}{dX} = \frac{df_{n+1}(X)}{dX} - \frac{df_n(X)}{dX} < 0 \tag{3.10}$$

Then the geometry X_c where it happens is the crossing point. If one has this function for X_0 close to X_c, we get an approximation for it with equation 3.12

$$f_n(X_c) = f_{n+1}(X_c) \tag{3.11}$$

$$X_c \simeq X_0 - \frac{\Delta f_n(X_0)}{Df_n(X_0)} \tag{3.12}$$

For instance, since $df_2/dW_{corr} < df_1/dW_{corr}$, the CBG can occur between the two first bands. If for another parameter the energy deformation is identical in the two bands

then the bandwidth is constant or increases.

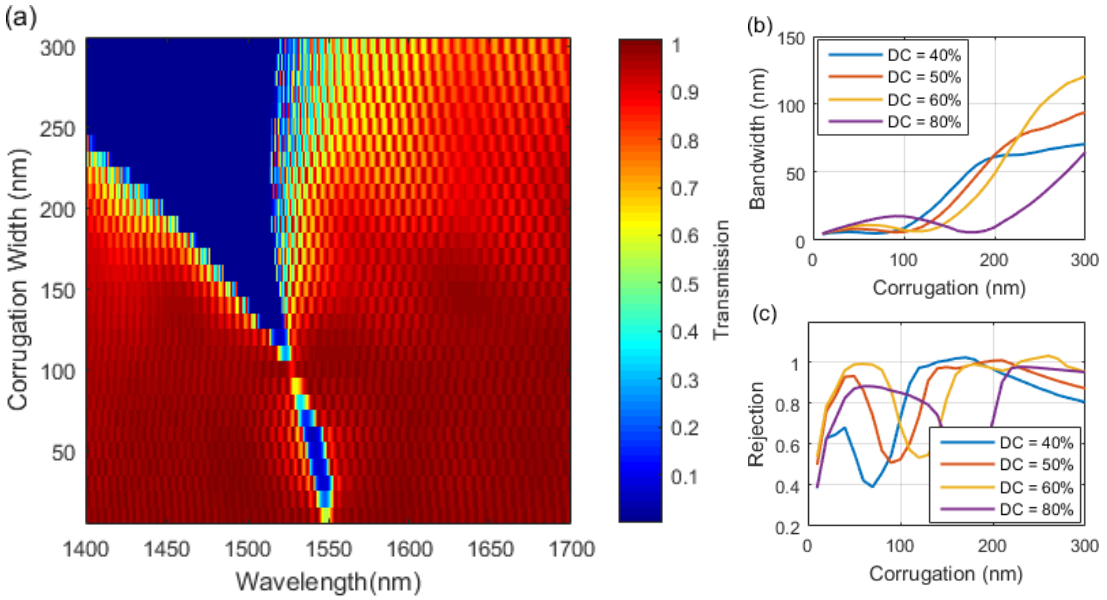

Figure 3.14.: (a) Plot of the simulated (2.5D Lumerical simulation) TE spectrum as a function of the corrugation, each line is a spectrum of the transmission of a Bragg filter with an average width of 450 nm, a pitch of 320 nm and a length of 50 μm. (b) and (c) Plot of the 3 dB bandwidth and rejection, respectively, of (a) as a function of the corrugation and for different duty cycles.

Simulating the full 3D band structure requires a lot of computational power. We can reduce the load by doing 2.5D simulations with Lumerical MODE Solution [172]. A geometry is implemetent over 50 micons with waveguides to connect the grating. An excitation mode is injected and two power monitors are placed at each ends, to measure the transmission and reflection. Looking at the transmission of the simulated grating gives us the band edges and the gap values. Using 2.5D instead of 3D simulation reduces our accuracy but should retain the geometrical behavior of the CBG.

Let us simulate the regular rectangular Bragg grating from section 3.2. If we change the corrugation or the structure duty cycle, we do not affect the two Bloch modes in the same way. As for both parameters, we are compressing one and dilating the other. This has the effect of moving the bands relative to each others, see figure 3.14). By looking at the bandwidth, we can directly find the dependency of each Bloch mode to the geometrical parameters.

The pitch and the average waveguide width ($W_{avg} = W_{wg} + W_{corr}$) have similar effects, see figure 3.15. In this case, the two bands are moved by the same frequency shift. This can be seen if we look at the field profiles of the two modes. Changing the pitch or the average width stretches the two modes in a similar fashion. The pitch expends them along the propagation direction, whereas the average width stretches them perpendicular to it.

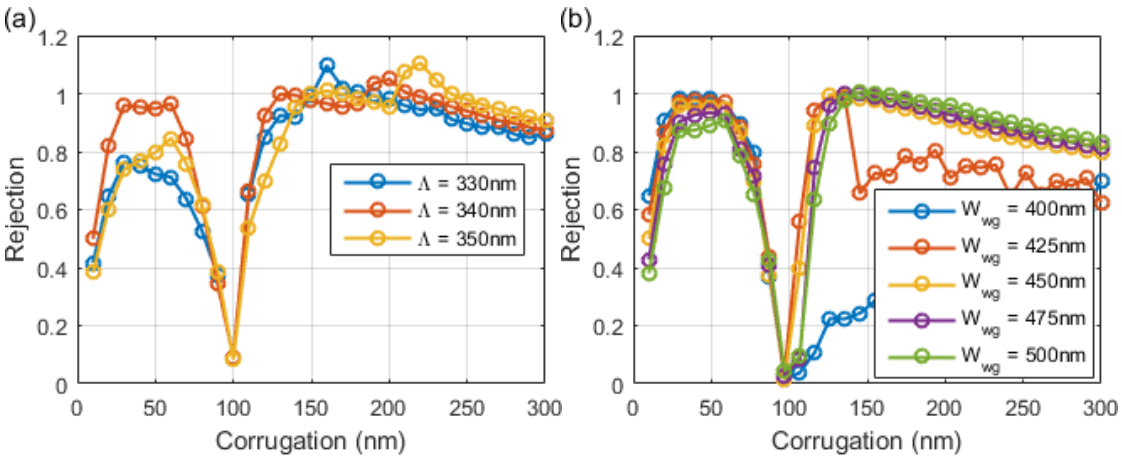

Figure 3.15.: Simulated rejection of the filter as a function of its corrugation for (a) pitch width and (b) different average. It is extracted from simulated spectra with 2.5D FDTD. Only the deepest rejection is consider whatever the wavelength. In (a) one can see rejection higher than 1, these are artifacts in the simulation where numerical errors allow the reflected power to be larger than the injected one.

The shape of the corrugation has also a large role to play in the mode swapping effect. For instance, going from rectangular to sinusoidal perturbations moves the CBG to a much larger corrugation, figure 3.16a. This effect and the CBG can be observed in the other geometries. For instance, multi-mode filters where coupling can occur between two different modes (*e.g.* TE0 and TE1). They have an asymmetric corrugation that we will see in more details in next section 3.5. They exhibit a CBG and the same shape effect can be seen when using a sinusoidal corrugation, pushing the CBG corrugation from 280 nm to 110 nm, see figure 3.16b and 3.16c. This is probably due to the smoother transition between the waveguide widths. This relaxes the pressure imposed by the corrugations on the Bloch mode fields, allowing for a larger corrugation to be applied.

The cladding has an important effect as well as the set of corrugation/duty cycle that can lead to the CBG effect. Since the *slit mode* (mode localized mostly between the teeth) has a much greater amount of energy in the low index region, any change in this area affects it much more than the *tooth mode* (mode localized mostly in the teeth). Figure 3.17, shows the difference between an air and PMMA claddings. It represents the rejection of the grating as a function of the corrugation and duty cycle. A valley can be seen for large corrugations (>50 nm), which corresponds to the CBG dimensions. Its slope depends on the cladding of the grating, the higher the index, the stronger the slope. It means that, for the same duty cycle, the CBG corrugation decreases when the index of the cladding increases. This could even be used for sensing [211].

To show experimentally the CBG effect, we fabricated symmetrical square corrugation gratings with two duty cycles of 50% and 60%. All the filters are 1 mm long to make sure a resonance appears close to the CBG. We scanned the corrugation of each to find the

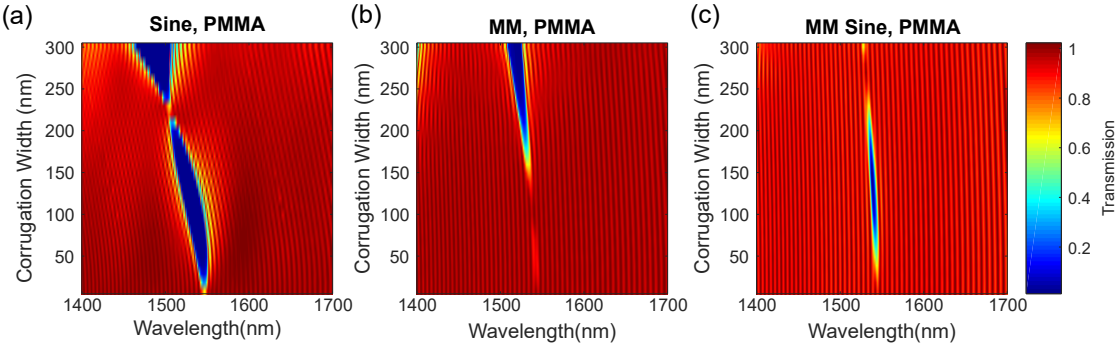

Figure 3.16.: Plots of the simulated Bragg grating waveguide transmission spectra as a function of the Bragg filter corrugation, each line is a spectrum of the transmission for a set corrugation width and a filter length of 50 μm. (a) is a grating with a sinusoidal shape with a PMMA cladding. (b) and (c) are for asymmetric multi-mode gratings with a PMMA cladding with rectangular and a sinusoidal corrugations, respectively.

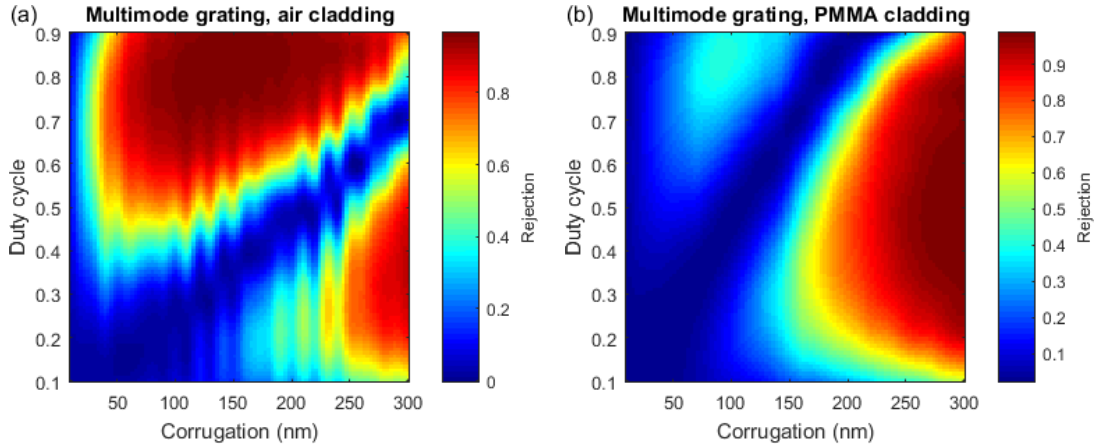

Figure 3.17.: Plot of the simulated rejection of multi-mode Bragg filter in the corrugation dimensions phase space for a fixed filter length of 50 μm, with in x the corrugation and in y the duty cycle, (a) is with an air cladding ($n_{clad} = 1$), (b) is with a PMMA cladding ($n_{clad} = 1.44$). A line with no rejection appears for large dimensions in both cases which is the CBG.

CBG conditions. As previously, the considered Bragg filters have a pitch $\Lambda = 320$ nm, an average width of $W_{avg} = 450$ nm and a PMMA cladding. Figure 3.18a plots typical collected experimental results. We can clearly see the CBG when plotting the bandwidth as a function of its corrugation. As predicted, the corrugation where the bandwidth is null increases with the duty cycle. A systematic discrepancy of 60 nm between the corrugations of the gap closing in the 2.5D simulation and the measurement is observed. This could be due to the rounding of the rectangular shapes. As we have seen the geometry of the shape is important and changes the condition of the CBG appearance

and strength.

We also tested the CBG effect for multi-mode grating structures with asymmetric corrugations (see section 3.5) for both rectangular and sinusoidal gratings. Using now a pitch $\Lambda_{\mathrm{mm}} = 290$ nm and an average waveguide width $W_{\mathrm{mm,avg}} = 1100$ nm, we modified the corrugation and measured the related structure spectra. The filter bandgap bandwidths are shown in figure 3.18b, for both rectangular and sinusoidal grating. As visible, the CBG corrugation is larger for the sinusoidal corrugation as predicted by the simulations. However, just like the regular gratings, although the overall trend is correct, a systematic error seems to appear between simulation and experimental results.

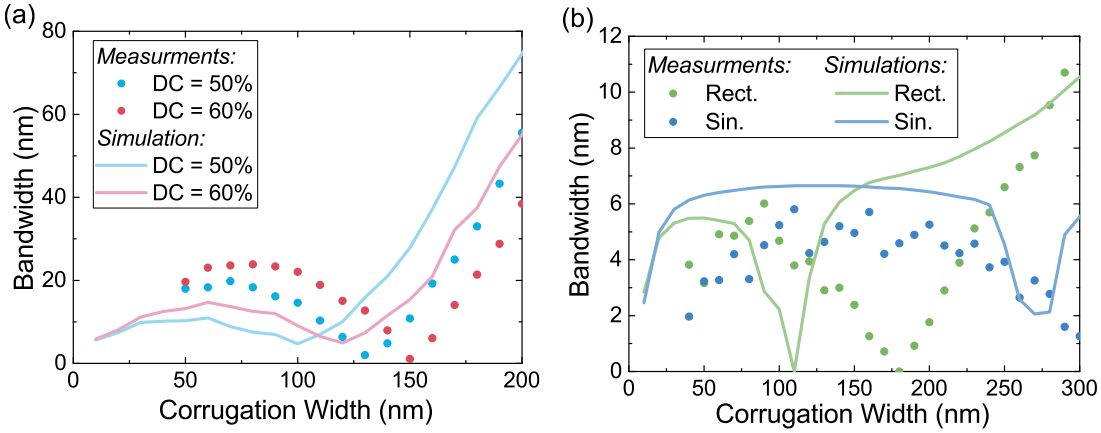

Figure 3.18.: Experimental and simulated bandwidth as a function of the corrugation, (a) for a conventional symmetrical grating with two different duty cycles, (b) for multi-mode asymmetric gratings with a rectangular and sinusoidal corrugations.

If we return to the more general context of the thesis, using the CBG to realize narrow-band filters can relax fabrication constraints. For the rectangular geometry, the corrugation width and the pitch are easy to control. The waveguide width is more difficult as it depends on the exposition process during the lithography and the etching processes. However, as we have seen it, this does not affect the CBG. The main limitation then comes from the duty cycle and the tooth shapes. Any variation on the dose or the exposition can change the Bragg grating duty cycle. Similarly, the waveguide shapes are affected by proximity effects, *e.g.* roundings of the rectangular corrugations, moving the CBG dimensions. It is yet possible to compensate this in the Graphic Database System file preparation.

For a rectangular grating, we are trading the large corrugation for the precision of the duty cycle, so of the fabrication. In an industrial foundry, it is not a problem, as the reproducibility and precision of the fabrication process is very good, ± 5 nm in dimension between samples. We are in the reversed case; we can achieve much smaller minimum feature sizes at the cost of fabrication tolerances. This is nonetheless a great tool we to have to shape waveguide Bragg filters.

A possible solution would be to use sinusoidal gratings. As shown, they have a much

higher CBG making them ever further than from the minimum feature size. The lack or sharp edges make them less sensitive to proximity effects. This could reduce the fabrication tolerances for such filters.

All the measured filters show a large discrepancy of the CBG corrugations compare to the simulations. This systematic error of 60 nm in corrugation can be explained by multiple factors. The strongest one is due to the shape. The fabricated filter are affected by a rounding (or deformations) due to the Electronic Beam Lithography proximity effect. This changes their shapes compare to their designs. As we have seen, the exact shape of the corrugation is critical; going from a perfect rectangle to a sinusoidal more than double the corrugation of CBG. So that the simulations do not match the fabrication. Of course fluctuations of the electron beam dose also affect the duty cycle as the teeth will grow or shrink larger than expected. On top of this the simulation is only 2.5D which is not as accurate as a 3D simulation. Finally, the mesh used for the simulation is limited to 10 nm. This pixel size also limit the accuracy of simulated sine corrugations. All these factors explain the experiment/simulation discrepancy.

However, It is important to refine our simulations in the future. Getting a accurate simulations of the CBG is fundamental to exploit it. It is also important to fabricate more geometries (Multimode, 2D map DC/Corr, etc.) to confront the model with as many fabricated geometries as possible. This would also help understand in more details its nature.

The CBG strategy of Bragg grating corrugation gives large geometrical parameters which are easy to fabricate. Typical industrial processes require a minimum feature size (smallest length of any line) larger than 100 nm. We can see that this is achievable in all cases, making it very accessible to any industrial fabrication platform while keeping the flexibility of performances. Unfortunately, this strategy does not address the saturation of the filter. We are still limited here an issue, that we will tackle in the next section.

3.5. Multimode filters and cascading effect

All the previous strategies to create a Bragg filter still suffer from the filter optical rejection saturation problem. This limits our ability to achieve rejections larger than 50 dB in our case. To remedy this, it proved interesting to explore multi-mode Bragg gratings, *i.e.* gratings where the reflection is achieved in another mode than the incident one. We will see that such gratings can be cascaded, allowing to break the saturation limiting us so far.

We can indeed engineer a phase matching between any guided modes of a given multimode waveguide. To do so, we not only modify geometrical parameters but also the symmetry itself of the grating waveguide [207, 212]. Such multi-mode Bragg gratings make good selective mode converters, allowing for wavelength (de)multiplexing when used with a multi-mode coupler [179] (see section 2.7.2). They also have a natural narrow bandwidth useful in our case and they provide a possible solution to the rejection saturation, as seen hereafter.

We have seen that the rejection of the filters was limited. To preserve our all-passive

filters from actively compensating the phase defects, we can reduce the defect's effects by using a multi-modal strategy [15], as shown in figures 3.19(a) and 3.19(b). The waveguide gratings are shaped to yield back-reflections propagating in a high-order spatial modes. These back-reflections are radiated away in single-mode waveguides interconnecting adjacent filter stages, precluding coherent interaction. This generic strategy allows the implementation of high-rejection filters by all-passive cascading of modal-engineered Bragg gratings with relaxed performance requirements. Recently, a similar approach was used to demonstrate deep rejection with mode separated in space [213, 214]. In these works, the back-reflections are extracted by a separate waveguide removing interactions between the filters.

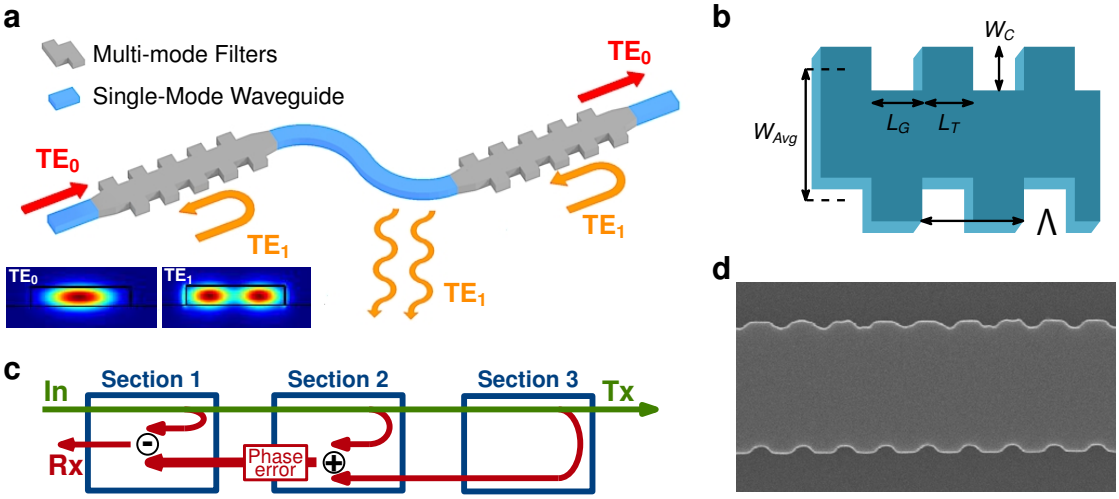

Figure 3.19.: (a) Schematic view of the proposed cascaded filter approach. Fundamental mode (TE0) is back-reflected into first order mode (TE1). Single-mode waveguide sections separating adjacent filters radiate the back-reflected TE1 mode away, precluding coherent interaction among different stages. (b) Schematic of shifted Bragg geometry providing Bragg back-reflections in higher order TE1 mode. (c) Block diagram illustrating the detrimental effect of phase errors in cascaded Bragg gratings with coherent interaction. (d) SEM image of a fabricated shifted grating. [15]

Waveguide Bragg gratings reflect light back into the input waveguide by constructive interference of partial reflections in each period [215]. This resonant back-reflection occurs when the Bragg phase-matching condition, equation 3.5, is satisfied. To achieve the theoretical rejection level, partial reflections in all periods of the filter must interfere constructively. Punctual phase errors in the grating do not have an important effect on the total resonant wavelength as they do not affect the resonant wavelength of other periods. However, even very small fabrication imperfections alter the phase along the filter, distorting the constructive interference. Such errors accumulate when increasing filter length, setting the saturation level. Cascading conventional Bragg filters does not address this issue.

Conventional cascaded Bragg gratings interfere coherently. This is indeed the principle harnessed in Fabry-Perot cavities [216, 217]. Thus, rejection in cascaded Bragg filters may be degraded by destructive interferences due to the phase shift induced by propagation through the interconnecting waveguides, see figure 3.19 (c). Even if this waveguide had the optimal length and width to induce a phase shift producing a constructive interference (*i.e.* free of fabrication imperfections), back-reflections from each stage still need to propagate in phase through the previous gratings. This has two detrimental consequences: first, the effectiveness of cascading is affected by relative phase shifts between stages; second, fabrication imperfections in each section distort back-reflections generated by the following sections. Here, Bragg gratings are designed to yield back-reflections propagating in the first higher order mode.

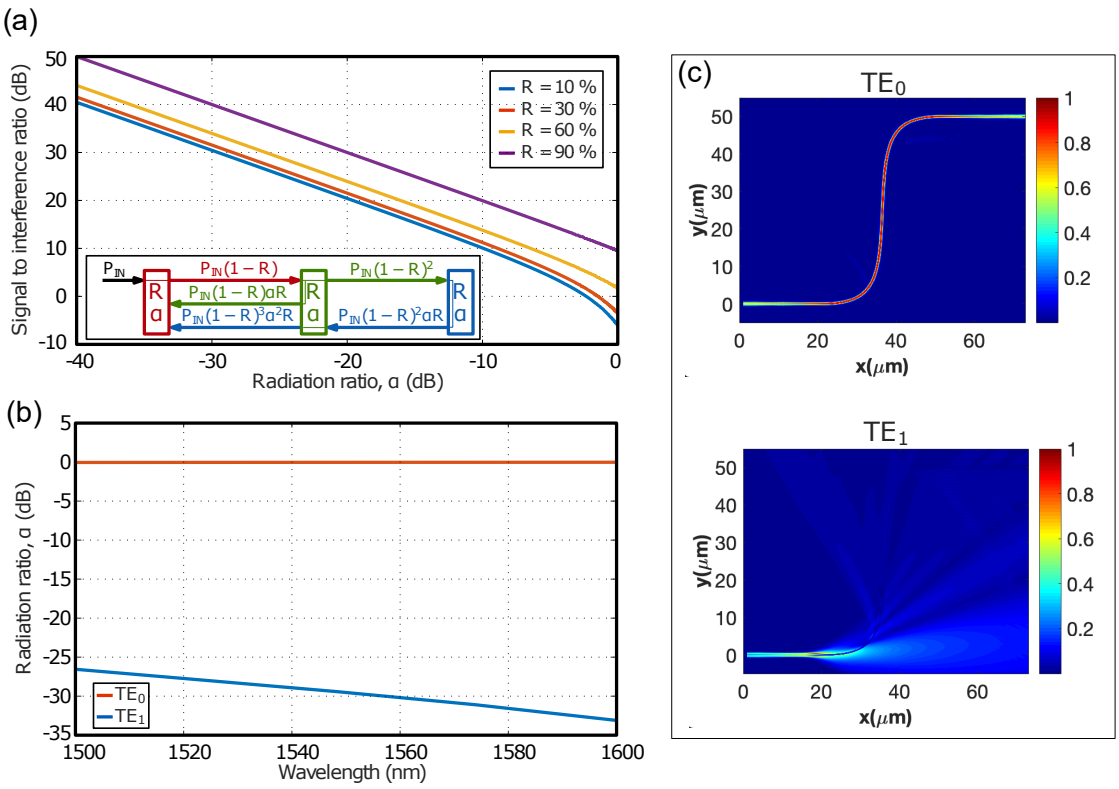

Figure 3.20.: (a) Signal to interference ratio calculated from Eq. 3.13 and Eq. 3.14 as a function of the radiation radio, for different values of the reflectivity (R). (b) Radiation ratio, calculated with 2.5D-FDTD (see [172]) when the fundamental and first order modes are injected in the proposed interconnection section, comprising 25-micron-long tapers, S-bends with 15 micron radius and single-mode straight waveguide section with 20 micron length. (c) shows the propagation for the fundamental and first order modes at 1550 nm wavelength.

To consider that reflected waves in one filter are not distorted by all other filters of the cascaded geometry, it is necessary to ensure that the reflection in this filter is

substantially larger than the sum of all reflections arriving from the following filters. Let the reflection in the first filter be called signal (S), while the sum of the reflection in all other filters, arriving to the first filter, is I. As schematically shown in the inset of Fig. 3.20(a), the signal and interference can be calculated as:

$$S = P_{IN} R \tag{3.13}$$

$$I = P_{IN} R \sum_{n=2}^{N} (1-R)^{2n-3} \alpha^{n-1}, \tag{3.14}$$

where α is the radiation ratio, P_{IN} the incident power, and N is the total number of cascaded gratings. Figure 3.20(a) shows the signal to interference ratio calculated as a function of α for different values of the power reflectivity R of each grating. It can be seen that radiation ratios of 20 and 30 dB yield at least 2 and 3 orders of magnitude difference between the signal and the interference, respectively, thereby precluding distortion of the reflection in the first filter.

To radiate the first-order-mode reflection, we introduce tapers to single-mode waveguides, and a cosine-shaped S-bend with a central straight waveguide section. Both the S-bend and the straight section are implemented with a single-mode waveguide. We chose a waveguide width of 400 nm, providing single-mode behavior. This interconnection section should also provide low insertion loss for the fundamental mode outside the rejection band to avoid degrading the total filter rejection. Hence 25-μm-long linear tapers are implemented between the filter and the single mode waveguide to achieve adiabatic transition, thus minimizing the loss for the fundamental mode and the transference of energy among modes. A 15 μm radius is used in the S-bend to minimize bending loss for the fundamental mode. Figure 3.20b shows the radiation ratio for the fundamental and first order modes calculated using 2.5D FDTD [172], considering a central waveguide section with 20 μm length. The proposed interconnection section yields a loss of only -0.05 dB for the fundamental mode and a radiation ratio in excess of -25 dB for the first-order one, thereby ensuring negligible interference among cascaded gratings. As an example, the insets in Fig 3.20c show the propagation for the fundamental (TE_0) and first order (TE_1) modes at 1550 nm wavelength.

From the coupled mode theory, the rejection of conventional filters ideally scales with the length following equation 3.8. However, our broken-coherency cascaded filter follows a different law where each section is independent from the others and the rejections are accumulated:

$$R = \left[\tanh^2(\kappa L_S)\right]^{N_S}, \tag{3.15}$$

where L_S is the section length and N_S is the number of sections. For a given length and coupling coefficient, κ, this law yields a weaker rejection in the ideal case. However, we show experimentally that the resilience to phase errors in the broken-coherency approach allows substantial rejection improvement in practical implementations.

For the implementation of multi-mode Bragg gratings, we selected a fully-etched process and a shifted-teeth geometry, as presented in figure 3.19b. As illustrated in figure 3.19, the grating lattice is defined by the average waveguide width (W_{Avg}), the corrugation depth (W_C), the length of the teeth (L_T), its gaps (L_G) and the period ($\Lambda = L_T + L_G$). By shifting the corrugation in one side of the grating half a period with respect to the other, this grating geometry prevent Bragg reflections in the fundamental mode [212], while providing the asymmetry required to excite Bragg back-reflections in the first higher order mode [207].

We designed the shifted Bragg grating to operate with TE polarized light near 1550 nm wavelength using modal analysis and FDTD simulation [172]. An average waveguide width W_{Avg} of 1150 nm provides a sufficiently multi-mode waveguide. The second TE mode is well defined but not the higher ones. The two first TE modes (TE0 and TE1) have effective index values of $n_{eff}^{TE0} \simeq 2.77$ and $n_{eff}^{TE1} \simeq 2.45$, respectively. We see in equation 3.5 that we need a pitch of $\Lambda_M \simeq 290$ nm. A corrugation W_C of 50 nm and a duty cycle of 50% ($L_T = L_G = 145$ nm) were considered for testing this strategy. These dimensions are typically compatible with state-of-the-art immersion lithography. While the period of 290 nm ensures a spacing between teeth larger than 100 nm, well within the capabilities of standard deep-Ultraviolet (UV) lithography [218], the 50-nm-wide corrugation may be challenging to implement. Nevertheless, the design could be easily adapted to increase the corrugation width to 100 nm.

Figure 3.19d shows the scanning microscope image of one of the gratings. It can be noticed that the filter teeth are rounded, with local defects. We verified by simulation that rounding of the grating teeth did not affect the operation principle of the proposed filter.

First, a series of single-section shifted Bragg gratings with different lengths were considered to illustrate the effect of optical rejection saturation. Rejection level was estimated as the difference between off-band transmission and the peak level inside the grating reflection band. As shown in figure 3.21a, the rejection level saturates near 40 dB for filter lengths beyond 300 μm. This weak rejection, compared with state-of-the-art Bragg filters [188], may be attributed to errors in the electron-beam lithography and to the strong index contrast between silicon and air that accentuates the detrimental effect of fabrication imperfections. We compared the optical transmission of the filters to that of a reference strip waveguide to demonstrate the low insertion loss of this kind of shifted geometry and showed that the lower transmission at shorter wavelengths mainly arised from the response of the fiber-chip grating couplers.

The potential of the globally proposed approach for non-coherent cascading was shown by the characterization of a set of cascaded shifted Bragg gratings separated by single-mode waveguides. The cascaded filters have the same total lengths as the single-section structures shown in figure 3.21a, but they are implemented by cascading multiple 50-μm-long grating sections. The 50 μm section length was chosen just as an illustrative example, the main conclusions remaining valid for other section lengths. The transmission spectra of the cascaded filters with total length ranging between 50 μm and 500 μm (comprising ten sections of 50 μm length) are presented in figure 3.21b. Figure 3.21c

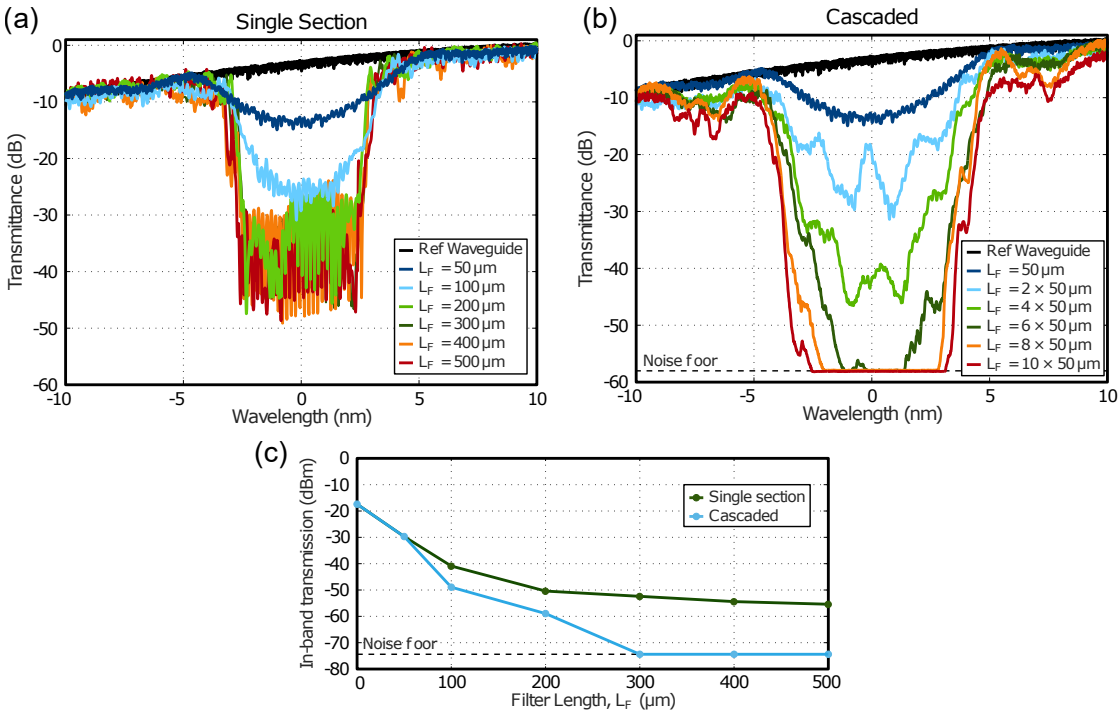

Figure 3.21.: Measured transmission spectra of (a) single section Bragg filters with increasing lengths, and (b) proposed cascaded Bragg filter with a fixed section length of 50 micron, and number of sections ranging from 1 to 10. (c) Comparison of in-band optical transmission as a function of the filter length of single-section and proposed cascaded geometry, showing a clear rejection saturation only for the single-section approach.

shows the transmission level within the rejection band as a function of the filter length for both single-section and cascaded configurations. The 0-filter-length point represents the transmission for a reference waveguide (without Bragg gratings).

The proposed cascading approach yields a substantial increase in filter rejection, showing no clear evidence of saturation with the filter length. Note that for total lengths beyond 300 μm, the on-resonance transmission of the cascaded filter lies below the noise floor level of the automatic wavelength sweeping and detection system (CT400 from Yenista). The oscillations observed in some cascaded filters were attributed to random fabrication defects in the taper section that convert the second-order-mode reflection into the fundamental one and create some cavity effects. These imperfections may be attributed to local defects in the resist, *e.g.* due to the presence of dust, or stitching errors in the electron beam lithography (3σ of 20 nm). The number of non-controlled errors may be minimized by fabricating the filters using industrial-like processes, *e.g.* by multi-project wafers, and deep-UV lithography instead of electron-beam lithography.

In addition to a higher optical rejection, the cascaded filters exhibit a wider bandwidth. As discussed below, this wider rejection does not arise from relative wavelength shifts

among different filter sections, but from the non-coherent nature of their interaction. From Eq. (3.7) it follows that, for a given Bragg grating geometry (fixed n_g and κ), filter bandwidth decreases with the length. This could be qualitatively explained from the point of view of Fourier transform, as a longer spatial perturbation results in a narrower spectral response. However, different sections in the modal-engineered filter do not interact coherently. Thus, the bandwidth of the proposed filter is not determined by the total length, but by the length of the sections. This non-coherent interaction effect can be observed in Fig. 3.21(b), showing that filters comprising 50-μm-long grating sections have a similar bandwidth, regardless the total length.

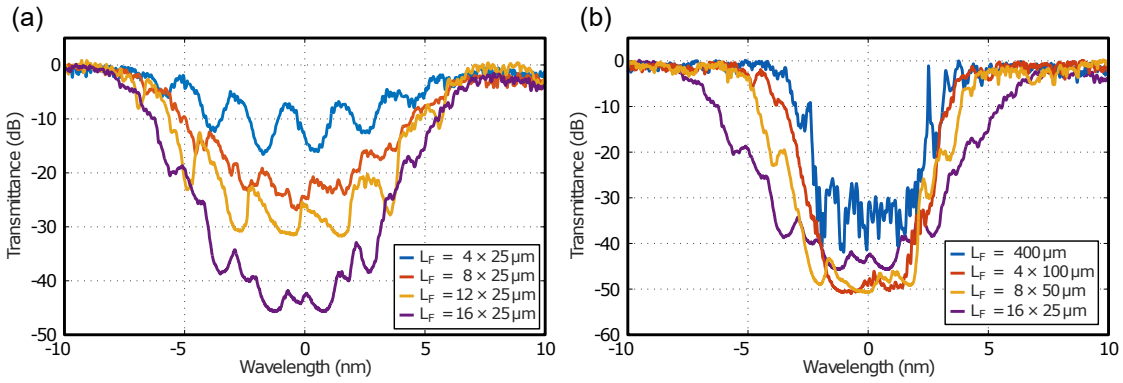

Figure 3.22.: Measured transmission spectra of proposed cascaded filters for (a) fixed section length, of 25 microns, and increasing number of sections, showing no clear evidence of bandwidth increase with the number of sections, and (b) fixed total filter length, of 400 microns, and decreasing section length. Filter bandwidth is determined by section length rather than by total length due to non-coherent cascading.

Aiming at confirming the incoherent cascading in the proposed approach, we fabricated and characterized two different sets of filters. Note that while all the devices fabricated at the same time have a very repeatable response, *e.g.* central wavelength, due to variations in the fabrication conditions the response of this new set of filters is not directly comparable with the ones shown in figure 3.21. First, we fixed a section length of 25 μm and cascaded different numbers of sections, from 4 to 16, resulting in total filter lengths ranging between 100 μm and 400 μm. Measured spectra, shown in figure 3.22a, demonstrate that bandwidths of the cascaded filters do not significantly increase with an increasing number of sections. Hence, relative wavelength shifts can be discarded as the major reason for the wider bandwidth in the cascaded filters. Note that all the sections of the filter were placed close together in the chip, minimizing the effects of uneven silicon and resist thicknesses, while all sections in the same filter were written consecutively in the electron-beam lithography, minimizing beam current drifts over the time. Then, any deviation of the central Bragg grating wavelength was similar for all filter sections, yielding minimal relative shifts.

Then, we implemented the same total filter length, of 400 μm, by a single-section

device, and by cascading 4, 8 and 16 sections of 100 μm, 50 μm, 25 μm lengths, respectively. The different measured spectra are presented in figure 3.22b. It can be noticed that, even if the total filter length is always the same, the filter bandwidth increases with decreasing section lengths. These results clearly demonstrate the incoherent cascading in the proposed geometry, as the total filter bandwidth is mainly determined by the bandwidth of the individual Bragg gratings sections, rather than by the total filter length.

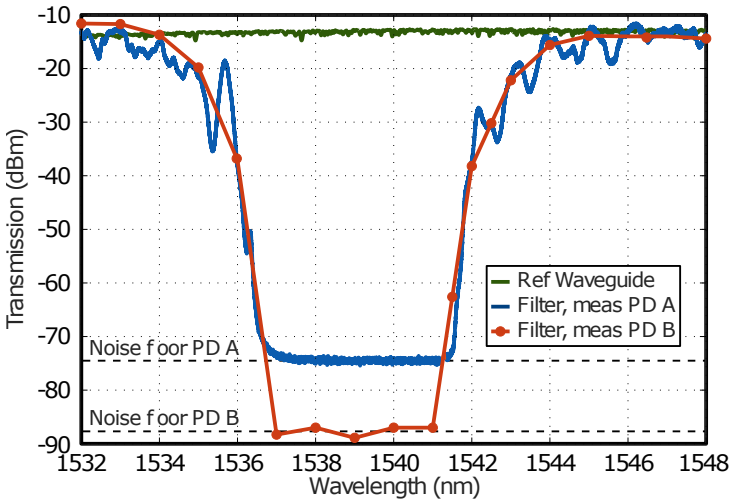

Figure 3.23.: Transmission spectrum of cascaded shifted Bragg filters with total length of 2.5 mm, implemented by 10 modal-engineered Bragg grating sections of 250 microns length. Measurements are performed with automatic wavelength sweep and detection system (CT400 form Yenista), PD A, and high-sensitivity photodetector, PD B, in OSA (Anritsu MS9710B). Transmission of 3.5-mm-long strip waveguide is shown for comparison.

Finally, to demonstrate the large rejection capabilities of the proposed broken-coherency approach, we implemented a 2.5-mm-long filter, comprising 10 modal-engineered Bragg grating sections of 250 μm length. Rejection in single section filters saturates after 300 μm length, see figure 3.21. Thus, we choose a section length of 250 μm, below the saturation regime. The length of 2.5 mm was chosen to yield strong rejection. In this case, we used an optimized grating coupler design allowing a 5 dB improvement in the transmitted signal, compared to the previous examples. As shown in figure 3.23, the response of the filters was characterized using an automatic wavelength sweep and detection system (CT400 from Yenista) and the high-sensitivity photo-detector in OSA Anritsu MS9710B. For comparison, in figure 3.23, we also included the response of a reference strip waveguide of 3.5 mm length. This length includes the grating lengths (total of 2.5 mm), and the lengths of the input/output tapers S-bends and single-mode sections. The proposed filter exhibits negligible off-band insertion loss, within the variability determined by fiber alignment precision and fabrication tolerances. The on-resonance transmission level of the cascaded filter lies within the noise floor of the OSA, with (at

least) 80 dB of on-chip optical rejection. Such rejection may be suitable for our quantum system needs.

It is worth noting that in the single-section case the transmission decay saturates near 55 dBm (*i.e.* ∼40 dB rejection) for filter lengths beyond 300 μm. Hence, these results prove the potential of non-coherent cascading to increase filter rejection. Using the rejection of a single 250-μm-long section to fit the coupling coefficient in Eq. (3.15), the filter with 10 cascaded sections would have a rejection near 300 dB. Still, such value might be compromised by imperfections like partial polarization rotation and radiation due to waveguide roughness. Nevertheless, the measurement of a deeper rejection would probably require more sensitive detectors and specific treatment of the substrate scattering. We used a fiber circulator at the input of the filter to collect all back-reflections. We retrieved a broadband and quasi-flat signal with no signature of the Bragg grating resonance and nearly -40 dBm level (mainly arising from reflections in gratings and backscattering in waveguide roughness). This result further confirms that back-reflections are effectively radiated away in the single-mode waveguide sections.

3.6. Implementations

3.6.1. Filter strategies

Now that we have a satisfying filter and an efficient strategy to avoid rejection saturation, we can engineer a narrow band deep filter using our all previously mentioned techniques. Let us try three types of filters, small (triangular[1]), subwavelength and CBG corrugations. We can see them all in figure 3.24 (a, b, and c). They all have asymmetric corrugation allowing the multimode reflection mechanism, *i.e.* a shift of half a period is applied between each sides of the waveguide.

We fabricated a series of 500 μm-long filters with various corrugations and average waveguide widths. The triangular corrugation was increased from 10 nm up to 50 nm, the subwavelength one from 10 nm (shift) to 100 nm, and the rectangular corrugation from 50 nm to 300 nm. We can see the shift in wavelength due to the corrugation increase in figure 3.24 (d), (e), and (f). The triangular and rectangular Bragg grating resonances shift in the same direction: when the corrugation increases, the bandgap wavelength decreases, whereas the subwavelength Bragg filter presents the opposite effect. When plotting filter bandwidth as a function of the rejection, all filters follow a line predicted by Coupled Mode Theory (CMT) in equation 3.9, see figure 3.24 (g), (h), and (i). We can see that both the triangular and subwavelength filters have a similar behavior with a monotonous growth in bandwidth and rejection when the perturbation increases. The rectangular corrugation starts approximatively where there the triangular ends. But its strength starts decreasing to arrive to zero before going back up. We clearly have the CBG effect here (section 3.4).

This allows us to calibrate the dimensions of the filter we want for cascading. No

[1] A triangular corrugation allows to keep the minimum feature size larger than the pitch while having a corrugation as small as possible. This is however limited by the lithographic precision

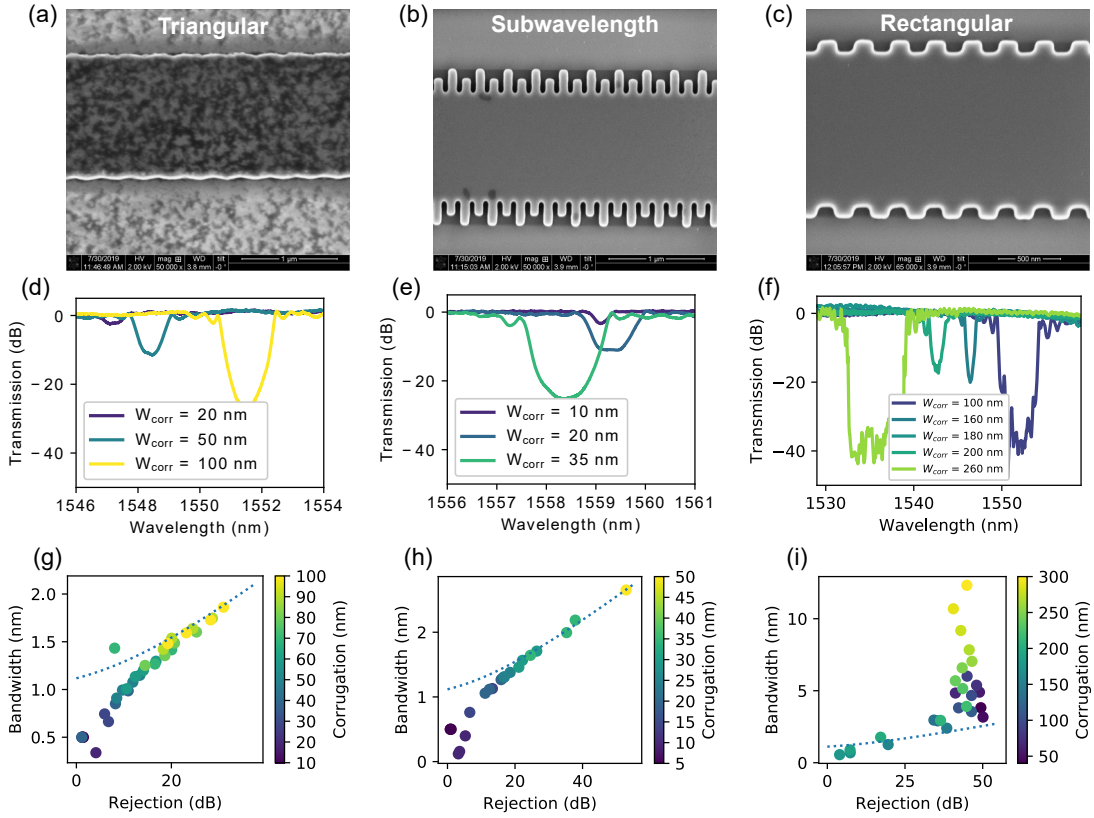

Figure 3.24.: Schematics and performances of the three Bragg grating strategies. (a), (b), and (c) are SEM images of the triangular, subwavelength, and rectangular corrugations, respectively. (d), (e), and (f) are transmission spectrum of a few of Bragg filters with various corrugations for the triangular, subwavelength, and rectangular corrugations, respectively. (g), (h), and (i) are the filtering bandwidth as a function of the filter rejection with the corrugation color coded, for the triangular, subwavelength, and rectangular corrugations, respectively. The blue doted line is the coupled mode theory (CMT) prediction for a group index of 4.3.

PMMA top cladding was added on the structure in order to reduce residual propagating Transverse-Magnetic (TM) modes. This prevents photons from getting trapped in the cladding and simplifying the fabrication process. We also proceeded with corrugations of 25 nm, 100 nm, and 225 nm, for the triangular, subwavelength, and rectangular corrugations, respectively. This provided a bandwidth of around 1.6 nm for the triangular and subwavelength grating. This is to avoid destroying the closest resonance from the pump. It also ensures a bandwidth close to 3.2 nm, for the rectangular grating, so corresponding to two ring FSR. This sacrifices the two first resonances of the cavity, in exchange for a deeper rejection. Accordingly, cascaded filters were fabricated with 9 sections of 325 μm.

The fabricated structures have 3.3, 4.3, and 4.7 nm 3 dB-bandwidth corresponding

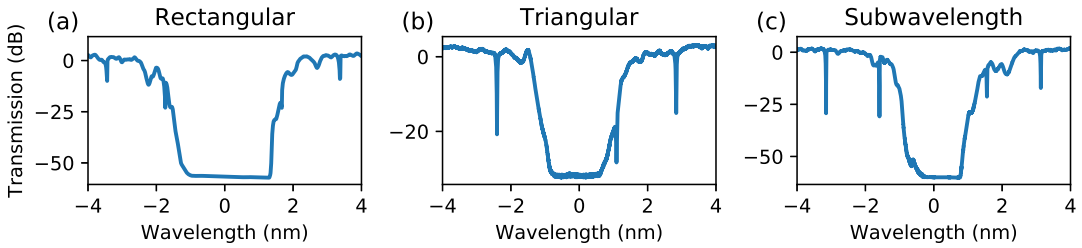

Figure 3.25.: Transmission spectra of the pump rejection filter for the three types of corrugation, (a) rectangular, (b) triangular, and (c) subwavelength, composed of 9 sections of 325 microns.

to the triangular, subwavelength, and rectangular gratings, respectively see figure 3.25. But this is not the quantum usable bandwidth. Due to the large depth required by the quantum application, we can only use the deepest rejection region. In figure 3.25, we can observe that the rectangular and subwavelength gratings have similar 3 dB-bandwidth but the 20 dB-bandwidth is much larger for the rectangular grating. Their respective 20 dB-bandwidths are indeed 2.1, 2.2, and 3.3 nm. They are close to the single section bandwidth values. While the increase in 3 dB-bandwidth compare to the single section is due to the accumulation of the sidebands, visible on the filter spectrum, see figure 3.24d, 3.24e, and 3.24f.

These filters have a predicted rejection from CMT larger than 180 dB. Measuring large rejection on chip can be tricky, any noise with a level larger than the filter rejection prevents its measurement. For instance: the polarization of the input light must be perfect to limit the coupling of TM modes; scattered light along waveguides or at the coupling stage can be coupled back into the output bypassing the filter; amplified spontaneous emission from the laser can also create a background residual signal. Detectors without spectral dependency can detect any residual unfiltered photon. Rather than spending time measuring the depth of these filters, we decided to directly move to on-chip quantum experiments. Our approach was to indirectly demonstrate the proper operation of the pump rejection filter by collecting quantum measurements and progress towards the global objective of our global study.

3.6.2. Interaction with the circuit

At this stage, we finally have all the components to design and create the needed quantum circuits. Both the photon-pair comb source and the entangled photon-pair generator of section 2.1 will be constructed. We have seen how to design the pump rejection filter with 3 corrugation strategies that will be tested in photon-pair comb sources. The cavity, modal add-drop, and grating couplers seen in chapter 2 are combined with a cascaded filter. This is the basis of any of silicon quantum circuit that will be studied in more details in chapter 4. The pump rejection filter stays the pivot of the system, so we will make three families of circuits based each on a filter design.

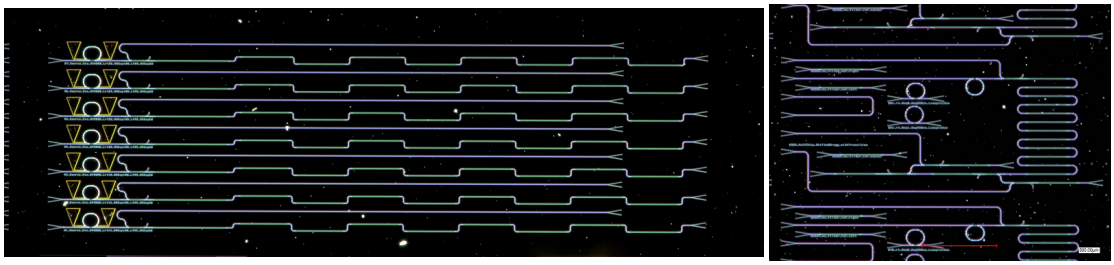

Figure 3.26.: Images of the photon-pair comb sources and a entangled pairs generator on the left and the right, respectively. The purple lines correspond to the waveguides while the green ones are Bragg gratings.

To implement these strategies, we fabricated a series of entangled photon-pair comb sources with different coupling lengths for the ring resonators. A variation from 14 μm to 26 μm was chosen to ensure finding critical coupling conditions within the investigated devices, see figure 3.26. Three multimode Bragg filters were implemented with triangular (tri), subwavelength (SWG), and closure of the bandgap (CBG) type corrugations. All the components used have been described in chapter 2.

Their spectral characteristics are shown in figures 3.27, 3.28, and 3.29. As previously, they were measured using a tunable laser Tunics paired with a CT400 detection system. The polarization of the input laser was controlled thanks to a polarization controller. The cavity resonances were monitored in order to determine their coupling regime. Bandwidth of the filters were measured both in transmission and with *feedback* port (see figure 4.1 page 116) giving access to the rejected light. The feedback signal is connected to a Modal Add-Drop (MAD) drop port which collected reflected light coming form the first section of filter. This is also where we could see the pumped resonance and its spectral alignment with the pump rejection filter.

A heater was deposited on the triangular corrugation sample next to the ring resonator cavity to align it with the pump filter. Unfortunately, it was not possible to do this for the other sources, limiting the choice of the full circuit to one cavity naturally aligned with the filter. However, this did not affect the general behavior of the system.

One circuit was chosen in each series, for the tri sources using the ring with the best performances, while for the SWG and CBG sources a good filter/ring alignment was preferred. The sources classical performances are shown in table 3.1. The tri source has a coupling length of 14 μm and shows well over coupled regime, see figure 3.27. Similarly, the SWG source has the same coupling length of 14 μm but is not as over coupled as possible but at least is aligned with the filter rejection wavelength, see figure 3.28. Finally, the CBG source has the worst ring with a close to critical coupling with an average resonance depth of only 8.2 dB, see figure 3.29.

As mentioned in section 3.6, the tri., SWG, and CBG filters have 20 dB-bandwidths of 2.1, 2.2, and 3.3 nm, respectively. This is the bandwidth usable for the rejection of the pump. The pumped resonance should be placed in the center of the rejection bandwidth. However, the 3 dB-bandwidth (3.3, 4.3, and 4.7 nm, respectively) is larger, which limits

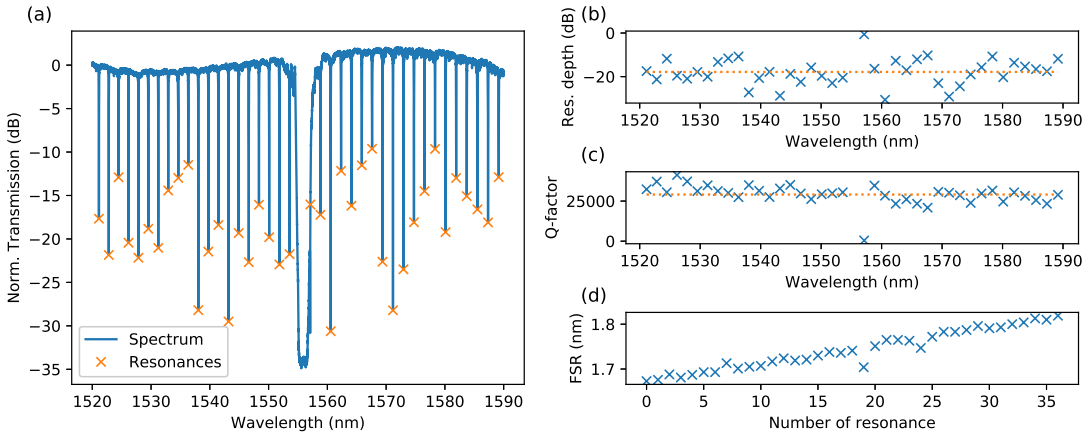

Figure 3.27.: (a) Spectrum of the comb source with triangular fibers, the filter has a 3 dB-bandwidth of 3.3 nm and a 20 dB-bandwidth of 2.1 nm, the resonances shown here are the one studied in the other plots. (b) Plot of the resonance depth as a function of wavelength and its average of 17.9 dB, it is mostly flat even if there are large variations. (c) Plot of the resonances Q-factor as a function of wavelength and its average of $29 \cdot 10^3$. (d) Plot of the FSR as a function of theirs number on plot (a), it increases with wavelength as expected and is close to 200 GHz.

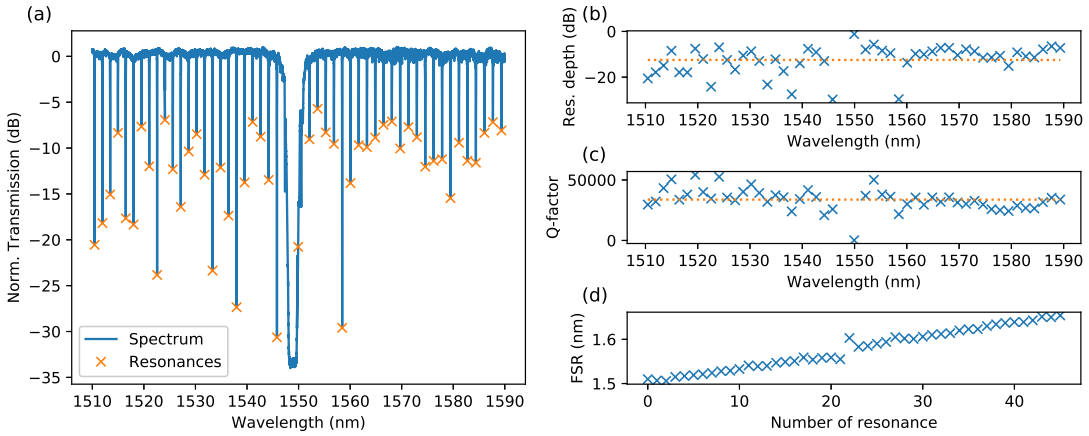

Figure 3.28.: (a) Spectrum of the comb source with SWG fibers, the filter has a 3 dB-bandwidth of 4.3 nm and a 20 dB-bandwidth of 2.2 nm, the resonances shown here are the one studied in the other plots. (b) Plot of the resonance depth as a function of wavelength and its average of 12.5 dB, there is no tendency even if there are variations. (c) Plot of the resonances Q-factor as a function of wavelength and its average of $34 \cdot 10^3$. (d) Plot of the FSR as a function of theirs number on plot (a), it increases with wavelength as expected and is close to 200 GHz.

the closest pairs that can be collected. Even if the pairs are generated outside of the deepest region, the filter losses reduce enormously their rate. Moreover, note that we

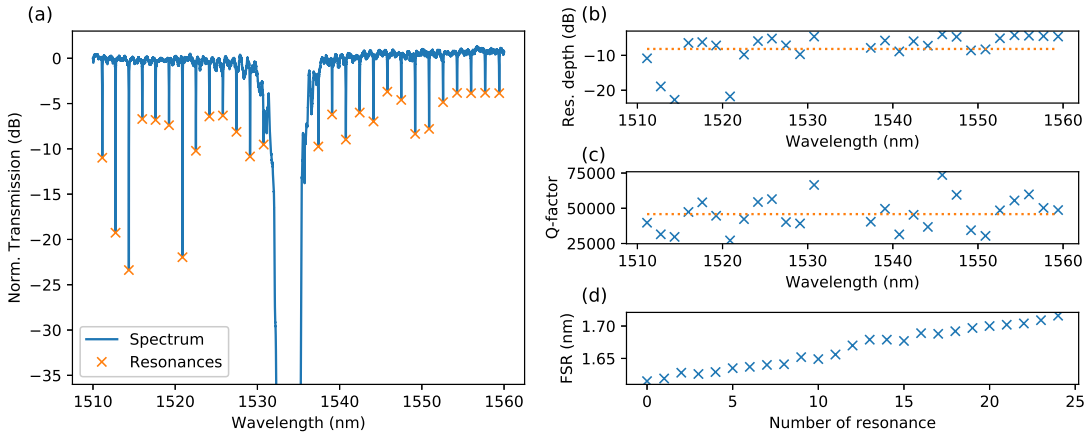

Figure 3.29.: (a) Spectrum of the comb source with CBG fibers, the filter has a 3 dB-bandwidth of 4.7 nm and a 20 dB-bandwidth of 3.3 nm, the resonances shown here are the one studied in the other plots. (b) Plot of the resonance depth as a function of wavelength and its average of 8.2 dB, it is mostly constant. (c) Plot of the resonances Q-factor as a function of wavelength and its average of $46 \cdot 10^3$. (d) Plot of the FSR as a function of their numbers on plot (a), which increases with wavelength as expected and is close enough to 200 GHz.

need both photons of the pairs to be transmitted. So, if one of the resonance is lossy, its partner becomes a noise.

The MAD used for the pumped resonance feedback has a crosstalk of about 10 dB around the closest resonance filter, as shown in figure 4.2. This is the same component as seen in chapter 2 section 2.7.2. This is enough as we do not use it to demultiplex the pairs here.

Filter type	Triangular	Subwavelength	CBG
Filter 3dB-bandwidth (nm)	3.3	4.3	4.7
Filter 20dB-bandwidth (nm)	2.1	2.2	3.3
Coupling length (μm)	14	14	18
Avg. resonance depth (dB)	17.9	12.5	8.2
Mean Q-factor	$29 \cdot 10^3$	$34 \cdot 10^3$	$46 \cdot 10^3$

Table 3.1.: Summary of the classical performances of the three sources.

Due to a lack of time, we have chosen one corrugation strategy to proceed with the integration and quantum characterization of the full photonics circuits. We will focus on the CBG in the rest of this work. The other approaches, the SWG and tri filters based circuits, were considered for future works.

If we now take this source and an integrated demultiplexing stage, we get an on-chip photon-pair generator, see figure 3.26. At the output, instead of a comb of photon pairs, pairs are separated into idler and signal ports. They can then be further de-

multiplexed or directly used. As a demultiplexing stage, we chose a modal add-drop device (see section 2.7.2). It has the advantage of being fully passive, to have a tunable bandwidth, and to be amenable to cascaded configurations. If we use the same type of grating as one of the pump rejection filter, we can easily align them in wavelength by tuning their respective average waveguide widths. We fabricated such device, see figure 4.6, with the CBG strategy and a strong filter with $W_{corr} = 100$ nm. These gratings have a bandwidth of 5.2 nm, they are used for the pump filter (PF) and for the demultiplexing stages (MAD feedback, signal, and idler). A 2-MAD cascade is used for the multiplexing of the signal/idler to reduce the crosstalk between the channels to -20 dB. Due to fabrication problems, the transmission is lowered to -19 dB. But also, large propagation losses make the signal and idler transmission down to -30 dB. No heater could be deposited but luckily a ring resonance was well aligned with the center of the filter response, see figure 3.30.

The grating couplers (CG) are spaced by 127 μm, so a fiber array can be used to send light in and out of the circuit (figure 4.6). Alignment is done using a reference waveguide, then the feedback level monitors the transmission.

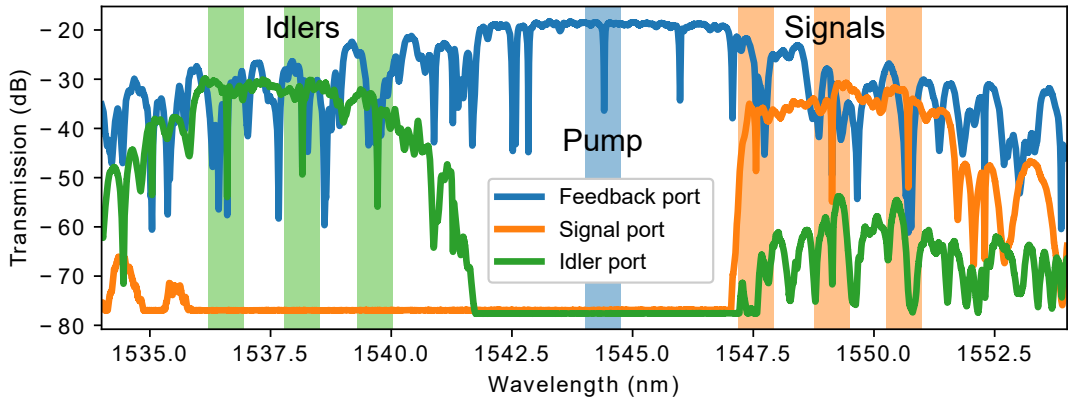

Figure 3.30.: Spectrum of the feedback, signal, and idler ports when injecting light in the pump port. The resonances of the ring are highlighted, in blue, green and orange for the pump, idler and signal, respectively. The two closest resonances from the pump (visible in feedback) are not usable as they are rejected by the PF.

The ring resonator has a FSR of 1.57 nm which is close to the International Telecommunication Union (ITU) grid allowing to uses standard off-the-shelf components. We can align the whole spectrum to the ITU grid by heating up the sample with a Peltier system.

The fiber array has a backward crosstalk of only 90 dB even after 6 channels, making direct use of the idler/signal output very noisy, on top of any photonic noise due to the scattering. As a consequence, a filter at the pump wavelength or a de-multiplexing stage of at least 20 dB is needed at each output.

3.7. Summary

We have seen in this chapter possible design tools that one can use to change the properties of conventional waveguide Bragg filters. In particular, with a view to a drastic increase in their power rejection ($\gg$ 50 dB), while maintaining a low rejection bandwidth, of a few nm at most. One-sided, triangular and subwavelength corrugations allow to reduce the perturbation seen by the light, providing a reduced coupling and narrow bandwidth. The closure of the band-gap effect promises a new approach to realize narrow filters with large corrugations with reduced fabrication constraints. In the current state of work, the most advanced approach for the production of narrow, high rejection filter that has been implemented. It is based on a cascading strategy of multimode Bragg filter enabling to push the limit of the possible rejections of ultra-long single Bragg filters. This technology-independent proposal indeed precludes coherent the interaction among nominally identical cascaded Bragg filters sections and provides a dramatic optical rejection increase. It overcomes one of the major on-chip performance limitations. While maximum rejection level in conventional wavelength filters is seriously hampered by phase errors arising from fabrication imperfections. Our approach allows effective cascading of low rejection level stages without the need for any active tuning. High rejection levels have been demonstrated for cascaded MZIs [185] and ring resonators [200]. However, these devices required active tuning of each stage in the circuit to compensate phase errors.

The innovative concept is to separate multi-mode Bragg grating sections by single-mode waveguides to break the coherency of the interaction. We engineer the grating to yield back-reflections propagating in a high-order spatial mode, which is radiated away in the single-mode waveguides. This way, different filter sections are completely independent with no phase relationship. It allows effective optical rejection accumulation, even in the presence of phase errors. Based on this concept, we have experimentally demonstrated on-chip non-coherent cascading of multi-stage silicon Bragg filters. We have implemented a notch wavelength filter with an optical rejection higher than 80 dB solely corresponding to the noise floor level of our experimental equipment. This is the largest optical rejection ever reported for an all-passive silicon photonic wavelength filter.

The approach proposed here could be translated to any other integrated photonic technology, as long as it allows the realization of multi-mode Bragg gratings and single-mode waveguides. Moreover, the concept could be applied to multi-corrugation geometries providing simultaneous Bragg grating resonances for both TE and TM modes [188] or to contra-directional couplers where reflected light is coupled to a different waveguide [219, 214]. However, special care needs to be taken to fulfill conditions required to achieve coherent interaction suppression, thereby obviating multi-filter effects that can affect the spectra of filters [214].

The broken-coherency strategy proposed here releases new degrees of freedom to tailor the shape of on-chip wavelength filters. More specifically, the bandwidth of the cascaded Bragg filter is mainly determined by the length of the single section, while the rejection depth is set by the number of sections.

Moreover, we have implemented this pump filtering strategy on both a micro-ring based entangled photon-pair source and an integrated entangled photon-pair generator. These devices show premising spectral characteristics and will be tested extensively in the next chapter.

Chapter 4.

Silicon Based Integrated Quantum Photonics

Quantum Information Science (QIS) exploits the fundamental properties of quantum physics to code and manipulate quantum states. QIS is regarded as the most promising pathway towards disruptive technologies, providing major improvements in processing capabilities and communication security [96, 97]. Yet, practical implementations, such as quantum key distribution systems or quantum processors, require a large amount of compatible building-blocks [98, 99, 100, 101]. Integrated photonics based on parametric sources ($\chi^{(2)}$ or $\chi^{(3)}$) provides an effective and reliable platform for realizing advanced quantum communication systems based on both linear and nonlinear elements [102, 103, 104, 105, 106, 107, 108].

In this chapter, we qualify a wavelength multiplexed entangled photon-pair source fully compliant with fiber telecom networks and semiconductor technology. We use demultiplexed entangled photon-pair sources that separate the pairs on-chip. To do so, we use all the structures designed described in chapter 2 with the filters of chapter 3. The increment in integration complexity requires proper changes in dimension to achieve wavelength alignment between the components. Proper interconnection and tapering is also fundamental to reduce the losses coming with each structure. The rejection filter cascading strategy has already been shown in chapter 3, showing large rejection [15]. The next step consists in integrating the entangled photon-pair comb source and entangled photon-pair generator which are described in section 2.1. The comb source outputs a multiplexed comb of photon pairs that must be manipulated outside the chip. The photon-pair generator demultiplexes those pairs into channels that can be sent directly to the user or used as a heralded single photon source.

All previous realizations face a crucial limitation as soon as on-chip suppression of photonic noise is concerned due to the substantially higher pump intensity compared to that of the photon-pairs. This operation is typically externalized, using fiber or bulk optical components, and removing the benefit of both the compactness and stability of the whole system [109].

In this chapter, a transmission spectrum is first performed to ensure alignment and assess the losses of the circuit. Then, nonlinear light is generated by pumping the ring resonator cavity. A spectral and a correlation measurements are performed to ensure that the generation process is indeed Spontaneous Four-Wave Mixing (SFWM). Separable state can be used as a heralded single photons. In this case, the source

generates idlers that, when detected, herald the signal photons. For this application, no multi-pairs should be generated as more than one photon is heralded. To quantify this, we can evaluate the normalized second order correlation function $g^{(2)}$. It allows to extract the probability of a multi-pair events. To check the versatile nature of the design, spectral characterization of the nonlinear light is performed. A joint spectral amplitude measurement can check the spectral correlation between the signal and idler photons.

Finally, we proceed to the qualification of energy-time entanglement carried by the photon-pair using a standard Franson-type interferometer [220]. We will characterize two-photon interference fringes over eleven complementary channels pairs spanning from both S and C telecom bands [221] along with a coincidence-to-accidental ratio. Such entanglement can be used directly on chip as a fully functionalized and scalable entanglement supplier [222]. As this measurement is very sensitive to residual photonic noise, it is a good criterion to evaluate the pump rejection. We will also see if the time-bin entanglement of the pairs is preserved even manipulated on-chip.

Qualifying quantum correlations in a stricter way, *i.e.* by means of a Bell-type entanglement witness [14], is essential for a large variety of quantum applications such as secret key distribution [223], superdense coding [224], teleportation [225], sensing [226], and computing [100]. Such an entanglement characterization remains unanswered whatever the exploited integration platform (silicon, III-V semiconductors, lithium niobate) for stand-alone devices embedding a pump-rejection solution. Yet, the degree of entanglement could be reduced by excess background noise or Raman photons induced inside the on-chip pump filter itself.

4.1. Spectral & correlation characterization

4.1.1. Micro-ring based entangled photon-pair source

We consider the entangled photon-pair comb source designed in the previous chapter in section 3.6. The source structure can see seen in figure 4.1, with the different components highlighted. A Modal Add-Drop device was added between the cavity and the filter to access the pumped resonances and ease spectral alignment, see figure 4.1. Without it, we can only guess where the desired ring resonance is in the filter, making it tricky to locate. The resonances exploited for the experiments are shown in figure 4.2a.

The cavity can be tested by measuring the *singles* (single photons) generated by the SFWM process inside of the ring. This is measured using a Superconducting Nanowire Single-Photon Detector (SNSPD) ID281 from ID Quantique and a motorized Yenista XTM-50 filter with a bandwidth of 400 pm. This combination is equivalent to a very high sensitivity spectrometer. The singles are generated in the resonances of the cavity located symmetrically to the pump frequency, see figure 4.2b. The decreasing rate as the distance from the pump increase is due to the grating coupler transmission. It is mostly flat when normalized. The pump can be seen through the Bragg filter. This is invariant to the design of the filter and is most likely due to reflection in the substrate

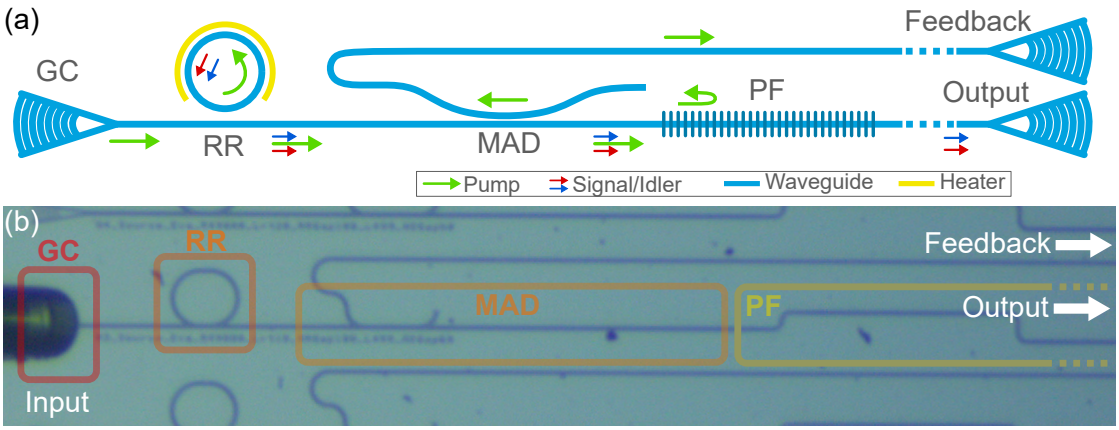

Figure 4.1.: (a) Schematic of a photon-pair comb source and (b) microscope image of the comb source, with highlights of the grating coupler (GC) in red, ring resonator (RR) in dark orange, the modal add-drop (MAD) device in light orange, and the pump rejection filter (PF) in yellow. Light is injected from the left via a single-mode fiber (visible here above the GC) and collected on the right (outside of the picture).

and scattering[1]. The effective rejection of the pump filter in this case, with a closure of the bandgap strategy (CBG) (section 3.4), is 85 dB. Additional protection could be implemented to reduce the residual pump. Absorbing materials, metals, or out-of-plane scattering gratings could be added on or around the waveguides to help. But since residual light level is 15 dB stronger than the signal, we can easily remove it during the de-multiplexing stage.

As shown in figure. 4.2a, the measured rejection of the filter is 60 dB (dark-blue curve) which corresponds to the noise floor (red dashed line) of our detector and not the real rejection value. This measured rejection rate is consistent with state-of-the-art realizations for single-chip pump filters [7, 8, 9].

To make sure we generate time correlated photons, a time correlation measurement is performed. Looking at the delay statistics between photons reveals a peak of coincidences. This corresponds to the pairs generated simultaneously by the conversion of two pump photons. Since they are entangled in energy-time, we can measure their travel time difference. It is constant and set by the length difference after demultiplexing. In other words, it is the time of flight difference since they were separated.

A Continuous Wave (CW) tunable laser is used to pump the ring. It is cleaned from the Amplified Spontaneous Emission (ASE) with a passband filter Yenista XTM-50 (50 dB rejection), then a Polarization Controler (PC) aligns its polarization with a Transverse-Electric (TE) mode grating coupler. A power detector is used to monitor the feedback port. At the output, a Beam Splitter (BS) and two Tunable passband Filter (TF), one for each wavelength, are used to send the signal and idler to different single-photon detectors (see figure 4.3). Then, a Hydra Harp Time-to-Digital Converter (TDC) allows

[1]This is also suggested by the increased number of photons measured when misaligned with the output grating coupler.

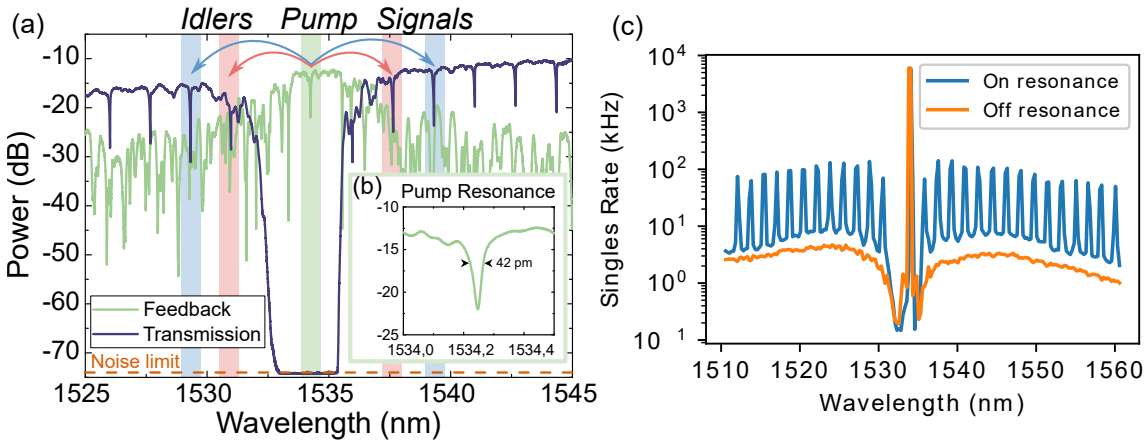

Figure 4.2.: (a) Spectra of the transmission and feedback ports of the comb source with a CBG filter. The pumped resonance is highlighted in green as well as the first available pair of signal/idler in red, and second pair in blue. (b) Spectrum of the pumped resonance showing a Full Width at Half Maximum of 42 pm. (c) Spectrum of the nonlinear emission of the source when pumped, the generation happens mostly in the cavity resonances, a background noise is also generated due partially to the rest of the structure where nonlinear processes can also happen. The pump is still visible, considering the input power and the losses, and an effective rejection of ∼85dB is found.

to compare the arrival times of each detection. Note that the real coincidences rate is 4 times higher because of the not-optimized demultiplexing strategy. Indeed, it is only when a single enters the signal TF and an idler enters the idler TF simultaneously, that we get a detection. All other cases create noise. But it has the advantage to work for all resonant wavelengths and is easy to reconfigure to other resonances. All the set-up components are fibered, no free space optics is used, see figure 4.3. The sample is stabilized in temperature with a Peltier stage set to 20°C. The whole spectrum can be shifted by changing the chip temperature with a Peltier system.

We can generate a histogram by selecting the first available resonance-pairs from the pump. This delay statistic shows the coincidence peak but also the background noise, see figure 4.4. The Coincidence-to-Accidental Ratio (CAR) gives us a direct insight into the pump rejection level. This is the ratio between the poissonian statistical noise and the coincidence peak.

The coincidence peak stands as a signature of the simultaneous emission of the photon pairs. The width of the coincidence peak is given by the convolution of the coherence time of the photons ($\sigma_{coherence} \sim 110$ ps), of the detectors' timing jitters ($\sigma_{jitter} \sim 100$ ps), and of the time resolution of the TDC ($\sigma_{resolution} \sim 1$ ps). The full width at half maximum of the coincidence peak is about 160 ps, which is consistent with $\sqrt{\sigma^2_{coherence} + \sigma^2_{jitter} + \sigma^2_{resolution}} \sim 150$ ps.

Tuning of the cavity to get the best pair rate output is not trivial. If we tune the pump wavelength over the resonance, we see an optical bistability [227, 228, 176]. This is due

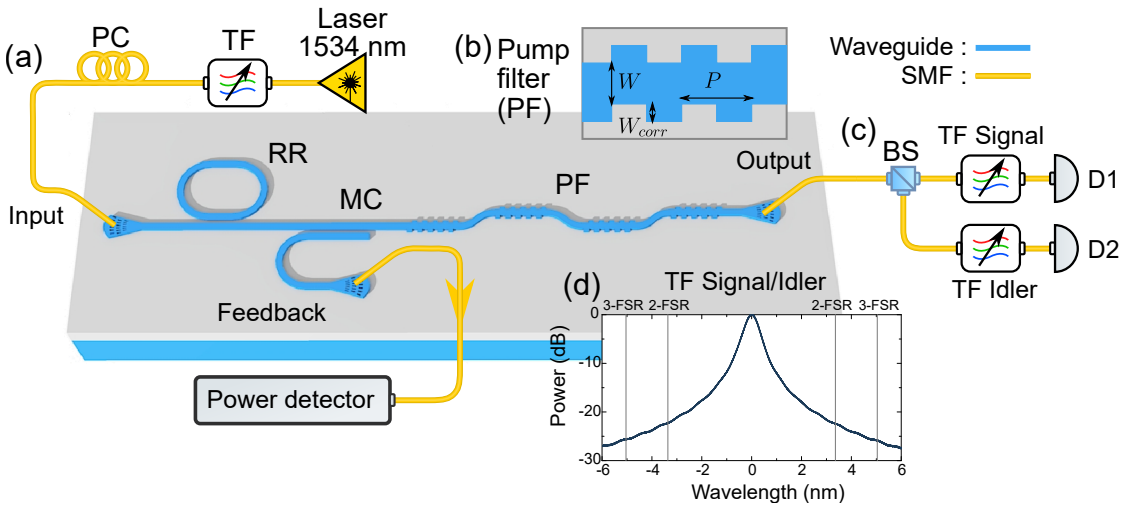

Figure 4.3.: Schematics of the experimental setup. (a) Input laser with associated filter (TF) rejecting the amplified spontaneous emission and a polarization controller (PC). Laser light is injected in the ring resonator (RR) through the grating coupler, and then propagates to a modal coupler (MC) and through the integrated pump filter (PF). (b) Schematic top-view of one of the cascaded Bragg filters (BF) composing the PF. The output of the chip is connected to a coincidence setup (c) with a beam splitter (BS) and bandpass filters to demultiplex signal and idler photons (TF signal/idler). (d) Spectrum of the signal and idler filters, which exhibit 22 dB and 25 dB rejection for the 2-FSR shift and 3-FSR shift configurations, respectively. All the setup is fibered using single mode fibers (SMF) for the experiments.

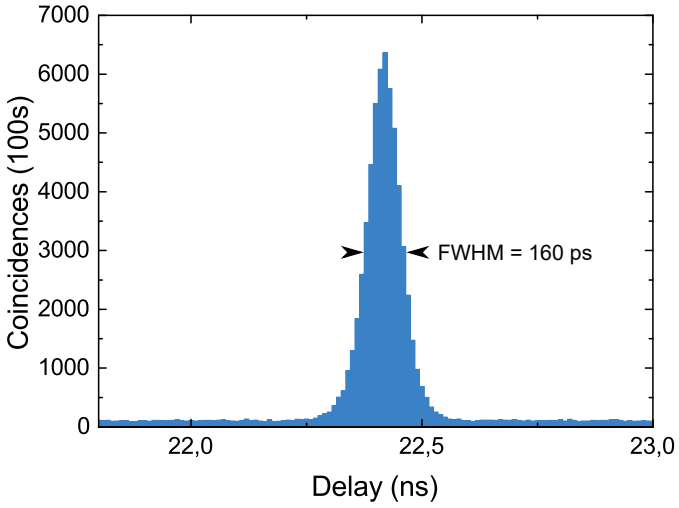

Figure 4.4.: Histogram of the arrival delay statistic between D1 and D2 for the 2-FSR resonances (see figure 4.3).

to free-carrier absorption effect inducing a thermal shift of the waveguide material index

values. The closer the laser is from the center of the resonance the stronger this effect becomes. Accordingly, the rate of photon pair generation changes with a hysteresis, see figure 4.5. Depending on the direction of the scan, the resonance shift changes too. The stronger the pump, the more extreme the hysteresis is. For low powers, the difference is almost negligible when aligning spectrally the ring resonance with the pump laser. But at high power, the bistability effect limits the ability to properly excite the cavity with the pump laser. To get an efficient photon-pair rate, the pump wavelength has to be closed to the cutoff, which allows fluctuations in the ring to make the pumping jump.

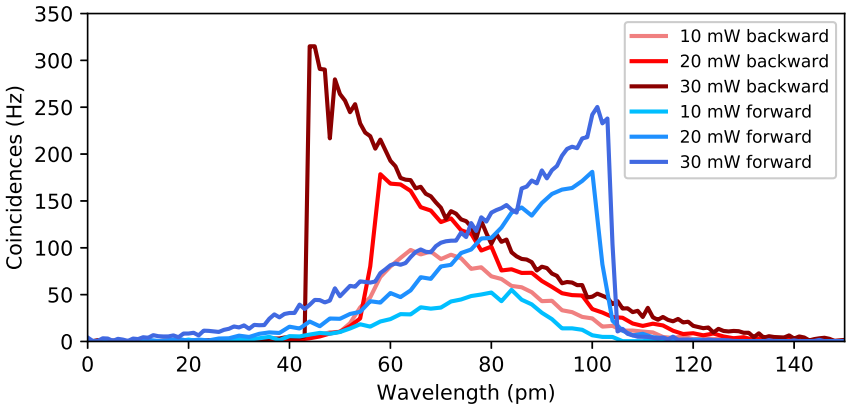

Figure 4.5.: Coincidence rates between D1 and D2 as a function of the pump wavelength at different power settings (external). The internal power can be estimated to -10 dB smaller, by increasing (forward) or by decreasing the wavelength (backward). A clear hysteresis is visible between the forward and backward measurements that increases with power.

We study more in depth the closest resonances from the pump, *i.e* with a paired channels distant by two and three Free Spectral Range (FSR). They may suffer preferably from the pump photonic noise. The related wavelength for the 2- and 3-FSR shift are highlighted in figure 4.2a. The pump is set to $\lambda_p = 1534.2$ nm (C band) with an input power of 2.8 mW after the polarization controller (figure 4.3a). Examples of a typical coincidence histogram is shown in figure 4.4a, where a coincidence peak emerges over a small background of accidental counts.

We now consider the internal brightness of the ring. The overall losses of the setup, including the input/output and propagation losses of the chip, are outlined in Table 4.1. The single count rates in the coincidence experiment are of $4 \cdot 10^4$ signal counts per seconds and $3 \cdot 10^4$ idler counts per seconds, with 20 dB and 27 dB of losses, respectively. Coupling coefficient of the ring was evaluated using the spectral signature of the resonances. With a finesse of 39.3 and losses of $\alpha = 0.16$ cm^{-1}, we found a coupling coefficient $k \simeq 0.38$ [176] The overall coincidence peak spreads over several time bins and shows an average of 120 coincidences per second over a time window of 400 ps, see figure 4.4. With all those figures, we can infer an internal photon-pair rate of

Table 4.1.: Summary of the losses experienced by the 2-FSR photon pair

Components	Signal (dB)	Idler (dB)	Pair (dB)
Ring coupling	4.2 ± 0.2	4.2 ± 0.2	8.4 ± 0.4
Integrated filter	3 ± 0.1	$(3+5) \pm 0.1$	11 ± 0.2
Grating coupler	5.5 ± 0.2	6 ± 0.2	11.5 ± 0.4
Beam splitter	3 ± 0.2	3 ± 0.2	6 ± 0.2
Bandpass filters	2 ± 0.5	2.5 ± 1.5	4.5 ± 2
SSPD	2 ± 0.2 ($\sim 60\%$)	3 ± 0.2 ($\sim 50\%$)	5 ± 0.4
Total	19.7 ± 1.4	26.7 ± 2.4	46.4 ± 3.8

$(4.2 \pm 0.2) \cdot 10^6$ pairs/s. The ring shows resonances of about 42 pm width and the power in the ring is estimated from the transmission measurements to be 0.9 mW. We estimate an internal brightness of ~ 500 pairs/s/mW^2/MHz. Due to the non-deterministic wavelength separation induced by the beam splitter (figure 4.3) and the spectral filtering ensured by the bandpass filters in each arm, the rate at the output of the chip is 4 times higher, *i.e* about 480 pairs generated per second for each channel pair. Let us stress that this coincidence rate, stands among the best values reported for photonic devices embedding several key components [11, 229, 230, 231, 102, 232, 233]. In comparison, similar realizations suffer from low coincidence rates due to prohibitive losses, preventing any further analysis of entanglement [11, 10]. Note that the other interesting feature reported in Table 4.1 is the 2 dB-loss for the pump filter which is almost only due to propagation. This low value associated with a high rejection level and a narrow bandwidth shows that the proposed pump filtering strategy is a promising basic brick for the realization of next generation quantum photonic circuits.

4.1.2. Integrated entangled photon-pair generator

The experimental set-up for the photon-pair generator is similar to the comb source one (figure 4.3). A tunable CW pump laser (Tunics EXFO or Tunics Yenista HP) is cleaned from its ASE. Then a PC aligns the polarization with the Grating Couplers (GC). Three outputs are measured simultaneously. The feedback port monitors the spectral alignment of the ring with the pump and the transmission levels. Signal and idler are filtered externally with a standard International Telecommunication Union (ITU) Dense Wavelength-Division Multiplexers (DWDM) to select a pair of resonances and reduce the photonic noise. Due to the large bandwidth of the filter, the 1 and 2 FSR resonances from the pump are very lossy. The usable pairs are from 3, 4, and 5 FSR, see table 4.2.

To make sure the ring resonator is working and that the circuit does not affect the pairs, we perform a coincidence measurement. Each pair of channels is probed separately with two single-photon detectors ID230 (~ 20 % eff.) and a TDC Hydra Harp. We see a clear peak for each one with different rates due to the transmission variations, see figure 4.7. The CAR for 3, 4, and 5 FSR are equal to 84, 120, and 100, respectively. Then, the photon-pair rate is also investigated as a function of power propagating in the waveguide. The coincidences increase quadratically with the pump power until about

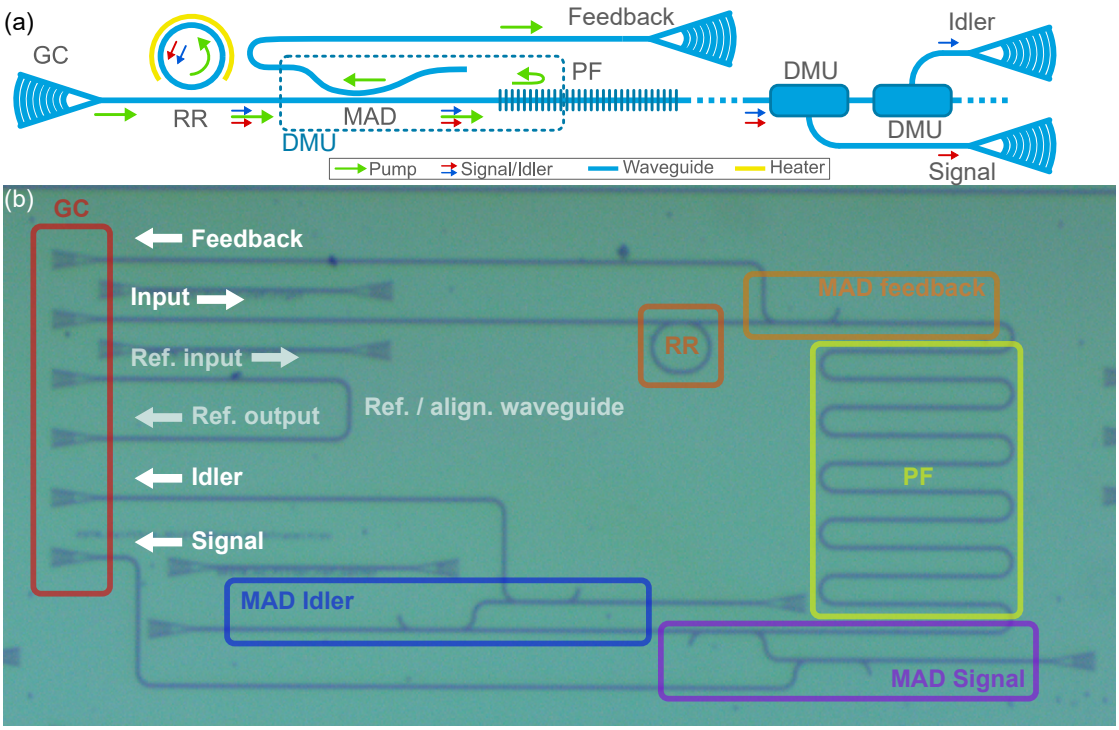

Figure 4.6.: (a) Schematic of the entangled photon-pair generator and (b) optical microscope image of the photon-pair generator, with highlights of the grating couplers (GC) in red, ring resonator (RR) in dark orange, the modal add drop (MAD) device feedback in light orange, the pump rejection filter (PF) in yellow, MAD idler and signal in blue and purple, respectively. Light is injected and collected on the left via a fiber array (no visible here). The use of each GC in indicated next to its waveguide.

2 mW in the waveguide. At which point the Two-Photon Absorption (TPA) process in silicon starts having a detrimental effect. Then the rate increases linearly with the power, but it is still advantageous to go slightly beyond. Whenever possible, we will be around 3 mW of injected power, which provides an increase in pair rate while keeping the CAR around 100. The CAR, on the other hand, decreases exponentially versus the power, in good agreement with results reported in previous works [234].

4.2. Photon statistical characterization

There are three types of photon statistics: Poissonian, super-Poissonian, and sub-Poissonian [69]. They correspond to different types of light generation, coherent (*e.g.* LASER), chaotic (*e.g.* thermal source), or quantum (*e.g.* single photon light source), respectively, see figure 4.8. Different laws describe the probability of having n photons per time interval in the case of monochromatic sources, see table 4.3. The poissonian statistics are characterized by a constant intensity $I(t) = C^{te}$, whereas the thermal one

FSR	λ_{res} (nm)	ITU channel	λ_{ch} (nm)	$\Delta\lambda$ (nm)
-5	1535.812	52	1535.82	-0.008
-4	1537.379	50	1537.4	-0.021
-3	1538.946	48	1538.98	-0.034
-2	1540.513	46	1540.56	-0.047
-1	1542.08	44	1542.14	-0.06
0	1543.647	42	1543.73	-0.083
1	1545.214	40	1545.32	-0.106
2	1546.781	38	1546.92	-0.139
3	1548.348	36	1548.51	-0.162
4	1549.915	34	1550.12	-0.205
5	1551.482	32	1551.72	-0.238

Table 4.2.: Wavelengths of the pump (0 FSR) and the 5 closest pairs or channels with theirs associated ITU channel and distances from the resonances. All distances are smaller than 0.35 nm, so none are at the edge of a channel.

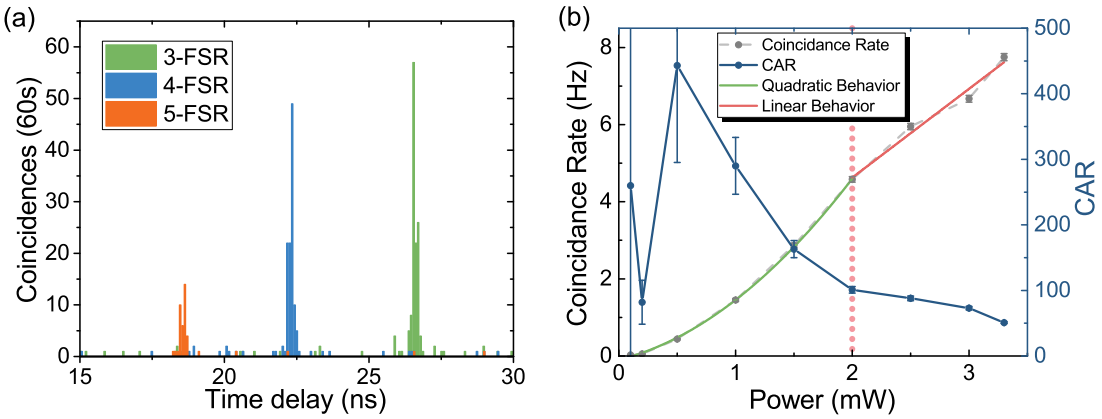

Figure 4.7.: (a) Coincidence histogram of the three available resonances in the photon-pair generator. (b) Plot of the coincidence rate and CAR of the 3-FSR channel pairs as a function of the on-chip power. The rate starts by increasing quadratically before been slowed by two-photon absorption (TPA) limiting its growth. The CAR decreases exponentially with the power of the pump due to the rapid increase in background noise.

have fluctuations [235], resulting in bunching of photons. Finally, non-classical photon sources sends indistinguishable photons at a fixed rate.

The fluctuations in the intensity of a chaotic source has a short memory. This means that these fluctuations appear if the detection time is shorter than the coherence time of the light. Otherwise, the photon statistics is poissonian. Similarly, true a single photon sources never sends two photons at the same time. This implies that the system has anti-correlations. This is not the case in a poissonian source, as photons are sent completely independently of the others.

	Super-Poissonian	Poissonian	Sub-Poissonian
Type	*Thermal*	*Coherent*	*Quantum*
P_n	$\frac{\langle n\rangle^n}{n!}e^{-\langle n\rangle}$	$\frac{1}{(\langle n\rangle+1)}\left(\frac{\langle n\rangle}{\langle n\rangle+1}\right)^n$	1 if $n=\langle n\rangle$ else 0

Table 4.3.: Probability distributions of having n photons in a random bin for an average number of photon $\langle n\rangle$.

Here different correlation properties can be observed and where the quality of optical sources depends on it. It is interesting to evaluate the normalized second order correlation function, which represents the intensity-based time correlations of light:

$$g^{(2)}(\tau) = \frac{\langle I(t)I(t+\tau)\rangle}{\langle I(t)\rangle^2}. \tag{4.1}$$

The brackets denote the average over times t. This function is constant for a monochromatic coherent light source $g^{(2)}(\tau) = 1$. For a chaotic source, it is $g^{(2)}(\tau) \geq 1$, the normalized first order correlation function. For a non-classical light source $g^{(2)}(\tau) \leq 1$.

This criterion is a way to identify which statistics one is dealing with. In general, $g^{(2)}(\tau) \leq 0.5$ is required to claim a single-photon state [236], see figure 4.8d. It can be measured with a Hanbury-Brown and Twiss (HBT) type experiment [70]. After splitting light using a 50/50 BS, intensity correlations are recorded at the two BS outputs as a function of the relative delay between the photons of each pair. However, note that this is true only for monochromatic light when resolving the fluctuations in intensity (number of photons). When using single photon detectors, only light with low $\langle n\rangle$ can be properly studied. The average photon number can be increased when using a multi-photon detector (detector giving the number of photons in the detection) depending on the maximum detectable number of photons.

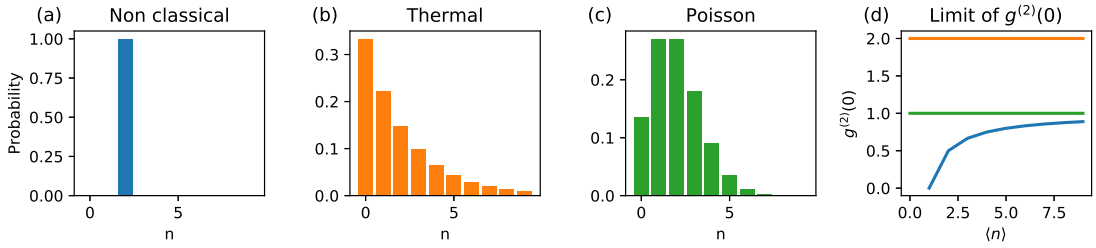

Figure 4.8.: (a), (b), and (c) are probabilities of having n photons when looking at a average number of photons $\langle n\rangle = 2$. (d) Plot of the value of the normalized second order correlation function at zero delay $g^{(2)}(0)$ for increasing the average number of photons. Note that the non-classical $g^{(2)}(0)$ is null only at $\langle n\rangle = 1$. [237]

Developing a true single-photon source [4] is technologically challenging and suffers from inherent defects as the emitted wavelengths are usually not compatible with telecom bands and due to a lack of scalability. On the other hand, we can emulate such a source

by heralding a photon from a parametric source. If a pair of photons is created at the same time, one photon can be used to announce the other. The proper non-classical statistics is created by selecting when light is created and arriving at the output. So, an extra condition is added: the detection of the heralding photon. The arrival statistics of photons is completely different. Naturally, each signal/idler beam exhibits a thermal statistic ($g^{(2)}(\tau) \geq 1$) as a result of the amplification of vacuum fluctuations [237]. However, once heralded, anti-correlations can be measured at zero delay.

We have characterized the statistical properties of photon pairs created by pumping the ring resonator. A photon pair source can be used as a heralded single photon source, providing that the pair is in a separable state. This is the case in a ring resonator when we use a pump with a large enough bandwidth compared to the resonance bandwidth [238]. The circuit then acts as a heralded single photon source, the signal photon being detected to announce the idler. However, this is true only if we get pairs of photons, no double pairs, nor more, simultaneous photons. In those cases, a multi-photon state is heralded, the output no longer is a single photon. We can evaluate the number of multi-pairs but also the heralding efficiency of the circuit. The ring produces pairs with a state:

$$|\phi\rangle_{\mathrm{II}} = \sum_{n=0}^{\infty} c_n \, |n\rangle_s \, |n\rangle_i \, . \tag{4.2}$$

So that the state of light after the heralding is

$$|\phi\rangle = \underbrace{c_0 \, |0\rangle}_{\text{removed by heralding}} + c_1 \, |1\rangle + \underbrace{c_2 \, |2\rangle + c_3 \, |3\rangle + ...}_{\text{unwanded}} . \tag{4.3}$$

Here, each of the terms is a Fock state with its corresponding coefficient. The indices correspond to the number of photons. The vacuum state $|0\rangle$ is removed by the heralding process as we only consider the photons when heralded. Then, we want to investigate the probability to have any multi-photon state.

The $g^{(2)}(\tau)$ function is measured using a beam splitter and two SNSPD (Detection efficiency $\eta_{det} \sim 60$ %). Any double trigger in the idler arm (D2 and D3) can then only be due to multi-photons states, see figure 4.9. For a perfect on-demand single photon source, $g^{(2)}(0) = 0$, meaning that when a photon is detected in one of the detector, nothing is detected in the other-one.

However, we must differentiate it from a heralded photon source. Such source outputs a single photon only when a heralding photon is detected. Then the correlation function becomes $g_h^{(2)}(\tau)$, which is conditioned by the measurement of an heralding photon.

When detector D1 clicks, then we perform the correlation measurement. The detector D2 is then used as a *start* (or t_0) for a coincidence measurement with D3. The detector D3 is left in a free running state until another trigger from D1 resets the system (or the time exceed 100 ns). During the 6 hours of experiment, the TDC records all events. Then, in a post analysis using a python script, coincidences are extracted. To avoid any

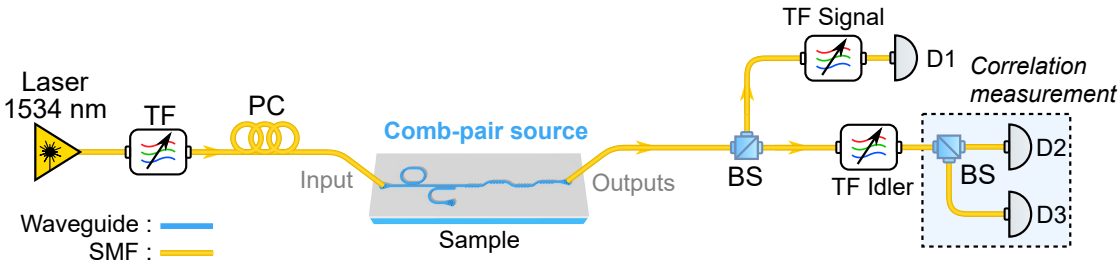

Figure 4.9.: Schematics of the experimental setup. An input laser with an associated filter (TF) rejecting the amplified spontaneous emission and a polarization controller (PC) is used. Laser light is injected in the comb-pair source. The output of the chip is connected to a corration setup, the signals are sent to D1. The idlers are sent to a beam splitter (BS) a detector at each output, D2 and D3. D1 is used as heralding for the detection in D2 and D3. All detector are free running SNSPD with detection efficiency around 60%.

artifact in the analysis, an *all* coincidence algorithm is chosen [239, 240]. It records all *stop* events in a time window after the *start*.

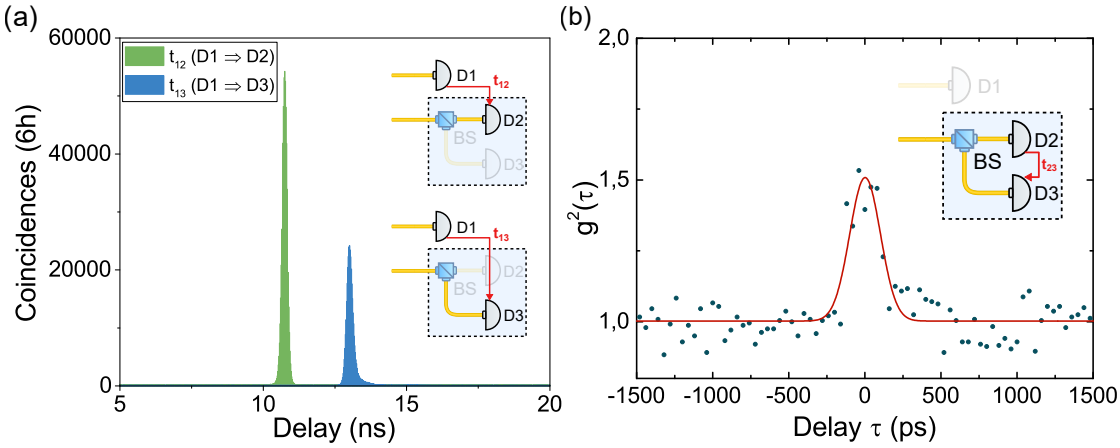

Figure 4.10.: (a) Coincidence histogram between D1 and D2 or D1 and D3, setting the time for the experiments. (b) Plot of the second order correlation function $g^{(2)}(\tau)$ between the detector D2 and D3, a peak can be seen above one indicating the chaotic nature of the pair generation process.

First, we simply do a correlation measurement between D1 and D2/D3. This is to make sure we have a peak of pairs and to set the delays as respective t_0 (figure 4.10). If we look only at the correlations between the D2 and D3 detectors, we see a thermal statistic of the $g^{(2)}(\tau)$, see figure 4.10. We found a peak of $g^{(2)}(\tau) \simeq 1.5$ showing a clear thermal signature even if not going up to 2 [241]. This could be due to a second mode being measured at the same time as:

$$g^{(2)}_{thermal}(0) = 1 + \frac{1}{M}, \tag{4.4}$$

with M the number of measured thermal modes. A possibility is also that the poissonian background noise reduces the peak. But the most likely is that we are in between the poissonian and the thermal regimes. This is because the time jitter of the detector ($T_{\text{jitter}} \approx 150$ ps) and the photon coherence time ($T_{\text{coherence}} \approx 200$ ps) are of the same order. When we introduce the heralding condition, the correlation function $g_h^{(2)}(\tau)$ is completely different.

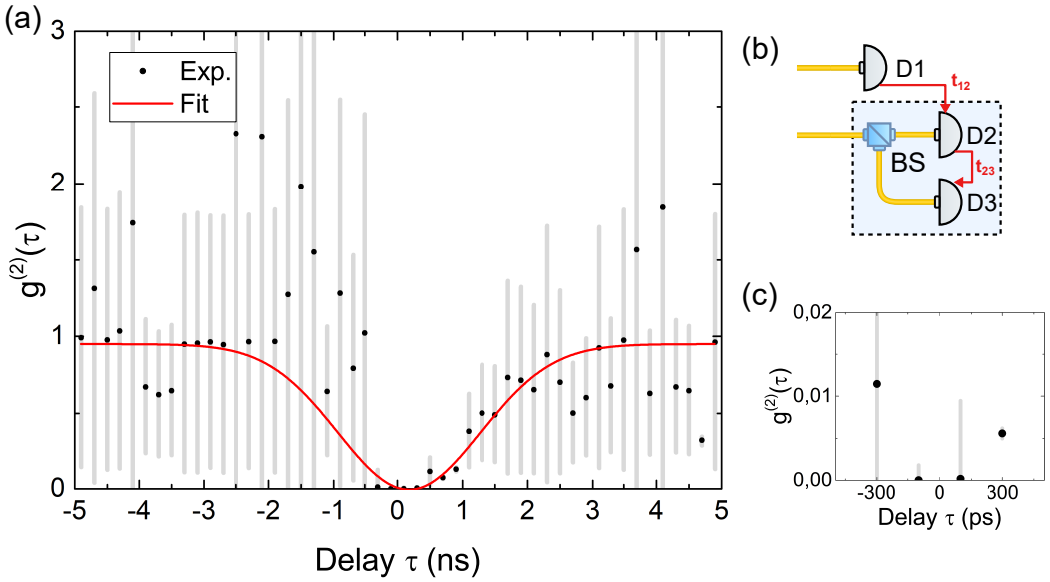

Figure 4.11.: (a) Plot of the heralded second order correlation function $g_h^{(2)}(\tau)$ between (b) the detector D1, D2, and D3, dip appears at zero delay showing the non-classical nature of the photon been generated, so only single photons are been sent in each channels. (c) Zoom around the zero delay of the curve (a).

To construct the $g_h^{(2)}(\tau)$ function, we need to count the number of triple detections done by the system, *i.e.* every heralded double. A triple coincidence is counted when a photon has been detected by D2 in the peak at $t_{12} = 10.8$ ns after a D1 trigger, then we wait for a photon in D3. If it arrives with a delay of $t_{13} = 13.1$ ns, it is counted as a triple coincidence with a delay $\tau = 0$ ns. If it arrives later or earlier, it has a positive or negative delay, respectively.

The $g_h^{(2)}(\tau)$ function is then estimated as [241]

$$g_h^{(2)}(t_{12}, t_{13}) = \frac{R_{123}(t_{12}, t_{13})}{r(0)^3 g_{12}^{(2)}(t_{12}) g_{13}^{(2)}(t_{13})} \tag{4.5}$$

where $r(0)$ is the first-order correlation function, $g_{12}^{(2)}$ and $g_{13}^{(2)}$ are the second-order cross-correlation functions which are the ratio $R_{coinc}(\tau)/R_{acc}(\tau)$ of the coincidence rates over the accidental rates. Simply considering $g_h^{(2)}(\tau) = g_h^{(2)}(0, \tau)$, with τ the delay between the trigger of D2 and D3. After measuring the histograms between D1-D3, D2-D3, and

D1-D2-D3, we can use equation 4.5 and plot the data, see figure 4.11. We can fit the data with a bounded Gaussian. We get a $g_h^{(2)}(0) \simeq 2.52 \cdot 10^{-5} \pm 1.86 \cdot 10^{-3}$, which is much lower than 0.5 and indicates the non-classical nature of the generation process. This value shows that the number of double pairs, which should be the main limitation of the $g_h^{(2)}(0)$, is in fact negligible. The large error rate on the measurement is due to the small amount of triple events recorded (on average 1.56 per 200 ps bin over the 6 hours). Thus, this should be considered as a best case. A more conservative value can be found by using the photon number probabilities.

Time interval $\Delta\tau$	200 ps	1 ns
Events N_{12}	133413	339722
Events N_{13}	395786	597637
Events N_{123}	1	17

Table 4.4.: Summary of the events measured over 6 hours with $N_1 \simeq 4.3 \times 10^8$ triggers of D1.

We can construct the statistics of generated photons using the number of events. Once heralded, the probability to get a single photon is $P_1 \approx (N_{12} + N_{13})/N_1$ (N_1 is the number of detections in D1 over the 6 hours), since we know that the number of multi pairs is negligible. We can also approximate the probability to get heralded pairs by $P_2 \approx N_{123}/N_1$. Since $g_h^{(2)}(0) \approx 2P_2/P_1^2$ when P_1 is small, we get $g_h^{(2)}(0) \simeq 3.07 \cdot 10^{-3}$ from the values shown in tables 4.4 and 4.5. Most of the time, when a heralding photon is detected, the source outputs nothing. This is due to the low heralding efficiency $\eta = (N_{12} + N_{13})/(N_1\eta_{det}) = 0.15\%$, with η_{det} the detection efficiency of the detector, due to the poor transmission. But when we get an output it is almost always a single photon. There are 6 orders of magnitudes between the chance to get a single photon and getting any other photon state (2, 3, etc. photons).

Properties	Value
N_1	4.3×10^8
P_0	0.999
P_1	1.23×10^{-3}
$P_2 + P_3 + ...$	2.33×10^{-9}
Heralding eff. η (%)	0.15
$< n >$ per bin	10^{-5}
Bin size (ps)	200
Int. time (s)	21600
$g^{(2)}(0)$	3.07×10^{-3}

Table 4.5.: List of the parameters extracted from the measurements.

4.3. Joint spectral amplitude measurement

When a pair of photons is generated, they have spectral correlations. Some pairs of wavelength (λ_i, λ_s) are more likely than others. These correlations determine the level of entanglement of the pair. In equation 1.40, the two photon state $|\psi\rangle_{\text{II}}$ is made up of the Biphoton Wave Function (BWF) $\phi(\omega_i, \omega_s)$, which depends on the frequency of both photons of the pair, seen in section 1.1.5. The probability for having a pair (ω_i, ω_s) is then $|\phi(\omega_i, \omega_s)|^2$, called the Joint Spectral Amplitude (JSA). As mentioned in section 1.1.5, if the BWF is the product of two functions, the pair is not entangled. This can be translated into a more circular shape of the JSA in the (ω_i, ω_s) space, in our case. On the other hand, an elongated JSA indicates an entangled state. This can be understood as the following: in a (an anti-)diagonal distribution, knowing the x coordinate allows to deduce the y position, thus there are correlations between the two. While in a circular distribution, knowing a x coordinate does not provide information on the exact y position.

The JSA of a ring resonator can be simulated [16] by making some approximations. The two possibilities are that the ring pumped resonance sees a white light source or a monochromatic one. Using Lumerical MODE solution [172], the properties of the ring waveguide are investigated at 1541 nm (pump wavelength), we get an effective index of 2.537, a group index of 4.002, and a dispersion of 1856 ps/nm/km, see figure 4.12. These values can be used to simulate the ring properties like the FSR, $\omega_{FSR} = 2\pi c/(n_g L)$. We also need the wave-vectors to compute the JSA. For the pump, it is $k_p = \omega_p/\nu_p$, with $\nu_p = c/n_{eff}$ the phase velocity. For the signal and idler, it can be approximated to $k_{i,s} = k_p \pm N\omega_{FSR}/\nu_p + (N\omega_{FSR})^2 D_{GVD}$, where N is the number of FSR from the pump, and D_{GVD} is the group velocity dispersion. It can be deduced using $D_{GVD} = -D\lambda_p^2/(2\pi c)$ with D the dispersion from figure 4.12c.

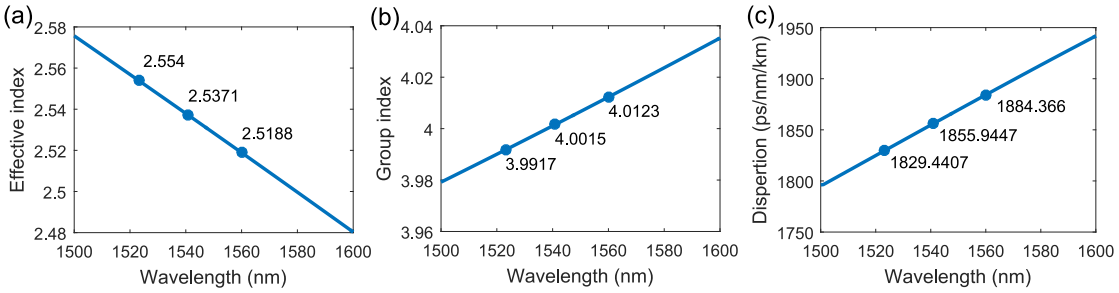

Figure 4.12.: Properties of the ring waveguide as a function of wavelength, Silicon-On-Insulator (SOI) 600 nm wide with air cladding. (a), (b), and (c) are the effective index, the group index, and the dispersion, respectively. On each one the values at the idler, pump, and signal wavelengths are written.

We can now use the model from [16] to simulate the JSA of the ring for two pump types. The pump can be a pulsed or a CW, with a large and a narrow spectral widths, respectively. The pulse pump acts as a white source for the ring if pulse duration is short enough ($T_{pulse} \simeq 5$ ps) compared to the resonance bandwidth ($\Omega = \pi c \Delta\lambda/\lambda_p^2$).

In that case, we get uncorrelated photons from each pair, see figure 4.13a, spectral dependency with the signal (idler) can be deduced from a single idler (signal) as the pump is broadband and any "pump wavelength" in the resonance could have generated the pair. A CW laser can be approximated by a very long pulse ($T_{pulse} \simeq 5$ ns), which is well defined spectrally. This creates a correlation between the two photons, *i.e.* entanglement, see figure 4.13b. As now the pump is fixed, knowing precisely the wavelength of a signal (idler) allows using the conversation of energy to deduce the properties of its sister idler (signal).

A criterion to characterize the entanglement of the state is the purity $P = K^{-1}$, where K is the Schmidt number. This is not the case in general but true in this case of parametric conversion. The Schmidt number is defined as $K = (\sum_n e_n)$ where e_n are the eigenvalues of the reduced density operator. We get as expected a high purity 96% ($K = 1.037$) for the pulse pump and a low purity of 0.01% (high Schmidt number $K = 106.8$) for the CW pump, indicating a high entanglement of the photon pairs. Finally, another approach to estimate the JSA is to directly measure the wavelength of the resonances and convert them to the k-space. In this case, only the group index must be simulated. This provides very similar JSA and Schmidt number values.

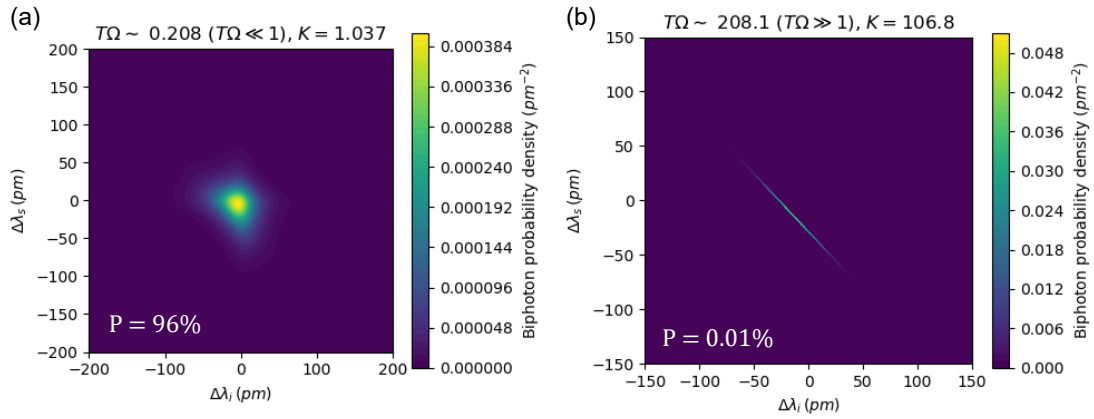

Figure 4.13.: Simulated JSA for, (a) a short pulse approximation with 5 ps pulse duration, (b) a long pulse approximation (CW) with a 5 ns pulse duration. The purity P and Schmidt number K are indicated on each plot, as well as the approximation condition $T\Omega$ for the product of the pulse duration and resonance width.

To probe the BWF, we can use the Stimulated Emission Tomography (SET) technique [238]. Instead of relying on spontaneous emission of pairs to probe the BWF, as each pair must be spectrally analysed separately, the SET exploits the higher efficiency of the stimulated four-wave mixing process. A seed laser is injected in the sample with the pump: this forces photon generation at this wavelength (slice of the BWF) that can be then spectrally analyzed.

The setup was constituted of two CW Tunics lasers for the pump and seed signals. After each, a Yenista XTM-50 filter were used to clean them from the ASE. PC where

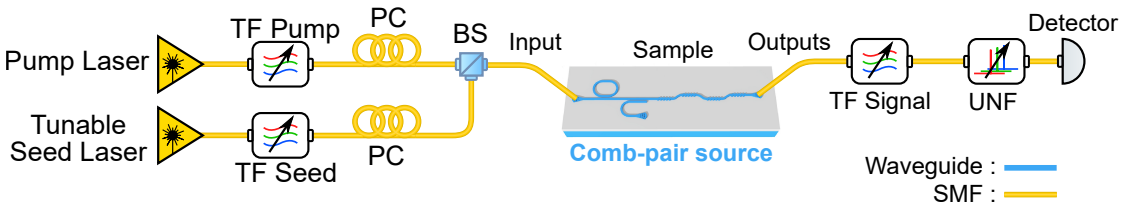

Figure 4.14.: Schematics of the experimental JSA measurement setup by SET. The pump and seed laser are cleaned with filters (TF Pump/Seed), rejecting the amplified spontaneous emission and polarization controllers (PC) are used to align them with the sample input. The lasers are combined using a beam splitter (BS). The output of the chip is connected to a filter to reject the seed light (TF signal) and an ultra-narrow filter of 6 pm bandwidth is used as a spectrometer. Due to the low amount of four wave mixing generated, a SPAD ID230 is used to measure the spectrum.

used to align the polarization with the grating coupler input of the sample. A BS combined the two lasers before light injection. At the output, a Yenista XTM-50 filter was used to remove partially the noise from the seed. Finally, an Ultra-Narrow Filter (UNF) from Advanced Optics Solutions and a Single Photon Avalance Detector (SPAD) ID230 from IDQ was used as a high accuracy Optical Spectrum Analyzer. The UNF had a bandwidth of 6 pm or 0.75 GHz and was tunable over 500 pm starting at 1560.2 nm.

The JSA measurements were performed on a comb-pair source to accommodate the UNF wavelength range. The pump was set at 1541.3 nm and the seed scanned the wavelength from 1522.4 to 1522.7 nm with a step of 5 pm. For each seed wavelength, the UNF was tuned over its entire range while the detector measured the light generated. Each point was integrated for 250 ms. The measured spectrum is plotted in figure 4.15. We can see a clear anti-correlation between the seed and signal wavelength. The sample used a ring with a resonance Full Width at Half Maximum (FWHM) of 105 pm and a FSR of 1.55 nm. The resonances tested corresponds to ± 14 FSR from the pump.

We can then reconstruct the full JSA by fitting the data with a 2D Gaussian function

$$f(x,y) = Ae^{-\left(\frac{(x-x_0)^2}{2\sigma_x^2}+\frac{(y-y_0)^2}{2\sigma_y^2}\right)} \tag{4.6}$$

with A its amplitude, (x_0, y_0) the position of the maximum, σ_x and σ_y the FWHM in the x and y direction, respectively. From the full JSA, we can extract the Schmidt number. We get a $K = 5.52$ which is much lower than the predicted value. This can be attributed to the large bandwidth of the UNF compared to the JSA's simulated spectral width. We also found back the FWHM of the ring resonances of about 100 pm in the JSA.

As shown in figure 4.16, the fit is slightly tilted compared to the anti-diagonal by 5.2°. This could be due to instability during the measurements as the total integration time was more than 2 hours. A thermal drift in the UNF or the sample could result in such a deformation.

This measurement confirms the entangled nature of the pairs being generated. The

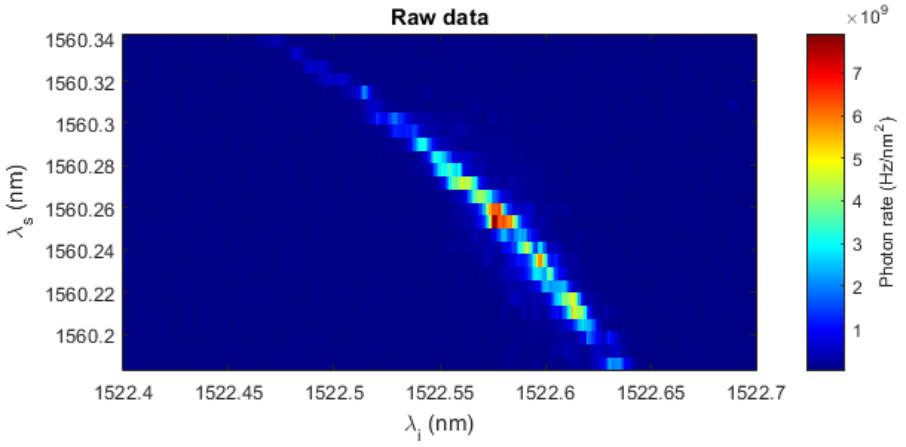

Figure 4.15.: Raw experimental results from changing the seed λ_i wavelength and measuring the spectrum generated λ_s by turning the UNF. A clear anti-correlation can be seen, as expected with a CW pump laser.

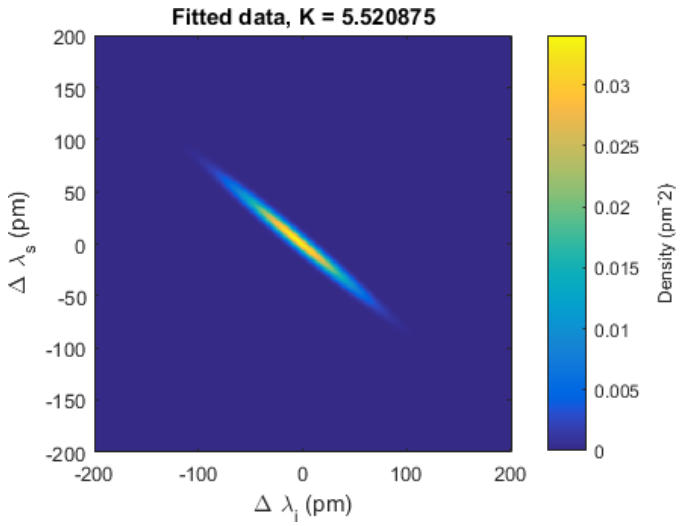

Figure 4.16.: Fit of the raw date using a 2D Gaussian is 5.2° off the anti-diagonal, with $\sigma_{anti-diag} = 44.3$ pm and $\sigma_{diag} = 4.0$ pm. The Schmidt number K is close to 5.5, limited by the bandwidth of the UNF.

wavelength correlation is a characteristic of a non-separable two photon state. We were limited by the resolution of the UNF to determine with accuracy how close the BWF is to a theoretical state. To push this limit, we could change our strategy and try to create interferences between the two photons. This is called Franson interferometry, which is presented in the next section.

4.4. Visibility measurements

The photon pairs are genuinely energy-time entangled as they are produced by SFWM [242, 243, 244, 245, 246, 144, 247, 248]. This is thanks to the conservation of energy but also the simultaneous generation of the two photons. As we know the spectral properties of the two-photon state that are generated, we can characterize further their entanglement.

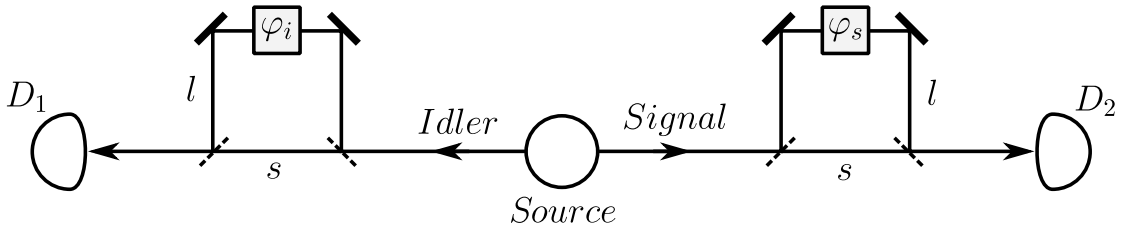

Figure 4.17.: Schematics of the interferometric setup used by Franson [14, 42]: a pair of entangled particles are generated by the source and sent to MZI interferometers. Then, correlations between the arrival times are measured between the detectors D_1 and D_2.

Time-bin entanglement can be qualified by using a Franson-type interferometer setup [14, 42], see figure 4.17. It is constituted of two Mach-Zehnder (or Michelson) interferometers, with a large delay in one arm. The delay ΔL between the two arms must be larger than the coherence length of the individual studied photon $L_C^{s,i} \ll \Delta L$. This is to avoid first order interference of each photon, meaning the photon cannot interfere with itself. Moreover, the delays must also be smaller that the coherence length of the pump $\Delta L \ll L_C^p$. This condition is necessary so that the regardless of which paths are taken in the interferometers so the two-photon waves can interact. Finally, the two interferometers must be strictly identical in length, within the coherence length of the single photon. Any variation creates a partial distinguishability of the two states. This reduces our ability to measure the entanglement between the pairs. All these conditions insure that only second order (or two photon) interferences can be measured.

Since each interferometer has a long and a short paths, there are two possible paths taken by each photon. Either they take the long or the short paths. This creates states with of an early (short path s) and late (long path l) components, see equation 4.7.

$$|\phi\rangle = \frac{1}{\sqrt{2}}(|s\rangle + e^{i\varphi}|l\rangle) \tag{4.7}$$

Since each photon can explore both paths, it makes 4 total possibilities. It creates the two photon state of equation 4.8. The subscript i (idler) and s (signal) indicate from which photon the component come from and $\varphi_{i,s}$ is the phase accumulated by each photon in their respective Mach-Zehnder Interferometer (MZI).

$$|\phi\rangle_{\mathrm{II}} = \frac{1}{2}\left(|s\rangle_i|s\rangle_s + e^{i\varphi_i}|l\rangle_i|s\rangle_s + e^{i\varphi_s}|s\rangle_i|l\rangle_s + e^{i(\varphi_i+\varphi_s)}|l\rangle_i|l\rangle_s\right) \tag{4.8}$$

When measuring the arrival times, $|l\rangle_i |s\rangle_s$ and $|s\rangle_i |l\rangle_s$ are distinguishable but not $|s\rangle_i |s\rangle_s$ and $|l\rangle_i |l\rangle_s$. The probability amplitude of the latter ones will interfere leading to two-photon interference fringes. Their amplitude depends on the sum of the two interferometers phases $\varphi_i + \varphi_s$. The detection in D_1 and D_2 can be completely correlated or anti-correlated depending on the total phase. The minimum amplitude will create anti-correlation. This is used to determine the entanglement quality of the pairs. A perfectly indistinguishable pair with perfect detectors and no noise will yield a null coincidence rate. Thus the visibility V of the measurement would be 100 % since $V = (C_{max} - C_{min})/(C_{max} + C_{min})$, with C the coincidence rates.

Entanglement was analyzed using a folded Franson arrangement consisting of an unbalanced fiber Franson-type Michelson Interferometer (F-MI) (figure 4.18c) [14, 249]. In this case, pairs are sent to the same Michelson interferometer and are spectrally separated after. This configuration requires less stabilization. Our F-MI are completely fibered, with one arm connected to a piezo-electric stage that stretches the fiber. At the end of each fiber is a Faraday mirror such that the reflected light is always perpendicular in polarization with the incoming one. This prevents classical interferences from happening. A piezo-transducer was used to extend the fiber in one arm, changing the imbalance of the interferometer, and thus the relative phase between the two arms. Everything is sealed in a box with a large mass, and a polystyrene thermal isolation. This provides a large thermal inertia allowing a stability of a few minutes without any tuning. Finally, a heater is added in the interferometer to provide a thermal stabilization when necessary.

Energy-time entanglement is revealed by the coherent superposition of the contributions coming from identical two-photon paths (short-short and long-long) contrarily to the contributions coming from different paths (long-short, or conversely). Consequently, a coincidence histogram with the emergence of 3 peaks is recorded [104](figure 4.19b). The central peak gathers the two indistinguishable contributions leading to interference. The total and average numbers of coincidences in the central and side peaks, respectively, (figure. 4.19(b)) are used to plot the patterns shown in figure 4.20.

As mentioned above, the F-MI imbalance ($\sim$ 350 ps) needs to be greater than the coherence time of the single photons ($\sim$ 100 ps) to avoid first-order interferences and shorter than the coherence time of the CW pump laser ($\sim$ 100 ns) in order to have a coherent superposition between short-short and long-long contributions in the central peak. By using a narrow coincidence window that excludes the side peaks, entanglement can be revealed according to the coincidence counting evolution $N_0(1 - V cos(2\phi))$, where V and ϕ represent the fringe visibility and the phase accumulated by the single photons in the interferometer, respectively. The visibility stands as our main figure of merit, and correlations described by such a coincidence function with a visibility higher than 70.7 % cannot be described by any local hidden-variables theory [250].

4.4.1. Visibility of the entangled photon-pair source

The full experimental setup is presented in Fig. 4.18. Light from a narrowband tunable telecom CW laser (Yenista Tunics Plus laser) is coupled to the device. Before the silicon chip, a tunable bandpass filter (Yenista XTM-50) is used to clean the laser from the ASE,

which would otherwise be coupled to the chip and not filtered by any other components. Then, a polarization controller is used to set the laser light to the TE polarization mode (Fig. 4.18a). The Transverse-Magnetic (TM) polarization is suppressed by both grating couplers (about 40 dB each) of the circuit as well as by the waveguide itself due to the asymmetric cladding (silicon waveguide between silica and air layers). Finally, a Peltier device driven by a temperature controller (Thorlabs TED 200C) is used to ensure a thermal regulation of the sample to (21 ± 0.01) °C.

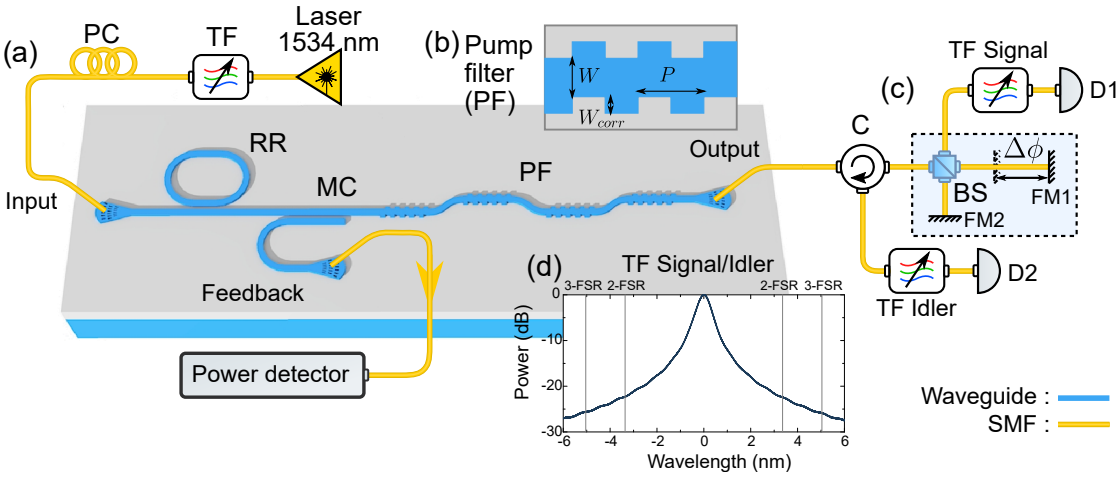

Figure 4.18.: Schematics of the experimental setup. (a) Input laser with an associated filter (TF) rejecting the amplified spontaneous emission, and a polarization controller (PC). Laser light is injected in the ring resonator (RR) through the grating coupler, and then propagates to a modal coupler (MC) and through the integrated pump filter (PF). (b) Schematic top-view of one of the cascaded Bragg filter (BF) composing the PF. The output of the chip is connected to the entanglement qualification setup (c) in a folded-Franson configuration. (e) Spectrum of the signal and idler filters, which exhibit 22 dB and 25 dB rejection for the 2-FSR shift and 3-FSR shift configurations, respectively.

For the time correlation measurements, we employ after the sample a beam splitter followed in each arm by a bandpass tunable filter (OZ optics). Each one has about 600 pm bandwidth and 22 dB extinction ratio (Fig. 4.18a). This is for the demultiplexing signal and idler photons. One wavelength is being sent to the signal filter and the other to the idler one (Fig. 4.18d). It is a not an optimized demultiplexing process as only a fourth of the pairs can be counted. We use two SNSPD ID Quantique ID281 connected to a TDC (PicoQuant HydraHarp 400) for recording coincidence counts with a bin precision of 1 ps.

Before addressing entanglement analysis, a relevant figure of merit associated with time correlation measurements consists in evaluating the CAR. The CAR is between the coincidence peak and the background noise. In the measurements presented in Fig. 4.19a, the CAR is greater than 60 for both histograms (2-FSR shift and 3-FSR shift). Accidental counts mainly come from successive pairs events, when one of the two

photons has lost its paired companion. This CAR could be improved by using a lower pump power at the price of reduced coincidence counts and of longer integration times [251]. There, our strategy is slightly different and promotes pragmatic realizations of QIS experiments. We emphasize the high-coincidence counts while keeping a moderate but safe CAR [104].

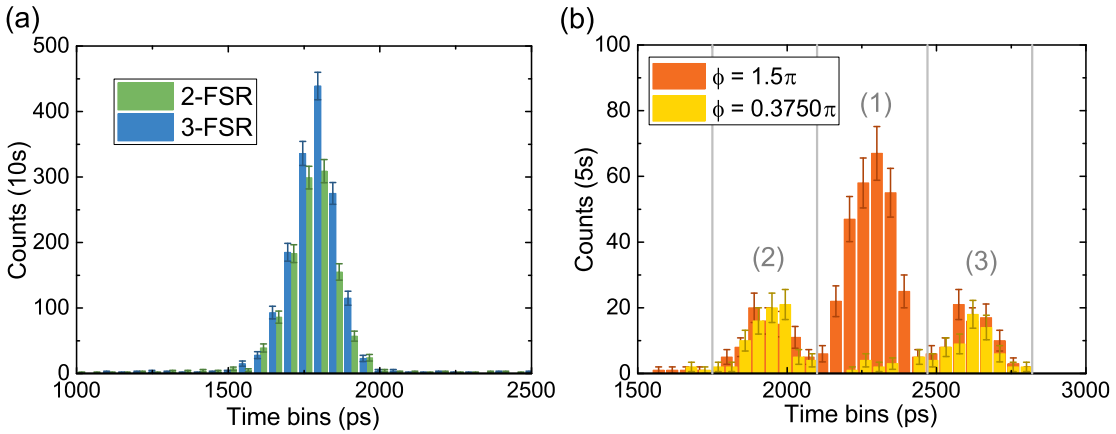

Figure 4.19.: Recorded coincidence histograms. (a) The histograms represent the recorded coincidences for both 2-FSR shift and 3-FSR shift resonances. The overall integration time is 10 seconds and the measurements are done with SNSPD detectors (Fig. 4.3). The 2-FSR rate is of about 116 counts/s with an CAR of 67.5, while the 3-FSR coincidence rate is of about 151 counts/s with a CAR of 100. The noise level within the peak is between 1.5 counts/s and 1.7 counts/s. (b) The histograms represent the coincidences at the output of the interferometric setup sketched in Fig.4.18 for the 2-FSR shift resonances. They show a maximum and a minimum of interference (region (1)). Here, the overall integration time is of 5 seconds. The error bars for all points come from Poissonian statistics associated with the pairs (e.g. $\sqrt{N}$, N being the number of coincidences). Note that similar histograms are obtained for the 3-FSR shift case.

Exploiting energy-time observable relies on the systematic lack of information of the pair creation times within the coherence time of the employed CW pump laser. In practice, the twin photons pass through the unbalanced interferometer (see Fig. 4.18c) following either the same path (short-short or long- long) or different paths (long-short, or conversely) [104]. These contributions are distinguished by measuring the arrival times of the idler photons with respect the signal photons using the TDC. This enables recording a coincidence histogram comprising three peaks (see figure 4.19b). The side peaks (labeled (2) and (3)) correspond to the situations where the paths are different. The central peak (labeled (1)) gathers the two indistinguishable cases (short-short and long-long) leading to two-photon interferences.

Interference patterns recorded for resonances 2-FSR (Fig. 4.20a) and 3-FSR (Fig. 4.20b) from the pump are obtained with a phase resolution of $\frac{2\pi}{20}$, compliant with the F-MI stability. The interferometer 2π-dephasing time-scale is within the hour range which leaves enough time to perform a scan without being subject to detrimental phase drifts.

The side peak in Fig 4.19(b) also shows the stability of the photon generation process. The typical acquisition time for recording two fringes is 6 minutes. The noise figure in the central peak is of about 0.5 and 0.9 counts/s for the 2-FSR shift and 3-FSR shift resonances, respectively.

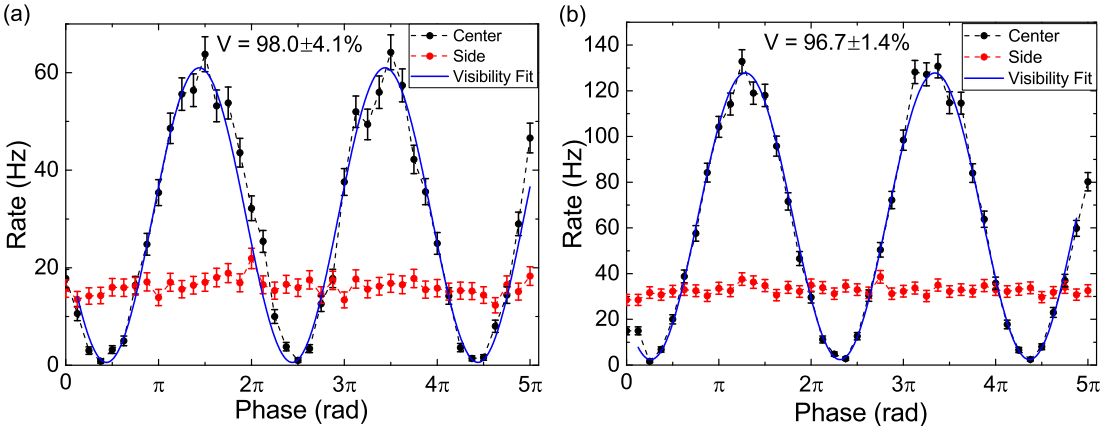

Figure 4.20.: Plots of the coincidence rates (blue curve) for the central (Region (1) in Fig. 4.19b) and the average of the side peaks (Regions (2) and (3) in Fig. 4.19b). Each point is obtained with a 5 seconds integration time and the step increment of $\pi/8$. The side peak rates show the stability of the measurement. Here, noise counts are not removed from the measurements, (a) corresponds to the 2-FSR shift resonances with a noise of 0.5 counts/s, (b) is the 3-FSR shift resonances with a noise of 0.9 counts/s. The error bars for all points come from a Poissonian statistic.

The two-photon interference fringes are fitted with respect to $N_0(1-Vcos(2\phi))$, where N_0 is the mean number of coincidences, and V the fringes visibility considered as a free-fit parameter to infer the visibility. Raw visibilities of (98.0 ±2)% and (96.7±3)% are obtained without subtraction of photonic nor detector noise, for the 2-FSR pairs (R-squared of 0.96) and for the 3-FSR pairs (R-squared of 0.99), respectively. The net normalized visibility is obtained by subtracting photonic noise originating from the detectors' dark counts (200 counts/s). They correspond to (99.6 ±1.5)% and (98.0 ±1.2)% for the 2-FSR shift and 3-FSR shift pairs, respectively.

We extend our investigations according to the same methodology for subsequent paired-channels within the S-band and the full C-band [221]. More precisely, we explore the entanglement quality of 9 extra paired-channels, *i.e* up to 11-FSR. They spread over 40 nm (1515-1555 nm) on both sides of the pump channel, leading to the ability of supporting a high number of users in a multiplexing scenario [104]. The details for the signal and idler wavelengths correspond to i-FSR, with $2 \leq i \leq 11$. The raw visibilities for all the paired-channels exceeds 92% for an internal rate $\geq$ 1 MHz as shown in Fig. 4.21.

Note that two other photonic noise contributions have been evaluated before being neglected: multiple photon-pair events and non-perfect overlap between the two identical two-photon paths ("short-short" and "long-long"). The former was not considered

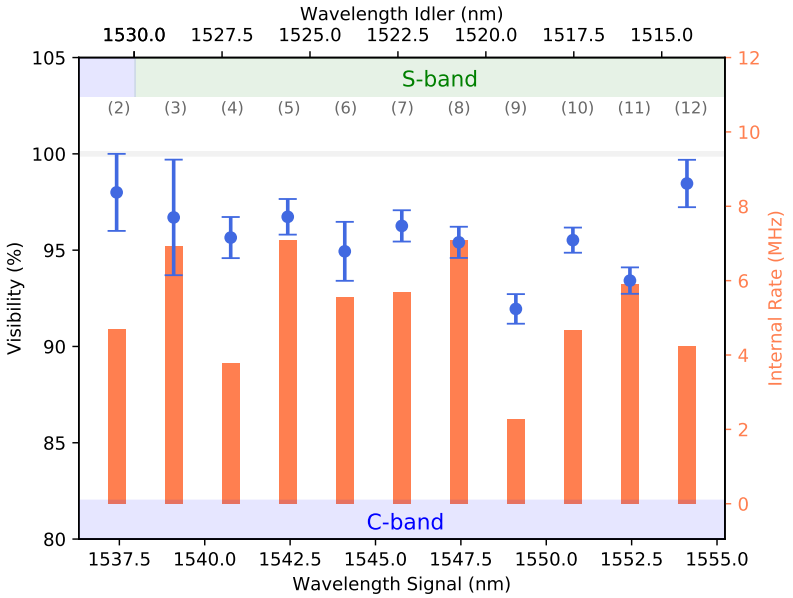

Figure 4.21.: Raw and net normalized visibilities and internal rate plotted as a function of the signal and idler wavelengths. For the sake of clarity, we associate the signal and idler wavelengths to their corresponding telecom bands.

because of the low mean number of photon pairs per gate window ($\bar{n} = 3.10^{-4}$). The origin of the latter contribution lies in the wavelength difference between the signal and the idler over the full range of analysis ($\sim$ 50 nm). This leads to potentially slightly distinguishable "short-short" and "long-long" two-photon paths. The time arrival difference was evaluated lower than $< 10^{-5}$ ps, whereas the full width at half maximum of the coincidence peak was equal to 160 ps (Fig. 4.19a), *i.e.* several orders magnitudes higher than the shift between the "short-short" and "long-long" paths.

This result not only stands as among the highest raw quantum interference visibility for time-energy entangled photons from a micro/nanoscale integrated circuit over such a large spectral window (partially over the S band and fully over the C band) but also as the first entanglement qualification of a complex integrated circuit including the pump filter [231, 102, 252]. Furthermore, generating genuinely a pure maximally entangled state from an integrated source associated with a high coincidence rate is of special interest for QIS experiments.

4.4.2. Visibility of the entangled photon-pair generator

We have repeated this measurement for the photon-pair generator, which include the generation, the pump filter and the demultiplexing stages. Although the principle was the same, its measurement was more complicated simply due to the lower transmission (-30 dB) of the sample compared to the comb sources (-15 dB). Three different inter-

Table 4.6.: Summary of signal and idler wavelengths. The pump is set to $\lambda_p = 1534.2$ nm.

FSR	λ_{idler} (nm)	λ_{signal} (nm)	V_{raw} (%)	V_{net} (%)	Rate (MHz)
2	1530.8	1537.4	98.0	99.6	2.1
3	1529.1	1539.0	96.7	98.0	2.5
4	1527.4	1540.8	95.6	96.4	1.4
5	1525.8	1542.4	96.7	97.4	2.6
6	1524.2	1544.1	94.9	95.5	2.0
7	1522.5	1545.8	96.3	97.3	2.0
8	1520.9	1547.5	95.4	96.0	2.6
9	1519.2	1549.2	91.9	92.5	0.8
10	1517.6	1550.9	95.5	96.2	1.7
11	1516.0	1552.6	93.4	94.0	2.1
12	1514.4	1554.3	98.5	99.2	1.5

ferometric setups were used. They were also different from the previous measurement as, at the output of the sample, the photon pairs were already separated into different channels by the sample.

Two interferometer configuration

This is the most interesting configuration as it is the closest to the Franson original experiment [14]. We have now two fibered F-MI. Even if they are identical physically, it is clear that here the pairs have no classical natural means of interacting. So we can observe the quantum interferences while moving the interferometer arbitrarily far from one another. This is indeed the principle behind time-bin encoding in QKD.

The setup, see figure 4.22, is constituted of the same first part as for the correlation measurement of the photon-pair generator. At the output, we still monitor the power in the feedback port to insure good coupling with the fiber array and a good spectral alignment of the cavity with the pump laser. The signal and idler are cleaned from any residual photonic noises by DWDM at channels 33 and 49, respectively. This noise comes from scattering in the substrate that is then collected at the grating coupler, from the cross-talk in the filter array, even from TM or ASE from the laser can still accumulate. Photons are then sent to the F-MI and its output is directly sent to the detector. Here, the detectors are ID230 ($\sim$ 20% efficiency). Due to the low rate and the difficulty to maintain the phase stable, the interferometers are left thermalized and not actively controlled. Every measurement is effectively marked with a random phase. It is not possible to make a visibility curve as for the source in section 4.4.1, but we can estimate it. By making repeated measurements and extracting the minimum and maximum values, we can get a rough value for the visibility.

The rate of coincidences in the interferogram is only 0.5 Hz, to have enough data an integration time of 60 seconds is chosen. After 45 measurements, we get a minimum and maximum in the central peak, as shown in figure 4.23, 68 and 7 coincidences, respectively.

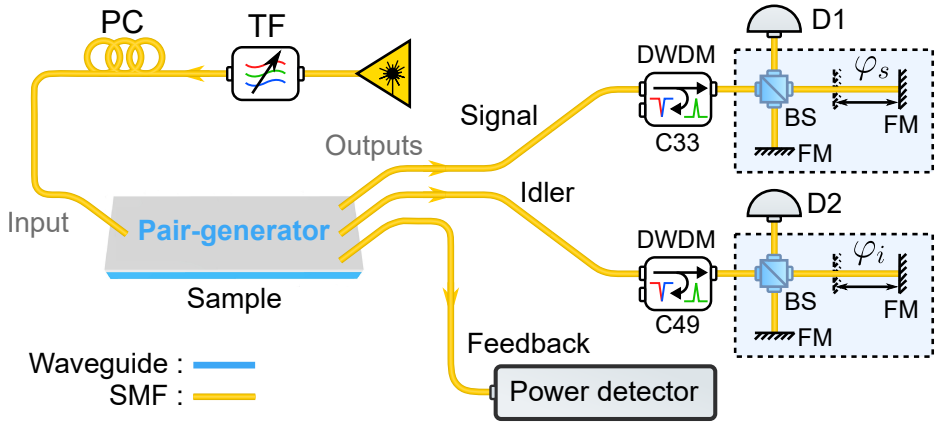

Figure 4.22.: Schematics of the two interferometer visibility measurement, the pump laser is cleaned from the ASE with a tunable filter (TF) and aligned in polarization with a polarization controller (PC). At the output, the signal and idler pairs are cleaned up from the photonics noise with DWDM, then are sent into interferometers and single-photon detectors (D1 and D2) ID230 ($\sim$ 20 % eff.). A time-digital converter is then used to perform the coincidence measurements between D1 and D2.

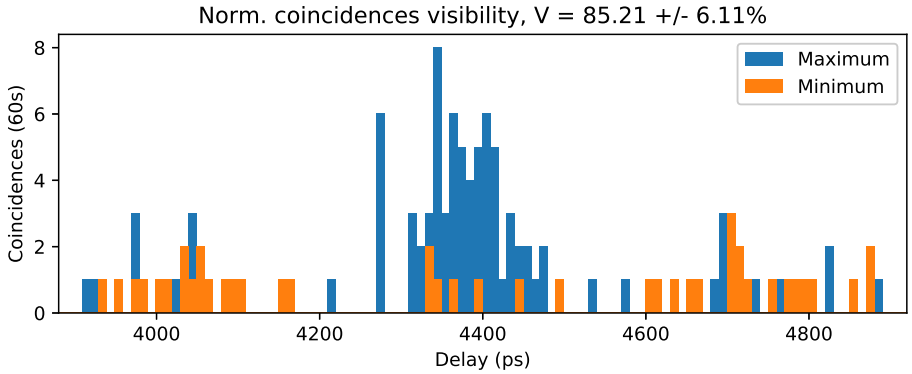

Figure 4.23.: Histogram of the maximum and minimum of coincidences form the two-interferometer setup. Each measurement has a 60s integration time and was taken from a set of 45 measurements with random phase.

If we use the side as a reference, we can normalize the central peak by the average of its sides. Using these values, we get a visibility $V = 85.2 \pm 6.1\%$. While not outstanding, it is clearly in the quantum regime ($> 70\%$).

This configuration is very inefficient as we are losing half of the photons in the interferometer. Since we are looking at only one output or each BS, half of the signal and half of the idler are sent back to the DWDM. Moreover, the two phases' fluctuations add up, increasing the drift. This requires shorter integration time to be approximated as constant.

Single interferometer configuration

To improve the stability and rate of coincidences, we can remove one of the interferometers and recombine the signal and idler. Figure 4.24 shows this configuration. As previously, the signal and idler are cleaned with DWDM and sent to the same F-MI. But this time we add circulators at each output. They collect any light coming back from the BS and send it to the detectors (ID230).

We collect all the photons we send inside as there is no filtering nor uncollected light. But this has the consequence to create a second interferogram. We have the 4 possibilities in the case D1 detect a signal and D2 detect an idler. This is the same as previously. But we have also the possibility that D1 detects the idler and D2 the signal, which also has 4 possibilities. This creates 6 coincidence peaks, as visible in figure 4.25a.

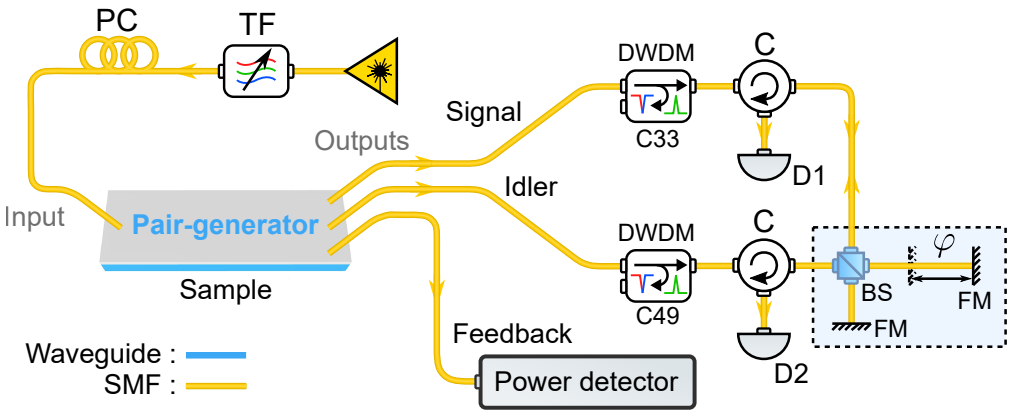

Figure 4.24.: Schematic of the one interferometer visibility measurement, the pump laser is cleaned from the ASE with a tunable filter (TF) and aligned in polarization with a polarization controller (PC). At the output the signal and idler pairs are cleaned up from photonic noise with DWDM, then are sent into the F-MI. Light is then collected by circulators (C) and by detected single-photon detectors (D1 and D2) ID230 ($\sim$ 20 % eff.). A time-digital converter is then used to perform the coincidence measurements between D1 and D2.

Each interferogram has a rate about 0.5 coincidence per second. This is still low but the improvement in stability of the phase allows for a free-phase measurement. Coincidence measurements are repeated every minute, collecting both coincidence peak. Since the phase thermally drifts, it is slow enough to continuously see its changes in a given direction. This reveals the visibility curve from figure 4.25b. We can fit this curve and get $V = 87.5 \pm 3.7\%$ (R-square of 0.99). It is improved compared to the previous setup but is still below 90 %. We can see that the two curves are perfectly synchronized in both cases and they experience the same F-MI phase. This allows to collect all the interfering photon pairs and provides the opportunity to double the rate compared to the previous F-MI as we can simply add the two histograms together. There is also no need to normalize it by the side peak as the rate is constant, as it can be seen in figure 4.25b.

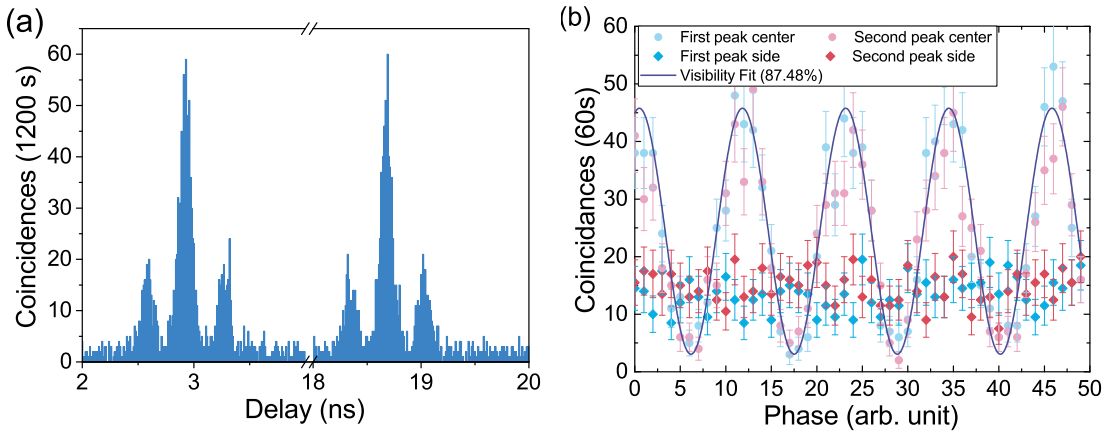

Figure 4.25.: (a) Histogram of the average interference pattern, taken over 20 minutes: it shows the 6 coincidences peaks created by the configuration of figure 4.24. (b) Visibility of both coincidence histograms plotted as a function of the phase. A fit of the two data sets gives a visibility of 87.5 %. The error bars for all points come from a Poissonian statistic.

The rate/integration time compared to the stability is still low, limiting the measurement. The period of the visibility was close to 12 minutes during the measurement. Since the rate was already optimized, the only other new option would be to increase the interferometric phase stability.

Actively stabilized interferometer configuration

We now inject a reference laser inside the interferometer, figure 4.26. Any change in its intensity can be dynamically compensated by the piezo-electric stage. This provides a reduction of phase drift to $\pi/3$ over 35 hours. This comes at a heavy cost of increased losses; the interference coincidence rate is down to 0.13 Hz. Each point requires an integration time of 40 minutes. Since we use the piezo stage to stabilize the F-MI, we cannot use it to change the phase. To change it, the simplest solution is then to change the pump wavelength, with the consequence of also shifting the signal and idler wavelengths. As the index of refraction is frequency dependent, it effectively changes the path length seen by the signal and idler. However, we have to deal with a non-constant rate of pairs as visible in figure 4.5.

In this stabilized setup, photon pairs are directly sent to the F-MI. The reference laser, ROI Orion, is set to $\lambda_{ref} = 1560.49$ nm. It is cleaned from ASE with a DWDM at channel 21 and sent to a 2:98 BS to be injected in the F-MI. The reference is then collected at the drop port of the signal DWDM and sent to a photodetector. The output voltage of this diode is stabilized on a maximum by adjusting the piezo of the interferometer, see appendix B.

Two filters are added at each output of the F-MI to detect the pairs, a DWDM and tunable filter (OZ optics) that provide more than 70 dB of rejection. This added filtering

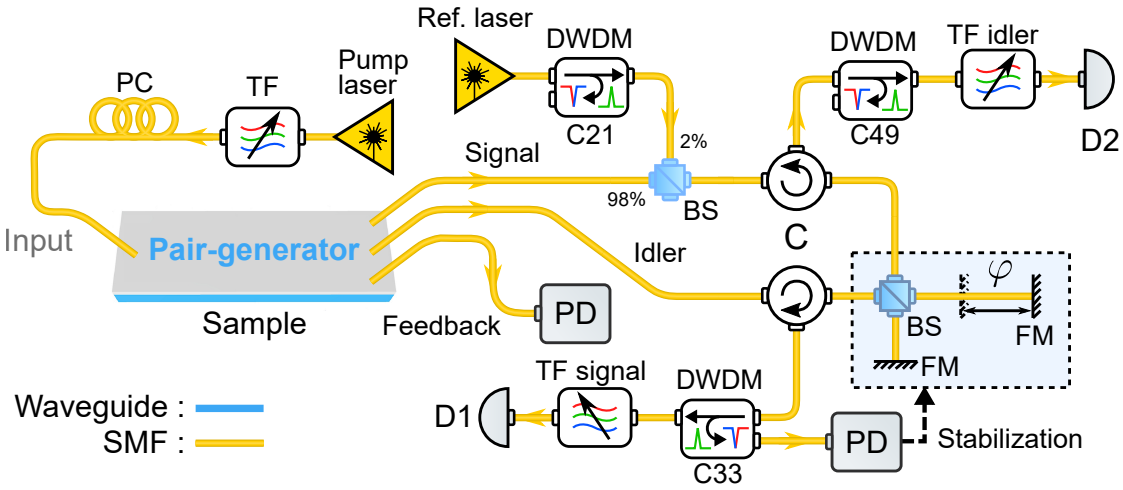

Figure 4.26.: Schematic of the one interferometer visibility measurement, the pump laser and reference laser are cleaned from the ASE with a tunable filter (TF) and a DWDM, respectively. A polarization controller (PC) is used to align the polarization of the pump with the sample. The reference laser is sent in the interferometer via a 2:98 beam splitter (BS) and is collected by a photo-detector (PD) to compensate the phase shift of the interferometer. The signal and idler pairs are collected by circulators (C), then filtered from the reference laser by a DWDM and a TF. Single-photon detectors D1 and D2 (ID230, $\sim$ 20 % eff.) are connected to a time-digital converter to perform the coincidence measurements.

stage is mostly used here to reject the reference laser as no other component removes it before the single-photon detectors. The pump laser is tuned from 1544.38 to 1544.47 nm and a coincidence measurement is performed every 2 pm. The resulting measurement is shown in figure 4.27a but it cannot be used directly to measure the visibility. If we take the ratio of the side and central peak coincidences, we have to normalize the interference pattern by the generation rate. This gives us a flat interference pattern, from which we can apply a fit and extract the visibility. The raw visibility is $V_{raw} \sim 90$ % and when we remove the background accidental coincidence noise the visibility increases to $V_{net} = 99.3 \pm 8.0$ % (R-square of 0.925), see figure 4.27.

Even with the large error bars, it is a good visibility close to unity (above > 95 %). Obviously, the pump rejection properties are not strictly related to the measurement of the visibility anymore due to the high filtering done out of the chip. But it shows than the photon-pair generator produces high indistinguishable pairs and that no component in the chip affects their performances.

4.5. Summary

In this chapter, we have studied the quantum performances of both a comb-pair source and a photon-pair generator. In both cases, on-chip pump rejection was sufficient to perform all the required experiments. Rejection above 85 dB was measured probably

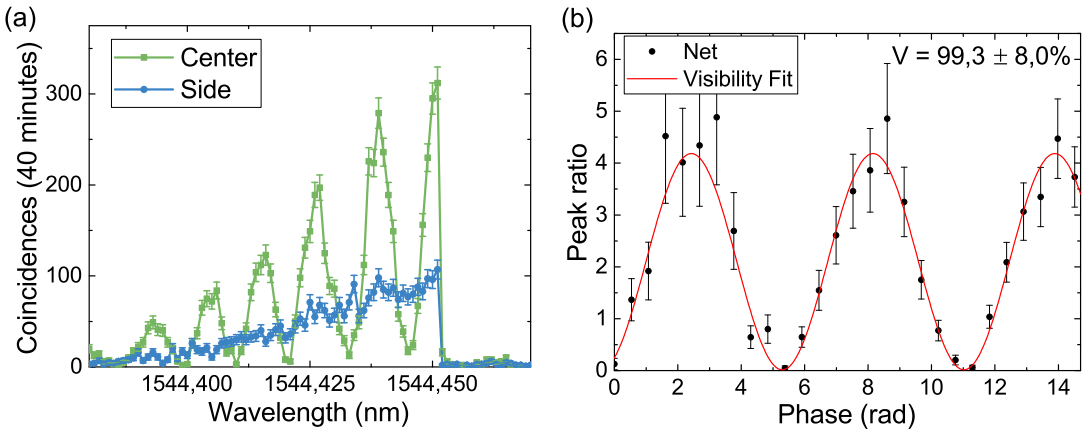

Figure 4.27.: (a) Coincidence rate of the central and side peaks created by the interferometer as a function of the pump wavelength. The rate rises due to thermal effect pushing the resonance cavity, the large drop is when the thermal effect is not compensated and the resonance returns to its resting position. The interference oscillations are visible. (b) Normalized net ratio between the center and the side of b as function of the phase, fit of the curve gives a visibility of 99.3 %. The error bars for all points come from a Poissonian statistic.

limited by on-chip photonic noise.

With a $g_h^{(2)}(0) \simeq 3.07 \times 10^{-3}$, the statistical characterization provided evidence that no multi-pairs were generated. The circuit designed and fabricated was suitable as a heralding source of single photons. Even if a heralding efficiency of $\eta = 0.15\%$ was found that limits the extraction of photon states. Improvements in extraction and lower propagation losses would make the circuit state-of-the-art if a 2 dB total transmission could be achieved for the photon pairs.

When using a CW laser, generated two-photon states are maximally entangled. This was confirmed by the state tomography with a good agreement between theoretical and experimental values of the Schmidt number. Both results indicated an entanglement with $K_{exp} = 5.5$ and $K_{sim} = 107$, both values $\gg 1$. The experimental value of the Schmidt number was limited to the spectral resolution of the setup, whereas the simulated one was limited by the matrix size. For a perfect monochromatic CW laser, the Schmidt number goes to infinity.

The two-photon interference visibility measurements performed for both the source and the generator showed high indistinguishability (> 90 %) of the photon-pair. It was observed over 40 nm of S and C telecom band and that none of the internal components of the circuits affected the quantum performances. Overall, the results presented in this chapter show that the integration of the pump filter can be achieved without affecting the generated states and that multiple sources could be combined in a single circuit to create more advanced functionalities.

Conclusion

The integration of quantum optics brings great promises in the telecommunication and computing fields. However, this integration is still a challenging step that requires redesigning components or rethinking a platform completely.

Our strategy is geared towards developing "Plug-&-Play" and scalable quantum photonic systems by exploiting silicon-based components and architectures combined with off-the-shelves telecom components [7, 8, 9, 10, 11]. A complete photonics platform was redesigned with quantum applications in mind. High Q-factor ring cavities with anomalous dispersion waveguides allows for the possible use of a spontaneous four-wave mixing over a large bandwidth (> 40 nm). This allows the generation of photon-pairs over a large portion of the S and C telecom bands. Moreover the free spectral range of the cavity close to 200 GHz makes the resonances naturally aligned with some International Telecommunication Union (ITU) channels.

The elementary components for on chip manipulation were also tested, with active and passive de-multiplexing with small (< 200 pm) and wide (> 3 nm) bandwidths, respectively. Tunable beam splitters were implemented in the form of a Mach-Zehnder Interferometer (MZI). All these devices allow for a flexible on-chip manipulation of the pairs generated by the cavity.

Multiple pump rejection strategies were explored. The several corrugation designs developed propose choices to achieve any bandwidth performance needed. On top of this, the ability to cascade the filters push further the possible filter rejection. This was made possible by breaking the phase coherency between the cascaded sections of the filter and taking advantage of the multimode conversion. Such filter exhibits overall a very deep rejection > 80 dB suitable for quantum applications.

The integration of the feedback demultiplexing stage allows the exploitation of the rejected signal, in order to match the frequency combs from the ring resonator with the pump laser. We used this strategy to demultiplex signal and idler photons in an all-passive way by cascading several modal couplers of this type. In this case, the period of the gratings that are part of the pump filter has to be adjusted according to the signal and the idler wavelengths. Furthermore, the slope of the edges corresponding to the transition from high blocking to high transmission of the pump filter is evaluated to be of 22.3 dB/100 pm, therefore being compatible with narrower spectral channels. Hence, the exploitation of a ring resonator associated with a 50 GHz free spectral range instead of 200 GHz stands as a relevant improvement in order to enhance the number of users supported by the chip up to 44 pairwise users [253]. This solution would neither impact the design of the pump filter nor the demultiplexing stages as 50 GHz stands as a standard for the ITU channel grid.

By combining all these components, we were able to create two functional circuits: a

micro-ring based entangled photon-pair comb source and an integrated entangled photon-pair generator. They provide a base for quantum photonics systems. The quality of entanglement carried by the photon pairs is fundamental for its use in any complex quantum systems. Indeed, both the statistic and the entanglement of the photon-pairs show promising characteristics, with low multi-pair generation and very well entangled two-photon states, respectively.

Notably, the high coincidence-to-accidental ratio (> 60) and the low noise observed in both coincidence and interference experiments (figure 4.19 and 4.20) show the effectiveness of our pump rejection solution, achieved in an all-passive manner. Furthermore, the acquisition time for recording the interference patterns is on the order of several minutes, allowing a setup free of complex stabilization systems for the Franson type Michelson interferometer. Note that the on-chip pump rejection is complemented by two bandpass filters, corresponding to a total amount of 107 dB, which is slightly larger than the typical necessary value of 100 dB [10].

We have demonstrated near perfect entanglement quality out of a single photonic chip embedding both generation and pump rejection building blocks. We have measured raw visibilities exceeding 92 % for 11 channel pairs over telecom bands covering the spectral range 1515-1555 nm. Our approach, combining high performance, flexibility, scalability and compliance with telecom standards, stands promising for operational quantum information applications. This brings an essential step closer to demonstrate ambitious photonic quantum devices enabling on-chip generation, filtering and manipulation of quantum states.

The statistical characterization and state tomography confirmed the type of non-classical states generated by the circuits. A $g_h^{(2)}(0) \simeq 3.07 \times 10^{-3}$ is a promising sign that the photon-pairs generator could be used as a heralding source of single photons if the pump laser is changed to a pulsed regime, as no multi-photon are outputted when heralded. Moreover, the tomography confirmed the state type emitted by the cavity. With an experimental Schmidt number of 5.5, the entanglement is well defined, confirming the nature of visibility measurements.

A heralded photon-number states generator (figure 2.1) was also fabricated on the same samples. As mentioned in section 2.1, it is constituted of two pairs generators with a tunable beam splitter (*i.e.* a MZI). It was not possible to deposit the heaters at the time of writing the manuscript. Since these circuits requires perfect alignment of the two cavities to work, it is the only circuit that requires active tuning to be tested. Moreover, the MZI must be controlled to the generate NOON states and other number states. This is left for future works.

Appendix A.

Closure of the band gap of higher bands

If we consider a two-index period, a grating that has two mode effective index values $n_1 = \sqrt{\epsilon_1 \mu_1}$ and $n_2 = \sqrt{\epsilon_2 \mu_2}$, and impedance values $z_1 = \sqrt{\mu_1/\epsilon_1}$ and $z_2 = \sqrt{\mu_2/\epsilon_2}$, with sub-period lengths L_1 and L_2, respectively and $\Lambda = L_1 + L_2$ the Bragg period. In this case, the dispersion relation 3.4 can be simplified as

$$\cos q\Lambda = \cos k_1 L_1 \cos k_2 L_2 - \frac{1}{2}\left(\frac{z_1}{z_2} + \frac{z_2}{z_1}\right) \sin k_1 L_1 \sin k_2 L_2 \tag{A.1}$$

where q is the Bloch wavevector, $k_1 = \omega n_1/c$ and $k_2 = \omega n_2/c$ the wavevectors in region 1 and 2, respectively. We can define some parameters to better understand this expression.

$$\begin{cases} \alpha = \frac{n_1 L_1}{n_2 L_2} \\ \gamma = \frac{\omega}{c}(n_1 L_1 + n_2 L_2) \\ \tau = \frac{1}{2}(\frac{z_1}{z_2} + \frac{z_2}{z_1}) \end{cases} \tag{A.2}$$

The parameter α is the ratio of the optical path in region 1 and 2, γ is the phase delay in a unit cell, and τ is the impedance mismatch[1]. Note that the impedance mismatch is always equal or larger than one ($1 \leq \tau$). A bandgap appears in the spectrum whenever the right-hand side (rhs) of equation A.1 is larger than one or lower than minus one, making $q\Lambda$ complex. This happens as soon as we have a perturbation, *i.e.* $z_1 \neq z_2$ ($1 < \tau$).

However, we can find a condition where even with a non-zero perturbation no gap appears. This is the case when $\alpha = m_1/m_2$ is a rational number, with $m_1, m_2 \in \mathbb{N}^*$ [254].

To demonstrate this condition, we first consider the $\sin k_2 L_2 = 0$, we see that q is real. Since for any k_1, L_1, k_2, L_2, we have

$$|\cos k_1 L_1 \cos k_2 L_2 - \tau \sin k_1 L_1 \sin k_2 L_2| \leq 1 \tag{A.3}$$

We follow one band. In this case, we are at the frequency $\omega = m_2 \pi c/(n_2 L_2)$, so indeed $\sin k_2 L_2 = 0$ but also $\cos k_2 L_2 = (-1)^{m_2}$ and $\cos k_1 L_1 = (-1)^{m_1}$. So that the lhs of equation A.1 is equal to $\cos q\Lambda = (-1)^{m_1+m_2}$. The Bloch wave vector q is 0 if $m_1 + m_2$ is even and is $\pm\pi/\Lambda$ if $m_1 + m_2$ is odd.

Now, we can rewrite equation A.1 using the identity $\cos a \cos b = \cos(a+b) - \sin a \sin b$.

[1] Note that in the case $\mu_1 = \mu_2$ or $\epsilon_1 = \epsilon_2$, the parameter $\tau = \frac{1}{2}(\frac{n_1}{n_2} + \frac{n_2}{n_1})$

$$\cos q\Lambda = \cos\gamma - (\tau - 1)\sin k_1 L_1 \sin k_2 L_2 \tag{A.4}$$

In this case, we can investigate two situations (i) $\gamma = (2m-1)\pi$ and (ii) $\gamma = 2m\pi$, with $m \in \mathbb{N}^*$. The condition (i) imposes that the we are in the band gap since the rhs of equation A.4 is smaller or equal than minus one.

$$\begin{cases} \cos\gamma = -1 \\ \sin(k_1 L_1)\sin(k_2 L_2) \geq 0 \\ \tau > 1 \end{cases} \Rightarrow \cos\gamma - (\tau-1)\sin k_1 L_1 \sin k_2 L_2 \leq -1 \tag{A.5}$$

Similarly, the condition (ii) forces also that the we are in the band gap as the rhs of equation A.4 is now larger or equal than one.

$$\begin{cases} \cos\gamma = 1 \\ \sin(k_1 L_1)\sin(k_2 L_2) \leq 0 \\ \tau > 1 \end{cases} \Rightarrow \cos\gamma - (\tau-1)\sin k_1 L_1 \sin k_2 L_2 \geq 1 \tag{A.6}$$

This means that if a frequency satisfies $\gamma = m\pi$ (either (i) or (ii)), it must be on the forbidden band gap. However, if we find a point where this is true, and simultaneously the guided band condition ($\sin(k_1 L_1) = 0$ or $\sin(k_2 L_2) = 0$) is verified, then there cannot be a stop band. Since this point is on the band and in the forbidden gap, the two bands $m_1 + m_2 - 1$ and $m_1 + m_2$ must be crossing, there is a closing of the band gap.

$$\begin{cases} \gamma = m\pi \\ \sin(k_1 L_1) = 0 \\ \sin(k_2 L_2) = 0 \end{cases} \Rightarrow \alpha = \frac{n_1 L_1}{n_2 L_2} = \frac{m_1}{m_2} \quad , \; m_1, m_2 \in \mathbb{N}^* \tag{A.7}$$

To summarize, the conditions A.7 imposes that no gap can appear. This is because they force the Bragg mirror eigen-mode frequencies ω_m to be both in a guided band and in the band gap. The frequency of the gap closure between the bands $m_1 + m_2 - 1$ and $m_1 + m_2$ is

$$\omega_m = \frac{m\pi c}{n_1 L_1 + n_2 L_2} \tag{A.8}$$

Using the condition A.7, we can predict for which geometries the closure of the band can appear. Looking at the closure conditions for between the first and second bands, we see in figure A.1 that the index difference $\Delta n = n_2 - n_1$ increases the condition on the duty cycle (L_1/Λ) also has to increase. As the average index $n_{avg} = (n_1 + n_2)/2$ increases, the condition slope gets smaller.

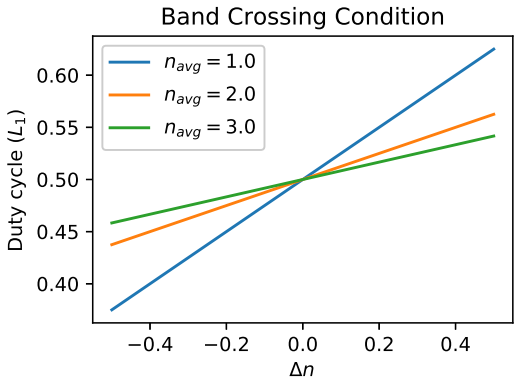

Figure A.1.: Plots of the geometrical conditions for the closure of the band gap to occur at different average effective indices when $\alpha = 1$.

Appendix B.

Interferometer Stability

The stability of fibered interferometers is fundamental to perform quantum experiments. Its phase indeed tends to drift over time, setting limitation of what can or cannot be measured. We present here the properties and settings chosen to improve the phase stability.

Our interferometers are composed of a Beam Splitter (BS) connected to two Faraday mirrors. To two other outputs of the BS are connected to the outside. One of the arm is placed on a piezo-electric stage that stretches the fiber, changing the imbalance of the interferometer and its phase. Everything is closed in a sealed box with polystyrene walls for isolation. A large metallic mass of a few kg is placed inside with a flat heater. This mass increases the thermal inertia of the system.

To measure the phase, we send a Continuous Wave laser in the interferometer at a fixed wavelength. The fluctuations of the intensity are directly due to the phase shift. The slower the oscillations, the more stable the phase of the interferometer is.

B.1. Thermal stabilization

The large thermal inertia of our interferometers allows for a good natural stability without any thermal tuning. After sitting in a 2 to 3 days in a climatized room the interferometer is thermalized. However, temperature changes in the room still induce large perturbation, see figure B.1. The number of people in the room, the outside temperature are all factors slowly affecting the heat propagation. We can see, for example, that in figure B.1 that the frequency of the oscillation spikes at lunch time when people leave and enter the room much more. Then, when researchers are absent, the frequency goes back to its stable value.

This is not an ideal situation but for short experiments of a few minutes, it can be enough provided that one can control the access to the experimental room and have a stable temperature. We can see that the period, once settled, is relatively stable, at least for an hour.

To improve the phase stability, one can heat up the interferometer. The larger temperature difference with the environment reduces the effect of thermal fluctuations. This increased the period of the oscillations to about 1 hour (figure B.2a). Of course, it is still completely passive so we can add a controller to compensate any heat flux changes. We re-purposed a TEC controller Thorlabs TED200C to be used with the heating element.

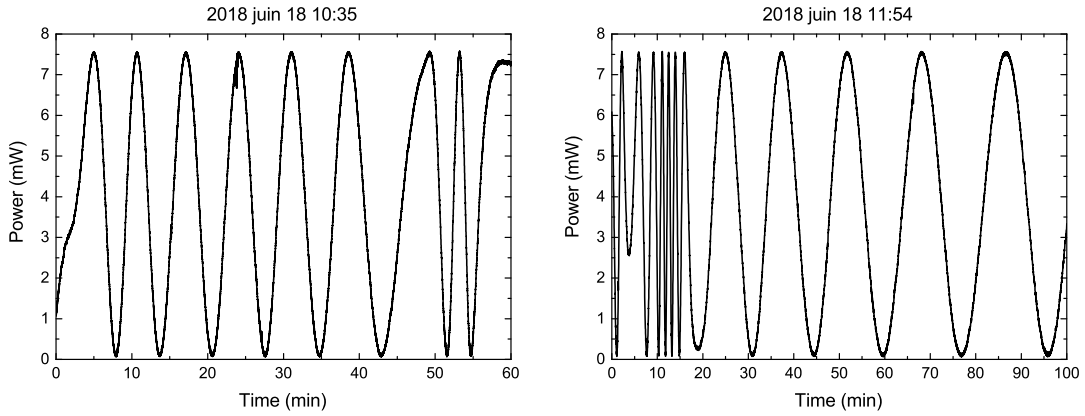

Figure B.1.: Plots of the interferometers output over time with thermal inertia. Large fluctuations can happen quickly due to a change of heat flux. The period oscillates between 2 to 20 minutes.

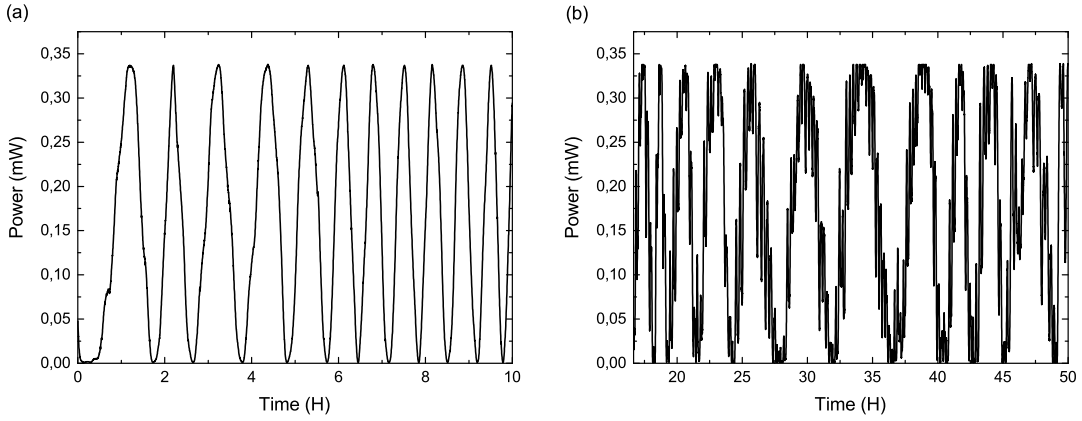

Figure B.2.: (a) and (b) are the fluctuations of a laser light sent in the interferometer over time; the interferometer is heated with a fixed 2 A current or with an extra TEC controllers, respectively. The fixed current (a) has a period of 1 hour which increases to 4h30 when adding the TEC controller, however this also adds smaller oscillations every 20 minutes.

When a negative current is applied, a diode shorts the heater. This increased the period to about 4h30 (figure B.2b), but the slow reaction time of the system creates secondary fluctuations of about 20 minutes period (figure B.3).

In this last case, the TEC max current is set to 200 mA to limit the over shoot. The P is maximized while the I and D are set to zero. And No temperature changes can be read from the temperature sensor[1] ($\pm 0.01°C$).

A better approach would be to use a Peltier system with a TEC controller or a custom

[1]However, this not optimal either since the TEC is trying the cool down the system, but cannot which affect it settings.

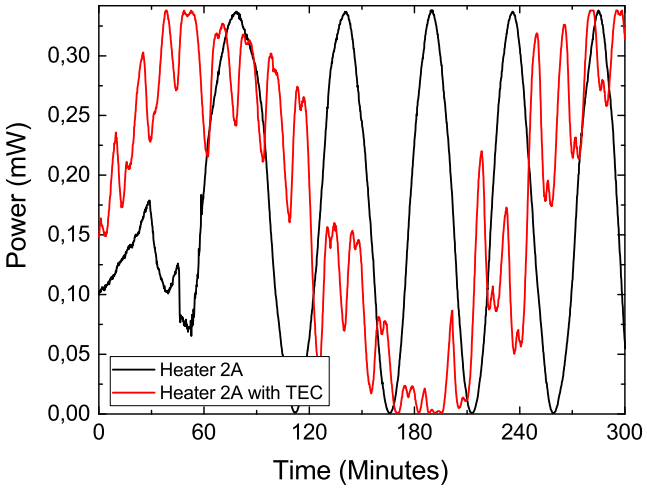

Figure B.3.: Comparison between the fixed current and the fixed current with the TEC controller, the period of oscillation increases but smaller fluctuations appear.

PID system for only heating. Due to the size of the system, a Peltier might be too small to be effective, leaving a custom PID controller as the best possible upgrade.

B.2. Actively stabilization

Stabilizing further the phase requires an active compensation. We can use the piezo-stage inside of the interferometer to compensate thermal fluctuations. In this case, a reference laser is sent in the interferometer as before. It must be constantly measured, with a stable wavelength and power output. Light coming out of the interferometer can be used to tell if the phase shifts. A photo-diode is used to collect it and the voltage is then sent a lock-in system. The system locks on either a maximum or a minimum of interference fringe. However, to know which compensation applies requires a know perturbation. We can either drive the wavelength of the reference laser or drive the piezo with a small oscillation.

B.2.1. Driving the reference laser

The perturbation can be made by driving the reference laser. A sinusoidal oscillation is applied to the wavelength. The signal measured by the photo-diode at the output of the interferometer is sent to the lock-in system. The feedback signal is first filtered in frequency to reduce its noise. Then the driving sine wave and the derivative of the feedback signal are subtracted to get the error signal. It corresponds to the deviation from the equilibrium.

Once we have the error signal, we can use it to compensate the phase. An integrator plays the role of PI system. It minimizes the error signal by acting on the piezo stage.

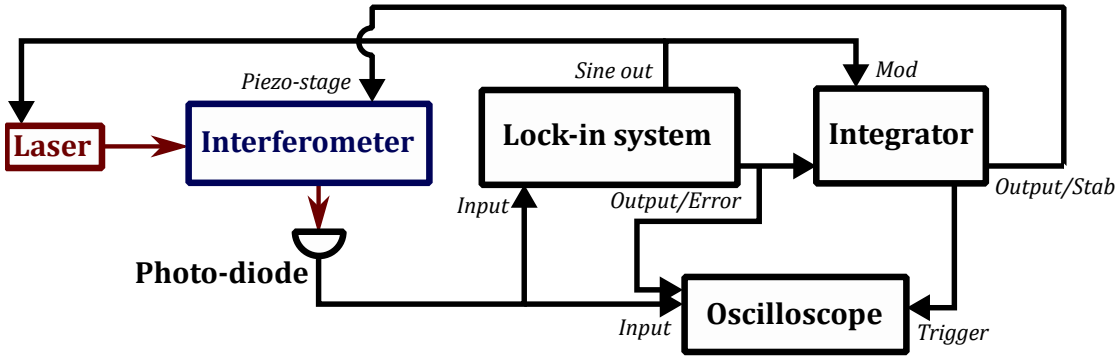

Figure B.4.: Setup schematic of the interferometric stabilization when driving the reference laser.

Once stabilized, the interferometer can be considered as stable. If the integrator has to compensate the phase shift in the same direction for too long it may get stuck. Both the piezo and integrator have a limited range. To prevent a re-initialization of the system, a new stability point should be applied.

B.2.2. Driving the piezo-electric stage

We can also instead of changing the reference point, change the phase itself. A small perturbation compared to the thermal drift can be applied to the piezo stage. A sine perturbation is used to drive the piezo. Its amplitude must be the smallest as possible before the signal becomes too noisy. This can generate a feedback signal in the photo-diode. As before, the feedback and driving signals are used to generate an error signal sent to the integrator. The integrator both plays the role of the PI controller and add the sine perturbation to the control voltage of the piezo stage.

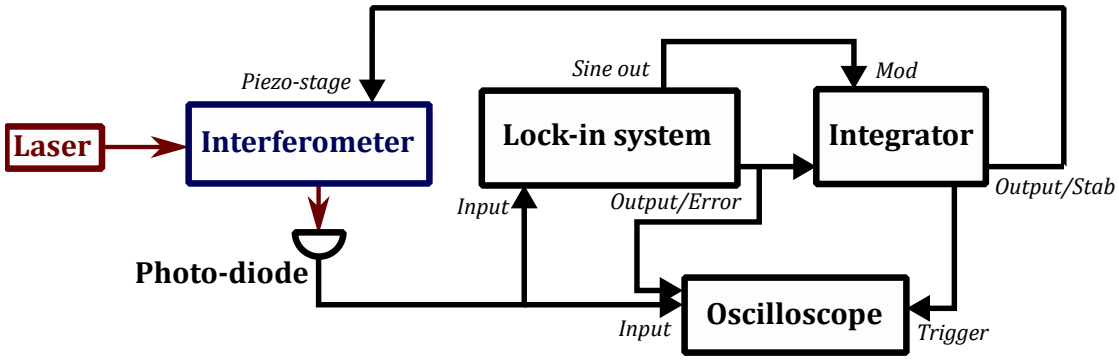

Figure B.5.: Setup schematic of the interferometric stabilization when driving the piezo-electric stage.

Such configuration is used for the stabilization of the interferometer. No difference between the two configurations could be observed. But a typical stability curve is shown

in figure B.6. We can see a relatively good stability over 24 h. However, if a shift is constant in one direction, the reference laser might jump to the next fringe if the interferometer. This can create a jump in the phase as seen in figure B.6 at around 50 h.

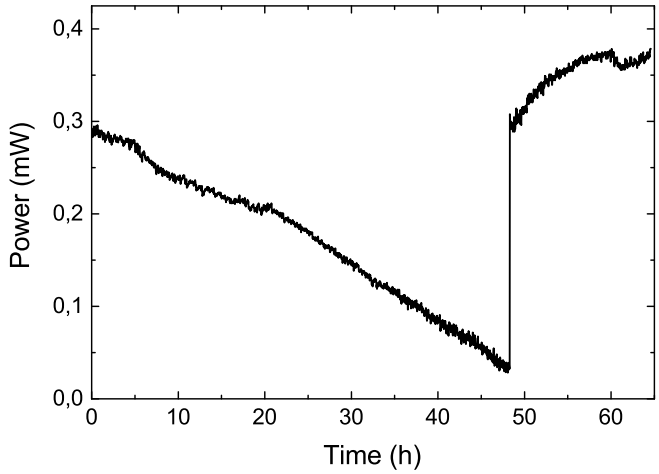

Figure B.6.: Plot of the interferometer power output for a laser at the signal wavelength when stabilized with the piezo.

Appendix C.

Some Principles for Quantum Design

Here are a few advices for the integration of photonic quantum systems. These are mostly general advices that arise from working with quantum systems and are not usually (such) a problem in classical photonics.

C.1. There will be noise

Noise is a killer, and it is everywhere. In quantum applications, the typical signal level is characterized in number of photons or rates. This already says something about the noise philosophy. Classical applications require laser light or signal measured in mW or dBm. To give an rough idea, 1 mW of laser light is $\sim 7.8 \times 10^{15}$ photon/s at 1550 nm. Even -50 dBm, which is considered as a low level, is still $\sim 7.8 \times 10^{10}$ photon/s. For a nonlinear signal in the MHz (-90 dBm) range a negligible noise (< 0.1 MHz) would be lower than -110 dBm. This means that one needs to take much more care in the possible noise source compared to systems built with classical applications in mind.

Lasers or any light source have background emissions due to secondary processes. For instance, Amplified Spontaneous Emission in lasers is a broadband signal typically with a -90 dB level lower than the coherent emission. Not only its level is close to a quantum signal but the broadband nature make it impossible to remove if not preemptively filtered.

Even thin fibers can be a problem. In a light up room, thin fibers typically used in telecoms components will not prevent the ambient light to get in the core. The resulting noise is still low (a few kHz) but can impact long experiments.

It is thus important to separate specially the "classical" and "quantum" channels. Absorbers, tranches, or gratings should be placed to avoid noise from the substrate. Fibered telecoms off-the-shelf components are not always suitable for manipulation of "classical" and "quantum" channels at the same time, even when contra-propagated between crosstalk between two modes can easily be larger than -90 dB. So, separation the input/output of the two channel types is important. Using separated components at large distances is critical.

Finally, polarization control can be tricky. A slight polarization misalignment can let both polarizations be exited in waveguides. Most photonic platforms have a strong birefringence. In other words, the transmission and performances of components in Transverse-Electric (TE) or Transverse-Magnetic (TM) polarizations are different. One

can be filtered while the other is transmitted. Making sure both polarizations are taking care of out of and on chip can also limit the noise level. This can be achieved by having either a fully bi-polarization system or a components radiating the unwanted polarization.

C.2. The transmitted, the lost and the unwanted

Power of quantum technologies grows exponentially with the number of particles interacting in the system, but so does the losses. Let N photons states be used as a cluster state for computing. They experience the losses of a single photon to the N-th power. This is simply due to the fact that the N photons must survive for the state to stay intact. As soon as a multi-photon states looses a photon, it becomes noise as it does not have the proper superposition of states. Losses not only reduce the signal but they increase the noise level as well.

Amplification cannot be used on quantum light. Any amplification disturbs or destroys the photon states, rendering them useless. When used, it can partially clone states [255, 256] but it reduces their fidelity in the process. This weakens the system. For instance in QKD applications, it can allow eavesdropping or increase dramatically the noise level. Keeping the losses as low as possible is fundamental in quantum optics and quantum photonics. The difference between a working circuits and one that nothing-can-get-out-of, can be of only 1 or 2 dB.

The inputs/outputs are usually the most lossy parts of the system: they must be improved on their own. Low losses (typically large multi-mode) waveguides can be a good solution to reduce the propagating losses. The apodization and tapering at the beginning of any structure must be standard. The smoother, the transition between one mode to the other, the better.

Bibliography

[1] Ki Young Kim. *Recent Optical and Photonic Technologies*. BoD–Books on Demand, 2010.

[2] Richard Phillips Feynman, Matthew Sands, and Robert B Leighton. *The Feynman Lectures on Physics: Quantum Mechanics. III*. Addison-Wesley, 1965.

[3] Peter W Shor and John Preskill. Simple proof of security of the bb84 quantum key distribution protocol. *Physical review letters*, 85(2):441, 2000.

[4] Pascale Senellart, Glenn Solomon, and Andrew White. High-performance semiconductor quantum-dot single-photon sources. *Nature nanotechnology*, 12(11):1026, 2017.

[5] Kaoru Sanaka, Karin Kawahara, and Takahiro Kuga. New high-efficiency source of photon pairs for engineering quantum entanglement. *Physical Review Letters*, 86(24):5620, 2001.

[6] Nicholas C Harris, Davide Grassani, Angelica Simbula, et al. Integrated source of spectrally filtered correlated photons for large-scale quantum photonic systems. *Physical Review X*, 4(4):041047, 2014.

[7] Milos A. Popović, Tymon Barwicz, Michael R. Watts, et al. Multistage high-order microring-resonator add-drop filters. *Optics Letters*, 31:2571, 2006.

[8] Xianshu Luo, Junfeng Song, Shaoqi Feng, et al. Silicon High-Order Coupled-Microring-Based Electro-Optical Switches for On-Chip Optical Interconnects. *IEEE Photonics Technology Letters*, 24:821–823, 2012.

[9] Po Dong, Ning-Ning Feng, Dazeng Feng, et al. GHz-bandwidth optical filters based on high-order silicon ring resonators. *Optics Express*, 18:23784, 2010.

[10] Mateusz Piekarek, Damien Bonneau, Shigehito Miki, et al. High-extinction ratio integrated photonic filters for silicon quantum photonics. *Optics Letters*, 42(4):815, 2017.

[11] Nicholas C. Harris, Davide Grassani, Angelica Simbula, et al. Integrated Source of Spectrally Filtered Correlated Photons for Large-Scale Quantum Photonic Systems. *Physical Review X*, 4, 2014.

[12] Jun Rong Ong, Ranjeet Kumar, and Shayan Mookherjea. Ultra-High-Contrast and Tunable-Bandwidth Filter Using Cascaded High-Order Silicon Microring Filters. *IEEE Photonics Technology Letters*, 25:1543–1546, August 2013.

[13] Ali W. Elshaari, Iman Esmaeil Zadeh, Andreas Fognini, et al. On-chip single photon filtering and multiplexing in hybrid quantum photonic circuits. *Nature Communications*, 8, 2017.

[14] James D Franson. Bell inequality for position and time. *Physical Review letters*, 62(19):2205, 1989.

[15] Dorian Oser, Florent Mazeas, X Le Roux, et al. Coherency-broken bragg filters: surpassing on-chip rejection limitations. *arXiv preprint arXiv:1806.08833, accepted to be published in Laser & Photonics Review*, 2018.

[16] LG Helt, Zhenshan Yang, Marco Liscidini, and JE Sipe. Spontaneous four-wave mixing in microring resonators. *Optics letters*, 35(18):3006–3008, 2010.

[17] Submarine cable map. `https://www.submarinecablemap.com`. Accessed: 2019-08-18.

[18] Norman F Ramsey. Quantum mechanics and precision measurements. *Physica Scripta*, 1995(T59):26, 1995.

[19] Max Tillmann, Borivoje Dakić, René Heilmann, et al. Experimental boson sampling. *Nature Photonics*, 7(7):540, 2013.

[20] Hoi-Kwong Lo, Xiongfeng Ma, and Kai Chen. Decoy state quantum key distribution. *Physical review letters*, 94(23):230504, 2005.

[21] Renato Renner. Security of quantum key distribution. *International Journal of Quantum Information*, 6(01):1–127, 2008.

[22] Nicolas Gisin and Rob Thew. Quantum communication. *Nature photonics*, 1(3):165, 2007.

[23] T Chaneliere, DN Matsukevich, SD Jenkins, et al. Quantum telecommunication based on atomic cascade transitions. *Physical review letters*, 96(9):093604, 2006.

[24] Aram W Harrow and Ashley Montanaro. Quantum computational supremacy. *Nature*, 549(7671):203, 2017.

[25] Marlan O Scully and Kai Drühl. Quantum eraser: A proposed photon correlation experiment concerning observation and" delayed choice" in quantum mechanics. *Physical Review A*, 25(4):2208, 1982.

[26] Yoon-Ho Kim, Rong Yu, Sergei P Kulik, Yanhua Shih, and Marlan O Scully. Delayed "choice" quantum eraser. *Physical Review Letters*, 84(1):1, 2000.

[27] John M Martinis. Qubit metrology for building a fault-tolerant quantum computer, 2015.

[28] Fulvio Flamini, Nicolò Spagnolo, and Fabio Sciarrino. Photonic quantum information processing: a review. *Reports on Progress in Physics*, 82(1):016001, 2018.

[29] Sherwood Parker. A single-photon double-slit interference experiment. *American Journal of Physics*, 39(4):420–424, 1971.

[30] Izhar Neder, Nissim Ofek, Y Chung, et al. Interference between two indistinguishable electrons from independent sources. *Nature*, 448(7151):333, 2007.

[31] Julian Hofmann, Michael Krug, Norbert Ortegel, et al. Heralded entanglement between widely separated atoms. *Science*, 337(6090):72–75, 2012.

[32] Hoi-Kwong Lo, Marcos Curty, and Kiyoshi Tamaki. Secure quantum key distribution. *Nature Photonics*, 8(8):595, 2014.

[33] Morton H Rubin, David N Klyshko, YH Shih, and AV Sergienko. Theory of two-photon entanglement in type-ii optical parametric down-conversion. *Physical Review A*, 50(6):5122, 1994.

[34] Paul G Kwiat, Klaus Mattle, Harald Weinfurter, et al. New high-intensity source of polarization-entangled photon pairs. *Physical Review Letters*, 75(24):4337, 1995.

[35] Philip Sibson, Jake E Kennard, Stasja Stanisic, et al. Integrated silicon photonics for high-speed quantum key distribution. *Optica*, 4(2):172–177, 2017.

[36] Alexander S Solntsev, Frank Setzpfandt, Alex S Clark, et al. Generation of nonclassical biphoton states through cascaded quantum walks on a nonlinear chip. *Physical Review X*, 4(3):031007, 2014.

[37] Joshua W Silverstone, Damien Bonneau, Kazuya Ohira, et al. On-chip quantum interference between silicon photon-pair sources. *Nature Photonics*, 8(2):104, 2014.

[38] Alberto Peruzzo, Mirko Lobino, Jonathan CF Matthews, et al. Quantum walks of correlated photons. *Science*, 329(5998):1500–1503, 2010.

[39] Matthew A Broome, Alessandro Fedrizzi, Saleh Rahimi-Keshari, et al. Photonic boson sampling in a tunable circuit. *Science*, 339(6121):794–798, 2013.

[40] Nicolo Spagnolo, Chiara Vitelli, Marco Bentivegna, et al. Experimental validation of photonic boson sampling. *Nature Photonics*, 8(8):615, 2014.

[41] Benjamin J Metcalf, Justin B Spring, Peter C Humphreys, et al. Quantum teleportation on a photonic chip. *Nature photonics*, 8(10):770, 2014.

[42] JD Franson. Two-photon interferometry over large distances. *Physical Review A*, 44(7):4552, 1991.

[43] Olivier Alibart, Virginia D'Auria, Marc De Micheli, et al. Quantum photonics at telecom wavelengths based on lithium niobate waveguides. *Journal of Optics*, 18(10):104001, 2016.

[44] Jürgen Brendel, Nicolas Gisin, Wolfgang Tittel, and Hugo Zbinden. Pulsed energy-time entangled twin-photon source for quantum communication. *Physical Review Letters*, 82(12):2594, 1999.

[45] Wolfgang Tittel, Jürgen Brendel, Nicolas Gisin, and Hugo Zbinden. Long-distance bell-type tests using energy-time entangled photons. *Physical Review A*, 59(6):4150, 1999.

[46] Florent Mazeas, Michele Traetta, Marco Bentivegna, et al. High-quality photonic entanglement for wavelength-multiplexed quantum communication based on a silicon chip. *Optics Express*, 24(25):28731–28738, 2016.

[47] Albert Einstein, Boris Podolsky, and Nathan Rosen. Can quantum-mechanical description of physical reality be considered complete? *Physical review*, 47(10):777, 1935.

[48] John S Bell. On the einstein podolsky rosen paradox. *Physics Physique Fizika*, 1(3):195, 1964.

[49] Asher Peres. All the bell inequalities. *Foundations of Physics*, 29(4):589–614, 1999.

[50] Reinhard F Werner and Michael M Wolf. Bell inequalities and entanglement. *arXiv preprint quant-ph/0107093*, 2001.

[51] John F Clauser, Michael A Horne, Abner Shimony, and Richard A Holt. Proposed experiment to test local hidden-variable theories. *Physical review letters*, 23(15):880, 1969.

[52] Franco Selleri. *Quantum mechanics versus local realism: the Einstein-Podolsky-Rosen Paradox*. Springer Science & Business Media, 2013.

[53] Alain Aspect, Jean Dalibard, and Gérard Roger. Experimental test of bell's inequalities using time-varying analyzers. *Physical review letters*, 49(25):1804, 1982.

[54] Wolfgang Tittel, Jürgen Brendel, Hugo Zbinden, and Nicolas Gisin. Violation of bell inequalities by photons more than 10 km apart. *Physical Review Letters*, 81(17):3563, 1998.

[55] Rupert Ursin, F Tiefenbacher, T Schmitt-Manderbach, et al. Entanglement-based quantum communication over 144 km. *Nature physics*, 3(7):481, 2007.

[56] Takahiro Inagaki, Nobuyuki Matsuda, Osamu Tadanaga, Masaki Asobe, and Hiroki Takesue. Entanglement distribution over 300 km of fiber. *Optics express*, 21(20):23241–23249, 2013.

[57] Bas Hensen, Hannes Bernien, Anaïs E Dréau, et al. Loophole-free bell inequality violation using electron spins separated by 1.3 kilometres. *Nature*, 526(7575):682, 2015.

[58] Yuji Hasegawa, Rudolf Loidl, Gerald Badurek, Matthias Baron, and Helmut Rauch. Violation of a bell-like inequality in single-neutron interferometry. *Nature*, 425(6953):45, 2003.

[59] DN Matsukevich, Peter Maunz, DL Moehring, Steven Olmschenk, and Chris Monroe. Bell inequality violation with two remote atomic qubits. *Physical Review Letters*, 100(15):150404, 2008.

[60] David L Moehring, Martin J Madsen, Boris B Blinov, and Cris Monroe. Experimental bell inequality violation with an atom and a photon. *Physical review letters*, 93(9):090410, 2004.

[61] Thomas E Tkacik. A hardware random number generator. In *International Workshop on Cryptographic hardware and embedded systems*, pages 450–453. Springer, 2002.

[62] Stefano Pironio, Antonio Acín, Serge Massar, et al. Random numbers certified by bell's theorem. *Nature*, 464(7291):1021, 2010.

[63] Carlos Abellán, A Acin, A Alarcon, et al. Challenging local realism with human choices. *arXiv preprint arXiv:1805.04431*, 2018.

[64] Christoph Simon and William TM Irvine. Robust long-distance entanglement and a loophole-free bell test with ions and photons. *Physical review letters*, 91(11):110405, 2003.

[65] R García-Patrón, Jaromır Fiurášek, Nicolas J Cerf, et al. Proposal for a loophole-free bell test using homodyne detection. *Physical review letters*, 93(13):130409, 2004.

[66] Lukas Gordon Helt. *Nonlinear quantum optics in artificially structured media*. University of Toronto, 2013.

[67] Dimitrios Dimitropoulos, Varun Raghunathan, Ricardo Claps, and Bahram Jalali. Phase-matching and nonlinear optical processes in silicon waveguides. *Optics express*, 12(1):149–160, 2004.

[68] Govind P Agrawal. Nonlinear fiber optics (academic press, new york, usa), 2007.

[69] Rodney Loudon. *The quantum theory of light*. OUP Oxford, 2000.

[70] R Hanbury Brown, Richard Q Twiss, et al. Correlation between photons in two coherent beams of light. *Nature*, 177(4497):27–29, 1956.

[71] Stefan Strauf, Nick G Stoltz, Matthew T Rakher, et al. High-frequency single-photon source with polarization control. *Nature photonics*, 1(12):704, 2007.

[72] Charles Santori, Matthew Pelton, Glenn Solomon, Yseulte Dale, and Yoshihisa Yamamoto. Triggered single photons from a quantum dot. *Physical Review Letters*, 86(8):1502, 2001.

[73] Shuo Sun, Hyochul Kim, Glenn S Solomon, and Edo Waks. A quantum phase switch between a single solid-state spin and a photon. *Nature nanotechnology*, 11(6):539, 2016.

[74] Constantin Dory, Kevin A Fischer, Kai Müller, et al. Complete coherent control of a quantum dot strongly coupled to a nanocavity. *Scientific reports*, 6:25172, 2016.

[75] Elke Neu, David Steinmetz, Janine Riedrich-Möller, et al. Single photon emission from silicon-vacancy colour centres in chemical vapour deposition nano-diamonds on iridium. *New Journal of Physics*, 13(2):025012, 2011.

[76] Tim Schröder, Friedemann Gädeke, Moritz Julian Banholzer, and Oliver Benson. Ultrabright and efficient single-photon generation based on nitrogen-vacancy centres in nanodiamonds on a solid immersion lens. *New Journal of Physics*, 13(5):055017, 2011.

[77] Igor Aharonovich, Dirk Englund, and Milos Toth. Solid-state single-photon emitters. *Nature Photonics*, 10(10):631, 2016.

[78] Hamamatsu Photonics. High-speed, high sensitivity photodiodes having an internal gain mechanism. `https://www.hamamatsu.com/resources/pdf/ssd/si_apd_kapd0001e.pdf`. 2019-01-07.

[79] Malte Avenhaus, Andreas Eckstein, Peter J Mosley, and Christine Silberhorn. Fiber-assisted single-photon spectrograph. *Optics letters*, 34(18):2873–2875, 2009.

[80] Yoon-Ho Kim and Warren P Grice. Measurement of the spectral properties of the two-photon state generated via type ii spontaneous parametric downconversion. *Optics Letters*, 30(8):908–910, 2005.

[81] Wojciech Wasilewski, Piotr Wasylczyk, Piotr Kolenderski, Konrad Banaszek, and Czeslaw Radzewicz. Joint spectrum of photon pairs measured by coincidence fourier spectroscopy. *Optics Letters*, 31(8):1130–1132, 2006.

[82] Bin Fang, Offir Cohen, Marco Liscidini, John E Sipe, and Virginia O Lorenz. Fast and highly resolved capture of the joint spectral density of photon pairs. *Optica*, 1(5):281–284, 2014.

[83] Kevin Zielnicki, Karina Garay-Palmett, Daniel Cruz-Delgado, et al. Joint spectral characterization of photon-pair sources. *Journal of Modern Optics*, 65(10):1141–1160, 2018.

[84] Leonard Mandel. Quantum effects in one-photon and two-photon interference. In *More Things in Heaven and Earth*, pages 460–473. Springer, 1999.

[85] Markus Müller, Samir Bounouar, Klaus D Jöns, M Glässl, and P Michler. On-demand generation of indistinguishable polarization-entangled photon pairs. *Nature Photonics*, 8(3):224, 2014.

[86] Harishankar Jayakumar, Ana Predojević, Thomas Kauten, et al. Time-bin entangled photons from a quantum dot. *Nature communications*, 5:4251, 2014.

[87] Chong-Ki Hong, Zhe-Yu Ou, and Leonard Mandel. Measurement of subpicosecond time intervals between two photons by interference. *Physical review letters*, 59(18):2044, 1987.

[88] G Di Giuseppe, L Haiberger, F De Martini, and AV Sergienko. Quantum interference and indistinguishability with femtosecond pulses. *Physical Review A*, 56(1):R21, 1997.

[89] Manuel Gschrey, Alexander Thoma, Peter Schnauber, et al. Highly indistinguishable photons from deterministic quantum-dot microlenses utilizing three-dimensional in situ electron-beam lithography. *Nature communications*, 6:7662, 2015.

[90] Niccolo Somaschi, Valerian Giesz, Lorenzo De Santis, et al. Near-optimal single-photon sources in the solid state. *Nature Photonics*, 10(5):340, 2016.

[91] Alp Sipahigil, Kay D Jahnke, Lachlan J Rogers, et al. Indistinguishable photons from separated silicon-vacancy centers in diamond. *Physical review letters*, 113(11):113602, 2014.

[92] Sébastien Tanzilli, Hugues De Riedmatten, Wolfgang Tittel, et al. Highly efficient photon-pair source using periodically poled lithium niobate waveguide. *Electronics Letters*, 37(1):26–28, 2001.

[93] Justin B Spring, Benjamin J Metcalf, Peter C Humphreys, et al. Boson sampling on a photonic chip. *Science*, 339(6121):798–801, 2013.

[94] Alexander I Lvovsky, Barry C Sanders, and Wolfgang Tittel. Optical quantum memory. *Nature photonics*, 3(12):706, 2009.

[95] Christoph Clausen, Imam Usmani, Félix Bussières, et al. Quantum storage of photonic entanglement in a crystal. *Nature*, 469(7331):508, 2011.

[96] Charles H. Bennett and David P DiVincenzo. Quantum information and computation. *Nature*, 404:247–255, 2000.

[97] Antonio Acín, Immanuel Bloch, Harry Buhrman, et al. The quantum technologies roadmap: a European community view. *New Journal of Physics*, 20(8):080201, 2018.

[98] E Knill, Laflamme R, and Milburn G. A scheme for efficient quantum computation with linear optics. *Nature*, 409(9):46–52, 2001.

[99] Eleni Diamanti, Hoi-Kwong Lo, Bing Qi, and Zhiliang Yuan. Practical challenges in quantum key distribution. *npj Quantum Information*, 2:16025, 2016.

[100] Xiaogang Qiang, Xiaoqi Zhou, Jianwei Wang, et al. Large-scale silicon quantum photonics implementing arbitrary two-qubit processing. *Nature Photonics*, 12:534–539, September 2018.

[101] Farid Samara, Anthony Martin, Claire Autebert, et al. High-Rate Photon Pairs and Sequential Time-Bin Entanglement with Si$_3$N$_4$ Ring Microresonators. *arXiv:1902.09960 [quant-ph]*, 2019.

[102] Davide Grassani, Stefano Azzini, Marco Liscidini, et al. Micrometer-scale integrated silicon source of time-energy entangled photons. *Optica*, 2:88–94, 2015.

[103] Yan Chen, Jiaxiang Zhang, Michael Zopf, et al. Wavelength-tunable entangled photons from silicon-integrated iii-v quantum dots. *Nature Communications*, 7:10387, 2016.

[104] Djeylan Aktas, Bruno Fedrici, Florian Kaiser, et al. Entanglement distribution over 150 km in wavelength division multiplexed channels for quantum cryptography. *Laser and Photonics Reviews*, 10:451–457, 2016.

[105] Adeline Orieux, Marijn A M Versteegh, Klaus D Jöns, and Sara Ducci. Semiconductor devices for entangled photon pair generation: a review. *Reports on Progress in Physics*, 80:076001, 2017.

[106] Jianwei Wang, Stefano Paesani, Yunhong Ding, et al. Multidimensional quantum entanglement with large-scale integrated optics. *Science*, 2018.

[107] H. Jin, F. M. Liu, P. Xu, et al. On-chip generation and manipulation of entangled photons based on reconfigurable lithium-niobate waveguide circuits. *Physics Review Letters*, 113:103601, 2014.

[108] Panagiotis Vergyris, Thomas Meany, Tommaso Lunghi, et al. On-chip generation of heralded photon-number states. *Scientific reports*, 6:35975, 2016.

[109] Imad I. Faruque, Gary F. Sinclair, Damien Bonneau, John G. Rarity, and Mark G. Thompson. On-chip quantum interference with heralded photons from two independent micro-ring resonator sources in silicon photonics. *Opt. Express*, pages 20379–20395, 2018.

[110] Joshua W Silverstone, Damien Bonneau, Jeremy L O'Brien, and Mark G Thompson. Silicon quantum photonics. *IEEE Journal of Selected Topics in Quantum Electronics*, 22(6):390–402, 2016.

[111] Nicholas C Harris, Gregory R Steinbrecher, Mihika Prabhu, et al. Quantum transport simulations in a programmable nanophotonic processor. *Nature Photonics*, 11(7):447, 2017.

[112] Jeremy L O'brien, Akira Furusawa, and Jelena Vučković. Photonic quantum technologies. *Nature Photonics*, 3(12):687, 2009.

[113] Jeremy L O'Brien, Geoffrey J Pryde, Andrew G White, Timothy C Ralph, and David Branning. Demonstration of an all-optical quantum controlled-not gate. *Nature*, 426(6964):264, 2003.

[114] Marco Fiorentino and Franco NC Wong. Deterministic controlled-not gate for single-photon two-qubit quantum logic. *Physical review letters*, 93(7):070502, 2004.

[115] Sara Gasparoni, Jian-Wei Pan, Philip Walther, Terry Rudolph, and Anton Zeilinger. Realization of a photonic controlled-not gate sufficient for quantum computation. *Physical review letters*, 93(2):020504, 2004.

[116] Robert H Hadfield. Single-photon detectors for optical quantum information applications. *Nature photonics*, 3(12):696, 2009.

[117] Chandra M Natarajan, Michael G Tanner, and Robert H Hadfield. Superconducting nanowire single-photon detectors: physics and applications. *Superconductor science and technology*, 25(6):063001, 2012.

[118] Di Zhu, Qing-Yuan Zhao, Hyeongrak Choi, et al. A scalable multi-photon coincidence detector based on superconducting nanowires. *Nature nanotechnology*, 13(7):596, 2018.

[119] Maria Moshkova, Alexander Divochiy, Pavel Morozov, et al. High-performance superconducting photon-number-resolving detectors with 86% system efficiency at telecom range. *JOSA B*, 36(3):B20–B25, 2019.

[120] Lorenzo De Santis. *Single photon generation and manipulation with semiconductor quantum dot devices*. PhD thesis, Paris Saclay, 2018.

[121] A Dousse, L Lanco, J Suffczyński, et al. Controlled light-matter coupling for a single quantum dot embedded in a pillar microcavity using far-field optical lithography. *Physical review letters*, 101(26):267404, 2008.

[122] A Dousse, J Suffczyński, R Braive, et al. Scalable implementation of strongly coupled cavity-quantum dot devices. *Applied Physics Letters*, 94(12):121102, 2009.

[123] Ali W Elshaari, Iman Esmaeil Zadeh, Andreas Fognini, et al. On-chip single photon filtering and multiplexing in hybrid quantum photonic circuits. *Nature communications*, 8(1):379, 2017.

[124] IP Kaminow, V Ramaswamy, RV Schmidt, and EH Turner. Lithium niobate ridge waveguide modulator. *Applied Physics Letters*, 24(12):622–624, 1974.

[125] L Young, WKY Wong, MLW Thewalt, and WD Cornish. Theory of formation of phase holograms in lithium niobate. *Applied Physics Letters*, 24(6):264–265, 1974.

[126] Wolfgang Sohler, Hui Hu, Raimund Ricken, et al. Integrated optical devices in lithium niobate. *Optics and Photonics News*, 19(1):24–31, 2008.

[127] Marco Bazzan and Cinzia Sada. Optical waveguides in lithium niobate: Recent developments and applications. *Applied Physics Reviews*, 2(4):040603, 2015.

[128] S Tanzilli, W Tittel, H De Riedmatten, et al. Ppln waveguide for quantum communication. *The European Physical Journal D-Atomic, Molecular, Optical and Plasma Physics*, 18(2):155–160, 2002.

[129] Anthony Martin, Olivier Alibart, MP De Micheli, DB Ostrowsky, and Sébastien Tanzilli. A quantum relay chip based on telecommunication integrated optics technology. *New Journal of Physics*, 14(2):025002, 2012.

[130] Olivier Alibart, Daniel Barry Ostrowsky, Pascal Baldi, and Sébastien Tanzilli. High-performance guided-wave asynchronous heralded single-photon source. *Optics letters*, 30(12):1539–1541, 2005.

[131] Han Chuen Lim, Akio Yoshizawa, Hidemi Tsuchida, and Kazuro Kikuchi. Stable source of high quality telecom-band polarization-entangled photon-pairs based on a single, pulse-pumped, short ppln waveguide. *Optics express*, 16(17):12460–12468, 2008.

[132] Han Chuen Lim, Akio Yoshizawa, Hidemi Tsuchida, and Kazuro Kikuchi. Wavelength-multiplexed entanglement distribution. *Optical Fiber Technology*, 16(4):225–235, 2010.

[133] Jonathan P Dowling. Quantum optical metrology–the lowdown on high-n00n states. *Contemporary physics*, 49(2):125–143, 2008.

[134] Regina Kruse, Linda Sansoni, Sebastian Brauner, et al. Dual-path source engineering in integrated quantum optics. *Physical Review A*, 92(5):053841, 2015.

[135] Frank Setzpfandt, Alexander S Solntsev, James Titchener, et al. Tunable generation of entangled photons in a nonlinear directional coupler. *Laser & Photonics Reviews*, 10(1):131–136, 2016.

[136] Moritz Mehmet, Stefan Ast, Tobias Eberle, et al. Squeezed light at 1550 nm with a quantum noise reduction of 12.3 db. *Optics express*, 19(25):25763–25772, 2011.

[137] Zhao Jun-Jun, Guo Xiao-Min, Wang Xu-Yang, et al. Continuous variable entanglement distribution for long-distance quantum communication. *Chinese Physics Letters*, 30(6):060302, 2013.

[138] Matthias Ulrich Staudt, Sara Rose Hastings-Simon, M Nilsson, et al. Fidelity of an optical memory based on stimulated photon echoes. *Physical review letters*, 98(11):113601, 2007.

[139] Alp Sipahigil, Michael Lurie Goldman, Emre Togan, et al. Quantum interference of single photons from remote nitrogen-vacancy centers in diamond. *Physical review letters*, 108(14):143601, 2012.

[140] Elena Durán-Valdeiglesias, Weiwei Zhang, Adrien Noury, et al. Integration of carbon nanotubes in silicon strip and slot waveguide micro-ring resonators. *IEEE Transactions on Nanotechnology*, 15(4):583–589, 2016.

[141] Brahim Lounis and William E Moerner. Single photons on demand from a single molecule at room temperature. *Nature*, 407(6803):491, 2000.

[142] J Hwang and EA Hinds. Dye molecules as single-photon sources and large optical nonlinearities on a chip. *New Journal of Physics*, 13(8):085009, 2011.

[143] Brahim Lounis and Michel Orrit. Single-photon sources. *Reports on Progress in Physics*, 68(5):1129, 2005.

[144] Joshua W Silverstone, Raffaele Santagati, Damien Bonneau, et al. Qubit entanglement between ring-resonator photon-pair sources on a silicon chip. *Nature communications*, 6:7948, 2015.

[145] David J Moss, Roberto Morandotti, Alexander L Gaeta, and Michal Lipson. New cmos-compatible platforms based on silicon nitride and hydex for nonlinear optics. *Nature photonics*, 7(8):597, 2013.

[146] Alberto Politi, Martin J Cryan, John G Rarity, Siyuan Yu, and Jeremy L O'brien. Silica-on-silicon waveguide quantum circuits. *Science*, 320(5876):646–649, 2008.

[147] Alexander L Gaeta, Michal Lipson, and Tobias J Kippenberg. Photonic-chip-based frequency combs. *Nature Photonics*, 13(3):158, 2019.

[148] Amir Arbabi and Lynford L Goddard. Measurements of the refractive indices and thermo-optic coefficients of si 3 n 4 and sio x using microring resonances. *Optics letters*, 38(19):3878–3881, 2013.

[149] G Cocorullo and I Rendina. Thermo-optical modulation at 1.5 mu m in silicon etalon. *Electronics Letters*, 28(1):83–85, 1992.

[150] Carsten Schuck, Xiang Guo, Linran Fan, et al. Quantum interference in heterogeneous superconducting-photonic circuits on a silicon chip. *Nature communications*, 7:10352, 2016.

[151] Martijn JR Heck, Jared F Bauters, Michael L Davenport, et al. Hybrid silicon photonic integrated circuit technology. *IEEE Journal of Selected Topics in Quantum Electronics*, 19(4):6100117–6100117, 2013.

[152] Lorenzo Pavesi, David J Lockwood, et al. Silicon photonics iii. *Topics in applied physics*, 119, 2016.

[153] SN Dorenbos, EM Reiger, U Perinetti, et al. Low noise superconducting single photon detectors on silicon. *Applied Physics Letters*, 93(13):131101, 2008.

[154] John E Bowers. Iii-v photonic integration on silicon, February 7 2012. US Patent 8,110,823.

[155] Hiroki Takesue, Yasuhiro Tokura, Hiroshi Fukuda, et al. Entanglement generation using silicon wire waveguide. *Applied Physics Letters*, 91(20):201108, 2007.

[156] Xiang Zhang, Yanbing Zhang, Chunle Xiong, and Benjamin J Eggleton. Correlated photon pair generation in low-loss double-stripe silicon nitride waveguides. *Journal of Optics*, 18(7):074016, 2016.

[157] Sven Ramelow, Alessandro Farsi, Stéphane Clemmen, et al. Silicon-nitride platform for narrowband entangled photon generation. *arXiv preprint arXiv:1508.04358*, 2015.

[158] Stefano Azzini, Davide Grassani, Matteo Galli, et al. Stimulated and spontaneous four-wave mixing in silicon-on-insulator coupled photonic wire nano-cavities. *Applied Physics Letters*, 103(3):031117, 2013.

[159] Graham D Marshall, Alberto Politi, Jonathan CF Matthews, et al. Laser written waveguide photonic quantum circuits. *Optics express*, 17(15):12546–12554, 2009.

[160] Raffaele Santagati, Joshua W Silverstone, MJ Strain, et al. Silicon photonic processor of two-qubit entangling quantum logic. *Journal of Optics*, 19(11):114006, 2017.

[161] Simeon Bogdanov, MY Shalaginov, Alexandra Boltasseva, and Vladimir M Shalaev. Material platforms for integrated quantum photonics. *Optical Materials Express*, 7(1):111–132, 2017.

[162] Yonatan Israel, Shamir Rosen, and Yaron Silberberg. Supersensitive polarization microscopy using noon states of light. *Physical review letters*, 112(10):103604, 2014.

[163] Graham T Reed and Andrew P Knights. *Silicon photonics: an introduction*. John Wiley & Sons, 2004.

[164] Maria Stepanova and Steven Dew. *Nanofabrication: techniques and principles*. Springer Science & Business Media, 2011.

[165] Mohammad Ali Mohammad, Mustafa Muhammad, Steven K Dew, and Maria Stepanova. Fundamentals of electron beam exposure and development. In *Nanofabrication*, pages 11–41. Springer, 2012.

[166] ZEONREX Electronic Chemicals. *ZEP520A Technical Report*.

[167] Nanobeam ltd. `http://www.nanobeam.co.uk/`. Accessed: 2019-07-01.

[168] gdspy python library. `https://github.com/heitzmann/gdspy`. Accessed: 2019-07-12.

[169] Dirk Taillaert, Peter Bienstman, and Roel Baets. Compact efficient broadband grating coupler for silicon-on-insulator waveguides. *Optics letters*, 29(23):2749–2751, 2004.

[170] Daniel Benedikovic, Pavel Cheben, Jens H Schmid, et al. Subwavelength index engineered surface grating coupler with sub-decibel efficiency for 220-nm silicon-on-insulator waveguides. *Optics express*, 23(17):22628–22635, 2015.

[171] Frederik Van Laere, Tom Claes, Jonathan Schrauwen, et al. Compact focusing grating couplers for silicon-on-insulator integrated circuits. *IEEE Photonics Technology Letters*, 19(23):1919–1921, 2007.

[172] Fdtd solutions, lumerical solutions, inc. `http://www.lumerical.com`. Accessed: 2019-08-01.

[173] Guy Beadie, Michael Brindza, Richard A Flynn, A Rosenberg, and James S Shirk. Refractive index measurements of poly (methyl methacrylate)(pmma) from 0.4–1.6 μm. *Applied optics*, 54(31):F139–F143, 2015.

[174] Jared F Bauters, Martijn JR Heck, Demis John, et al. Ultra-low-loss high-aspect-ratio si 3 n 4 waveguides. *Optics express*, 19(4):3163–3174, 2011.

[175] C Koos, L Jacome, C Poulton, J Leuthold, and W Freude. Nonlinear silicon-on-insulator waveguides for all-optical signal processing. *Optics Express*, 15(10):5976–5990, 2007.

[176] Wim Bogaerts, Peter De Heyn, Thomas Van Vaerenbergh, et al. Silicon microring resonators. *Laser & Photonics Reviews*, 6(1):47–73, 2012.

[177] Z Vernon, M Liscidini, and JE Sipe. No free lunch: the trade-off between heralding rate and efficiency in microresonator-based heralded single photon sources. *Optics letters*, 41(4):788–791, 2016.

[178] Xiyuan Lu, Steven Rogers, Thomas Gerrits, et al. Heralding single photons from a high-q silicon microdisk. *Optica*, 3(12):1331–1338, 2016.

[179] Maxim Greenberg and Meir Orenstein. Multimode add-drop multiplexing by adiabatic linearly tapered coupling. *Optics express*, 13(23):9381–9387, 2005.

[180] Jing Wang, Yi Xuan, Minghao Qi, et al. Broadband and fabrication-tolerant on-chip scalable mode-division multiplexing based on mode-evolution counter-tapered couplers. *Optics letters*, 40(9):1956–1959, 2015.

[181] Huiye Qiu, Jianfei Jiang, Ting Hu, et al. Silicon add-drop filter based on multimode bragg sidewall gratings and adiabatic couplers. *Journal of Lightwave Technology*, 35(9):1705–1709, 2017.

[182] Lucas B Soldano and Erik CM Pennings. Optical multi-mode interference devices based on self-imaging: principles and applications. *Journal of lightwave technology*, 13(4):615–627, 1995.

[183] Erika Andersson, Tommaso Calarco, Ron Folman, et al. Multimode interferometer for guided matter waves. *Physical review letters*, 88(10):100401, 2002.

[184] Comsol multiphysics, comsol group. `https://www.comsol.com/`. Accessed: 2019-08-01.

[185] Mateusz Piekarek, Damien Bonneau, Shigehito Miki, et al. High-extinction ratio integrated photonic filters for silicon quantum photonics. *Optics letters*, 42(4):815–818, 2017.

[186] Xu Wang, Wei Shi, Raha Vafaei, Nicolas AF Jaeger, and Lukas Chrostowski. Uniform and sampled bragg gratings in soi strip waveguides with sidewall corrugations. *IEEE Photonics Technology Letters*, 23(5):290–292, 2010.

[187] Diego Pérez-Galacho, Carlos Alonso-Ramos, Florent Mazeas, et al. Optical pump-rejection filter based on silicon sub-wavelength engineered photonic structures. *Optics letters*, 42(8):1468–1471, 2017.

[188] Charalambos Klitis, Giuseppe Cantarella, Michael J Strain, and Marc Sorel. High-extinction-ratio te/tm selective bragg grating filters on silicon-on-insulator. *Optics letters*, 42(15):3040–3043, 2017.

[189] Fengnian Xia, Mike Rooks, Lidija Sekaric, and Yurii Vlasov. Ultra-compact high order ring resonator filters using submicron silicon photonic wires for on-chip optical interconnects. *Optics express*, 15(19):11934–11941, 2007.

[190] Po Dong, Ning-Ning Feng, Dazeng Feng, et al. Ghz-bandwidth optical filters based on high-order silicon ring resonators. *Optics express*, 18(23):23784–23789, 2010.

[191] Yunhong Ding, Minhao Pu, Liu Liu, et al. Bandwidth and wavelength-tunable optical bandpass filter based on silicon microring-mzi structure. *Optics express*, 19(7):6462–6470, 2011.

[192] Folkert Horst, William MJ Green, Solomon Assefa, et al. Cascaded mach-zehnder wavelength filters in silicon photonics for low loss and flat pass-band wdm (de-) multiplexing. *Optics express*, 21(10):11652–11658, 2013.

[193] J Wang, I Glesk, and LR Chen. Subwavelength grating bragg grating filters in silicon-on-insulator. *Electronics Letters*, 51(9):712–714, 2015.

[194] Zhi Zou, Linjie Zhou, Minjuan Wang, Kan Wu, and Jianping Chen. Tunable spiral bragg gratings in 60-nm-thick silicon-on-insulator strip waveguides. *Optics express*, 24(12):12831–12839, 2016.

[195] Zeqin Lu, Jaspreet Jhoja, Jackson Klein, et al. Performance prediction for silicon photonics integrated circuits with layout-dependent correlated manufacturing variability. *Optics express*, 25(9):9712–9733, 2017.

[196] Ashish M Vengsarkar, Paul J Lemaire, Justin B Judkins, et al. Long-period fiber gratings as band-rejection filters. *Journal of lightwave technology*, 14(1):58–65, 1996.

[197] Natalia M Litchinitser, Benjamin J Eggleton, and Govind P Agrawal. Dispersion of cascaded fiber gratings in wdm lightwave systems. *Journal of lightwave technology*, 16(8):1523–1529, 1998.

[198] Francois Ouellette. Dispersion cancellation using linearly chirped bragg grating filters in optical waveguides. *Optics letters*, 12(10):847–849, 1987.

[199] Jonathan St-Yves, Hadi Bahrami, Philippe Jean, Sophie LaRochelle, and Wei Shi. Widely bandwidth-tunable silicon filter with an unlimited free-spectral range. *Optics letters*, 40(23):5471–5474, 2015.

[200] Jun Rong Ong, Ranjeet Kumar, and Shayan Mookherjea. Ultra-high-contrast and tunable-bandwidth filter using cascaded high-order silicon microring filters. *IEEE Photonics Technology Letters*, 25(16):1543–1546, 2013.

[201] Michael L Cooper, Greeshma Gupta, Mark A Schneider, et al. Statistics of light transport in 235-ring silicon coupled-resonator optical waveguides. *Optics express*, 18(25):26505–26516, 2010.

[202] Pochi Yeh et al. *Optical waves in layered media*, volume 95. Wiley Online Library, 1988.

[203] Jia-Ming Liu. *Principles of photonics*. Cambridge University Press, 2016.

[204] Amnon Yariv. Coupled-mode theory for guided-wave optics. *IEEE Journal of Quantum Electronics*, 9(9):919–933, 1973.

[205] Shengjie Xie, Jiahao Zhan, Yiwen Hu, et al. Add–drop filter with complex waveguide bragg grating and multimode interferometer operating on arbitrarily spaced channels. *Optics letters*, 43(24):6045–6048, 2018.

[206] Dorian Oser, Diego Pérez-Galacho, Carlos Alonso-Ramos, et al. Subwavelength engineering and asymmetry: two efficient tools for sub-nanometer-bandwidth silicon bragg filters. *Optics letters*, 43(14):3208–3211, 2018.

[207] Huiye Qiu, Jianfei Jiang, Ping Yu, et al. Silicon band-rejection and band-pass filter based on asymmetric bragg sidewall gratings in a multimode waveguide. *Optics letters*, 41(11):2450–2453, 2016.

[208] Jiří Čtyrokỳ, Juan Gonzalo Wangüemert-Pérez, Pavel Kwiecien, et al. Design of narrowband bragg spectral filters in subwavelength grating metamaterial waveguides. *Optics express*, 26(1):179–194, 2018.

[209] Robert Halir, Przemek J Bock, Pavel Cheben, et al. Waveguide sub-wavelength structures: a review of principles and applications. *Laser & Photonics Reviews*, 9(1):25–49, 2015.

[210] R Halir, I Molina-Fernández, JG Wangüemert-Pérez, et al. Characterization of integrated photonic devices with minimum phase technique. *Optics express*, 17(10):8349–8361, 2009.

[211] M Gnan, WCL Hopman, Gaetano Bellanca, et al. Closure of the stop-band in photonic wire bragg gratings. *Optics express*, 17(11):8830–8842, 2009.

[212] Xu Wang, Yun Wang, Jonas Flueckiger, et al. Precise control of the coupling coefficient through destructive interference in silicon waveguide bragg gratings. *Optics letters*, 39(19):5519–5522, 2014.

[213] Xiaomin Nie, Nina Turk, Yang Li, Zuyang Liu, and Roel Baets. High extinction ratio on-chip pump-rejection filter based on cascaded grating-assisted contradirectional couplers in silicon nitride rib waveguides. *Optics letters*, 44(9):2310–2313, 2019.

[214] Mustafa Hammood, Ajay Mistry, Minglei Ma, et al. Compact, silicon-on-insulator, series-cascaded, contradirectional-coupling-based filters with¿ 50 db adjacent channel isolation. *Optics letters*, 44(2):439–442, 2019.

[215] Jia-Ming Liu. *Photonic devices*. Cambridge University Press, 2009.

[216] Marcel W Pruessner, Todd H Stievater, and William S Rabinovich. Integrated waveguide fabry-perot microcavities with silicon/air bragg mirrors. *Optics letters*, 32(5):533–535, 2007.

[217] Y Painchaud, M Poulin, C Latrasse, and M-J Picard. Bragg grating based fabry-perot filters for characterizing silicon-on-insulator waveguides. In *The 9th International Conference on Group IV Photonics (GFP)*, pages 180–182. IEEE, 2012.

[218] Pavel Cheben, Robert Halir, Jens H Schmid, Harry A Atwater, and David R Smith. Subwavelength integrated photonics. *Nature*, 560(7720):565, 2018.

[219] Huiye Qiu, Guomin Jiang, Ting Hu, et al. Fsr-free add–drop filter based on silicon grating-assisted contradirectional couplers. *Optics letters*, 38(1):1–3, 2013.

[220] J. D. Franson. Bell inequality for position and time. *Physical Review Letters*, 62:2205–2208, 1989.

[221] Eugenio Iannone. *Telecommunication Networks*. CRC Press, 2011.

[222] Nobuyuki Matsuda, Peter Karkus, Hidetaka Nishi, et al. On-chip generation and demultiplexing of quantum correlated photons using a silicon-silica monolithic photonic integration platform. *Opt. Express*, 22:22831–22840, 2014.

[223] Artur K. Ekert. Quantum cryptography based on bell's theorem. *Physics Review Letters*, 67:661–663, 1991.

[224] Klaus Mattle, Harald Weinfurter, Paul G. Kwiat, and Anton Zeilinger. Dense coding in experimental quantum communication. *Physics Review Letters*, 76:4656–4659, 1996.

[225] H. de Riedmatten, I. Marcikic, W. Tittel, et al. Long distance quantum teleportation in a quantum relay configuration. *Physics Review Letters*, 92:047904, 2004.

[226] Florian Kaiser, Panagiotis Vergyris, Djeylan Aktas, et al. Quantum enhancement of accuracy and precision in optical interferometry. *Light: Science & Applications*, 7(3):17163, 2018.

[227] Vilson R Almeida and Michal Lipson. Optical bistability on a silicon chip. *Optics letters*, 29(20):2387–2389, 2004.

[228] Thomas J Johnson, Matthew Borselli, and Oskar Painter. Self-induced optical modulation of the transmission through a high-q silicon microdisk resonator. *Optics express*, 14(2):817–831, 2006.

[229] Stefano Azzini, Davide Grassani, Michael J. Strain, et al. Ultra-low power generation of twin photons in a compact silicon ring resonator. *Opt. Express*, 20:23100–23107, 2012.

[230] Wei C. Jiang, Xiyuan Lu, Jidong Zhang, Oskar Painter, and Qiang Lin. Silicon-chip source of bright photon pairs. *Optics Express*, 23:20884, August 2015.

[231] Ryota Wakabayashi, Mikio Fujiwara, Ken ichiro Yoshino, et al. Time-bin entangled photon pair generation from si micro-ring resonator. *Opt. Express*, 23:1103–1113, 2015.

[232] Jing Suo, Shuai Dong, Wei Zhang, Yidong Huang, and Jiangde Peng. Generation of hyper-entanglement on polarization and energy-time based on a silicon micro-ring cavity. *Optics Express*, 23(4):3985, 2015.

[233] R. Santagati, J. W. Silverstone, M. J. Strain, et al. Silicon photonic processor of two-qubit entangling quantum logic. *J. Opt.*, 19(11):114006, 2017.

[234] Yuan Guo, Wei Zhang, Ning Lv, et al. The impact of nonlinear losses in the silicon micro-ring cavities on cw pumping correlated photon pair generation. *Optics express*, 22(3):2620–2631, 2014.

[235] Leonard Mandel and Emil Wolf. *Optical coherence and quantum optics*. Cambridge university press, 1995.

[236] Mark Fox. *Quantum optics: an introduction*, volume 15. OUP Oxford, 2006.

[237] Lucia Caspani, Chunle Xiong, Benjamin J Eggleton, et al. Integrated sources of photon quantum states based on nonlinear optics. *Light: Science & Applications*, 6(11):e17100, 2017.

[238] Marco Liscidini and JE Sipe. Stimulated emission tomography. *Physical review letters*, 111(19):193602, 2013.

[239] W Guerin, A Dussaux, M Fouché, et al. Temporal intensity interferometry: photon bunching in three bright stars. *Monthly Notices of the Royal Astronomical Society*, 472(4):4126–4132, 2017.

[240] William Guerin, Jean-Pierre Rivet, Mathilde Fouché, et al. Spatial intensity interferometry on three bright stars. *Monthly Notices of the Royal Astronomical Society*, 480(1):245–250, 2018.

[241] Xiang Guo, Chang-ling Zou, Carsten Schuck, et al. Parametric down-conversion photon-pair source on a nanophotonic chip. *Light: Science & Applications*, 6(5):e16249, 2017.

[242] Stefano Azzini, Davide Grassani, Matteo Galli, et al. From classical four-wave mixing to parametric fluorescence in silicon microring resonators. *Optics letters*, 37(18):3807–3809, 2012.

[243] Wei C Jiang, Xiyuan Lu, Jidong Zhang, Oskar Painter, and Qiang Lin. Silicon-chip source of bright photon pairs. *Optics express*, 23(16):20884–20904, 2015.

[244] Davide Grassani, Angelica Simbula, Stefano Pirotta, et al. Energy correlations of photon pairs generated by a silicon microring resonator probed by stimulated four wave mixing. *Scientific reports*, 6:23564, 2016.

[245] Ryota Wakabayashi, Mikio Fujiwara, Ken-ichiro Yoshino, et al. Time-bin entangled photon pair generation from si micro-ring resonator. *Optics express*, 23(2):1103–1113, 2015.

[246] Stefan F Preble, Michael L Fanto, Jeffrey A Steidle, et al. On-chip quantum interference from a single silicon ring-resonator source. *Physical Review Applied*, 4(2):021001, 2015.

[247] J. W. Silverstone, D. Bonneau, K. Ohira, et al. On-chip quantum interference between silicon photon-pair sources. *Nature Photonics*, 8:104, December 2013.

[248] Imad I Faruque, Gary F Sinclair, Damien Bonneau, John G Rarity, and Mark G Thompson. On-chip quantum interference with heralded photons from two independent micro-ring resonator sources in silicon photonics. *Optics Express*, 26(16):20379–20395, 2018.

[249] Robert Thomas Thew, Sébastien Tanzilli, Wolfgang Tittel, Hugo Zbinden, and Nicolas Gisin. Experimental investigation of the robustness of partially entangled qubits over 11 km. *Physical Review A*, 66(6):062304, 2002.

[250] S Tanzilli, W. Tittel, H. De Riedmatten, et al. Ppln waveguide for quantum communication. *The European Physical Journal D - Atomic, Molecular, Optical and Plasma Physics*, 18:155–160, 2002.

[251] Steven Rogers, Xiyuan Lu, Wei C. Jiang, and Qiang Lin. Twin photon pairs in a high-q silicon microresonator. *Applied Physics Letters*, 107(4):041102, 2015.

[252] Steven Rogers, Daniel Mulkey, Xiyuan Lu, Wei C. Jiang, and Qiang Lin. High Visibility Time-Energy Entangled Photons from a Silicon Nanophotonic Chip. *ACS Photonics*, 3(10):1754–1761, 2016.

[253] Poolad Imany, Jose A. Jaramillo-Villegas, Ogaga D. Odele, et al. 50-GHz-spaced comb of high-dimensional frequency-bin entangled photons from an on-chip silicon nitride microresonator. *Optics Express*, 26(2):1825, 2018.

[254] Meng Xiao, ZQ Zhang, and Che Ting Chan. Surface impedance and bulk band geometric phases in one-dimensional systems. *Physical Review X*, 4(2):021017, 2014.

[255] Vladimir Bužek and Mark Hillery. Quantum copying: Beyond the no-cloning theorem. *Physical Review A*, 54(3):1844, 1996.

[256] Valerio Scarani, Sofyan Iblisdir, Nicolas Gisin, and Antonio Acin. Quantum cloning. *Reviews of Modern Physics*, 77(4):1225, 2005.

Titre : Photonique silicium intégrée appliquée à l'optique quantique

Mots clés : Photonique, Silicium, Optique quantique, Guides d'ondes, SFWM, Filtre de Bragg

Résumé : La photonique silicium est un domaine prolifique de l'optique intégrée. Elle permet de miniaturiser de nombreuses fonctionnalités optiques, l'émission laser (en considérant les stratégies d'intégration hybride), la modulation électro-optique, le routage, la détection, pour les télécoms, les LIDAR ou la spectroscopie, la métrologie, les capteurs et laboratoires sur puce, tout en offrant des possibilités de fabrication à grande échelle avec une grande précision et à bas coût (grâce au technologies CMOS de la microélectronique). L'optique quantique, quant à elle, est un domaine très riche de la physique mais ses réalisations souffrent d'une grande sensibilité aux vibrations et à l'environnement. Les montages optiques nécessitent en effet, stabilité, alignements parfaits et un grand nombre d'éléments optiques, ce qui limite son développement à grande échelle. Inversement, tous ces aspects sont naturels en photonique intégrée. Le développement de la photonique quantique est ainsi susceptible de permettre l'implémentation à large échelle des systèmes de clés de cryptage pour les télécoms et le calcul quantique. Les prérequis de la photonique quantique sont globalement plus sévères que ceux de la photonique classique. La génération d'états quantiques nécessite notamment un niveau de réjection de la pompe de plus de 100 dB ; le niveau de bruit photonique ambiant sur la puce est également un facteur à soigner particulièrement dans la mesure où les paires de photons générées par les processus quantiques sont par principe de très faible puissance. Dans ce contexte, cette thèse aborde le développement de composants et de circuits pour la photonique quantique silicium. Le but est de générer des états intriqués en énergie-temps et de pouvoir les manipuler sur une puce. Cela va de la conception à l'utilisation des paires de photons, en passant par la fabrication des circuits intégrés optiques. La qualification des propriétés quantiques est aussi explorée afin de cerner les limitations de la plateforme silicium pour le domaine applicatif visé. L'esprit de ce travail est également de proposer des solutions restant compatibles avec les canaux de télécommunications standard (ITU), de n'utiliser que des composants fibrés standards pour les connexions à réaliser, tout en restant compatibles avec les techniques de fabrication industrielle des grandes fonderies microélectroniques afin de permettre une future production à grand échelle des circuits photoniques quantiques.

Title : Integrated silicon photonics for quantum optics

Keywords : Photonic, Silicon, Quantum, Waveguide, SFWM, Bragg Filter

Abstract : Silicon photonics is a dynamic research field of integrated optics. It allows to miniaturize numerous optical functionalities such as lasers, electro-optical modulators, routers, detectors, for telecom wavelengths, LIDAR, sensing, metrology or even spectroscopy, all while being able to propose large scale production with high precision technologies. On another side, quantum optics suffers from difficulties to scale optical systems, requires extreme stability, perfect alignment, and many bulky optical elements, while solving these issues follows a natural path in integrated photonics. Development of integrated quantum photonics can thus open the door to cheap, powerful, and scalable systems for quantum cryptography, telecoms, and computation. In a significant way, quantum requirements are not the ones of classical circuits with respect to photonic components and circuits. The generation of quantum states indeed requires more than 100 dB of pump laser rejection, while being able to manage ultra-low useful optical signals and get rid of on-chip optical noise. In this context, this thesis is dedicated to the study, design, realization, and characterization of silicon photonic components and circuits for quantum optics on a chip. The target goal is to generate entangled states in energy-time and manipulate them on chip. The qualification of the quantum properties is also explored to better understand the limitations of the silicon platform in the followed objectives. Another choice of this work is to stay in telecom wavelengths aligned with the standard channels (ITU grid), to only use "off-the-shelf" components, all while compliant with standard fabrication processes, this to allow the possibility to produce on large scales.

Université Paris-Saclay
Espace Technologique / Immeuble Discovery
Route de l'Orme aux Merisiers RD 128 / 91190 Saint-Aubin, France